

Microwave Imaging of Brain Stroke: Contributions to Modeling and Inverse Problem Resolution

THÈSE N° 8511 (2018)

PRÉSENTÉE LE 8 JUIN 2018

À LA FACULTÉ DES SCIENCES ET TECHNIQUES DE L'INGÉNIEUR
LABORATOIRE DE TRAITEMENT DES SIGNAUX 5
PROGRAMME DOCTORAL EN GÉNIE ÉLECTRIQUE

ÉCOLE POLYTECHNIQUE FÉDÉRALE DE LAUSANNE

POUR L'OBTENTION DU GRADE DE DOCTEUR ÈS SCIENCES

PAR

Mina BJELOGRLIC

acceptée sur proposition du jury:

Prof. A. Skrivervik, présidente du jury
Prof. J.-Ph. Thiran, Dr M. Mattes, directeurs de thèse
Prof. R. Cruz Conceição, rapporteuse
Dr L. Crocco, rapporteur
Prof. D. Atienza Alonzo, rapporteur



ÉCOLE POLYTECHNIQUE
FÉDÉRALE DE LAUSANNE

Suisse
2018

Abstract

Brain stroke is an age-related illness which has become a major issue in our ageing societies. Early diagnostic and treatment are of high importance for the full recovery of the patient, as reminded in Anglo-Saxon countries by the abbreviation FAST (Face, Arm, Speech, Time) referring to both the four major visible signs, and the necessity to act fast. In this respect, Computed Tomography (CT) and Nuclear Magnetic Resonance (NMR) imaging are key diagnostic tools in clinical practice. Unfortunately, not only these modalities can neither be transported nor rapidly usable, which would allow early treatment (especially in rural environments), but also cannot be brought to the bedside of the patient to monitor the evolution of the disease. Microwave Imaging (MWI) is a potential candidate to provide fast and accurate diagnostic insights for brain stroke pathological states. The head of the patient is illuminated with low-power microwave waveforms (non-ionizing radiations), whose backscattered signals are used to generate either images of its internal structures, distributions, patterns and shapes (qualitative imaging) or directly its physical parameters such as the dielectric contrast and the permittivity values (quantitative imaging). The technology relies on the high sensitivity of microwaves on the water content of tissues to allow for the discrimination between pathological and healthy regions.

This thesis focuses on both the forward modeling of the electromagnetic phenomena arising in biological tissues and the inverse scattering problem for imaging in the differential MWI (dMWI) scenario for brain stroke monitoring. It is intrinsically interdisciplinary as it requires knowledge in Biology, Medicine, Physics, Chemistry, and Engineering.

In order to investigate the challenges arising in brain MWI, it is crucial to have accurate and efficient solvers to model electromagnetic (EM) fields at UHF/SHF-bands. The head is a distributed, heterogeneous, and lossy scatterer for which existing solvers are known to struggle at higher frequencies. Volume Integral Equation (VIE) formulations and MultiGrid (MG) approaches are investigated to find the actual solution of the field distributions for large scale problems.

The EM modeling also permits to analyze the feasibility of brain MWI, which depends on the power transmission from the antennas towards the human brain. In order to estimate this transmission, simplified but still representative models, including intermediate layers - skin, fat, bone, and CerebroSpinal Fluid (CSF) - of the head, are proposed in the framework of simulations (analytical tools) and experimental validations (3D printed head phantom).

For the imaging task, the physics of the EM scattering, leads to complex non-linear inverse

scattering problems (consisting in retrieving from a set of field measurements the physical parameters which produced them) for which reliable assumptions and approximations must be found. For brain MWI, estimating and quantifying the degree of non-linearity allows for determining the scope of application of existing algorithms, for which different regularizers are applied.

Modeling and inverse problem resolution for brain MWI investigated in the present work are ultimately meant to contribute to the development of a technology dedicated to brain stroke detection, differentiation, and monitoring.

Key words: Computational bio-electromagnetics, Volume Integral Equation (VIE), MultiGrid (MG), Acute Cerebrovascular Diseases (CVDs), differential Microwave Imaging (dMWI), Brain Stroke Monitoring, Degree of Non-Linearity (DNL), Spherical Wave Expansion (SWE), 3D printed phantom.

Résumé

L'Accident Vasculaire Cérébral (AVC) touche principalement les personnes âgées et est, pour cette raison, un enjeu majeur dans nos sociétés vieillissantes. Le diagnostic et le traitement rapide de cette pathologie sont indispensables pour le rétablissement complet du patient, comme le rappelle l'acronyme anglais FAST qui fait référence tant aux quatre symptômes visibles de la maladie (Face - visage, Arm - bras, Speech - parole, Time - temps) qu'à la nécessité d'une intervention rapide. A l'heure actuelle, ce sont principalement la scanographie et l'Imagerie par Résonance Magnétique (IRM) qui sont utilisées pour établir un diagnostic. Toutefois, ces dispositifs ne sont ni facilement transportables, ni rapidement utilisables (et ce surtout en milieu rural) et ne peuvent donc pas être amenés au chevet du patient pour suivre l'évolution de la maladie.

Une solution pour palier à ces inconvénients majeurs pourrait résider dans l'utilisation de l'imagerie hyperfréquence. Cette méthode consiste à soumettre la tête du patient à des micro-ondes de faible puissance (aux rayonnements non-ionisants), dont les signaux diffractés sont utilisés pour générer les images des structures internes, leurs répartitions et leurs formes (imagerie qualitative), voire directement des paramètres physiques tels que le contraste diélectrique et les valeurs de permittivité (imagerie quantitative). Cette technologie se base sur la sensibilité élevée des micro-ondes à la teneur en eau des tissus, laquelle est supposée varier de façon notable entre régions pathogène et saine.

Le présent ouvrage sera essentiellement consacré à la modélisation des phénomènes électromagnétiques ainsi qu'à la résolution du problème inverse que suscite l'imagerie hyperfréquence différentielle pour le suivi des AVC. Ce domaine est intrinsèquement interdisciplinaire puisqu'il demande à la fois des connaissances en biologie, en médecine, en chimie et en ingénierie.

L'étude de l'imagerie hyperfréquence cérébrale requiert des solveurs précis et efficaces de modélisation des champs électromagnétiques (EM) pour les bandes UHF / SHF. En effet, la tête étant une répartition hétérogène de milieux à pertes, les solveurs de modélisation EM peinent à converger. La formulation en Equations Integrales Volumiques (VIE) et un solveur basé sur une approche Multi-Grille (MG) sont étudiés pour trouver la distribution du champs pour des problèmes à grand nombre d'inconnues.

La modélisation EM permet également d'analyser la faisabilité de l'imagerie hyperfréquence qui dépend de la transmission du signal dans le cerveau. Le présent ouvrage propose des modèles simplifiés de têtes humaines, incluant les couches intermédiaires (peau, graisse, os,

liquide céphalorachidien), qui permettent l'analyse et l'appréciation des ordres de grandeur de la puissance transmise. Ces modèles peuvent être utilisés, soit dans le cadre de simulations (outil analytique), soit pour des expériences pratiques (au moyen d'un fantôme de tête).

Pour la résolution du problème inverse (retrouver sur la base de mesures les paramètres qui les ont induites) en vue d'obtenir une image, la physique de la diffusion EM conduit à des problèmes complexes et non linéaires pour lesquels sont souvent utilisés des hypothèses et des approximations. En matière d'imagerie hyperfréquences cérébrale, l'estimation et la quantification du degré de non-linéarité permet de déterminer la plage de résolution du problème inverse d'imagerie pour laquelle plusieurs approches d'inversion à l'aide de régulariseurs sont appliquées.

La modélisation et la résolution du problème inverse, auxquelles contribue le présent ouvrage, servent *in fine* à développer une technologie dédiée à la détection, la différenciation, et le suivi des AVC.

Mots clefs : Bio-électromagnétisme computationnel, Equations Integrales Volumiques, Multi-Grille (MG), Accident Vasculaire Cérébral (AVC), Imagerie hyperfréquence différentielle, Suivi des AVC, Degré de Non-Linéarité (DNL), Décomposition en harmoniques sphériques, fantôme basé sur l'impression 3D.

Acknowledgements

This thesis is the result of a personal continuous will and effort, nonetheless, it would have been impossible without the trust, the guidance and the never-ending inspiration of discrete personalities to which I have the sincere need of expressing my deep gratitude.

First of all, I would like to thank my supervisor Prof Juan Mosig. Among so many other contributions, you inspired me during my Bachelor and Master studies and through the wise hands of Ruzica and Marc, you introduced me to the LEMA projects and people. I thank Prof Jean-Philippe Thiran for welcoming my last year of PhD in LTS5 which such an ease and I am very glad to have met such an amazing group.

I cannot find words strong enough to describe the respect and gratitude I have towards Prof. Michael Mattes. The availability to discuss all the scientific problems with such vivacity and interest gave me the motivation to do research during the last 4 years. Also, I need to express here my gratitude to my unofficial but very present co-supervisor PhD Benjamin Fuchs. He introduced me to inverse problem challenges and was always available for giving helpful advices and ensured remotely that the thesis would advance in a positive way.

I would like to thank the COST MiMed which permitted me to speak on regular bases to the MicroWave Imaging community. A special thank goes to Prof Raquel Cruz Conceição and PhD Lorenzo Crocco for coming to Lausanne to be part of my jury. I would like to thank Prof David Atienza Alonzo and Prof Anja Skrivervik for representing EPFL at my oral exam and for being such inspiring professors during my studies.

I would like to thank the LEMA friendships that I have made during my first three years of PhD. I will start with Jovance which from the beginning became a dear friend. Santiago, thank you for your help, advices and friendship. My office mates first Apo, and then Anton with whom coming to work was a pleasure. Ioannis, Lei, Joana, Esteban, María, Marc, Nuno, Rafal, Danelys, Miroslav, Tanja, Michele, Roberto, Pietro, Baptiste, Eduardo, Mohsens, Hamed, Tomislav, Przemek, Ismael it was a pleasure working in the same laboratory. A special thanks goes to the LEMA satellites Nevena and Erwan. I would also like to thank the LTS5 people for welcoming me in such a nice way. Gabriel thank you for your long friendship and your help for the abstract. Marina, Vijay, Murat, Christophe, Saleh, Saeed, Damien, Ming, Besad, Hazim thank you for the relaxing moments during the writing of the thesis. Thanks to Diffusion MRI guys, Jonathan, Gaetan, Mohammed, Marco and David for the soccer energetic breaks, and to the US group, Florian, Dimitris and Adrien it was nice having you in the open space.

I would like to especially thank Eulalia Durussel and Mercedes Quintas for their availability, sensitivity and friendship it was a pleasure working with you. Also, I would like to thank Rosie

Acknowledgements

Del Pietro for taking over my special case and making everything work so smoothly.

I would like to thank my students, and especially Maxime.

Of course, I would like to thank all my friends Chlo  , Nilou, Ben, Coralie, Charlotte, C  leste, Lara, Salim, Michael, Marija, Denis, Jane which always were here to listen to my PhD life problems, a special thanks goes to the Thursday lunch crew, Sebastien, Fran  ois and Christophe. I would like to warmly thank Daniel for reviewing the abstract.

I cannot express my gratitude to Fran  ois for being such an incredible help in all the stressful moments of this thesis. Thank you for taking the time to understand my work and help me to find words to make this thesis accessible to a wider public. Thank you Isa for all our nice conversations in between two chapters.

Last but not least I would like to thank my family. This work would not have been possible without the moral support of Relja, Nada, Ivan, Nikola and Gala. To all of you, I dedicate this thesis!

Lausanne, 6 Avril 2018

A handwritten signature in blue ink on a light blue background. The signature reads "Nina Bjelogri  ".

Contents

Abstract	i
Résumé	iii
Acknowledgements	v
1 Introduction	1
1.1 Overall View and Description of the Scientific Problem	1
1.1.1 Brain Stroke: Main Facts and Numbers	1
1.1.2 Microwave Imaging: State-of-the-art and Challenges	2
1.1.3 Computational Electromagnetics for Bio-Medical Applications	4
1.2 Objectives and Scientific Work Plan	5
1.3 Outline and Contributions	7
2 Electromagnetic Scattering in Biological Tissues	11
2.1 Brain Stroke Monitoring	11
2.1.1 Technologies for Brain Imaging	12
2.1.2 Brain Imaging Challenges	13
2.2 Governing Equations	16
2.2.1 Maxwell's Equations and Constitutive Equations	17
2.2.2 Contrast-Source Formulation	18
2.2.3 Integral Equation Approach	20
2.3 Introduction to the Forward and Inverse Problem	20
2.4 Summary	23
3 Volume Integral Operator of Electromagnetic Scattering	25
3.1 State-of-the-art and Background	26
3.1.1 Volume Integral Equation (VIE) Formulations	28
3.1.2 Towards Green Functions with Vector and Scalar Potentials	29
3.1.3 Singular Integrals	31
3.2 Numerical Solution of VIE with Method of Moments (MoM)	37
3.2.1 Discretization: Mesh and Basis Functions	38
3.2.2 Galerkin Method of Moments: Discrete Form of the Green Dyadic	39
3.2.3 Iterative Solvers	42

Contents

3.2.4	Spectrum of the Volume Integral Operator of Electromagnetic Scattering	43
3.3	Numerical Experiments: Solvers for Large Number of Unknowns	49
3.3.1	Minimal Residual (MINRES) solver	49
3.3.2	Multi-Grid (MG) solver	51
3.4	Conclusion	55
4	Design of MWI Systems for Brain Imaging	57
4.1	Models and Electromagnetic Analysis	57
4.1.1	Planar Layered Model	58
4.1.2	Spherical Layered Model	62
4.1.3	Simulation Results and Discussion	63
4.2	Experimental Validation	65
4.2.1	Liquid Body Phantoms: Realization and Characterization	65
4.2.2	Measurement Results	67
4.3	Conclusion	77
5	Microwave Inverse Scattering Problem	79
5.1	Differential Microwave Imaging Setup	80
5.1.1	Setup	80
5.1.2	Microwave Imaging: Contrast-Source Formulation	81
5.1.3	Differential Microwave Imaging Scenario	81
5.2	Non-Linearity of the Scattering Problem	84
5.2.1	Degree of Non-Linearity	84
5.2.2	Quantification of the Degree of Non Linearity for dMWI	86
5.3	Inverse Problem Resolution	89
5.3.1	Truncated Singular Value Decomposition	90
5.3.2	Regularization via Norm Minimization	91
5.4	Differential Microwave Imaging Simulations	93
5.4.1	Numerical Experiments for DNL of dMWI	95
5.4.2	Numerical Experiments for Regularization of dMWI	100
5.5	Differential Microwave Imaging Experiments	102
5.5.1	Setup Configuration	102
5.5.2	Stroke Modeling and Tissue Characterization	102
5.5.3	Regularization Techniques: Experimental Validation	104
5.6	Conclusion	110
6	Conclusions and Perspectives	111
6.1	Thesis Summary	111
6.2	Perspectives	113
	APPENDICES	115
A	Spherical Wave Expansion: Scattering Framework and Mathematical Derivation	115

B 3D Printed Phantom: Geometries, Waterproofing and Gluing Tests	121
Bibliography	140
List of Figures	141
List of Tables	147
List of Acronyms and Abbreviations	149
Curriculum Vitae	151

1 Introduction

1.1 Overall View and Description of the Scientific Problem

Medical imaging technologies are an essential tool in clinical practice, both for providing an accurate initial diagnosis and for monitoring the evolution of pathological states. For some specific illnesses, such as Acute CerebroVascular Diseases (CVDs) (also referred to as brain stroke), they still lack of fast and transportable diagnostic tools, which would allow early treatment. MicroWave Technology (MWT) is investigated as a potential candidate for detecting, discriminating, and monitoring brain strokes. For that purpose, fast and accurate computational electromagnetic solvers need to be developed, especially for bio-medical applications.

1.1.1 Brain Stroke: Main Facts and Numbers

The brain is a central organ in the human physiology, enabling thinking, speaking, moving the body, memorizing, etc. Brain illnesses can therefore be devastating and have a huge impact on the life condition of the patient. Brain stroke is a leading cause of mortality in aging societies such as the United States [1] or Europe [2, 3]. It implies an abnormal blood flow inside the head, which can cause irremediable changes or, at worst, lead to death. There are several kinds of brain strokes, with different implications and treatments. Ischaemic strokes (68 – 80%) are the most common ones and imply an obstruction in the brain's blood flow (see Fig. 1.1a). The highest mortality is due to spontaneous intercerebral haemorrhages (7 – 20%), which are caused by a sudden blood vessel burst, as depicted in Fig. 1.1b. Subarachoid haemorrhages (1 – 7%) and sinus venous thromboses (1 – 2%) are less common occurrences [4].

The prevention on the "big five" major risk factors (hypertension, smoking, sedentary life, atrial fibrillation, and diabetes) leading to brain stroke [5, 6] is a way to decrease the stroke occurrences. However, all strokes cannot be avoided. An early diagnostic is very beneficial for the full recovery of the patient [7]. Today the diagnostic is mainly based on Computed Tomography (CT) (see Fig. 1.1a) and Nuclear Magnetic Resonance (NMR) images (see Fig. 1.1b),

Chapter 1. Introduction

which are taken at the hospital [8]. However none of these imaging modalities can be brought either to the patient's bedside, or to an ambulance to ensure an early and crucial diagnostic. The diagnostic is crucial as an early thrombolytic treatment which is normally administered to cure ischaemic strokes could have a disastrous outcome if performed on a patient with haemorrhagic stroke [7].

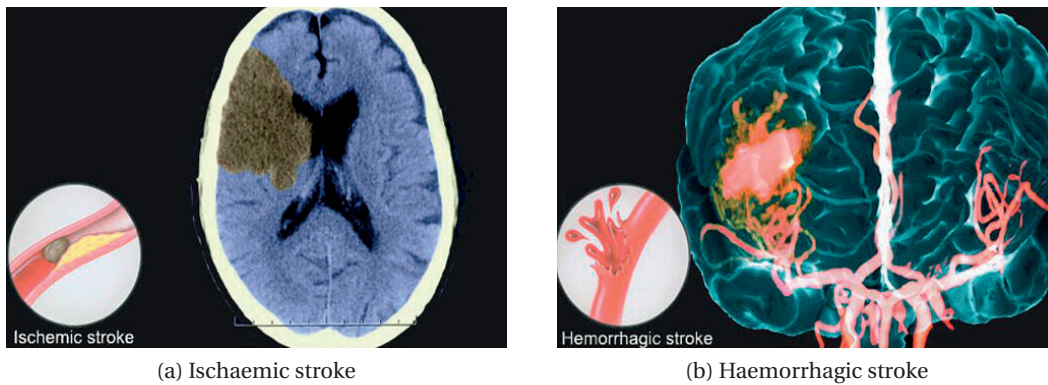


Figure 1.1 – Stroke representations [9]. CT scan of an ischaemic stroke (left) and NMR image of a haemorrhagic stroke (right) ©2016, WebMD LLC All rights reserved.

Besides the evident human impact of this pathology, it implies a prevalent annual cost (in Europe) of EUR 386 billion [3], with an average cost of EUR 22,000 per patient, without taking into account the additional social impact [4] such as work inability. Today, in Europe, CVDs are affecting 200 over 100,000 people [4] and the prediction for 2030 shows an increase of up to 40% of the stroke occurrence as the probability increases with age [10]. In our ageing society, brain stroke is today a major issue on both individual and societal scale leading to numerous research projects related to this topic [3].

1.1.2 Microwave Imaging: State-of-the-art and Challenges

Industrial, Scientific, and Medical applications in the radio frequency (RF) band (ranging from around 20 kHz to 300 GHz), excluding telecommunication applications, are known as ISM-applications. Three decades ago, the pioneering work of L.E. Larsen and J.H. Jacobi, showed the capability of imaging a dog's kidney in the S-band [11, 12]. Since then, Microwave Imaging (MWI) is considered as a tomographic modality which is able to image (in grey or color scale instead of single point measurements) the internal dielectric distribution of an object (considered as a scatterer) without altering it [13]. Quantitative imaging gives values of physical parameters such as the dielectric contrast, or the permittivity values, and qualitative imaging yields distributions, patterns and shapes [14, 15].

Microwave tomography for industrial processes [16] ranges from imaging solid, liquid or gas substances traveling in a pipeline [17], to imaging buried objects [18–20]. For biomedical

1.1. Overall View and Description of the Scientific Problem

applications, MWI involves the illumination of the portion of the body under investigation with low-power microwave waveforms (UHF/SHF-bands) and the use of the resulting backscattered signals to generate images of the internal structures of the body [14, 21, 22]. MWI is non-ionizing, low power, non-invasive and potentially low cost. These are important features to contribute to the deployment of the technology, and to the wider acceptance in terms of patient comfort. MWI is suitable for a broad range of applications including many in the context of an ageing society:

- (i) early detection and classification of breast cancer for which existing techniques fail [23, 24];
- (ii) contactless vital signs monitoring (heart and respiration) [25];
- (iii) non-invasive diagnostic methods for intracranial imaging applications and stroke detection [26, 27];
- (iv) injuries of joint tissues, such as ligaments, meniscus and cartilage (of the knee) [28];
- (v) contrast-enhanced MWI [29, 30].

MWI for brain stroke detection is getting increasingly attention as it could be a fast and portable diagnostic tool [26, 27]. Indeed, the high sensitivity of microwaves to water content could help distinguishing healthy from malignant tissues, such as tumors and brain strokes [31], to name only few. MWI, as a potentially low-cost and less cumbersome alternative technology, could be used in ambulances and at small/rural hospitals or private cabinets, and therefore provide earlier diagnostics to permit early stage treatment [32]. The two main companies present in Europe, which rely on Microwave Technology (MWT) for brain stroke related applications, are the Swedish company Medfield Diagnostics AB (StrokefinderTM) [33, 34], and an Austrian based company EMTensor GmbH (BRIMG1) [26, 35]. StrokefinderTM is used as a tool to detect and differentiate brain strokes. A classification based on machine-learning algorithms and trained on measured patient data is used to discriminate between ischaemic and haemorrhagic strokes [36]. Lately, the same device was used for investigations on Traumatic Brain Injuries (TBI) [34, 37]. As regards BRIMG1, it is a full MWI modality, in the sense that it might be able to reconstruct both quantitative and qualitative images. The solver is based on the Finite Element Method (FreeFem++ [38]), and relies on decomposing the imaging chamber domain into subdomains. This method may allow stroke detection, classification, and monitoring on a transportable device [39].

The challenges for brain stroke MWI are intrinsic to the physics of the scattering problem. Firstly, the kernel (operator describing the relation between data and unknowns) of the problem leads to ill-posed situations, for which regularization strategies need to be investigated. Secondly, the multiple scattering phenomena, which is not negligible for nonweak scatterers, result in a degree of non-linearity [40] which varies for every scattering configuration. Estimating and quantifying this parameter allows to discriminate between different potential

strategies (Compressed-Sensing (CS) [41, 42], Born [43]) to perform the imaging task [44, 45]. Also, the operating frequency and the background medium have a major impact on the performance of the overall method, and therefore investigating models to analyze the transmitted power or any related quantity is crucial [46, 47].

1.1.3 Computational Electromagnetics for Bio-Medical Applications

Bio-electromagnetics examines the electromagnetic phenomena arising in biological tissues. It is interdisciplinary and involves classical disciplines such as Biology, Medicine, Physics, Chemistry and Engineering. Particularly, the modeling of interactions of external electromagnetic fields with human organisms has gained increasing attention throughout the past. The reason for this are twofold: on the one hand we have an increasing number of electromagnetic and wireless devices (e. g. cellular phones or the emerging wireless power transmission) in our quotidian surroundings which bear concern in the public opinion about possible adverse health effects of electromagnetic fields. On the other hand, electromagnetic phenomena are used daily in many medical applications such as in examinations (e. g. Magnetic Resonance Imaging, Computed Tomography) or as therapeutic tools (e. g. Deep Brain Stimulation or trans-cranial direct and alternative current stimulation) in the personalized medicine era.

A simple and popular numerical technique to simulate problems of bio-electromagnetic effects, which requires to solve Maxwell's equations, is the Finite Difference Time Domain (FDTD) algorithm. However, FDTD solvers have considerable drawbacks, such as staircase effects due to rectangular meshes, and difficulties modeling thin and long geometries, open boundaries (e.g. radiation setups), or frequency-dependent materials. An alternative approach to solve Maxwell's equations in the frequency domain are integral equation methods which are a versatile technique. In recent years, fast integral equation (IE) techniques have received a substantial attention in the Computational Electromagnetics (CEM) community [48–50]. Their field of application is increasingly expanding with the advent of massive-parallel solvers and High Performance Computing (HPC) facilities. They enable precise solutions for a wide range of electromagnetic problems, giving an opportunity to solve scientific and technological challenges.

Methods based on integral equations have several advantages over differential formulations (such as FDTD or FEM). They show a high efficiency and stability in various situations and provide potentially a more accurate solution for the fields. However, while differential formulation produce sparse matrices, integral equation methods result, in general, in dense matrices. This disadvantage has been overcome with the development of methods such as the Multi-Level Fast Multipole Algorithm (MLFMA) [51, 52], the pre-corrected Fast Fourier Transform (pFFT) [53, 54] or the Adaptive Integral Method (AIM) [55]. These methods allow an efficient computation of matrix-vector products appearing in iterative solvers in which the computational burden resides when solving a linear system of equations. With (ML)FMA, pFFT or AIM as the acceleration engine, the Generalized Minimal Residual Method (GMRES)

as the iterative solver and a sparse matrix as pre-conditioner, a fast integral equation solver can be easily constructed to handle hundreds of millions of unknowns. This kind of fast integral equation solver has already shown its great relevance in a large number of electromagnetic problems such as the simulation of radar cross sections for aeroplanes [56], sea vessels or small motor vehicles. For example, frequencies in the range of 77 to 81 GHz were successfully used for simulating cars [57, 58] as 79 GHz was designated by the European Commission for the future anti-collision Short Range Radars (SRR). Another impressive scattering example is the NASA almond in the THz range [59].

From an electromagnetic point of view, the human body is a very challenging case study since it consists of an extremely inhomogeneous, penetrable, dispersive and distributed scatterer, with high-contrasts. The electromagnetic fields of such a three-dimensional (3D) structure within a free space environment can be described by volume integral equations involving the free space Green function. In such case, the FFT can be used to expedite the matrix-vector multiplication in the iterative solver and reduce the computational complexity and memory requirement [60–69]. As the involved matrix resulting from a Method of Moments is of (block) Toeplitz type, the matrix-vector product can be exactly computed by the FFT requiring only $\mathcal{O}(N \log N)$ operations. The fact that this approach is limited to rectilinear grids can be overcome with pre-corrected FFT methods [53, 55, 68, 70–72] or the AIM. The latter works also for tetrahedral meshes therefore greatly broadening the application range of volume integral equations. For volumetric scatterers, the computational and memory costs associated with the AIM [55, 73–76] scale as $\mathcal{O}(N \log N)$ and $\mathcal{O}(N)$, respectively.

For MWI applications, where the forward operator is located inside the optimization loop of the inverse scattering problem (process implying the retrieval of the physical parameter which have induced the measured scattered fields), a fast forward algorithm is mandatory. The precision of the solution of the inverse problem naturally depends on the accuracy of the forward method, which depends on both the detailed description of the model (e.g. mesh density of geometry, basis functions to represent physical unknowns) and the related numerical techniques (e.g. evaluation of singular integrals in the case of integral equations as forward operator).

1.2 Objectives and Scientific Work Plan

The research performed in the present thesis is closely related to the European Cooperation in Science & Technology (COST) Action TD1301 *Development of a European-based Collaborative Network to Accelerate Technological, Clinical and Commercialisation Progress in the Area of Medical Microwave Imaging* (MiMed) [77]. The main objective is to achieve a detailed understanding of the field distribution in the human tissues in order to establish reliable and relevant guidelines and exposure limits for electromagnetic fields and to optimize medical applications and imaging. Since measurements from the inside of living beings are almost

impossible or at least very difficult to perform, other possibilities to obtain the field distribution are necessary. Electromagnetic simulations can be of great benefit in this context, involving electromagnetic radiation effects as well as macroscopic effects such as heating or Specific Absorption Rate (SAR) distribution. The electromagnetic simulation of human tissue is very challenging because the human body represents a heterogeneous and dispersive medium that challenges any existing simulation algorithm. The objectives of the scientific work plan are organized in four main tasks:

T1 Volume IE (VIE) Method of Moment (MoM) full-wave solver

This task is dedicated to the implementation of a basic VIE solver for bio-electromagnetic problems by applying known analytical and numerical integration techniques for MoM integrals and the solution of small- to medium-sized problems without the need of specially tailored fast solvers. The implementation is focused on formulations for high contrast and extremely heterogeneous media. This will become useful later, when specialized routines for the various problems will be developed and implemented. In this regard, the currently available solver has been implemented in a modern fashion in MATLAB which has been chosen for rapid prototyping and its plug-and-play characteristics, allowing an easy exchange of routines.

T2 Large-scale problems

Inverse scattering techniques for imaging methods such as NMR or Microwave Imaging require a fast and accurate forward operator. Moreover, the amount of information to be treated is very large (dense mesh and/or large computational domain with respect to wavelength). For instance, a human head is meshed with over 20 millions voxels (cubic cells) of 1 mm side. Our VIE solver will serve as the forward operator. This task is specially dedicated to the application of fast methods for large-sized problems with methods such as FFT. The FFT algorithm has the advantage that implementations for GPUs are already at hand leading to a fast solver for inverse scattering problems.

T3 MWI Fast Modeling Tools

For every medical application, compromises should be done while designing a new imaging modality. The key point resides in extracting meaningful parameters and propose simplified but representative models in order to derive guidelines. This task is dedicated to investigating fast modeling tools to design MWI systems for brain imaging and especially brain stroke detection, monitoring and characterization.

T4 differential MWI and Inverse Scattering

In the framework of brain MWI, the differential imaging strategy has a certain number of advantages for the imaging procedure. To benefit from all the capabilities of the method it is important to be able to quantify the gain of using the differential scenario over the classical one. This task is dedicated to investigating inverse scattering schemes, for the specific application of brain differential MWI. Regularization schemes and non-linearity are qualitatively or quantitatively assessed both numerically and experimentally. Addi-

tionally the power transmission of a radiating field inside the human head is analyzed with various models.

1.3 Outline and Contributions

The outline of the thesis is presented with, for each chapter, a brief description and the contributions. Chapter 2 is a review chapter to better understand the original contributions which are presented in Chapter 3, Chapter 4, and Chapter 5. The Conclusions and Perspectives of this work are presented in the end, followed by the Appendixes. This thesis firstly focuses on challenges related to simulations of electromagnetic scattering of an ill-conditioned forward problem for highly heterogeneous tissues (Chapter 3). In a second step, the challenges related to the coupling of the microwave power into the tissue, tissue losses, and the choice of the frequency are investigated and several body models with increasing complexity are used to confront simulation based analysis with experimental validations (Chapter 4). In a third part, the challenges due to the non-linearity and ill-posedness of inverse scattering problems are discussed and illustrated with simulations and experimental measurements (Chapter 5).

Chapter 2: Electromagnetic Scattering in Biological Tissues

- *Description:* This chapter presents the state-of-the-art of MWI, namely the numerical analysis of the human head dielectric properties, the background on the governing equations, the general concepts and the main relevant facts behind electromagnetic scattering in biological tissues. In addition, Chapter 2 serves as a discussion on various electromagnetic phenomena present in biological tissues, which are relevant for MWI of brain stroke related pathologies, to introduce the major challenges to overcome for clinical applications.

Chapter 3: Volume Integral Operator of Electromagnetic Scattering

- *Description:* State-of-the-art introducing the different VIE formulations and related singular integrals, before moving to the implementation of two solvers targeting large number of unknowns, and for which the numerical solution of VIE is solved via the Galerkin Method of Moments (MoM) technique. Understanding the capabilities and the limitations of the modeling tools is crucial to faithfully model EM fields for MWI applications.
- *Contributions:* The development of the VIE solver and the investigation of the VIE-formulation for highly inhomogeneous and lossy scatterers in the microwave range. A Multi-Grid (MG) solver is tested yielding promising results for frequencies up to 2 GHz.

Chapter 4: Design of MWI Systems for Brain Imaging

Chapter 1. Introduction

- *Description:* Analysis of the power transmission of a radiating field inside the human head in the range of frequencies [0.5 – 4] GHz in order to propose and validate tools used to derive guidelines for the design of MWI systems for brain imaging. Firstly, two models, their electromagnetic analysis, and the discussion of simulation results are presented. Secondly, the experimental validation of a spherical layered model with the characterization and realization of a 3D printed head phantom with tissue mimicking liquids is performed.
- *Contributions:* Development of an analytical solver, a mode matching technique based on spherical wave expansion (Mie series) to analyze the scattering by spherically stratified media. Conception and realization of a multilayered head phantom based on the 3D printing technology and head tissue mimicking material made of Triton-based mixtures. The estimation and quantification of the normalized transmitted power and the experimental analysis of the influence of the main head layers separating the measurement setup from the imaging location, which is here the brain.

Chapter 5: Microwave Inverse Scattering Problem

- *Description:* Challenges due to the non-linearity and ill-posedness of inverse scattering problems and especially their implications for brain imaging applications in the microwave range are considered. The differential MWI (dMWI) modality for brain imaging applications is presented and the estimation and quantification of the Degree of Non-Linearity (DNL) for dMWI is introduced. Different regularization schemes are investigated to tackle the ill-posedness of the inverse problem using simple and complex head models and are later experimentally validated using the 3D printed multilayered head phantom.
- *Contributions:* The estimation and quantification of the DNL for dMWI. The investigation of regularization techniques which are promoting sparsity in the reconstruction, with corresponding experimental validations with the 3D printed multilayered head phantom.

Chapter 6: Conclusions and Perspectives

- *Description:* The summary and assessment of the achieved work in this thesis is followed by a discussion of potential future research directions.

APPENDICES

- *Description:* Two appendices both related to Chapter 4 are provided. The first one describes the key points to understand the spherical wave expansion in the corresponding scattering framework and its mathematical derivation. The second one is retracing

the important steps of the conception and realization of the 3D printed multilayered head phantom, from the precise description of the geometries, to the waterproofing and gluing tests performed on prototypes.

2 Electromagnetic Scattering in Biological Tissues

Since this thesis focuses on Microwave Imaging (MWI) of the head, the MWI state-of-the-art for biomedical applications and the numerical analysis of the human head dielectric properties are first presented. This chapter serves as a common base for investigations presented later on and aims at providing the basic knowledge about the governing equations, general concepts and main relevant facts behind electromagnetic scattering in biological tissues for this thesis purpose. In particular, the following concepts and important notions are presented:

1. a brief summary on the motivation why MWI could be a profitable technology in the framework of brain stroke related pathologies;
2. the major challenges to overcome for clinical applications and the comparison to existing more mature applications of MWI such as breast cancer early stage detection;
3. the mathematical background of electromagnetic modeling of biological tissues;
4. the forward and inverse scattering definitions and their mathematical considerations.

The chapter is meant as an introduction and a motivation for the later chapters that will investigate in more depth some of those aspects.

2.1 Brain Stroke Monitoring

There are two main kinds of stroke: ischaemic strokes (up to 80% of the strokes) that are caused by an abrupt blockage of blood circulation in the brain (i-stroke), or haemorrhagic strokes (h-stroke) caused by bleeding into the brain tissues when a blood vessel bursts. The effects of a stroke to the patient are - depending on which part of the brain is injured - sudden weakness, loss of sensation, or difficulties with speaking, seeing, or walking. Microwave Imaging (MWI) [14] is investigated as a candidate technology to monitor brain stroke related diseases [78], [46].

2.1.1 Technologies for Brain Imaging

Current clinical imaging methods, such as Magnetic Resonance Imaging (MRI) or Computed Tomography (CT) offer useful information on tissue properties and therefore are good tools for assessing diseases such as brain strokes. However, none of these facilities can be widely available at bedside in emergency departments or in paramedic services such as ambulances. MWI is a non-ionizing, non-invasive, cost-effective technology which may usefully complement current technologies for determining and monitoring cerebral vascular diseases. For brain stroke imaging, the six main requirements are:

1. Continuous Monitoring

Brain stroke is a fast evolving pathology and the continuous monitoring during the first hours after the administration of treatment is primordial. For i-strokes the main approved treatment is *intravenous thrombolysis with alteplase* which can have severe complications in the days following the stroke [8] and needs to be monitored.

2. Resolution

The resolution should be high enough (millimeters up to few centimeters) to detect small regions affected by the stroke, so that the nature of the anomalies can be assessed [7] and their location determined.

3. Costs

The success of the treatment is directly linked to the time between the first symptoms and the treatment. Therefore, the regionalization of stroke care is crucial for good treatment of the illness. Cost effective devices are easier to implement in regional health centers.

4. Safety

The non-ionizing radiation is defined as the lowest k-shell binding energy of the Hydrogen atom (^1H). When the radiation energy is beyond this limit, the atomic structure can be altered. The human body is mainly composed of water and therefore of hydrogen, changing the atomic structure of the latter can cause health complications such as cancer.

5. Tissue Functional Contrast

The nature of tissue in the human body gives insight on the pathological or healthy state of the patient. For brain stroke detection, differentiation and monitoring, it is crucial to know the exact functional state of matter to determine which treatment to use [78], the first step being to distinguish between i- and h-strokes. Applying medication for i-stroke in the case of h-stroke is counter-productive and can even be fatal [7].

6. Portability

In line with the need of regionalization of stroke care, portable devices can be brought to ambulances or rural areas so that decisions can be taken faster and earlier diminishing delayed admissions [8].

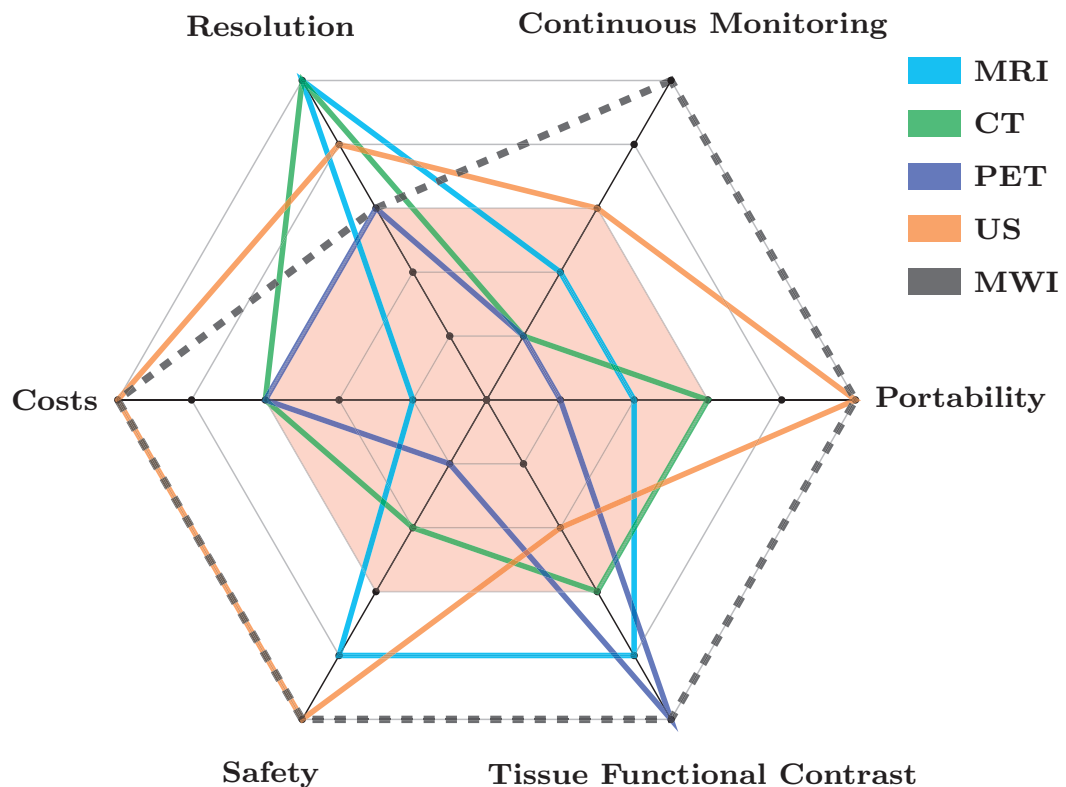


Figure 2.1 – Current technologies and main characteristics for imaging brain stroke pathologies. MRI: Magnetic Resonance Imaging; CT: Computed Tomography; PET: Positron Emission Tomography; US: Ultra-Sound Imaging; MWI: Microwave Imaging.

Fig. 2.1 visually describes the complementary advantages that MWI could provide with respect to well-established clinical technologies. The scores for each requirement go from 1 to 5, with 5 representing the complete fulfillment. The red area represents scores for which the technology is not providing satisfactory options for brain stroke detection, differentiation and monitoring. Ultra-Sound (US) imaging has several advantages, however, the penetration into the head is very bad (theoretically less than 1%, as it is almost completely attenuated by the cortical bone) and to the author's best knowledge, only imaging of fetus heads is feasible with US imaging. Positron Emission Tomography (PET) is ionizing as γ - emitters (radioactive positrons) are directly injected into the body and there is no wide utilization for stroke applications [79]. There is therefore a gap in existing technologies to fulfill all the above mentioned requirements and MWI (black dotted line) is a possible answer to bridge this gap.

2.1.2 Brain Imaging Challenges

Microwave imaging as a clinical application is striving to make an entrance into the highly competitive world of medical imaging [23]. Nonetheless, during the last decade, MWI for breast cancer early detection was getting more mature [24]. The challenges arising in MWI for

the brain are similar to the one arising in breast MWI and benefit from the experience in that field. The main challenges and their evolution are reviewed hereafter.

- **Tissue Heterogeneity**

Biomedical MWI strongly depends on tissue composition, and therefore every application encounters different intrinsic challenges. For breast cancer detection, breast tissues are usually modeled as different proportions of glandular and fatty tissues [80–82] surrounded by the skin. The nature of head tissues is more heterogeneous than breast tissues, therefore, the electromagnetic modeling of wave propagation is more complex. The whole head from neck to scalp is composed of approximately 24 distinctive parts with different dielectric properties in the microwave range. This number can be reduced by a factor of two if we take into account only the different tissues around the brain area closer to the top of the head. In Fig. 2.2 different views of a human realistic model [83] at 1GHz are shown. The relative permittivity ϵ_r and conductivity σ [S/m] are values defining the dielectric properties of the tissues.

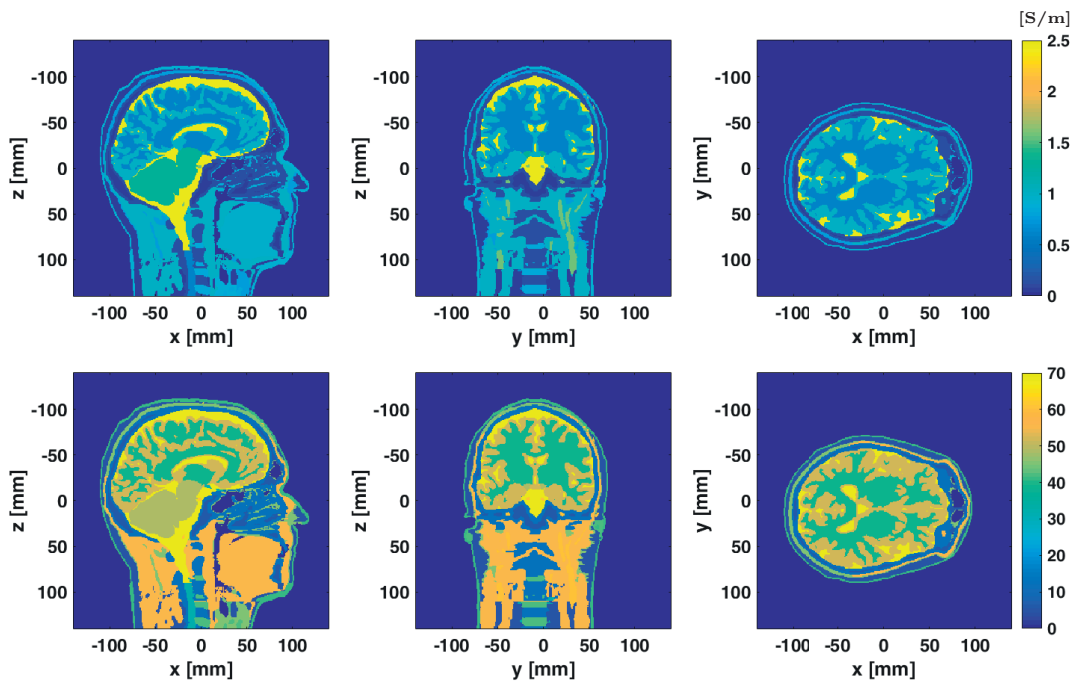


Figure 2.2 – Sagittal (left), coronal (center) and axial/transverse (right) views of the conductivity (top) and relative permittivity (bottom) of a human realistic model [83] at 1 GHz.

- **Coupling Microwave Power into the Tissues**

The biological tissues have a strong dependency on frequency, called dispersion, therefore the transmitted power also depends on frequency. In Fig. 2.3 some statistics about dispersion of the overall head tissues are given. The central mark is the median, the

edges of the box are the 25th and 75th percentiles, the whiskers extend to the most extreme data points not considered as outliers, which are plotted individually in red.

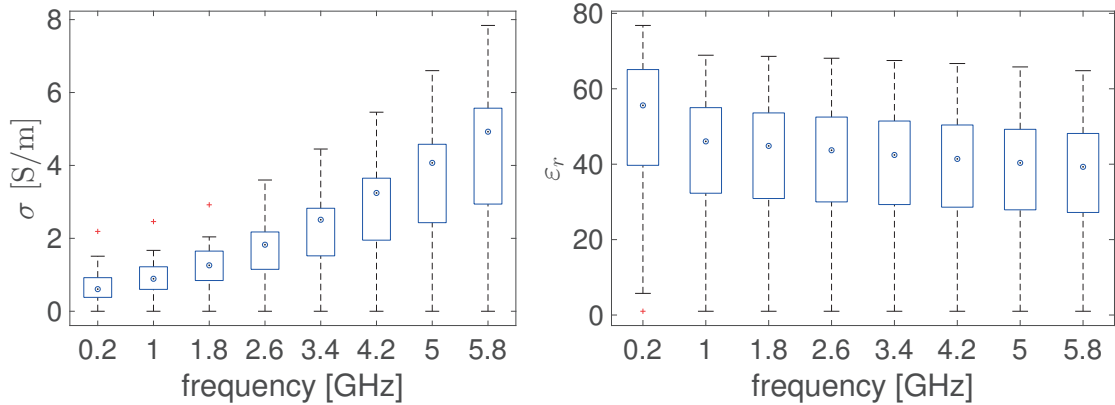


Figure 2.3 – Statistics about dispersion of the overall head tissues; median (blue circled dot), 25th and 75th percentiles (blue boxes), extreme data points (whiskers) and outliers (red crosses).

The antennas, also called sensors, are placed outside the body. The emitted power needs to be transmitted into the investigation domain. There is a strong contrast (mismatch) between air and the average head dielectric properties. Therefore the power radiated by an antenna in the air does not penetrate easily in the head as it will be strongly reflected. To inject the maximum quantity of power into the brain, either the antennas and the top head region must be immersed in a matching medium [84] or the sensors must be in direct contact with the skin [23].

- **Tissue Losses**

The penetration depth depends on the losses induced by the tissues conductivities. In Fig. 2.3 it appears clearly that the overall losses in the head increase with frequency. The power coupled into the tissues and the penetration depth will define the sensitivity needed to be able to detect scattered fields due to an anomaly [47].

- **Resolution Limits**

The resolution depends on the wavelength λ of the medium in which the transmitters are located. The wavelength inversely depends on the frequency and the dielectric permittivity of the medium where the wave propagates. Devaney [85] first suggested that this limit of resolution was about $\lambda/\sqrt{2}$, then Bolomey and Pichot [21] estimated it to $\lambda/2$. Chen and Chew [86] experimentally observed a resolution up to $\lambda/4$, for high contrast, but non-dispersive and lossy objects, which is a so-called super-resolution behavior, exploiting the near field and applying non-linear reconstruction algorithms. Meaney et al. [87] have suggested that image reconstruction "is fundamentally unlimited by wavelength" and "is restricted by signal-to-noise" ratio. The latter papers have been discussed by Semenov [88] and experiments have been conducted to test for the detection of myocardial ischemia and infarction. They concluded that the resolution

lies between a quarter and a half of a wavelength in the background medium.

- **Choice of the Frequency**

The choice of the frequency is a trade-off between penetration depth (upper bound) and resolution (lower bound). The resolution decreases with the frequency which means that small anomalies (few millimeters) cannot be detected at low frequencies (below 600 MHz). This challenge will be discussed in detail in Chapter 4.

- **Forward Model Simulations**

Computing the electromagnetic fields inside the human body may require huge computational resources. There is plenty of software available to model propagation in biological matter at low microwaves, however, high accuracy methods are still needed for reliable simulations especially at higher frequencies. This challenge will be discussed in detail in Chapter 3.

- **Tissue Motion**

As for every tomographic setup, unwanted motion results in a diminished sharpness and increased blurriness in the images. Rapid scanning, optical detection of boundaries [89] and body constriction [23] are physical solutions, and conformal imaging algorithms can be used to reduce the negative impact of motion on the reconstruction.

- **Contrast between Abnormal and Healthy Tissues**

There is a need for rapid stroke differentiation between different pathological states as the treatment should be taken as soon as possible to decrease the probability of having permanent cognitive damages [7, 8]. Treatments for i-strokes and h-strokes are very different and wrong administration can be fatal. The difference of contrast in the dielectric properties of healthy tissues and of pathological tissues is the key for diagnostics with MWI [82]. Thus, it is very important that this difference exists and can be detected. One possibility is to model the intercerebral stroke as a homogeneous region of dielectric properties, $\epsilon_r = 36$, $\sigma = 0.72$ [S/m] for the i-stroke [47] and $\epsilon_r = 61$, $\sigma = 1.58$ [S/m] for the h-stroke [90] at 1 GHz. The second option is to model the stroke as a -10% change of the baseline (healthy parameters of head region affected by the stroke) for the i-stroke and the mean value between the baseline and dielectric properties of blood for the h-stroke [78]. The subarachnoid h-stroke (happens in the region between the skull and the brain) is not yet investigated in the MWI community and no models are therefore available in the literature.

2.2 Governing Equations

The electromagnetic field is governed by a set of equations known as *Maxwell's equations* which relate the fields to their sources. The combination of these equations leads to the *wave equation* which describes the electromagnetic radiation and propagation. This section focuses on propagation in biological matter.

2.2.1 Maxwell's Equations and Constitutive Equations

Maxwell's equations relate the field vectors to their sources. For time-harmonic fields with the time factor $e^{j\omega t}$, the local form of Maxwell's equations is:

$$\nabla \times \mathbf{E}(\vec{r}) = -j\omega\mathbf{B}(\vec{r}) \quad (2.1a)$$

$$\nabla \times \mathbf{H}(\vec{r}) = j\omega\mathbf{D}(\vec{r}) + \mathbf{J}(\vec{r}) \quad (2.1b)$$

$$\nabla \cdot \mathbf{D}(\vec{r}) = \rho(\vec{r}) \quad (2.1c)$$

$$\nabla \cdot \mathbf{B}(\vec{r}) = 0 \quad (2.1d)$$

Here \vec{r} denotes the position vector [m], \mathbf{E} is the electric field [V/m], \mathbf{B} is the magnetic flux density [Wb/m²], \mathbf{H} is the magnetic field [A/m], \mathbf{D} is the electric flux density [C/m²], ρ is the volume charge density [C/m³], and \mathbf{J} is the electric current density [A/m²]. The equations (2.1) are supplemented by the constitutive equations that contain the information about the media in which the electromagnetic phenomena occur. The human body biological matters, treated as linear, isotropic, non-magnetic and lossy media in the microwave range [0.3 – 300] GHz [14], have the following general constitutive relations:

$$\mathbf{D}(\vec{r}) = \varepsilon_0\varepsilon_r(\vec{r})\mathbf{E}(\vec{r}) \quad (2.2a)$$

$$\mathbf{B}(\vec{r}) = \mu_0\mu_r(\vec{r})\mathbf{H}(\vec{r}) \quad (2.2b)$$

Here ε_0 is the vacuum permittivity [F/m] and μ_0 the vacuum permeability [H/m]. The values $\varepsilon_r(\vec{r})$ and $\mu_r(\vec{r})$ are their relative counterparts (dimensionless). It is important to note that permittivity is not constant for a material at a given temperature and pressure, and changes with frequency, $\varepsilon_r(\omega, \vec{r})$, however, for clarity reasons these dependencies will be omitted in the notation. The human body does not have any particular magnetic macroscopic properties and we assume $\mu_r = 1$. Biological tissues are conductive and therefore lossy, the induced current $\mathbf{J}_i(\vec{r})$, induced by the field in conducting media, is described by Ohm's law:

$$\mathbf{J}_i(\vec{r}) = \sigma(\vec{r})\mathbf{E}(\vec{r}) \quad \text{with} \quad \mathbf{J}(\vec{r}) = \mathbf{J}_i(\vec{r}) + \mathbf{J}_0(\vec{r}) \quad (2.3)$$

Here $\mathbf{J}_0(\vec{r})$ is the electric source density if an external source (other than the media) is present,

and σ [F/m] is the conductivity. The Maxwell-Ampère Law (2.1b) can be rewritten as:

$$\nabla \times \mathbf{H}(\vec{r}) = (j\omega\epsilon_0\epsilon_r(\vec{r}) + \sigma(\vec{r}))\mathbf{E}(\vec{r}) + \mathbf{J}_0(\vec{r}) = j\omega\boldsymbol{\epsilon}(\vec{r})\mathbf{E}(\vec{r}) + \mathbf{J}_0(\vec{r}) \quad (2.4)$$

Here $\boldsymbol{\epsilon}(\vec{r})$ is the complex permittivity and is defined as :

$$\boldsymbol{\epsilon}(\vec{r}) = \epsilon_0 \left(\epsilon_r(\vec{r}) - \frac{j\sigma(\vec{r})}{\epsilon_0\omega} \right) \quad (2.5)$$

2.2.2 Contrast-Source Formulation

In this section, for clarity reasons only, the E-field is of interest, and the H-field can be retrieved from it if needed. By substituting (2.4) in (2.1), one can get the *wave equation*:

$$\nabla \times \nabla \times \mathbf{E}(\vec{r}) - \omega^2\mu_0\boldsymbol{\epsilon}(\vec{r})\mathbf{E}(\vec{r}) = -j\omega\mu_0\mathbf{J}_0(\vec{r}) \quad (2.6)$$

The solution of this system of 3 differential equations can be intuitively separated into a solution when there is no scatterer present, called the incident field $\mathbf{E}_i(\vec{r})$ that is a known quantity, created by a known source, and a solution when there is a scatterer present, called the scattered field $\mathbf{E}_s(\vec{r})$, which is unknown. In the domain of investigation Γ , the electric field without the anomaly is called the background field $\mathbf{E}_b(\vec{r})$ and is equal to the incident field $\mathbf{E}_i(\vec{r})$ if the background medium is defined as infinite. The interaction between the background field and the object under investigation is: $\mathbf{E} = \mathbf{E}_b + \mathbf{E}_s$ in Γ . The *wave equation* in the background ($\boldsymbol{\epsilon}(\vec{r}) = \boldsymbol{\epsilon}_b$), by analogy with (2.6) is defined as:

$$\nabla \times \nabla \times \mathbf{E}_b(\vec{r}) - \omega^2\mu_0\boldsymbol{\epsilon}_b\mathbf{E}_b(\vec{r}) = -j\omega\mu_0\mathbf{J}_0(\vec{r}) \quad (2.7)$$

By substituting (2.7) in (2.6):

$$\nabla \times \nabla \times \mathbf{E}_s(\vec{r}) - \omega^2\mu_0\boldsymbol{\epsilon}_b\mathbf{E}_s(\vec{r}) = \omega^2\mu_0(\boldsymbol{\epsilon}(\vec{r}) - \boldsymbol{\epsilon}_b)\mathbf{E}(\vec{r}) = \omega^2\mu_0\boldsymbol{\epsilon}_b\boldsymbol{\chi}(\vec{r})\mathbf{E}(\vec{r}) \quad (2.8)$$

Equation (2.8) is called *contrast-source* formulation and its physical interpretation is shown in Fig. 2.4. It relates the scattered field $\mathbf{E}_s(\vec{r})$ to the currents induced in the scattering object

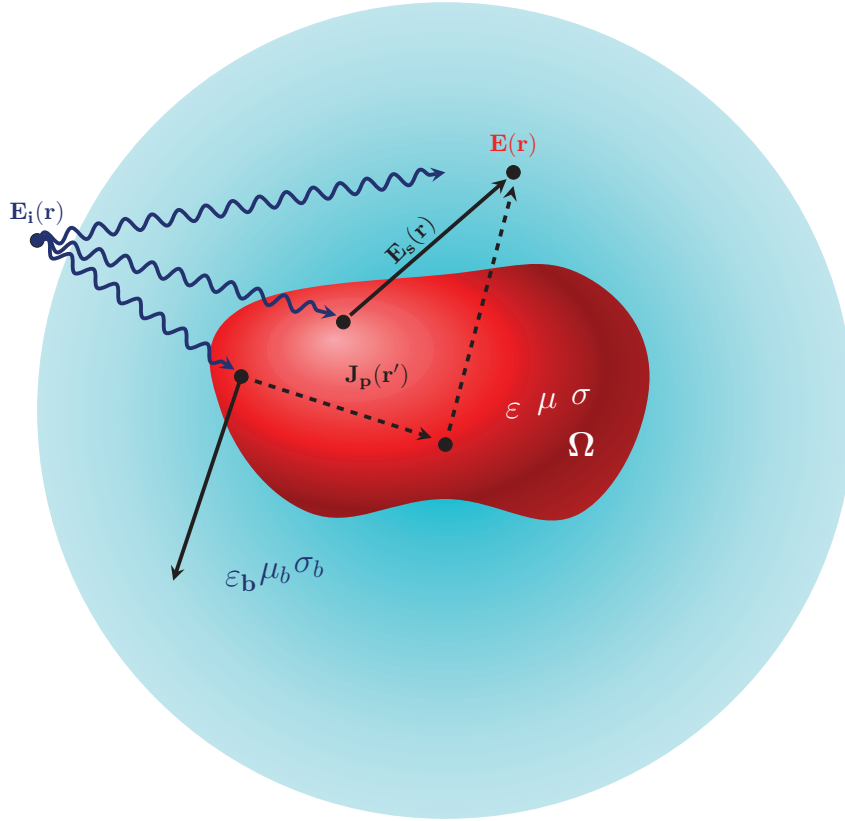


Figure 2.4 – Representation of a scatterer (red) with its domain denoted by Ω with constitutive parameters $\epsilon(\vec{r})$, $\mu(\vec{r})$ and $\sigma(\vec{r})$, immersed in an infinite background medium of dielectric properties ϵ_b , μ_b and σ_b . The dark blue lines represent the incident field and the black (full and dashed lines) represent the scattered field (produced by currents $\mathbf{J}_p(\vec{r})$).

present in a domain Ω . The name *contrast-source* comes from the fact that the right-hand side represents the virtual source of the scattered field $\mathbf{E}_s(\vec{r})$, which is proportional to the contrast, $\chi(\vec{r})$, between scatterer and background. The contrast $\chi(\vec{r})$ is a complex scalar and is defined as the normalized difference between the complex permittivities of the scatterer $\epsilon(\vec{r})$ and of the background medium ϵ_b :

$$\chi(\vec{r}) = \frac{\epsilon(\vec{r})}{\epsilon_b} - 1 \quad (2.9)$$

Note that as $\epsilon(\vec{r}) \neq \epsilon_b$ for $\vec{r} \in \Omega$, the contrast $\chi(\vec{r})$ differs from zero only in the domain of the scatterer, that is for $\vec{r} \in \Omega$. Having a formulation which describes the scattering object only by its contrast $\chi(\vec{r})$ has the advantage of having constitutive parameters which scale accordingly to the background medium. For the contrast-source formulation, the unknown field is the scattered field $\mathbf{E}_s(\vec{r})$ excited by a source defined as the polarization current $\mathbf{J}_p(\vec{r}) =$

$$j\omega\epsilon_b\chi(\vec{r})\mathbf{E}(\vec{r}).$$

2.2.3 Integral Equation Approach

Biological matter can be discretized in piece-wise homogeneous parts with its electromagnetic characteristics being completely described by its complex permittivity $\epsilon(\vec{r})$. One possibility to describe the scattering of monochromatic electromagnetic radiation is the Volume Electric Field Integral Equation formulation [91] based on a purely dielectric formulation and the *contrast-source* formulation,

$$\mathbf{E}(\vec{r}) = \mathbf{E}_b(\vec{r}) + \int_{\Omega} \bar{\bar{\mathbf{G}}}_e(\vec{r}, \vec{r}') \chi(\vec{r}') \mathbf{E}(\vec{r}') d\Omega' \quad (2.10)$$

where the dyadic Green function $\bar{\bar{\mathbf{G}}}_e$ is:

$$\bar{\bar{\mathbf{G}}}_e(\vec{r}, \vec{r}') = \frac{k_b^2}{4\pi} \left[\bar{\bar{\mathbf{I}}} + \frac{1}{k_b^2} \nabla \nabla \right] \frac{e^{-jk_b|\vec{r}-\vec{r}'|}}{|\vec{r}-\vec{r}'|} \quad (2.11)$$

where $k_b = \omega\sqrt{\mu_b\epsilon_b}$ is the propagation wavenumber in the background medium, and $\bar{\bar{\mathbf{I}}}$ is the unit dyadic. The considerations to compute the integral will be examined in Chapter 3.

2.3 Introduction to the Forward and Inverse Problem

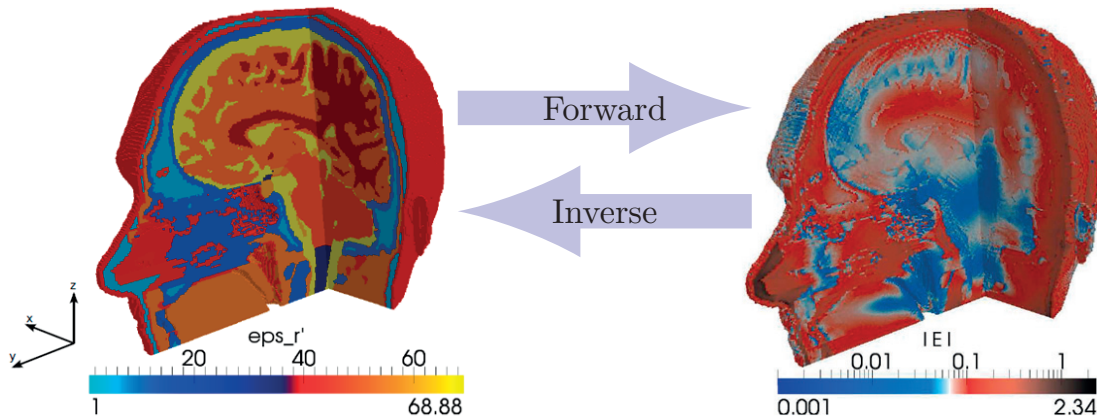


Figure 2.5 – Framework of Forward and Inverse scattering problems.

The forward problem (see Fig. 2.5) yields the fields produced from a known scatterer (described by its constitutive parameters) in a given volume (in the scatterer and/or around it for example). For this purpose several techniques exist, the most popular ones are the Finite

2.3. Introduction to the Forward and Inverse Problem

Differences Time Domain (FDTD) method, Finite Elements Method (FEM), and Integral Equation (IE) methods. In the framework of this thesis, we opted for a Volume Integral Equation (VIE) formulation to compute the forward problem.

The inverse problem (see Fig. 2.5) consists of finding the scatterer's composition, or, more precisely, its constitutive parameters in a given volume, from a set of field measurements. In bio-medical applications, the field measurements are usually performed outside the scatterer, at various known positions, for example in the case of brain MWI, at probes surrounding the head.

In electromagnetic modeling and inverse scattering, some important mathematical considerations need to be understood and dealt with carefully.

- **Non-linearity**

The scattered field $\mathbf{E}_s(\vec{r})$ depends on the total electric field $\mathbf{E}(\vec{r})$ (2.8). The total field in

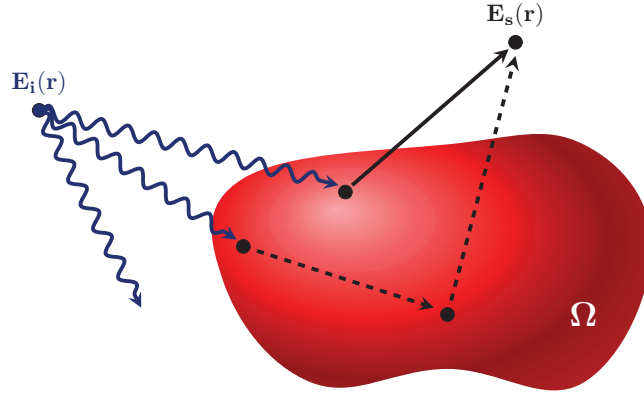


Figure 2.6 – Representation of the field incident on and scattered by the head model. The solid line represents a direct or first order interaction (5.11), while the dashed line is an example of a second order interaction.

(2.10) can be rewritten recursively as:

$$\begin{aligned}
 \mathbf{E}(\vec{r}) &= \mathbf{E}_b(\vec{r}) + \int_{\Omega} \bar{\bar{\mathbf{G}}}_e(\vec{r}, \vec{r}') \chi(\vec{r}') \left[\mathbf{E}_b(\vec{r}') + \int_{\Omega} \bar{\bar{\mathbf{G}}}_e(\vec{r}', \vec{r}'') \chi(\vec{r}'') \mathbf{E}(\vec{r}'') d\Omega'' \right] d\Omega' \\
 &= \underbrace{\mathbf{E}_b(\vec{r}) + \int_{\Omega} \bar{\bar{\mathbf{G}}}_e(\vec{r}, \vec{r}') \chi(\vec{r}') \mathbf{E}_b(\vec{r}') d\Omega'}_{\text{first order interaction}} + \underbrace{\int_{\Omega} \bar{\bar{\mathbf{G}}}_e(\vec{r}, \vec{r}') \chi(\vec{r}') \left[\int_{\Omega} \bar{\bar{\mathbf{G}}}_e(\vec{r}', \vec{r}'') \chi(\vec{r}'') \mathbf{E}_b(\vec{r}'') d\Omega'' \right] d\Omega'}_{\text{second order interaction}} \\
 &\quad + \underbrace{\int_{\Omega} \bar{\bar{\mathbf{G}}}_e(\vec{r}, \vec{r}') \chi(\vec{r}') \left[\int_{\Omega} \bar{\bar{\mathbf{G}}}_e(\vec{r}', \vec{r}'') \chi(\vec{r}'') \left[\int_{\Omega} \bar{\bar{\mathbf{G}}}_e(\vec{r}'', \vec{r}''') \chi(\vec{r}''') \mathbf{E}(\vec{r}''') d\Omega''' \right] d\Omega'' \right] d\Omega'}_{\text{higher order interactions}}
 \end{aligned} \tag{2.12}$$

The system is non-linear as the output of the system is not directly proportional to the input. The non-linearity comes from the *multiple scattering phenomena* as represented in Fig. 2.6 and is expressed by second and higher order interactions in (2.12).

- **Ill-conditioning**

If a small change in the input data $\Delta \mathbf{x}$, results in a large change in the output or solution $\Delta \Phi(\mathbf{x})$, the problem is called ill-conditioned (see Fig. 2.7) [92]. The condition number quantifies the ill-conditioning and is defined as the value of the asymptotic largest relative change in output for a relative change in input. For the forward problem the consequence of an ill-conditioned problem is a difficulty of convergence when applying an iterative technique and appropriate pre-conditioning is required. For the inverse scattering problem, it implies that a small change in measurement data could lead to a large change in the reconstruction and regularization approaches are then necessary.

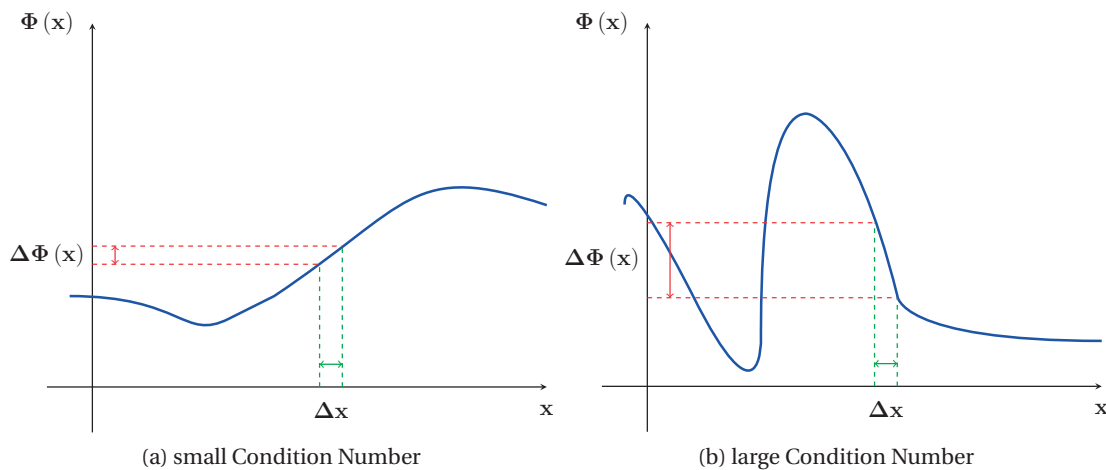


Figure 2.7 – Well-conditioned and ill-conditioned 1D representations.

- **Ill-posedness**

The majority of inverse scattering problems are ill-posed. *Well-posed* problems are *well-defined* (existence and uniqueness of the solution) and the solution has to have a continuous dependency on data [93]. If any of these three conditions are not satisfied the problem is called *ill-posed*. For inverse scattering problems non-existence can arise if there is more data M , than unknowns N , with M linearly independent equations, and only a solution in the least square sense exists. On the other hand if there is lack of information, i.e. less measurement data than unknown to retrieve or linear dependencies between equations, the solution can be non-unique.

2.4 Summary

The most important information about brain stroke related pathologies were presented, and current imaging technologies such as CT or MRI discussed for brain stroke detection, differentiation and monitoring. MWI seems to be a good alternative to the existing imaging technologies as a dedicated device to brain stroke related pathologies.

The challenges inherent to brain MWI have been reviewed and compared to breast MWI imaging whose readiness level is much higher. The global vision of brain MWI challenges is a motivation and justification for the need of deeper understanding in several aspects which will be discussed in the following three chapters.

Then, the mathematical background of electromagnetic modeling of biological tissues was presented, and the contrast source formulation was explained. The latter prepared for the introduction to forward and inverse scattering concepts which are the core and framework of this thesis. Similar to the presentation of the MWI challenges, explaining from the beginning the mathematical considerations intrinsic to the electromagnetic scattering problem, is a motivation and justification for further investigation.

3 Volume Integral Operator of Electromagnetic Scattering

Interaction of the human body with electromagnetic (EM) fields is widely used in the development and design of medical devices and technologies as well as for diagnostic and therapeutic purposes. Over the last decades, there has been a continuous trend to replace X-ray based devices in favour of EM-based ones like Magnetic Resonance Imaging (MRI) or Microwave Imaging [94] to name only but a few. Additionally, wireless communication of implanted devices is gaining importance. The main challenge during the development of these technologies and devices is the detailed understanding of the field distribution inside the body since measurements inside living beings are almost impossible. Here EM simulations can be of great benefit. Fast and accurate numerical methods can be enabled in many ways. For example, patient-specific data like MRI screens could be used for the development of patient-adapted devices.

In the framework of bio-electromagnetic applications, the numerical technique of choice is often the Finite Difference Time-Domain (FDTD) method. However, with the development of the Multi-Level Fast Multipole Algorithm (MLFMA) [51] or FFT-accelerated matrix-vector products [95], frequency domain integral equation (IE) solvers are becoming an attractive alternative for modeling scattering from strongly inhomogeneous objects [48–50, 96, 97]. Since the human brain/body represents a distributed scatterer, we focus, in this thesis, on FFT-based matrix-vector products and volume integral equations which are a versatile technique to model inhomogeneous scattering objects. Numerical tests show excellent convergence properties of the technique for strongly inhomogeneous media with high dielectric contrast.

This chapter is organized in three parts:

1. a brief state-of-the-art introducing the different VIE formulations and related singular integrals;
2. the numerical solutions of VIE via Galerkin Method of Moments (MoM) technique with a discussion on the spectrum of the volume integral operator;
3. the numerical experiments of two solvers targeting large number of unknowns.

The chapter aims at giving in detail the IE solver description and performance. The IE solver is the first step to investigate scattering in biological tissues in the targeted microwave range. Knowing the capabilities and the limitations of the modeling tools is crucial for any further investigation of MWI.

3.1 State-of-the-art and Background

The numerical solution of Maxwell's equations is often found via the FDTD algorithm. However, while simulating problems of bio-electromagnetic effects, the FDTD encounters several issues which are listed here:

- FDTD requires the complete computational domain to be meshed and the grid size to be sufficiently fine to resolve both the smallest electromagnetic wavelength and the smallest geometrical feature in the model. Especially, models with long, thin features – like wires or leads – are difficult to model in FDTD because they result in excessively large computational domains.
- In the FDTD method, space and time steps must satisfy the Courant–Friedrichs–Lewy condition (CFL condition) otherwise time integration is likely to be unstable. The CFL condition is very strong and the required time step can therefore become very short leading to extreme simulation times, especially if thin geometries are present. This is acceptable where broadband responses are required, but, for applications with narrow band excitation like safety issues of wireless power transmission or NMR systems which work with dedicated frequencies, the simulation time can become prohibitive.
- The FDTD's solution is limited to the computational domain, that is, the electric and magnetic fields are found on the mesh. In the event that the electromagnetic field must be determined outside the computational domain, either this domain must be extended – leading to larger memory requirements and longer simulation times – or far-field extensions have to be applied to the FDTD.
- The finite computational domain also requires that open boundary problems (e.g. radiation problems) be solved with special techniques like absorbing boundary conditions (ABCs) or perfectly matched layers (PMLs) in order to approximate the radiation condition.
- In FDTD the solution is normally obtained by propagating the field forward in time; thus the electromagnetic time response of the medium must be modeled explicitly. For dispersive media, this implies a computationally expensive time convolution in order to account for the medium's frequency behaviour.

To avoid these drawbacks, we pursue a different approach in the frequency domain. As previously outlined, time-harmonic scattering by inhomogeneous 3D structures and located within

a free space environment can be described by volume integral equations (VIEs) involving the free space Green function. Electromagnetic VIEs have been solved numerically by many researchers over the years.

In 1984, Schaubert et al. [98] formulated for the first time the Galerkin solution of the Electric Field VIE (EF-VIE) for dielectric scatterers in terms of the electric flux density with conforming (Raviart–Thomas) vector basis functions. This approach and its counterpart based on collocation (together referred to as moment methods [99, 100]) have found wide ranging applications ever since, e.g.: particle scattering [101, 102], optical near field calculation [103, 104], polarizability analysis [105], indoor radio-wave propagation modeling [106], etc. Various features were added to this formulation, such as fast solvers enabling large-scale analysis [107], coupling with surface integral equations (SIEs) [108], low-order solenoidal basis functions to model flux densities more realistically [109, 110], and a special version for low-frequency analysis [111] – but the basic projection formulation has essentially remained unchanged.

The idea of solving the Magnetic Field VIE (MF-VIE) for dielectric scatterers instead (analogous to solving either the EF- or MF surface IE in the case of conducting scatterers [99]) has not received much attention, though it has been proposed in [112, 113]. Moreover, VIE-based analysis of structures with inhomogeneity in both ϵ and μ has almost not been considered at all. Recently, Botha [48] presented a comprehensive overview of Galerkin Method of Moments (MoM) formulations for the numerical solution of VIEs together with comparative numerical results. Newly proposed formulations involve solving the curl-conforming fields, which can be discretized with fewer unknowns than div-conforming ones, implying lower computational costs [48].

The authors of [49] and [96, 114] applied VIEs to penetrable objects of high-contrast and extremely anisotropic materials (e. g. metamaterials), respectively. In the former, the electric and magnetic VIE are compared and their properties investigated. Numerical experiments show that if Galerkin’s method with the lowest mixed-order basis functions is used to discretize the equations the accuracy of the MF-VIE can be significantly poorer than the accuracy of the EF-VIE, in particular, for high-contrast objects at high frequencies. The accuracy of the MF-VIE can be essentially improved with full first order (linear) basis functions. The linear basis functions are found to be useful also when a single volume integral equation is used to model a general scatterer where both permittivity and permeability differ from the background [49]. In [96] is shown that VIEs based on equivalent currents expanded with piece-wise constant basis functions and the Galerkin scheme for testing is more stable than the behaviours of more conventional formulations based on fluxes or fields when the scatterer is extremely anisotropic.

Given the above discussion, it is clear that the numerical solution of electromagnetic VIEs continues to be a relevant topic, and that such methods are widely used, and formulations for generally inhomogeneous scatterers deserve attention.

3.1.1 Volume Integral Equation (VIE) Formulations

There are several possibilities to settle a VIE for inhomogeneous objects, depending on which quantity will be the unknown (\mathbf{X}, \mathbf{Y}) . For the special case of non-magnetic objects, such as the human body in the microwave range, the generic formulation of IEs for the magnetic fields can be retrieved from the electric field which is reduced to:

$$\mathbf{E}_b(\vec{r}) = \alpha \mathbf{X}(\vec{r}) - (\nabla \nabla \cdot + \mathbf{k}_b^2) \Pi(\beta \mathbf{X}) \quad (3.1)$$

where:

$$\Pi(\mathbf{X}) = \int_{\Omega} g(\vec{r} - \vec{r}') \mathbf{X} d\Omega' \quad , \quad g(\vec{r} - \vec{r}') = \frac{e^{-j\mathbf{k}_b|\vec{r}-\vec{r}'|}}{4\pi|\vec{r} - \vec{r}'|} \quad (3.2)$$

with $g(\vec{r} - \vec{r}')$ the Green function, \vec{r} the position vector, and \mathbf{k}_b the propagation wavenumber in the background medium. Among many possibilities for (\mathbf{X}, \mathbf{Y}) , there are essentially three sets:

1. electric and magnetic fields (\mathbf{E}, \mathbf{H}) ,
2. electric and magnetic fluxes (\mathbf{D}, \mathbf{B}) ,
3. electric and magnetic polarization currents $(\mathbf{J}_p, \mathbf{M}_q)$.

for which the parameters α and β read:

$$(\alpha, \beta) = \begin{cases} (1, \chi) & \text{for } (\mathbf{X}, \mathbf{Y}) = (\mathbf{E}, \mathbf{H}) \\ \left(\frac{1}{\epsilon}, \epsilon \chi\right) & \text{for } (\mathbf{X}, \mathbf{Y}) = (\mathbf{D}, \mathbf{B}) \\ \left(\frac{1}{\chi}, \frac{1}{j\omega\epsilon_b}\right) & \text{for } (\mathbf{X}, \mathbf{Y}) = (\mathbf{J}_p, \mathbf{M}_q) \end{cases} \quad (3.3)$$

These three formulations are equivalent with respect to the existence and uniqueness of the solution if both the permittivity and permeability functions are coercive and bounded, and are invertible [115].

From the numerical point of view, the main difference in these formulations is the choice of the basis and testing functions. Basis functions are used for representing the unknowns; hence, they should satisfy the continuity conditions of the unknowns. Especially, it is crucial

not to enforce any extra continuities. In other words, basis functions should span a proper vector space. Normal components of the flux densities must be continuous across the material interfaces, and therefore, the (\mathbf{D}, \mathbf{B}) -formulation is usually discretized with the divergence-conforming basis functions, known as the SWG functions or 3D RWG functions [98]. In [116] the anisotropic (\mathbf{E}, \mathbf{H}) -formulation was discretized with curl-conforming functions [117] which keep the tangential continuity. The (\mathbf{E}, \mathbf{H}) -formulation has also been discretized with piecewise constant and linear functions in order to obtain a non-conformal method [118, 119]. In this case, the continuity of the fields is not directly enforced, but the solution will approximately satisfy these conditions. Polarization currents have no continuity across the material interfaces, therefore in the $(\mathbf{J}_p, \mathbf{M}_q)$ -formulation it is essential that basis functions do not enforce any continuity across material boundaries. The equivalent currents are usually expanded with piecewise constant functions, and point-matching/Nyström techniques are applied to test the equations [120, 121]. The choice of the testing functions is also important in order to obtain an efficient numerical method. Therefore, we need to look at the mapping properties of the equations

1. (\mathbf{E}, \mathbf{H}) -formulation: $H(\text{rot}) \rightarrow H(\text{div})$
2. (\mathbf{D}, \mathbf{B}) -formulation: $H(\text{div}) \rightarrow H(\text{rot})$
3. $(\mathbf{J}_p, \mathbf{M}_q)$ -formulation: $L_2 \rightarrow L_2$

where L_2 is a function space with square integrable functions, and

$$H(\text{div}) = \{\mathbf{f} \mid \mathbf{f} \in L_2 \text{ and } \nabla \cdot \mathbf{f} \in L_2\} \quad (3.4a)$$

$$H(\text{rot}) = \{\mathbf{f} \mid \mathbf{f} \in L_2 \text{ and } \nabla \times \mathbf{f} \in L_2\} \quad (3.4b)$$

The testing should be done in the dual space and the above considerations are the basis for a proper application of the MoM.

3.1.2 Towards Green Functions with Vector and Scalar Potentials

The procedure to obtain the VIE formulation for the scattering operator from Maxwell's equations is explained in the following section. Maxwell's equations are a set of coupled 1st order partial differential equations (2.1) relating electric and magnetic fields. They imply three dimensional unknown vector fields $\mathbf{E}(\vec{r}) = (E_x(\vec{r}), E_y(\vec{r}), E_z(\vec{r}))$ and $\mathbf{H}(\vec{r}) = (H_x(\vec{r}), H_y(\vec{r}), H_z(\vec{r}))$. To solve them, we use a mathematical procedure, called Gauge fixing. It aims to diminish the degrees of freedom and obtain a smaller number of unknowns of a system of equations, by introducing new defined quantities. Based on the vanishing divergence of the magnetic flux

Chapter 3. Volume Integral Operator of Electromagnetic Scattering

(2.1d), the vector potential $\mathbf{A}(\vec{r})$ is defined as:

$$\mu_b \mathbf{H}_A(\vec{r}) = \nabla \times \mathbf{A}(\vec{r}) \quad (3.5)$$

where, the subscript $_A$ stands for fields excited by the potential $\mathbf{A}(\vec{r})$. By substituting the latter into Faraday's Law (2.1a), $\nabla \times (\mathbf{E}_A(\vec{r}) + j\omega\mathbf{A}(\vec{r})) = 0$, the scalar potential is defined as:

$$\mathbf{E}_A(\vec{r}) + j\omega\mathbf{A}(\vec{r}) = -\nabla V(\vec{r}) \quad (3.6)$$

The potentials $\mathbf{A}(\vec{r})$ and $V(\vec{r})$ are not unique, applying the Lorenz Gauge defines the specific relation:

$$\nabla \cdot \mathbf{A}(\vec{r}) = -\frac{j\mathbf{k}_b^2}{\omega} V(\vec{r}) \quad (3.7)$$

By inserting (3.6) in Gauss's equation (2.1c) and (3.5) in Faraday's equation (2.1a), with the mathematical identity $\nabla \times \nabla \times \bullet = (-\nabla^2 + \nabla \nabla \cdot) \bullet$, and the relation between the two potentials, the resulting system of equations is called inhomogeneous Helmholtz system of equations, that hold independently for each of the three components of \mathbf{A} :

$$[\nabla^2 + \mathbf{k}_b^2(\vec{r})] \mathbf{A}(\vec{r}) = -\mu_b \mathbf{J}(\vec{r}) \quad (3.8)$$

$$[\nabla^2 + \mathbf{k}_b^2(\vec{r})] V(\vec{r}) = -\frac{\rho(\vec{r})}{\epsilon_b} \quad (3.9)$$

thus obtaining four scalar Helmholtz equations [122, (6-17)]. For the recall, ρ is the volume charge density [C/m³]. The scalar Green function $g(\vec{r}, \vec{r}')$ is the solution of the Helmholtz operator for a single source point positioned in \vec{r}' , defined as a Dirac distribution $\delta(\vec{r} - \vec{r}')$:

$$[\nabla^2 + \mathbf{k}_b^2(\vec{r})] g(\vec{r}, \vec{r}') = \delta(\vec{r} - \vec{r}') \quad (3.10)$$

For a homogeneous three-dimensional space, the only physical solution of this equation

is [122]:

$$g(\vec{r}, \vec{r}') = \frac{e^{\pm j k_b(\vec{r})|\vec{r}-\vec{r}'|}}{4\pi|\vec{r}-\vec{r}'|} \quad (3.11)$$

the plus sign denotes the solution for a wave traveling towards the source, and the minus sign is for a spherical wave that propagates towards infinity, away from the source. We will only retain the outward propagation.

Once the Green function $g(\vec{r}, \vec{r}')$ is determined, the fields for any source can be determined through the vector potential:

$$\mathbf{A}(\vec{r}) = -\mu_b \int_{\Omega} g(\vec{r}, \vec{r}') \mathbf{J}_p(\vec{r}') d\Omega' \quad (3.12)$$

The solution to (3.10) is a scalar quantity. To relate it to the vectorial behavior of the electric and magnetic fields, which is that of a source current in one direction leads to fields with x, y, z -components, the Green function should be adapted to a Green Tensor, called the *Dyadic Green function*. Starting from (3.6), the relation between the electric field $\mathbf{E}_A(\vec{r})$ and the vector potential $\mathbf{A}(\vec{r})$ is found to be

$$\mathbf{E}_A(\vec{r}) = -j\omega \left[\bar{\bar{\mathbf{I}}} + \frac{1}{k_b(\vec{r})^2} \nabla \nabla \cdot \right] \mathbf{A}(\vec{r}) \quad (3.13)$$

The Green dyadic is therefore defined as in (2.11) and the general solution for the electric fields expressed in (2.10).

3.1.3 Singular Integrals

The accuracy of the solution of the IE critically depends on its correct treatment. For this, a plethora of methods has been developed, mostly in the framework of SIEs since these have been in the focus of research in the last 30 years. Essentially, their evaluation can be achieved by applying either singularity extraction [123–125] or singularity cancellation [126–128] techniques, where the latter uses a coordinate transformation to remove the singularity. For the emerging VIE, these techniques need to be adapted, modified and extended where possible and new methods developed where necessary. Recently, the authors of [129, 130] have proposed two new singularity cancellation techniques with promising results for SIEs. Their possible application to VIE needs to be studied. For example, in the direct evaluation

Chapter 3. Volume Integral Operator of Electromagnetic Scattering

technique [129] the idea is to have a maximum of analytical integrations and reduce the numerical quadratures to a minimum. Another possibility to apply concepts from SIEs to VIEs is to reduce the volume integrals by means of Gauß' and Stokes' theorems to boundary surface integrals. The numerical evaluation of these integrals remains a challenging scientific issue. For the following discussion on singular integrals, equation (2.10) will be formulated as:

$$\mathbf{E}_i(\vec{r}) = \mathbf{E}(\vec{r}) - j\omega\mu_b \left[\mathbf{S}_j(\vec{r}) + \frac{1}{k_b(\vec{r})^2} \nabla \nabla \cdot \mathbf{S}_j(\vec{r}) \right] \quad (3.14)$$

with

$$\mathbf{S}_j(\vec{r}) = \int_{\Omega} g(\vec{r}, \vec{r}') \mathbf{J}_p(\vec{r}') d\Omega' \quad (3.15)$$

Equation (3.14) is an integral equation for $\mathbf{E}(\vec{r})$ over the volume Ω of the scatterer and is therefore called a *Volume Integral Equation* (VIE). The unknown $\mathbf{E}(\vec{r})$ appears inside and outside the integral, and the integral is *definite* (over Ω), which is the definition of a 2nd kind Fredholm-type integral equation. However, the scalar Green function becomes unbounded inside the scatterer when \vec{r} and \vec{r}' coincide. These integrals are called singular integrals and can be separated into two categories: weakly and strongly singular integrals. The evaluation of these integrals are different.

- **Weakly singular integrals**

The first important information is to know whether the fields excited by these sources are bounded for the contrast source formulation, especially when $\vec{r} = \vec{r}'$. In (3.14) there are two integrals to evaluate. The norm of both integrals is of the form:

$$|\mathbf{S}_j(\vec{r})| = C \left| \int_{\Omega} \frac{1}{|\vec{r} - \vec{r}'|^{\alpha}} d\Omega' \right| \quad (3.16)$$

The dimension of the manifold (the integration domain) being three, it is possible to integrate on a sphere around \vec{r}' :

$$|\mathbf{S}_j(\vec{r})| = C \left| \int_0^R \int_0^{2\pi} \int_0^{\pi} \frac{1}{r^{\alpha}} r^2 \sin\theta d\theta d\phi dr \right| = 4\pi C \left| \int_0^R r^{2-\alpha} dr \right| = 4\pi C \frac{R^{3-\alpha}}{3-\alpha} \quad (3.17)$$

with $r = |\vec{r} - \vec{r}'|$. The factor α is called the degree of singularity: for negative or null values of α , the integral is called *regular* and for strictly positive values of α , it is called *singular*. If α is smaller than the dimension of the manifold, the integral is called *weakly singular*

otherwise it is called *strongly singular*. For weakly singular integrals, the Jacobian cancels the singularity, and the integral can be directly evaluated. However, for strongly singular integrals, this is not the case and more care should be taken when evaluating the integral. In (3.15), one of the two integrals to evaluate is directly $\mathbf{S}_j(\vec{r})$ which is weakly singular and bounded with $\alpha = 1$.

• **Strongly singular integrals**

The second kind of integral to be considered is $\nabla\nabla\cdot\mathbf{S}_j(\vec{r})$. The two spatial differentiations (∇ and $\nabla\cdot$) would increase the degree of singularity to $\alpha = 3$ and if they are simply taken under the integral, the integral is *strongly singular*. This integral can still be bounded, however, more care should be brought to evaluate it. Let's first start with analyzing $g(\vec{r}, \vec{r}')$. To evaluate the integral, the first manoeuvre consists of decomposing $g(\vec{r}, \vec{r}')$ into two functions: $g_0(\vec{r}, \vec{r}')$ and $g_1(\vec{r}, \vec{r}')$:

$$g(\vec{r}, \vec{r}') = g_0(\vec{r}, \vec{r}') + g_1(\vec{r}, \vec{r}') \quad \text{with} \quad \begin{cases} g_0(\vec{r}, \vec{r}') = \frac{1}{|\vec{r} - \vec{r}'|} \\ g_1(\vec{r}, \vec{r}') = \frac{e^{-jk_b(\vec{r})|\vec{r} - \vec{r}'|} - 1}{|\vec{r} - \vec{r}'|} \end{cases} \quad (3.18)$$

The reason to make this procedure is that $g_1(\vec{r}, \vec{r}')$ is non-singular for $\vec{r} = \vec{r}'$ as:

$$\lim_{r \rightarrow 0} \frac{e^{-jk_b(\vec{r})|\vec{r} - \vec{r}'|} - 1}{|\vec{r} - \vec{r}'|} = -\frac{jk_b|\vec{r} - \vec{r}'|}{4\pi} \quad (3.19)$$

Therefore, after two spatial differentiations, $\alpha = 2$ and therefore the integral is weakly singular and does not need any special attention. On the other hand $g_0(\vec{r}, \vec{r}')$, which represents the static Green function ($\omega = 0$, $\mathbf{k}_b = 0$) is singular and therefore $\alpha = 3$. However, the added value of this separation is that the strongly singular part carried by $g_0(\vec{r}, \vec{r}')$ is now symmetric and other manoeuvres can be applied to solve it. The procedure consists of four distinct steps:

1. Introduce a (small) volume of arbitrary shape V_δ around \vec{r} , thus dividing again the integral into a regular and a strongly singular part.

The integral $\mathbf{S}_0(\vec{r})$ reads:

$$\mathbf{S}_0(\vec{r}) = \nabla\nabla\cdot \int_{\Omega} g_0(\vec{r}, \vec{r}') \mathbf{J}_p(\vec{r}') d\Omega' \quad (3.20)$$

We define V_δ around \vec{r} such that $V_\delta \rightarrow 0$ when $\delta \rightarrow 0$, and split $\mathbf{S}_0(\vec{r})$ into a sum of

two limits:

$$\mathbf{S}_0(\vec{r}) = \lim_{\delta \rightarrow 0} \mathbf{S}_1(\vec{r}) + \lim_{\delta \rightarrow 0} \mathbf{S}_2(\vec{r}) \quad \text{with} \quad \begin{cases} \mathbf{S}_1(\vec{r}) = \nabla \nabla \cdot \int_{\Omega \setminus V_\delta} g_0(\vec{r}, \vec{r}') \mathbf{J}_p(\vec{r}') d\Omega' \\ \mathbf{S}_2(\vec{r}) = \nabla \nabla \cdot \int_{V_\delta} g_0(\vec{r}, \vec{r}') \mathbf{J}_p(\vec{r}') d\Omega' \end{cases} \quad (3.21)$$

$\lim_{\delta \rightarrow 0} \mathbf{S}_1(\vec{r})$ is regular as it excludes all \vec{r} leading to a singularity, and, after two spatial differentiations, is simply expressed as:

$$\lim_{\delta \rightarrow 0} \mathbf{S}_1(\vec{r}) = \lim_{\delta \rightarrow 0} \int_{\Omega} \frac{3\hat{n}\hat{n}^\top - \bar{\bar{I}}}{|\vec{r} - \vec{r}'|^3} \mathbf{J}_p(\vec{r}') d\Omega' \quad (3.22)$$

with the unit vector $\hat{n} = \frac{\vec{r} - \vec{r}'}{|\vec{r} - \vec{r}'|}$ in radial direction in spherical coordinates. However, $\mathbf{S}_2(\vec{r})$ is strongly singular and we should go to step 2 to solve it.

2. Find a way to only keep the Green function below the singular integral.

The main idea here is to keep only the symmetric $g_0(\vec{r}, \vec{r}')$ under the integral and the two spatial differentiations. If we add and subtract $\mathbf{J}_p(\vec{r})$ on both sides we get:

$$\lim_{\delta \rightarrow 0} \mathbf{S}_2(\vec{r}) = \lim_{\delta \rightarrow 0} \mathbf{S}_3(\vec{r}) - \lim_{\delta \rightarrow 0} \mathbf{S}_4(\vec{r}) \quad \text{with} \quad \begin{cases} \mathbf{S}_3(\vec{r}) = \int_{V_\delta} \nabla (\nabla g_0(\vec{r}, \vec{r}')) d\Omega' \mathbf{J}_p(\vec{r}) \\ \mathbf{S}_4(\vec{r}) = \int_{V_\delta} \nabla (\nabla g_0(\vec{r}, \vec{r}')) [\mathbf{J}_p(\vec{r}) - \mathbf{J}_p(\vec{r}')] d\Omega' \end{cases} \quad (3.23)$$

Without going into detail if $|\mathbf{J}_p(\vec{r}) - \mathbf{J}_p(\vec{r}')| \leq C_r |\vec{r} - \vec{r}'|^\rho$, with $C_r < \infty$ and $\rho > 0$, then \mathbf{S}_4 exists as a Hölder continuous function and $\lim_{\delta \rightarrow 0} \mathbf{S}_4(\vec{r}) = 0$. The remaining singular part $\lim_{\delta \rightarrow 0} \mathbf{S}_3(\vec{r})$ goes to step 3.

3. Apply the Gauss theorem after understanding that by symmetry $\nabla = -\nabla'$

$$\begin{aligned}
 \mathbf{S}_3(\vec{r}) &= \int_{V_\delta} \nabla (\nabla g_0(\vec{r}, \vec{r}')) d\Omega' \mathbf{J}_p(\vec{r}) \\
 &= \int_{V_\delta} \nabla' (\nabla' g_0(\vec{r}, \vec{r}')) d\Omega' \mathbf{J}_p(\vec{r}) \\
 &= \int_{S_\delta} (\nabla' g_0(\vec{r}, \vec{r}')) \hat{n}^\top d\mathbf{S}' \mathbf{J}_p(\vec{r}) \\
 &= \int_{S_\delta} \frac{-\hat{n} \hat{n}^\top}{|\vec{r} - \vec{r}'|^2} d\mathbf{S}' \mathbf{J}_p(\vec{r})
 \end{aligned} \tag{3.24}$$

4. Solve (3.24) in terms of its *Principal Value*.

$$\mathbf{S}_3(\vec{r}) = -\bar{\bar{L}} J_p(\vec{r}) \quad \text{with} \quad \bar{\bar{L}} = \int_{S_\delta} \frac{\hat{n} \hat{n}^\top}{|\vec{r} - \vec{r}'|^2} d\mathbf{S}' \tag{3.25}$$

$\bar{\bar{L}}$ is called the source dyadic and solutions for several shapes of the principal volume V_δ are listed in [131]. In the case of a sphere of radius δ such that $|\vec{r} - \vec{r}'| \leq \delta$:

$$\bar{\bar{L}}_{\text{O}} = \frac{\bar{\bar{I}}}{3} \tag{3.26}$$

Later, as we will use voxels (cubic cells) for the discretization needed to solve numerically the problem, it is useful to already mention that the effective volume of a cube is the same as the volume of a sphere [132] and therefore its source dyadic is also equal to:

$$\bar{\bar{L}}_{\text{C}} = \frac{\bar{\bar{I}}}{3} \tag{3.27}$$

With all this information it is possible to numerically evaluate (3.14). Fig. 3.1 schematically depicts the manoeuvres explained above to evaluate equation (3.14).

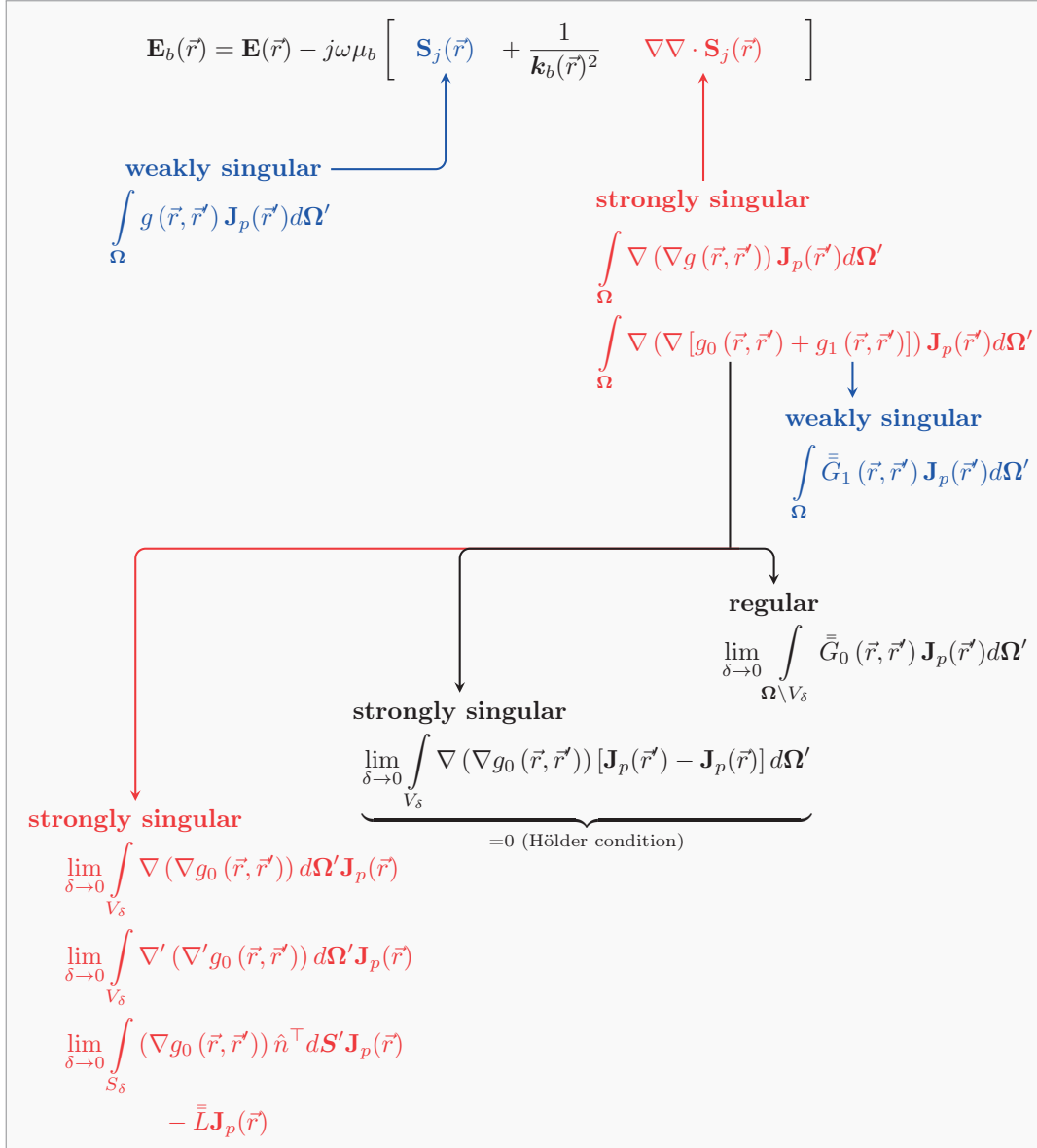


Figure 3.1 – Schematic summary of the singularity management in VIE for the contrast-source formulation.

After rearranging equations schematically depicted in Fig. 3.1, the final result is:

$$\begin{aligned}
 j\omega\epsilon_b\chi(\vec{r})\mathbf{E}_i(\vec{r}) &= \left(\bar{\mathbf{I}} + \chi(\vec{r})\bar{\mathbf{L}} \right) \mathbf{J}_p(\vec{r}) \\
 &\quad - \chi(\vec{r}) \left\{ \int_{\Omega} \left[\mathbf{k}_b^2(\vec{r})g(\vec{r}, \vec{r}') + \bar{G}_1(\vec{r}, \vec{r}') \right] \mathbf{J}_p(\vec{r}') d\Omega' + P.V. \int_{\Omega} \bar{G}_0(\vec{r}, \vec{r}') \mathbf{J}_p(\vec{r}') d\Omega' \right\}
 \end{aligned} \tag{3.28}$$

with:

$$\bar{\bar{G}}_0(\vec{r}, \vec{r}') = \nabla \nabla g_0(\vec{r}, \vec{r}') = \frac{3\hat{n}\hat{n}^\top - \bar{\bar{I}}}{|\vec{r} - \vec{r}'|^3} \quad (3.29)$$

and:

$$\begin{aligned} \bar{\bar{G}}_1(\vec{r}, \vec{r}') &= \nabla \nabla g_1(\vec{r}, \vec{r}') \\ &= g_1(\vec{r}, \vec{r}') \frac{3\hat{n}\hat{n}^\top - \bar{\bar{I}}}{|\vec{r} - \vec{r}'|^2} + j\mathbf{k}_b(\omega)g(\vec{r}, \vec{r}') \frac{3\hat{n}\hat{n}^\top - \bar{\bar{I}}}{|\vec{r} - \vec{r}'|} - \mathbf{k}_b(\omega)g(\vec{r}, \vec{r}')\hat{n}\hat{n}^\top \end{aligned} \quad (3.30)$$

3.2 Numerical Solution of VIE with Method of Moments (MoM)

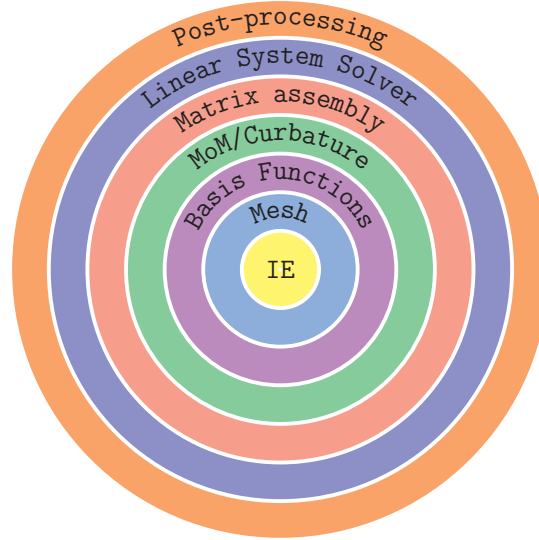


Figure 3.2 – Integral Equation solver layout. From core to surface: Integral Equation (IE) formulation, mesh, basis functions, MoM/curbature, matrix assembly, linear system solver, post-processing.

The solution of the integral equation (3.28), apart for very special cases called canonical cases that have simple geometries, cannot be evaluated analytically and is solved numerically. The typical layout of an integral equation solver is depicted as an onion structure in Fig. 3.2. When the IE formulation is set, the domain of the scatterer Ω is approximated by a mesh, that will provide a finite number of calculation points. Then the unknown quantity, here the polarization currents $\mathbf{J}_p(\vec{r})$, is approximated by an appropriate expansion (known basis functions). The Method of Moments is a procedure that translates the problem into an algebraic problem of linear equations. After a proper assembly in matrix form, the system of equations will be solved by a linear system solver, which is either a *direct* method (inversion of the whole matrix) for small size problems, or an *iterative* method otherwise. Post-processing steps are usually

visualizations of the solution representing the unknown quantity for a specific application. The IE-formulation was explained in the previous section. The six remaining steps are briefly explained here.

Let us first distinguish two different kinds of approaches while solving integral or differential problems numerically: either the mathematical operator is approximated, or the solution is approximated. For the first approach an example would be the FDTD method or Nyström's method. For the second approach the problem consists of finding the unknown coefficients of known functions, as typically does the method of Finite Elements. The advantage of the latter is that if the correct basis functions are found, the solution is proven to converge to the exact solution by increasing mesh density.

3.2.1 Discretization: Mesh and Basis Functions

The grid is approximated by N cells, which are cubes/voxels of side length h . The grid points are defined by their centers \vec{r}_n :

$$\vec{r}_n = \begin{pmatrix} n_x h \\ n_y h \\ n_z h \end{pmatrix} \quad \text{with} \quad \begin{cases} n_x = 0, 1, \dots, N_x - 1 \\ n_y = 0, 1, \dots, N_y - 1 \\ n_z = 0, 1, \dots, N_z - 1 \end{cases} \quad (3.31)$$

N_x , N_y and N_z being the number of voxels in the x , y , and z -direction respectively, such that $N = N_x N_y N_z$.

The unknown quantity $\mathbf{J}_p(\vec{r}) = J_x(\vec{r}) \hat{x} + J_y(\vec{r}) \hat{y} + J_z(\vec{r}) \hat{z}$ is expanded in terms of suitable vector basis functions:

$$\begin{cases} J_x(\vec{r}) = \sum_{l=1}^N j_x^{(l)} \cdot \psi_x^{(l)}(\vec{r}) \\ J_y(\vec{r}) = \sum_{l=1}^N j_y^{(l)} \cdot \psi_y^{(l)}(\vec{r}) \\ J_z(\vec{r}) = \sum_{l=1}^N j_z^{(l)} \cdot \psi_z^{(l)}(\vec{r}) \end{cases} \quad (3.32)$$

The functions $\psi^{(l)}(\vec{r})$ are known and are called *basis functions*. They are orthogonal with

3.2. Numerical Solution of VIE with Method of Moments (MoM)

respect to a scalar product. The simplest possibility is to choose *piece-wise constant* functions:

$$\psi_x^{(l)}(\vec{r}) = \psi_y^{(l)}(\vec{r}) = \psi_z^{(l)}(\vec{r}) = \delta^{(l)}(\vec{r}) = \begin{cases} 1 & \vec{r} \in \Omega^{(l)} \\ 0 & \vec{r} \notin \Omega^{(l)} \end{cases} \quad (3.33)$$

Piecewise constant basis functions means that the polarization current \mathbf{J}_p is constant in each cell and equals $\mathbf{j}^{(l)} = (j_x^{(l)}, j_y^{(l)}, j_z^{(l)})$.

It is now possible to define the equation (3.28) in terms of matrices. They represent a system of N equations, where the discretization needed to numerically solve the problem converts integration over a certain domain, into summations of discrete values for each cell.

Inserting (3.33) in (3.28):

$$j\omega\epsilon_b\chi(\vec{r})\mathbf{E}_i(\vec{r}) = \sum_{l=1}^N \left\{ \left(\bar{\bar{I}} + \chi(\vec{r})\bar{\bar{L}} \right) \delta_l(\vec{r}) - \chi(\vec{r}) \mathcal{L}_l(\vec{r}) \right\} \mathbf{j}^{(l)} \quad (3.34)$$

where $\mathcal{L}_l(\vec{r})$ is an operator defined as:

$$\mathcal{L}_l(\vec{r}) = \int_{\Omega^{(l)}} \left[\mathbf{k}_b^2(\vec{r}) g(\vec{r}, \vec{r}') + \bar{\bar{G}}_1(\vec{r}, \vec{r}') \right] d\Omega' + P.V. \int_{\Omega^{(l)}} \bar{\bar{G}}_0(\vec{r}, \vec{r}') d\Omega \quad (3.35)$$

The system of equation (3.34) has $3N$ scalar unknowns (N grid points and 3 polarizations). However the system has an infinite number of conditions as these equations are valid for any $\vec{r} \in \Omega$. The next subsection will explain how with the Method of Moments it is possible to select only $3N$ possibilities to numerically solve the problem.

3.2.2 Galerkin Method of Moments: Discrete Form of the Green Dyadic

MoM is a technique in which a specific scalar product is applied to a system of equations in order to turn, in our case, our integral equation into a set of algebraic equations. This procedure also called *testing* or *weighting* has a wide set of possibilities. In our case we will use the Galerkin MoM where the *test* functions $\phi^{(k)}(\vec{r})$ are the same functions as the basis functions. This is justified by our choice of VIE formulation. In 3.1.1 we saw that the $(\mathbf{J}_p, \mathbf{M}_q)$ -formulation maps L_2 on L_2 . Thus, we can choose as testing/weighting function the basis function, this technique is used for self-interactions terms. If the testing functions are Dirac distributions $\phi^{(k)}(\vec{r}) = \delta(\vec{r} - \vec{r}_n) = \delta_n$, the method is known as *collocation* method or *point testing*, and it is here used for the mutual interaction elements. The standard collocation

Chapter 3. Volume Integral Operator of Electromagnetic Scattering

method [133], gives an order h^2 accuracy, where h is the size of an elementary cubic cell. The testing is freely chosen to be performed on the center of the voxels \vec{r}_n . The scalar product reads:

$$\begin{cases} \langle \delta_n \hat{x}, j\omega \epsilon_b \chi(\vec{r}) E_{i,x}(\vec{r}) \rangle = j\omega \epsilon_b \chi(\vec{r}) E_{i,x}(\vec{r}_n) \\ \langle \delta_n \hat{y}, j\omega \epsilon_b \chi(\vec{r}) E_{i,y}(\vec{r}) \rangle = j\omega \epsilon_b \chi(\vec{r}) E_{i,y}(\vec{r}_n) \\ \langle \delta_n \hat{z}, j\omega \epsilon_b \chi(\vec{r}) E_{i,z}(\vec{r}) \rangle = j\omega \epsilon_b \chi(\vec{r}) E_{i,z}(\vec{r}_n) \end{cases} \quad (3.36)$$

with:

$$\begin{cases} j\omega \epsilon_b \chi(\vec{r}) E_{i,x}(\vec{r}_n) = \sum_{l=1}^N \left\{ \left(\bar{I} + \chi(\vec{r}_n) \bar{L} \right) \delta_l(\vec{r}_n) - \chi(\vec{r}_n) \mathcal{L}_l(\vec{r}_n) \right\} j_x^{(l)} \quad , \quad \vec{r}_n \in \Omega_n \\ j\omega \epsilon_b \chi(\vec{r}) E_{i,y}(\vec{r}_n) = \sum_{l=1}^N \left\{ \left(\bar{I} + \chi(\vec{r}_n) \bar{L} \right) \delta_l(\vec{r}_n) - \chi(\vec{r}_n) \mathcal{L}_l(\vec{r}_n) \right\} j_y^{(l)} \quad , \quad \vec{r}_n \in \Omega_n \\ j\omega \epsilon_b \chi(\vec{r}) E_{i,z}(\vec{r}_n) = \sum_{l=1}^N \left\{ \left(\bar{I} + \chi(\vec{r}_n) \bar{L} \right) \delta_l(\vec{r}_n) - \chi(\vec{r}_n) \mathcal{L}_l(\vec{r}_n) \right\} j_z^{(l)} \quad , \quad \vec{r}_n \in \Omega_n \end{cases} \quad (3.37)$$

Note that $\delta_l(\vec{r}_n)$ is non-zero and $\mathcal{L}_l(\vec{r}_n)$ is singular only for $n = l$. The later should be translated in matrix notations with the incident field vector E^i :

$$E^i = \begin{pmatrix} E_x^i \\ E_y^i \\ E_z^i \end{pmatrix} \in \mathbb{C}^{3N} \quad \text{with} \quad E_x^i = \begin{pmatrix} E_{i,x}(\vec{r}_1) \\ \vdots \\ E_{i,x}(\vec{r}_N) \end{pmatrix}, \quad E_y^i = \begin{pmatrix} E_{i,y}(\vec{r}_1) \\ \vdots \\ E_{i,y}(\vec{r}_N) \end{pmatrix}, \quad E_z^i = \begin{pmatrix} E_{i,z}(\vec{r}_1) \\ \vdots \\ E_{i,z}(\vec{r}_N) \end{pmatrix} \quad (3.38)$$

the total field E :

$$E = \begin{pmatrix} E_x \\ E_y \\ E_z \end{pmatrix} \in \mathbb{C}^{3N} \quad \text{with} \quad E_x = \begin{pmatrix} E_x(\vec{r}_1) \\ \vdots \\ E_x(\vec{r}_N) \end{pmatrix}, \quad E_y = \begin{pmatrix} E_y(\vec{r}_1) \\ \vdots \\ E_y(\vec{r}_N) \end{pmatrix}, \quad E_z = \begin{pmatrix} E_z(\vec{r}_1) \\ \vdots \\ E_z(\vec{r}_N) \end{pmatrix} \quad (3.39)$$

and the polarization currents vector J^p :

$$J^p = \begin{pmatrix} j_x^p \\ j_y^p \\ j_z^p \end{pmatrix} \in \mathbb{C}^{3N} \quad \text{with} \quad j_x^p = \begin{pmatrix} j_x^{(1)} \\ \vdots \\ j_x^{(N)} \end{pmatrix}, \quad j_y^p = \begin{pmatrix} j_y^{(1)} \\ \vdots \\ j_y^{(N)} \end{pmatrix}, \quad j_z^p = \begin{pmatrix} j_z^{(1)} \\ \vdots \\ j_z^{(N)} \end{pmatrix} \quad (3.40)$$

3.2. Numerical Solution of VIE with Method of Moments (MoM)

The Green Dyadic G is defined as:

$$[G_{mn}]_{ij} = \hat{i} \cdot \left\{ \chi(\vec{r}_n) \bar{L} \delta_m(\vec{r}_n) - \chi(\vec{r}_n) \mathcal{L}_m(\vec{r}_n) \right\} \cdot \hat{j} \quad \text{with } i, j = \{x, y, z\}, \quad \text{and } m, n = 1, \dots, N \quad (3.41)$$

In most of the CEM methods the numerical integration in one or more dimensions is found in the core of the algebraic computations. If it is taken into account that these integrals have to be computed $\mathcal{O}(N^2)$ times, N being the number of unknowns of the problem, then any non-optimality in accuracy and computational efficiency seriously deteriorates the behaviour of the whole algorithm. After a rather classical numerical integration the matrix elements are completely defined by:

$$[G_{mn}]_{ij} = h^3 \frac{e^{-j\mathbf{k}_b(\omega)|\vec{r}_m - \vec{r}_n|}}{|\vec{r}_m - \vec{r}_n|} \left(-\mathbf{k}_b^2(\omega) + \frac{3j\mathbf{k}_b(\omega)}{|\vec{r}_m - \vec{r}_n|} + \frac{3}{|\vec{r}_m - \vec{r}_n|^2} \right) \Theta_i(\vec{r}_m - \vec{r}_n) \Theta_j^\top(\vec{r}_m - \vec{r}_n) \\ + h^3 \frac{e^{-j\mathbf{k}_b(\omega)|\vec{r}_m - \vec{r}_n|}}{|\vec{r}_m - \vec{r}_n|} \left(\mathbf{k}_b^2(\omega) + \frac{-j\mathbf{k}_b(\omega)}{|\vec{r}_m - \vec{r}_n|} - \frac{1}{|\vec{r}_m - \vec{r}_n|^2} \right) \delta_{ij} \quad (3.42)$$

$\Theta_i(\vec{r}_m - \vec{r}_n) = \frac{\hat{i}_m - \hat{i}_n}{|\vec{r}_m - \vec{r}_n|}$ and $m, n = 1, 2, \dots, N$ with $m \neq n$. These elements represent the off-diagonal elements of the submatrices G_{ij} . For the diagonal elements of the main diagonal ($m = n$ and $i = j$) the terms are always the same and are:

$$\frac{2}{3} (1 + j\mathbf{k}_b a) e^{-j\mathbf{k}_b a} - 1 \quad \text{with } a = h \left(\frac{3}{4\pi} \right)^{1/3} \quad (3.43)$$

These terms represent the self interactions, all other entries of $[G_{mn}]_{ij}$ represent mutual interactions. The auxiliary diagonals ($m = n$ and $i \neq j$) have zeros in their diagonals.

Finally, the Green dyadic results in a $3N \times 3N$ matrix, completely filled with complex numbers:

$$G = \begin{pmatrix} G_{xx} & G_{xy} & G_{xz} \\ G_{yx} & G_{yy} & G_{yz} \\ G_{zx} & G_{zy} & G_{zz} \end{pmatrix} \quad (3.44)$$

From the contrast source formulation (see section 2.2.2), $\mathbf{J}_p(\vec{r})$ is here replaced by $j\omega\epsilon_b\chi\mathbf{E}(\vec{r})$, yielding the matrix equation $E^i = AE$, which reads:

$$\begin{pmatrix} E_x^i \\ E_y^i \\ E_z^i \end{pmatrix} = \begin{pmatrix} A_{xx} & A_{xy} & A_{xz} \\ A_{yx} & A_{yy} & A_{yz} \\ A_{zx} & A_{zy} & A_{zz} \end{pmatrix} \begin{pmatrix} E_x \\ E_y \\ E_z \end{pmatrix} \quad (3.45)$$

where $A = I - GX$ with I being the identity matrix and:

$$X = \begin{pmatrix} \text{diag}(\chi) & O & O \\ O & \text{diag}(\chi) & O \\ O & O & \text{diag}(\chi) \end{pmatrix} \quad (3.46)$$

is a diagonal matrix of the contrast function and the contrast diagonal $[N \times N]$ matrix :

$$\text{diag}(\chi) = \begin{pmatrix} \chi_1 & 0 & \cdots & 0 \\ 0 & \ddots & \ddots & \vdots \\ \vdots & \ddots & \ddots & 0 \\ 0 & \cdots & 0 & \chi_N \end{pmatrix} \quad (3.47)$$

3.2.3 Iterative Solvers

As soon as the IE-MoM matrix is fully populated, this Green dyadic is a dense matrix and iterative solvers used for the solution of the linear system are not very efficient. Their computational complexity is $\mathcal{O}(N_{\text{iter}}N^2)$, N being the number of unknowns of the problem and N_{iter} the number of iterations needed for the solver to converge, whereas direct solvers normally need $\mathcal{O}(N^3)$ operations. The system matrix (3.45) can be written in a compact way:

$$E^i = (I - GX)E \quad (3.48)$$

As the MoM-matrix $A = (I - GX)$ cannot be stored due to memory requirements, an iterative solver diminishes the computational effort from $\mathcal{O}(N^2)$ even to $\mathcal{O}(N \log N)$ if special techniques are used. These techniques are called Fast Solvers and there are three different approaches: the FFT-based method, the adaptive integral method (AIM) and the fast multipole method (FMM).

The first two take advantage of the convolution property that can be found in all the integrals that need to be computed, if the free space Green Function is used, whereas the last one is the most widespread in the CEM community and is based on the idea described below.

The FMM core idea is to firstly divide the current elements into groups by their physical locations in space. It is mainly used in Surface Integral Equation (SIE) formulations, for more or less distant scatterers. A group is a collection of current elements in close proximity to each other. The addition theorem is then used to translate the radiated fields of different elements to the common center of the group. Similarly, to calculate the received fields by each current element within a group, the fields radiated by all the other group centers are first received by the group center and then they are redistributed to the current elements within the group.

Since the human brain/body represents a distributed scatterer, we focus in this work on FFT-based matrix-vector products. G has a block-Toeplitz Toeplitz-block (BTTB) structure

3.2. Numerical Solution of VIE with Method of Moments (MoM)

and can therefore be extended to a block matrix with circulant blocks allowing the application of FFT-based matrix-vector products for computing A . For the iterative solver, we observe that A is a complex-symmetric matrix permitting thus the application of a minimum residual (MINRES) solver [134, 135].

3.2.4 Spectrum of the Volume Integral Operator of Electromagnetic Scattering

The spectrum of the Volume Integral operator in the contrast source formulation has been analyzed in [133]. In the framework of Microwave Imaging, the knowledge of the spectrum of this operator can give useful information about the complexity of both the forward and inverse problems. It connects explicitly the spectrum of the eigenvalues with parameters such as the background medium and the frequency.

The volume integral operator of 3D electromagnetic scattering has both a continuous essential spectrum, which dominates at lower frequencies, and discrete eigenvalues, which spread out at higher ones. The eigenvalues of the discretized operator accumulate on the continuous spectrum.

The matrix $A \in \mathbb{C}^{N \times N}$ has the (real or complex) eigenvalues $\sigma(A) = \lambda_1, \dots, \lambda_N$ and its spectrum is noted as $\sigma(A)$. The spectral radius $\rho(A)$, defined as $\rho(A) = \max\{|\lambda_1|, \dots, |\lambda_n|\}$, is the radius of the smallest circle that contains the whole spectrum $\sigma(A)$. Note that here λ_n represents eigenvalues and not wavelengths. In order to study the spectrum of the volume integral operator, a spherical geometry is here considered. Three test cases that can occur in a typical simulation in the framework of MWI are summarized in Table 3.1.

Table 3.1 – Case Study Parameters for the Sphere. Values of the wavenumber \mathbf{k}_b [1/m], the contrast χ , and the grid size [m] for three different scattering scenarios with variable contrast, for quasi-static (left) and dynamic (right) illuminations.

	Quasi-static	(frequency =	1 kHz)	Dynamic	(frequency =	1 GHz)
	$ \mathbf{k}_b $ [1/m]	χ	grid [m]	$ \mathbf{k}_b $ [1/m]	χ	grid [m]
Case 1	0.05	$2 + 3 \cdot 10^{-6} j$	$\frac{\lambda_b}{6 \cdot 10^6}$	70	$3.2 + 0.7 j$	$\frac{\lambda_b}{6}$
Case 2	0.05	$2 - 2 \cdot 10^{-5} j$	$\frac{\lambda_b}{3 \cdot 10^6}$	148	$-0.06 - 0.2 j$	$\frac{\lambda_b}{3}$
Case 3	0.09	$-0.1 + 9 \cdot 10^{-7} j$	$\frac{\lambda_b}{2.4 \cdot 10^6}$	178	$-0.3 - 0.06 j$	$\frac{\lambda_b}{2.4}$

Each of the three test cases has been chosen to illustrate the future discussions on frequency and matching medium for MWI of pathologies present in the brain region. The complex permittivity of the sphere is always chosen to be the average value of the complex permittivity of all tissues of the head at 1 GHz for the homogeneous sphere which are $\epsilon_r = 46$, $\sigma = 0.9$ [S/m] (Fig. 3.3) or randomly distributed values around it for the inhomogeneous cases (Fig. 3.4),

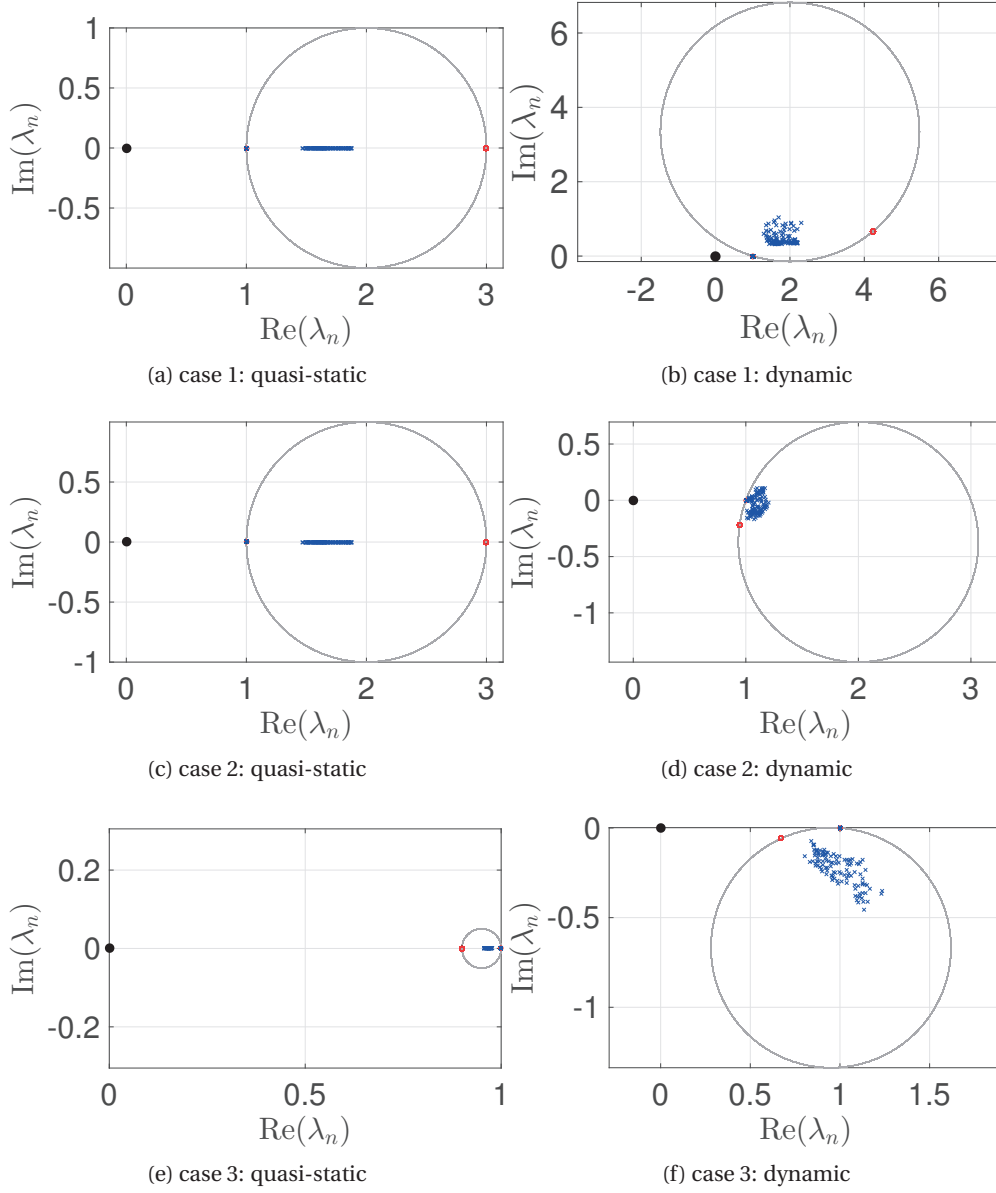


Figure 3.3 – Effect of frequency on the spectrum. Left: quasi-static, right: dynamic (cf. Table 3.1). From top to bottom background permittivity $\epsilon_b = 10, 50, 70$, and $\sigma = 0.3, 0.3, 1$ [S/m]. Sphere permittivity is $\epsilon_r = 46$, $\sigma = 0.9$ [S/m]. Grey circles represent the geometrical bounds of the location of each discrete eigenvalue in the complex plane; blue crosses are the discrete eigenvalues; and red dots are the ratios $\chi + 1 = \left(\frac{\epsilon(\vec{r})}{\epsilon_b}\right)$.

with a variance equal to one third of the median values for both ϵ_r and σ . The grid size is shown with respect to the background wavelength $\lambda_b = \frac{2\pi}{|\mathbf{k}_b|}$. The test cases are constructed by changing the value of the background medium:

3.2. Numerical Solution of VIE with Method of Moments (MoM)

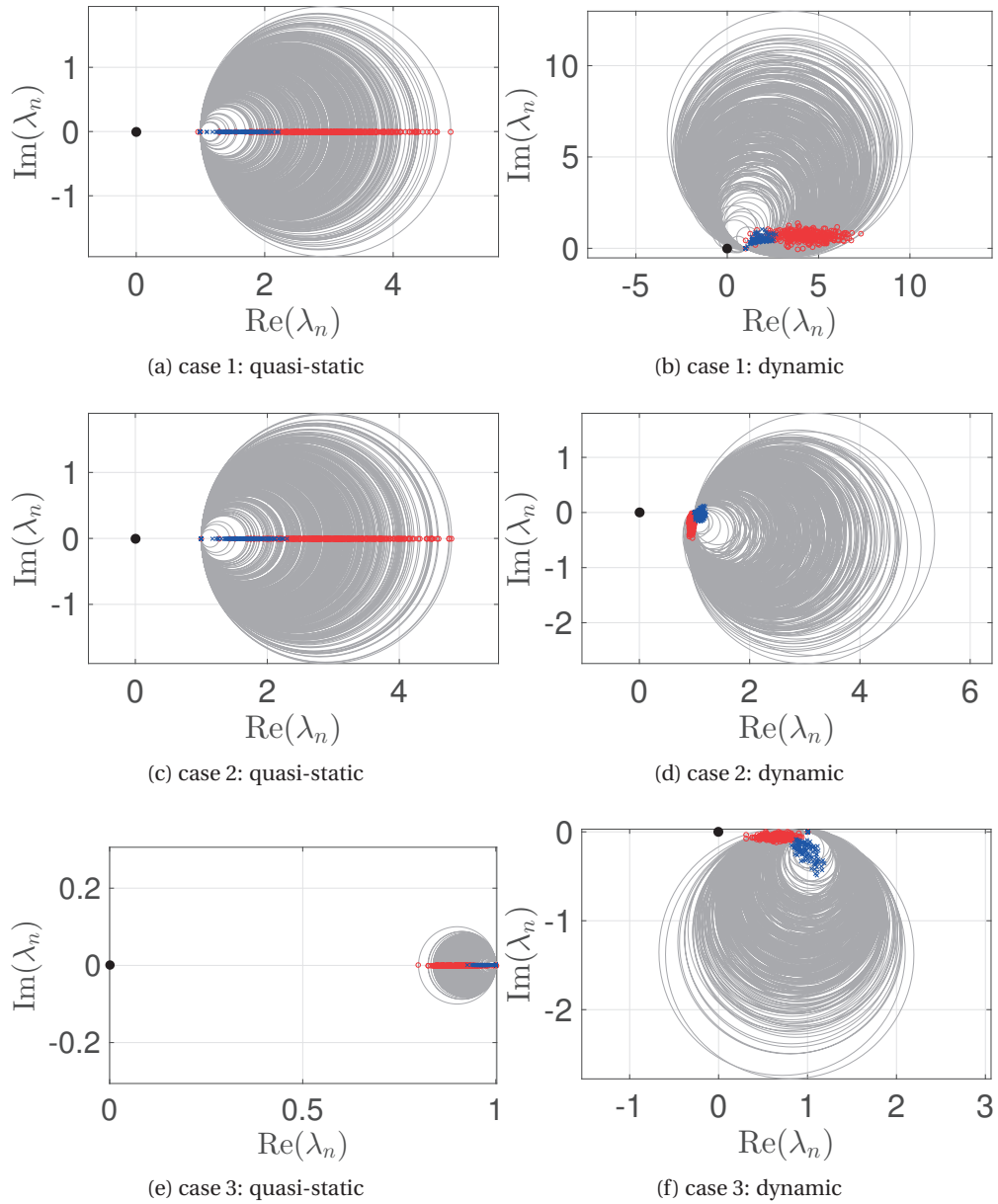


Figure 3.4 – Effect of frequency on the spectrum. Left: quasi-static, right: dynamic (cf. Table 3.1). From top to bottom background permittivity $\varepsilon_b = 10, 50, 70$, and $\sigma = 0.3, 0.3, 1$ [S/m]. Sphere permittivity is a random distribution around $\varepsilon_r = 46$, $\sigma = 0.9$ [S/m], with variance equal to a third of the median values for both ε_r and σ . Grey circles represent the geometrical bounds of the location of each discrete eigenvalue in the complex plane; blue crosses are the discrete eigenvalues; and red dots are the ratios $\chi + 1 = \left(\frac{\varepsilon(\vec{r})}{\varepsilon_b}\right)$.

1. **test case 1:** relatively big contrast for both quasi-static and dynamic cases, with smaller relative permittivity and conductivity in the background medium.

Chapter 3. Volume Integral Operator of Electromagnetic Scattering

2. **test case 2:** relatively big contrast for the quasi-static case and relatively small contrast for the dynamic case, with larger relative permittivity and smaller conductivity in the background medium.
3. **test case 3:** relatively small contrast for both quasi-static and dynamic cases, with larger relative permittivity and conductivity in the background medium.

As expected $|\mathbf{k}_b|$ is small for the quasi-static configurations, and large (> 70) for dynamic cases.

In Fig. 3.3 and Fig. 3.4 are plotted the eigenvalues of the discretized volume integral operator for a homogeneous sphere inside a homogeneous background medium. Both have losses, represented by the imaginary part of the complex valued contrast (see Table 3.1). For these cases an approximation of the distribution of the eigenvalues λ_n , can be derived [133]. The geometrical bounds are given by:

$$[\operatorname{Re}(\lambda_n) - C_r]^2 + [\operatorname{Im}(\lambda_n) - C_i]^2 < R_{\lambda_n}^2 \quad (3.49)$$

with:

$$C_r = \frac{1}{2} \left(\frac{\sigma_r}{\sigma_b} + 1 \right), \quad C_i = \frac{\omega (\epsilon_0 \epsilon_b - \epsilon_0 \epsilon_r)}{2\sigma_b} \quad \text{and} \quad R_{\lambda_n} = \sqrt{\frac{1}{4} \left(\left(\frac{\sigma_r}{\sigma_b} - 1 \right)^2 + \omega^2 \left(\frac{\epsilon_0 \epsilon_r - \epsilon_0 \epsilon_b}{\sigma_b} \right)^2 \right)} \quad (3.50)$$

In Fig. 3.3 and Fig. 3.4 the grey circles represent the geometrical bounds of the location of each discrete eigenvalue in the complex plain. The blue crosses are the discrete eigenvalues, the red dots are the ratios $\chi + 1 = \left(\frac{\epsilon(\vec{r})}{\epsilon_b} \right)$. At low frequencies, the eigenvalues are expected to spread out between 1 and this ratio. Table 3.1 gives two additional important parameters, the absolute value of the wavenumber $|\mathbf{k}_b|$ and the contrast function of the homogeneous sphere χ , for both quasi-static and dynamic configurations.

For both homogeneous and inhomogeneous spheres, the spectrum is explicitly bounded by this estimate which is important when choosing an iterative method. At low frequencies, the spectrum is a straight line, however at higher frequencies the eigenvalues spread out. This effect is even more important for the inhomogeneous sphere, with high initial contrast. For that case, the circle extends toward the zero of the complex plane and even if no eigenvalue is strictly equal to zero some of the eigenvalues may get close to it and the scattering problem to solve becomes unstable. In addition, these eigenvalues close to zero are responsible for the slow convergence of the iterative solution of the corresponding discretized problem. At higher frequencies, the kernel of the compact operator gets more "weight" and the norm of

3.2. Numerical Solution of VIE with Method of Moments (MoM)

the operator increases. The choice of the background medium influences the spectrum and the norm of the operator, therefore it should be chosen carefully.

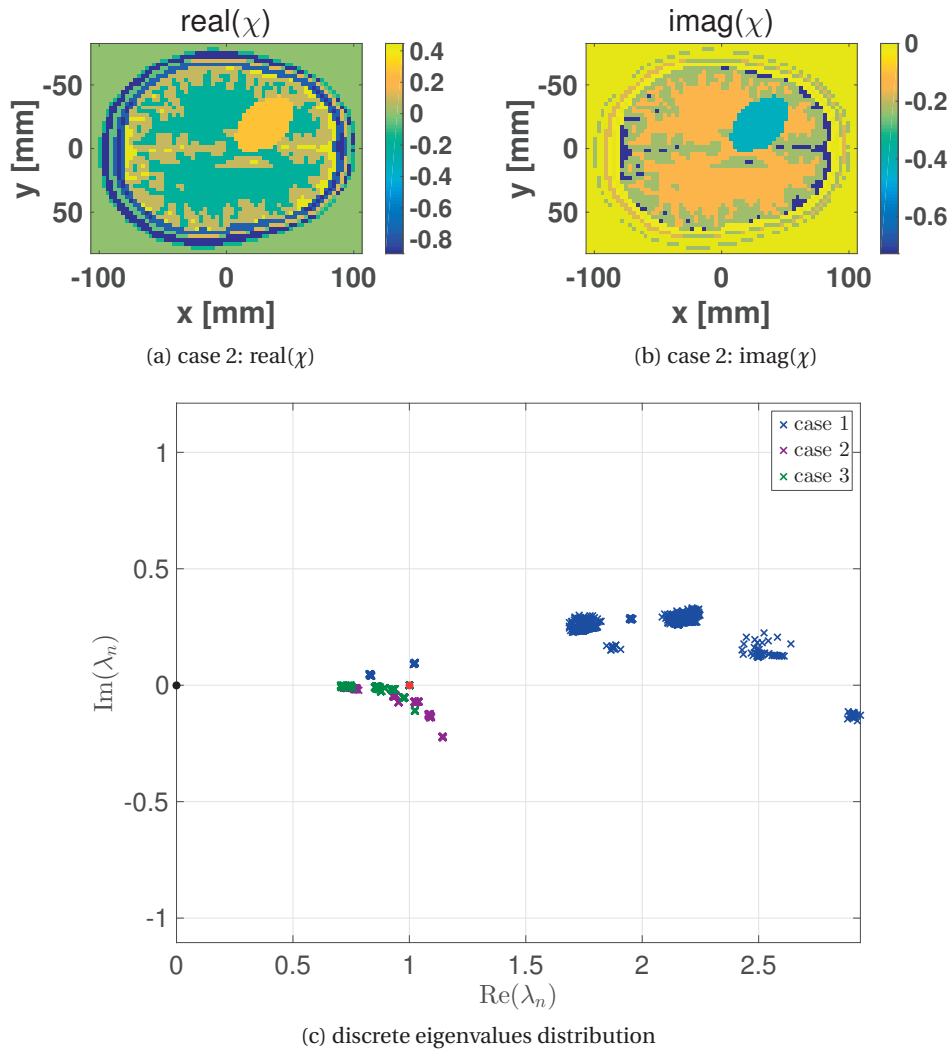


Figure 3.5 – Real part (a) and imaginary part (b) of the contrast function χ for a slice of the Duke model (3 mm side voxel length) with a haemorrhagic stroke at 1 GHz. (c) Discrete eigenvalues of the VIE operator. The background medium corresponds to the cases of Table 3.1: case 1 (blue), case 2 (violet), and case 3 (green).

Fig. 3.5 depicts the practical case of the discrete spectrum of the VIE operator for a slice of a realistic anthropomorphic head model, called the Duke model, of 3 mm voxel side length with a haemorrhagic stroke at 1 GHz. The background medium is one of the cases of Table 3.1: case 1 (blue), case 2 (violet) or case 3 (green). We see that the discrete spectrum is behaving as for the inhomogeneous sphere configurations, with a median value of the overall tissues of the head.

Chapter 3. Volume Integral Operator of Electromagnetic Scattering

The condition number $\kappa(A)$ is a value determining the ill-conditioning of a mathematical operator A . The ℓ_2 -norm condition number is:

$$\kappa(A) = \|A\|_2 \cdot \|A^{-1}\|_2 \quad (3.51)$$

The equation is also valid in the limit, that is for a singular matrix, for which $\kappa(A) = \infty$. In the practical case depicted in Fig. 3.5 the condition number for the test case 1, 2 and 3 is, respectively, 3.6, 1.6 and 1.5. As expected, case 1 is the most affected to ill-conditioning. The estimate of the convergence of MINRES is proportional to the condition number [136]:

$$\frac{\|r_n\|}{\|r_0\|} = 2 \left(\frac{\kappa(A) - 1}{\kappa(A) + 1} \right)^{\lfloor k/2 \rfloor} \quad \text{with} \quad r_n = b - Ax_n \quad (3.52)$$

So, for each iteration, the residual decreases by approximately $\sqrt{\frac{\kappa(A) - 1}{\kappa(A) + 1}}$. The latter demonstrates that a large condition number may lead to slow convergence.

3.3 Numerical Experiments: Solvers for Large Number of Unknowns

When the number of unknowns is too large, iterative solvers need to be applied. The biggest obstacle to overcome is the slow convergence of the iterative solver. For iterative solvers, a large condition number results usually in slow convergence. The goal of a preconditioner is to accelerate the convergence by modifying the spectrum of the matrix in the linear system $A\mathbf{x} = \mathbf{b}$. A preconditioner is basically an invertible square matrix $M \in \mathbb{R}^{n \times n}$ such that its inverse M^{-1} is easily computable (easier than applying A itself) and $M^{-1}A$, should be well-behaved in terms of convergence. If matrices A and M are symmetric the new condition number is unchanged whether M is applied as *left*, *right*, or *split* preconditioner.

In this section, firstly, a Minimal Residual (MINRES) solver with a diagonal preconditioning is presented, and secondly, a Multi-Grid (MG) solver, which shows better performance at higher frequencies, is investigated.

3.3.1 Minimal Residual (MINRES) solver

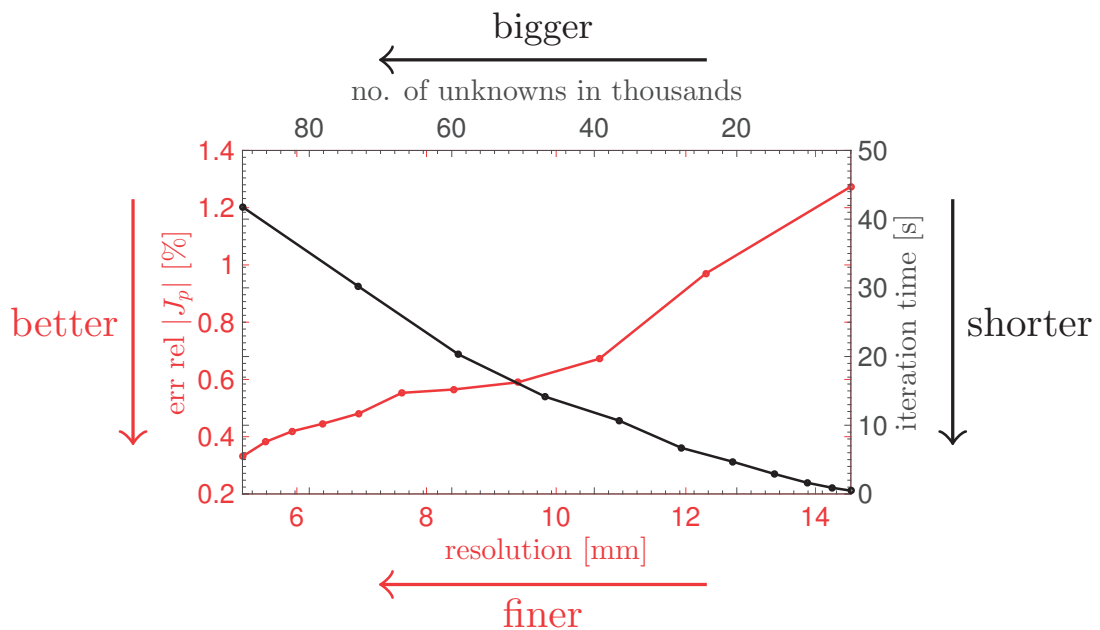


Figure 3.6 – Static case. Convergence of the relative error of \mathbf{J}_p in % for different grid size h (red), and the total simulation time for different number of unknowns (total number of unknowns) in black.

Firstly, we can test the overall accuracy of the method, by considering the case of a homogeneous dielectric sphere embedded in a homogeneous static electric field for which an analytical solution is at hand. There are staircase effects due to the approximated spherical surface, therefore we compare the analytic solution to the VIE solution only in the center voxel to measure the convergence of the method, which is the best error that could be achieved.

Fig. 3.6 shows in red the convergence of the relative error of \mathbf{J}_p in % for different grid sizes h , and in black the iteration time for different numbers of unknowns. The error in accuracy is decreasing linearly with decreasing grid size, and for a grid size of $h = 5$ mm, the relative error of \mathbf{J}_p in the center voxel is only 0.35%. The iteration time on a simple *Intel(R) Core(TM) i7-4770 CPU 3.40GHz* is of ≈ 43 seconds for $\approx 90k$ unknowns (grid size of $31 \times 31 \times 31$).

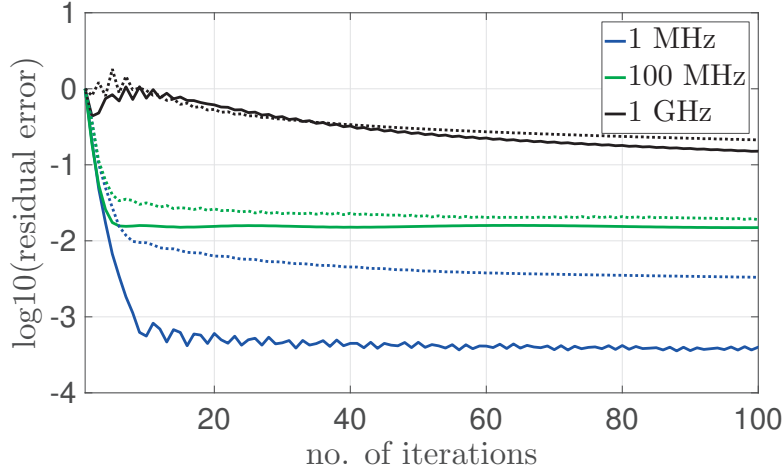


Figure 3.7 – Dynamic case. Residual error in dB vs. number of iterations of the iterative solver at 1, 100, 1000 MHz (blue, green, black). Convergence without preconditioner is plotted using dotted lines and with diagonal preconditioning using solid lines.

To test the robustness of the iterative solver we chose a grid of $11 \times 11 \times 11$ cells with a side length of 14.5 mm. In order to anticipate head imaging applications, we considered a homogeneous sphere of $\epsilon = 46$, $\sigma = 0.9$ [S/m] (median of the overall head tissues at 1 GHz as depicted in Fig. 2.3) embedded in a matching medium of $\epsilon = 10$, $\sigma = 0.3$ [S/m]. This test case was simulated for frequencies of 1, 100, 1000 MHz, representing $|\mathbf{k}_b|$ of 2, 16, 70. Fig. 3.7 summarizes the results (dotted lines): for 1 GHz the solver struggles to converge to a residual error of 10^{-1} , for 1 MHz the solver converge easily to a residual error of 10^{-2} . Another way of looking at the convergence of the solver, especially when the ultimate goal is imaging, is to calculate the average error per voxel which are respectively 2.7%, 5%, 22.5% for $|\mathbf{k}_b|$ of 2, 16, 70. The reason why the results are worse than the ones in statics (when $\mathbf{k}_b = 0$) is the spectrum of the volume integral operator (see Section 3.2.4) and preconditioning should be used.

For symmetric operators such as ours, a simple preconditioner to apply to (3.48) is the diagonal preconditioner in order to preserve the symmetry of the system. We introduce the intermediate variable \vec{y} yielding

$$\vec{b} = (I - K)\vec{y}; \quad \vec{b} = ME^i; \quad \vec{y} = M^{-1}E \quad (3.53a)$$

$$K = MGXM; \quad M = \text{diag}\sqrt{\chi_e} \quad (3.53b)$$

3.3. Numerical Experiments: Solvers for Large Number of Unknowns

From a computational point of view, we actually never compute K but rather perform the subsequent operations :

$$\vec{u} = M\vec{y} \quad (3.54a)$$

$$\vec{v} = GX\vec{u} \quad (3.54b)$$

$$\vec{w} = M\vec{v} \quad (3.54c)$$

where \vec{u} and \vec{w} are cheap matrix-vector products since M is diagonal. This type of preconditioning is expected to behave well for diagonal-dominant matrices K .

Table 3.2 – Condition Number and Convergence Estimate for increasing wavenumber / frequency without (left) and with (right) diagonal preconditioning.

k_b / frequency [GHz]	Without $\kappa(A)$	preconditioning convergence estimate	Diagonal $\kappa(A)$	preconditioning convergence estimate
2 / 0.001	1.9	0.56	1.4	0.41 (better)
16 / 0.1	1.9	0.56	1.5	0.45 (better)
70 / 1	2.7	0.68	3	0.71 (worse)

In Fig. 3.7 the diagonal preconditioner is applied (solid lines) to the homogeneous sphere for which the convergence was depicted in dotted lines for the original system without preconditioner (case 1 of Table 3.1). For small $k_b = 2$ (frequency of 1 MHz) the convergence is better by a factor of ten, and on the contrary not significant for higher frequencies such as 1 GHz ($k_b = 70$). The convergence is still rather fast but stagnation occurs later (at least at 1 MHz). The stagnation, which occurs for residues of 10^{-3} , 10^{-2} or 10^{-1} for higher frequency, could be explained as the matrix is not diagonal-dominant anymore. The condition number and the estimation of the convergence without preconditioning and when diagonal preconditioning is applied are listed in Table 3.2.

3.3.2 Multi-Grid (MG) solver

Multi-grid methods (MG) can be used either as a preconditioning scheme or as a solver itself. When it is used as a solver, the basic idea is to go back and forth between different grid levels and to solve a residual equation (Smoothing operations) instead of $A\mathbf{x} = \mathbf{b}$ itself. This equation is solved directly on the coarsest level. For the geometric multi-grid method, the concepts are depicted in Fig. 3.8. The details of MG can be found in [137].

The residual problem of the finer grid, which cannot be solved by a direct solver, is restricted to a coarser mesh. For the smoothing method, MINRES is used. The same three test cases are investigated for homogeneous and inhomogeneous spheres. Here, as the solutions will not be compared to the analytical solution, half spheres (geometrically closer to the actual cranial cavity) will be tested. The convergence is plotted for the V-cycle in Fig. 3.9 (homogeneous

Chapter 3. Volume Integral Operator of Electromagnetic Scattering

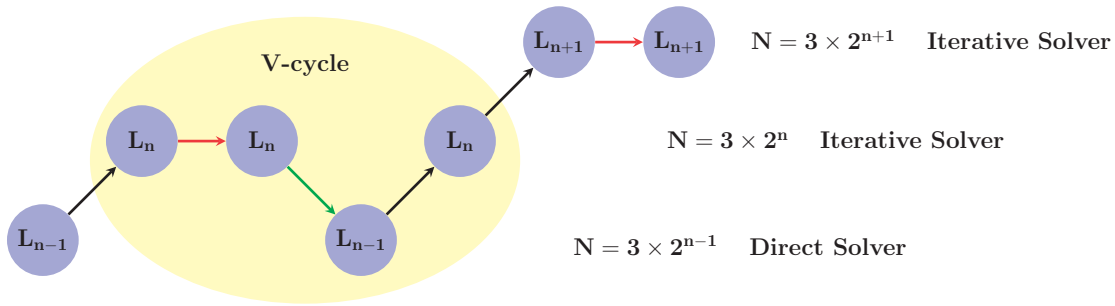


Figure 3.8 – Schematic of Full-MG (FMG) procedure, with the V-cycle procedure highlighted in yellow. Green, red and black arrows represent, respectively, Restriction, Smoothing and Prediction operations.

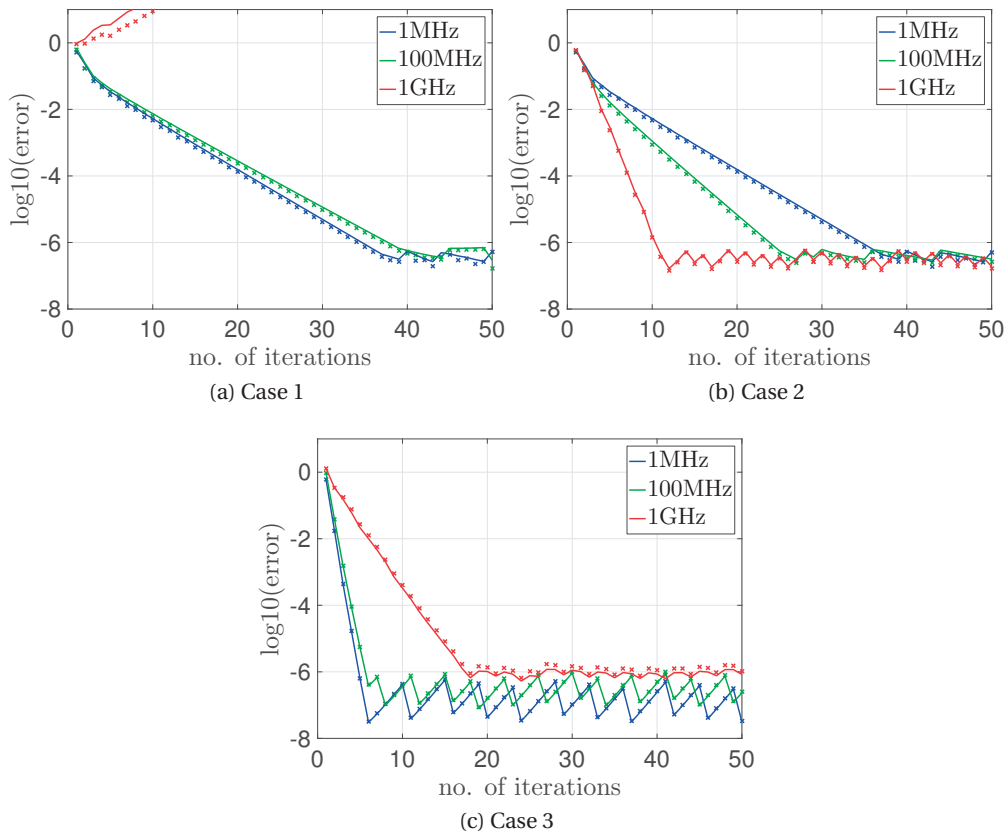


Figure 3.9 – Error in dB vs. number of iterations of the MG solver at 1, 100, 1000 MHz (blue, green, red) for the homogeneous half sphere of cases 1, 2, 3 (see Table 3.1) with voxels of 8 mm side length. The residue is plotted in solid lines and the absolute error with respect to the solution with the direct solver is plotted with cross markers.

case) and Fig. 3.10 (inhomogeneous case).

The V-cycle is performed between the L_2 (coarse grid: $N = 8 \times 8 \times 4$ cells of 16 mm side

3.3. Numerical Experiments: Solvers for Large Number of Unknowns

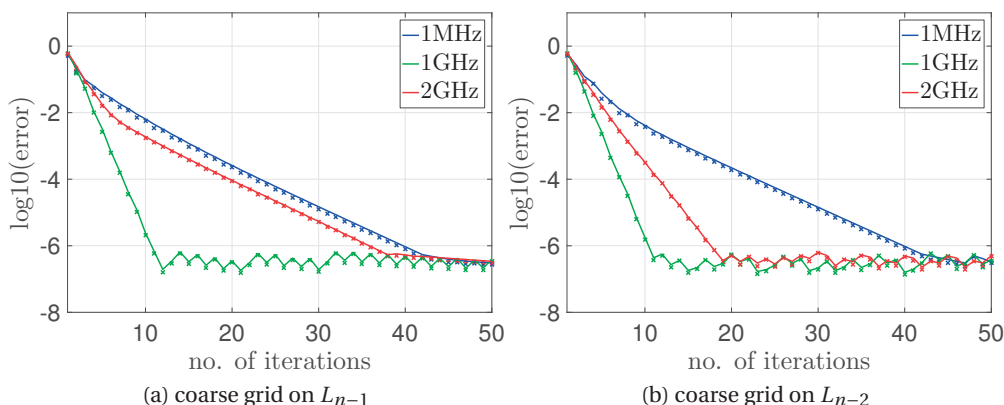


Figure 3.10 – Error in dB vs. number of iterations of the MG solver at 1 MHz, 1 GHz, and 2 GHz (blue, green, red) for the inhomogeneous half sphere of case 2 (see Table 3.1) with voxels of 8 mm side length. The residue is plotted in solid lines and the absolute error with respect to the solution with the direct solver is plotted with cross markers.

length) and L_1 (fine grid: $N = 16 \times 16 \times 8$ cells of 8 mm side length). A good convergence of the residual does not always mean that the solution found is the exact solution, therefore to double check the convergence towards the exact solution, the Root Mean Square (RMS) of the difference between the solution obtained with the direct solver and the one obtained with the MG-solver is also plotted in Fig. 3.9 with cross markers.

For the homogeneous case shown in Fig. 3.9 the results are good, with an overall fast convergence rate with low errors in general, except for one case. For the homogeneous half spheres, the case with high contrast already diverges for 1 GHz. With respect to the MINRES solver, the stagnation occurs on a much lower level, that is at 10^{-6} - 10^{-7} .

In Fig. 3.10 the robustness of MG schemes for the inhomogeneous case 2 (see Table 3.1) is shown for 1 MHz, 1 GHz and 2 GHz. The material distribution is equal to the third of the median values for both ϵ_r and σ . On the left side (see Fig. 3.10a), the V-cycle is performed between the L_2 (coarse grid: $N = 8 \times 8 \times 4$ cells of 16 mm side length) and L_1 (fine grid: $N = 16 \times 16 \times 8$ cells of 8 mm side length). To test whether the results are comparable for more than one level difference between the fine and the coarse grid, on the right side of Fig. 3.10b, the V-cycle is performed between the L_3 (coarse grid: $N = 4 \times 4 \times 2$ cells of 32 mm side length) and L_1 (fine grid: $N = 16 \times 16 \times 8$ cells of 8 mm side length). For both cases, the results are very promising as they show good convergence rates with an error of 10^{-6} for less than 45 iterations.

The encouraging results for the homogeneous and inhomogeneous cases at frequencies up to 2 GHz for the case 2 (see Table 3.1) were double checked with the direct solver each time (cross markers). Therefore the solver seems to converge to the exact solution and not to a local

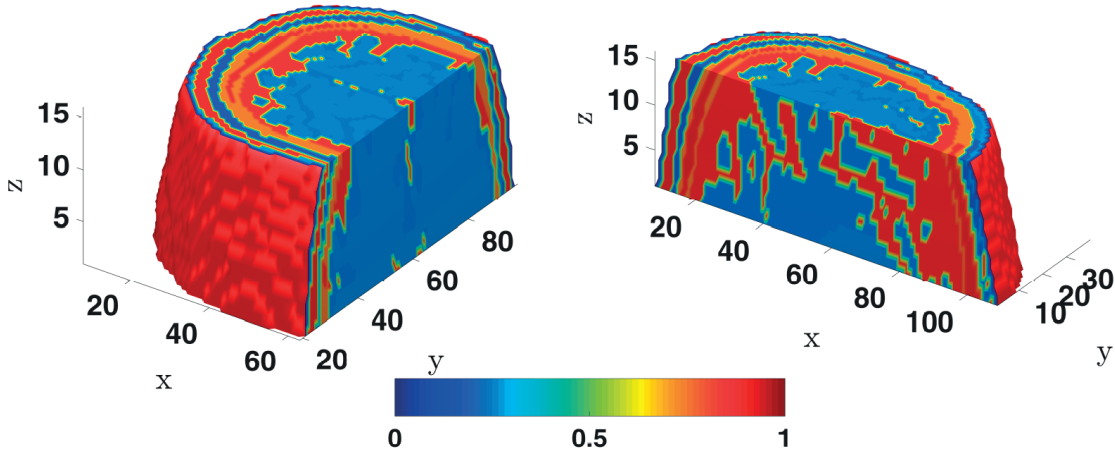


Figure 3.11 – Absolute value of the contrast function of the Duke Model [83] at 1 GHz on a $128 \times 128 \times 16$ grid with voxels of 2 mm side length. The background medium properties are $\epsilon = 50$, $\sigma = 0.3$ [S/m].

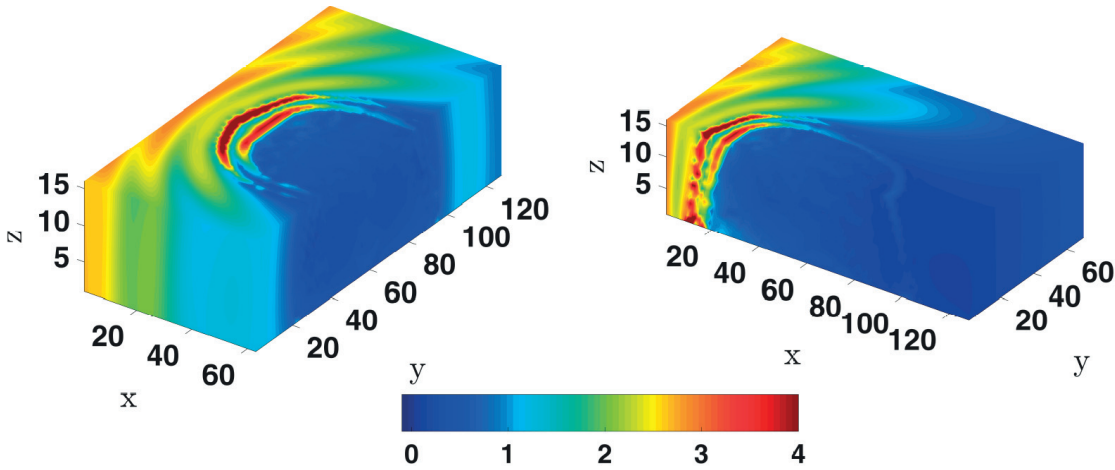


Figure 3.12 – Absolute value of the electric field produced by an impinging z -polarized plane wave on the Duke Model [83] (see Fig. 3.11) at 1 GHz on a $128 \times 128 \times 16$ grid with voxels of 2 mm side length. The background medium properties are $\epsilon = 50$, $\sigma = 0.3$ [S/m].

minima and anthropomorphic tissue distribution such as the Duke model [83] can be tested. Fig. 3.12 shows the absolute value of the electric field produced by an impinging z -polarized plane wave on the Duke Model [83] (see Fig. 3.11) at 1 GHz on a $128 \times 128 \times 16$ grid with voxels of 2 mm side length. The residual problem is solved with the direct solver on a $32 \times 32 \times 4$ grid with voxels of 8 mm side length. The background medium properties are $\epsilon = 50$, $\sigma = 0.3$ [S/m]. For 1 GHz the convergence rate is very good (see Fig. 3.13) with a residual error of 1.2×10^{-5} reached with only 30 iterations.

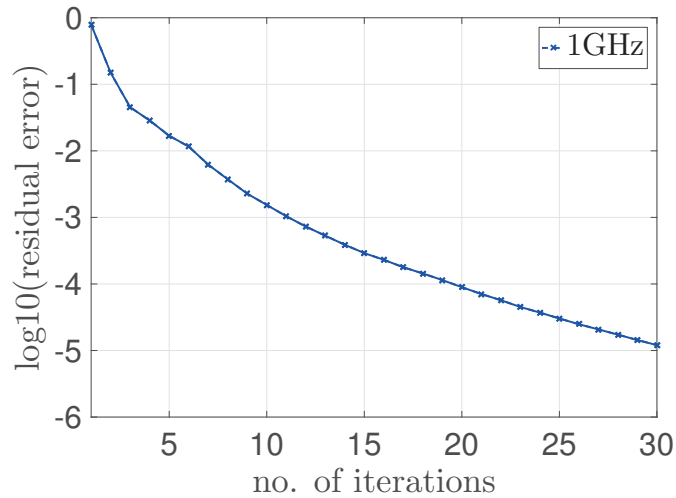


Figure 3.13 – Residual error in dB vs. number of iterations of the MG solver for the solution for the electric field produced by an impinging z -polarized plane wave on the Duke Model [83] (see Fig. 3.11) at 1 GHz on a $128 \times 128 \times 16$ grid with voxels of 2 mm side length. The background medium properties are $\epsilon = 50$, $\sigma = 0.3$ [S/m].

3.4 Conclusion

In this chapter, VIE formulations were presented and the procedure to treat the arising singularities in the Method of Moments were explained for the polarization currents (\mathbf{J}_p) based formulation. Direct methods to solve the discretized VIE cannot be used due to the large computational size of the problem. For example for a 1 mm resolution discretization of the head, there are $\sim 20,000,000$ unknowns. Therefore, iterative methods are used, such as MINRES, which suffer from no or slow-convergence rates as frequency and contrast increase. For these cases, which do arise when it comes to modeling EM fields for MWI applications, MG solvers have been explored. The results show very good convergence for homogeneous problems even at frequencies up to 2 GHz, if the contrast is kept low. For inhomogeneous cases the MG-scheme keeps a very good performance with increasing frequencies. This promising approach was tested on the Duke model and gave encouraging results with a residual of 10^{-5} obtained after only 30 iterations.

4 Design of MWI Systems for Brain Imaging

This chapter presents tools to address the design of MWI systems for brain imaging. More specifically, we analyze the power transmission of a radiating field inside the human head for Microwave Imaging applications. We aim at finding the range of frequencies that will optimize the received power of the scattering of the brain, which is the region of interest for imaging. For this purpose, planar and spherical layered models composed of representative dispersive biological tissues are investigated in the range of [0.5 – 4] GHz. The models, excited by plane waves, provide reasonable insights while remaining very convenient due to their analytical formulation. This chapter is organized in two parts:

1. the presentation of the two models, their electromagnetic analysis, and the discussion of simulation results;
2. the experimental validation of the spherical layered model with the characterization and realization of a 3D printed head phantom with tissue mimicking liquids.

This part aims at proposing and validating tools to derive guidelines for the design of MWI systems for brain imaging. From the major challenges listed in Chapter 2, the **coupling of microwave power into the tissue**, the body **tissue losses** and the **choice of the frequency** are addressed here.

4.1 Models and Electromagnetic Analysis

Microwave Imaging (MWI) [14] for bio-medical applications aims at localizing and reconstructing a pathological tissue region using scattered microwaves. In the framework of head MWI this non-invasive, non-ionizing technique could be suitable to monitor brain anomalies such as brain stroke [45, 138, 139], internal bleeding [34], etc. An important issue with MWI is to increase the signal to noise ratio in order to get better images. To do so, one possible solution is to maximize the scattering response of the brain anomaly, which is measured at the EM probes. To maximize the scattered power, several aspects influencing the imaging quality

must be analyzed before building a MWI setup. The choice of frequency for MWI is essential. The losses in dispersive biological tissues increase with the frequency. Meanwhile, the higher the permittivity of the matching medium (i.e the background medium where the transmitting/receiving probes are located), the higher is the spatial resolution for imaging the anomaly inside the brain [21]. Therefore, the choice of the frequency is a trade-off between a high resolution and small losses. In [47], guidelines to design an optimal MWI setup and to properly set the working frequency and the matching medium, needed to facilitate the penetration of the probing wave into the head, are determined using a plane wave Transmission Line (TL) model. We propose a multilayered spherical model as a head approximation representing a more accurate model than the plane-wave TL model, while allowing an analytical solution to the electromagnetic scattering problem [140].

This part of the chapter focuses on stratified planar and spherical models which are used to model and to estimate the normalized transmitted power into the human head. Also, the power transmission through the four main layers between the brain and the background medium, namely the Cerebrospinal Fluid (CSF), the cortical bone (always simply referred to as bone), the fat, and the skin are investigated.

4.1.1 Planar Layered Model

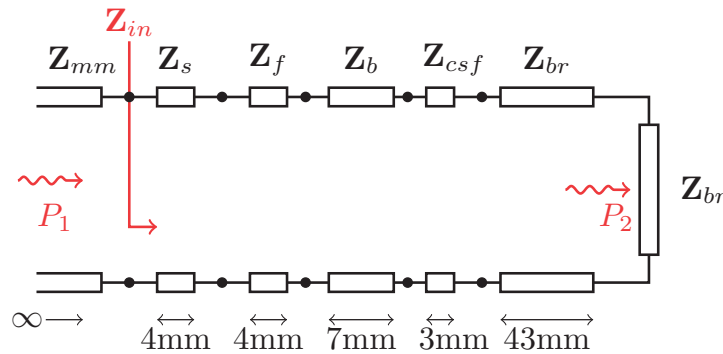
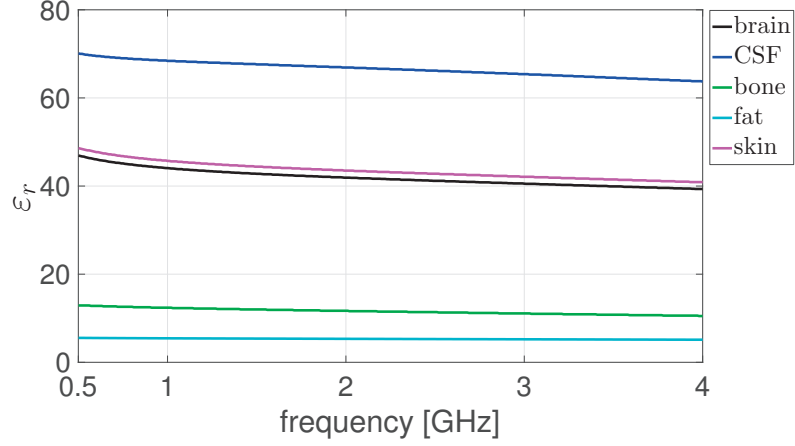


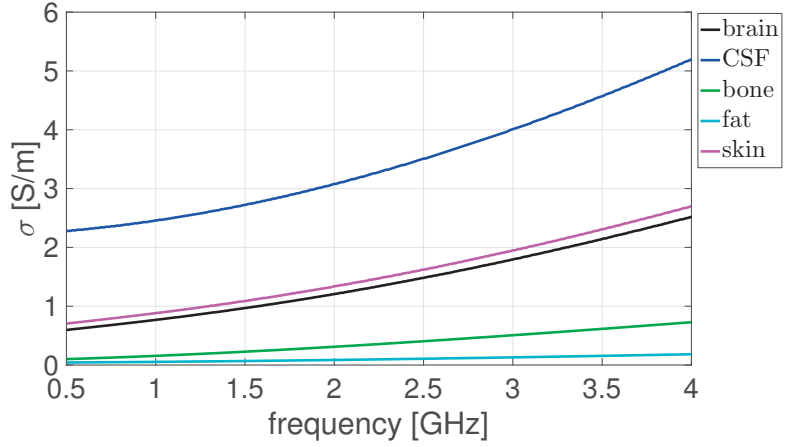
Figure 4.1 – Planar multilayered model to analyze the power transmitted into the human head.

The anomaly to detect and the wavelength of the excitation probe are smaller (ideally much smaller) than the head, therefore the head can be modeled by a sequence of planar layers. A first study was completed in [47] exploiting the transmission line (TL) formalism. The model consists of an equivalent TL in which each section corresponds to a tissue layer, as depicted in Fig. 4.1. The characteristic impedances Z_{mm} , Z_s , Z_f , Z_b , Z_{csf} , Z_{br} , and lengths of each TL represent, respectively, the matching medium, the skin (4mm), the fat (4mm), the bone (7mm), the CSF (3mm), and the half brain (43mm) where $Z = \sqrt{\frac{\mu_0}{\epsilon_0 \epsilon}}$ with ϵ_0 , μ_0 and ϵ are, respectively, the vacuum permittivity, the vacuum permeability and the complex relative permittivity of each material or tissue. The dielectric characteristics of the brain are set with a grey over

white matter ratio (GM/WM ratio) [141] of 1.5. Here we chose to use the dielectric properties provided in [142] and for which the properties are plotted in Fig. 4.2.



(a) relative permittivity ϵ_r



(b) conductivity σ [S/m]

Figure 4.2 – Theoretical dielectric properties [143] of brain (black), CSF (blue), bone (green), fat (light blue) and skin (magenta): (a) relative permittivity ϵ_r ; (b) conductivity σ [S/m].

In Figures 4.3a and 4.3b, the transmittance is plotted as a function of frequency and the coupling medium's permittivity and conductivity. The transmittance represents the effective transmitted power through a sample.

The transmittance at the interface between the matching medium and the skin (see Fig. 4.1) is:

$$T = 1 - \Gamma^2(\omega) \quad \text{with} \quad \Gamma(\omega) = \frac{|Z_{in}(\omega) - Z_{mm}(\omega)|}{|Z_{in}(\omega) + Z_{mm}(\omega)|} \quad (4.1)$$

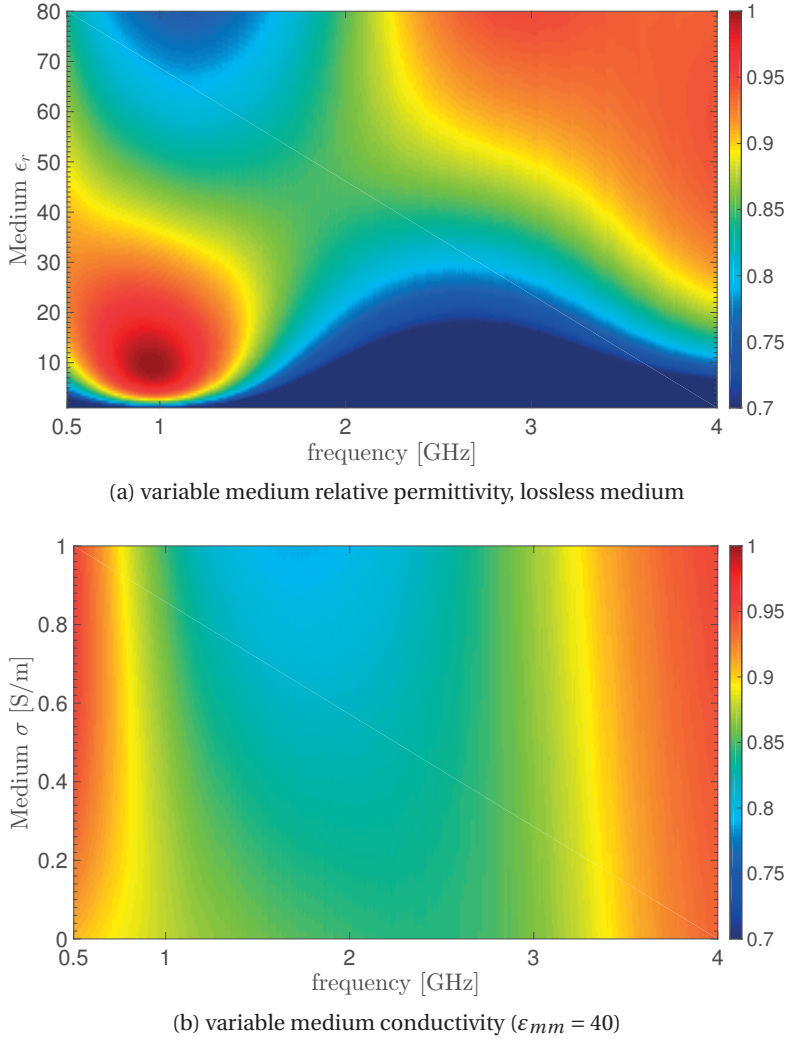


Figure 4.3 – Amplitude of the transmission coefficient as a function of frequency and medium permittivity [47]. (a) variable relative permittivity $\epsilon_r = [1 - 80]$, lossless medium $\sigma = 0$ [S/m]; (b) variable conductivity $\sigma = [0 - 1]$ [S/m], relative permittivity $\epsilon_r = 40$.

where Z_{mm} is the characteristic impedance of the matching medium, Z_{in} is the input impedance seen at the interface between matching medium and skin, and ω the angular frequency. The microwave band of interest is [0.5 – 4] GHz and the coupling medium range from air to water ($\epsilon_{mm} \in [1 - 80]$). The same graph has been shown in [47] and we can note in Fig. 4.3a a “forbidden band” around 2 GHz where the transmittance is the smallest, almost independently of the coupling medium. The conductivity of the matching medium does not really affect the amount of transmitted power in the frequency range of interest as we can see from Fig. 4.3b.

Below 600 MHz, the achieved resolution is higher than 3 cm which is not appropriate to observe the desired phenomenon. The frequencies above 4 GHz are not convenient due to low penetration into the tissues. Indeed, the approximation of the power attenuation through

the layers (the multi-reflections between the layers are omitted) is defined as:

$$A^2(\omega) = e^{2\sum_t \alpha_t(\omega)d_t} \tag{4.2}$$

with t representing the different tissues between the transmitter and the receiver, $\alpha_t(\omega)$ the linear attenuation coefficient, and d_t their respective thicknesses.

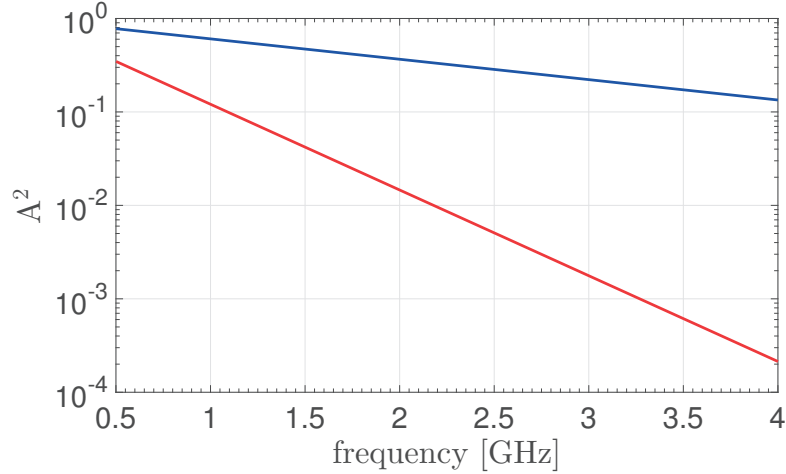


Figure 4.4 – Approximation of power attenuation through the head tissues in the exterior limit of the brain: close to the CSF (blue) and middle of the brain (at 43 mm from the CSF) in red.

Fig. 4.4 plots the approximated power attenuation for two different cases. For the worst case scenario (center of the head) at 4 GHz, the attenuation is such that less than 1 % of the power arrives to the anomaly if its location is at the center of the head, and only 6 % arrives in the best case scenario (when the anomaly is close to the CSF). This analysis is performed without counting for the reflections at the transitions between the different tissue layers. Therefore, this following study focuses on frequencies below 4 GHz. Also, it is important to note that the “forbidden band” is defined for the power entering the head. However this information is not sufficient for knowing the amount of power transmitted to a potential anomaly inside the brain region. In [46], a detailed analysis of the generalized transmission and reflection coefficients [144], which refers to the multilayered configuration, is made to consider the losses through the tissues and the transmittance through all the layers. Another way to assess the range of frequencies and matching media for microwave imaging systems for brain stroke detection is to directly analyze the power transmission, which is described in the following paragraph.

The normalized transmitted power $P_{Nt}(\omega)$ is defined as the ratio between the transmitted power into the load Z_{br} (from the middle of the head which is represented as an infinite half space) and the available power in the lossless background ($A^2 = 1, |\Gamma(\omega)|^2 = 0$) for the same

incident field. The normalized transmitted power is a physical measurable quantity linking the coupling into the tissue and the tissue losses to frequency. The goal is to assess up to which frequency the scattered fields induced by an anomaly can be detected. This frequency is crucial as it defines the maximal resolution based on which the imaging algorithm can reconstruct a stroke. In other words, the frequency defines the minimal detectable anomaly size.

4.1.2 Spherical Layered Model

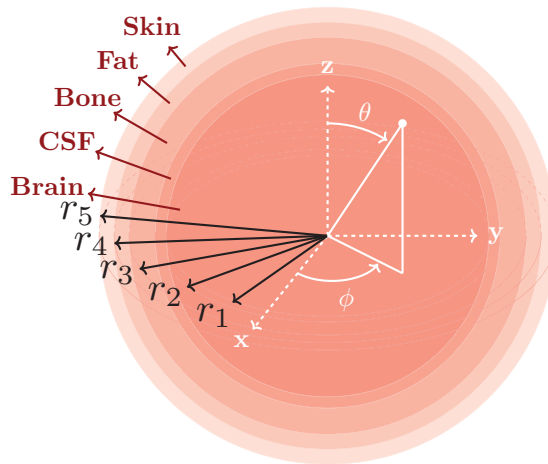


Figure 4.5 – Spherical multilayered model to analyze the power transmitted into the human head.

The spherically stratified head model, represented in Fig. 4.5, is a more realistic model of the human head than the planar model discussed in the previous section. Nevertheless, it still allows an analytic solution for the electric field distribution. The core of the sphere is the brain with a radius of $r_1 = 43\text{mm}$, the j^{th} layer (the core is the 1st layer) is given by $r \in [r_{j-1}, r_j]$, $j = 2, 3, 4, \dots, L$ and represents the same dimensions as the planar model (see Fig. 4.1).

In [145], for 7T MRI the Larmor frequency is around 50 MHz and the brain region is modeled as a combination of CSF, grey matter, and white matter. Since we deal with higher frequencies and, thus, shorter wavelengths, we model the CSF separately and the dielectric characteristics of the brain are set with a grey over white matter ratio (GM/WM ratio) of 1.5 as explained in [141]. A similar ratio was used in [146], as the dielectric properties of the latter two are similar in the frequency range of interest.

Due to the spherical geometry of the boundary conditions, the electric field can be expanded as an infinite sum of vector spherical harmonics and be expressed analytically. Reference [147] provides a review on the governing equations of the spherical wave expansion used to solve this problem, and gives a detailed analysis and validations of the implementation. All the

important steps from the solution of the scalar to the vectorial Helmholtz equation are shown in Appendix A. These results are valid for a plane wave impinging on the head phantom. This information needs to be taken into account when comparing theoretical and experimental results. However, because we are only interested in the transmission inside the head, this is not a real restriction and the results using a plane wave should be also valid for an antenna directly placed on the head. Indeed, the propagation of an electromagnetic wave depends only on the properties of the medium and not on the characteristics of the wave, that is plane wave, spherical wave, etc. Finally, we define the normalized transmitted power, $P_{Nt}(\vec{r}, \omega) = \frac{\int_V |\mathbf{E}(\vec{r}, \omega)|^2 dV}{\int_V |\mathbf{E}_b(\vec{r}, \omega)|^2 dV}$, as the ratio between the transmitted power into a bounded domain in the center of the brain and the power available in the lossless background in the same bounded domain.

4.1.3 Simulation Results and Discussion

The normalized transmitted power represents the incoming power that can excite any damaged area in the center of the head (worst case scenario) and therefore produce a scattered field. Fig. 4.6 represents maps of the normalized transmitted power plotted in dB for planar (Fig. 4.6a) and spherical (Fig. 4.6b) models. The permittivity of the matching medium is varying in the range $\epsilon_{mm} = [1-80]$ (from air to water) and frequencies [0.5-4] GHz. The color change corresponds to a drop in the normalized transmitted power in steps of 3 dB and up to -36 dB (all values below -36 dB are depicted as the same dark blue color). Cuts for $\epsilon_{mm} = 14, 56, 80$ of the P_{Nt} computed with the planar (full lines) and spherical (dotted lines) models are shown in Fig. 4.6c.

The power drop front is quasi constant, with respect to the matching medium and moves right in a constant way with increasing frequency. This is an indication that the power transmission is mainly affected by the tissue attenuation which is increasing with frequency. At 1 GHz for example, the optimum is at $\epsilon_{mm} \simeq 10$, however the normalized transmitted power drops only by 1 dB if $\epsilon_{mm} = 80$ (approximately water at 1 GHz), which would result in an imaging resolution increase of almost three times. A very similar behavior of the normalized transmitted power can be observed for the spherical model. There is even a stronger reflection of the incident wave for $\epsilon_{mm} < 5$ but only for frequencies above 1.5 GHz. If the working frequency is set to 1 GHz, the optimum is at $\epsilon_{mm} \simeq 1$, resulting in an unacceptable imaging resolution of 30 cm.

According to [40], to achieve a resolution of 10 mm, the matching medium should be $\epsilon_{mm} > 56$ at 1 GHz for a normalized power transmission of approximately -10 dB for both planar and spherical models, or $\epsilon_{mm} > 14$ at 2 GHz for a normalized power transmission of -20 dB and -15 dB according to the planar and spherical models, respectively. The resolution in water ($\epsilon_{mm} = 80$) for 1 GHz is 8.4 mm, for a P_{Nt} of -10 dB for both the planar and the spherical model. The same normalized transmitted power is obtained considering the field scattered by the anomaly and received by the probe. Therefore, the power level the imaging system should

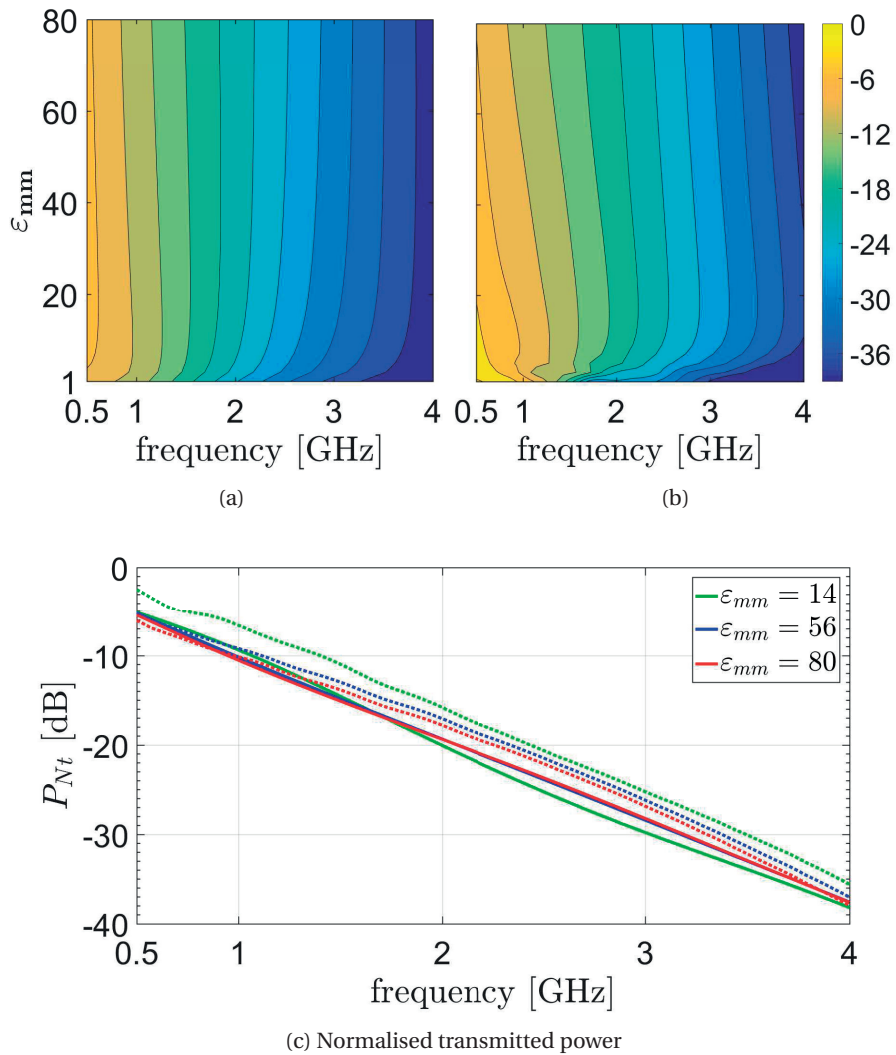


Figure 4.6 – Normalised transmitted power according to the frequency [0.5-4]GHz applying (a) the planar model, (b) the spherical model, for a matching medium of $\epsilon_{mm} = [1-80]$. Cuts for $\epsilon_{mm} = 14, 56$ and 80 of the P_{Nt} computed with the planar (full lines) and spherical (dotted lines) models are shown in (c).

be able to detect is at least twice the depicted normalized transmitted power in dB. According to these observations of simulation results, the general guidelines for designing a MWI setup are to chose the highest matching medium as the latter does not influence a lot the transmission but enhance the resolution. At frequencies around 1 GHz, the attenuation of the head tissues is still reasonable.

4.2 Experimental Validation

Several groups have developed complex imaging setups and algorithms for imaging brain anomalies [27, 148–150]. Experimental phantoms for the head have been designed, the most complex one using molded semi-rigid parts assembled inside an outer solid cavity [151]. The complex molding procedure and the high number of used ingredients makes this approach precise, however not easily repeatable. Moreover, the skin is not represented realistically as it is included in the fat/bone layer printed in a plastic material with dielectric constant of 6 at 2 GHz [143]. These models are very useful to realistically simulate the dielectric properties inside the brain itself and are used for imaging [148]. To validate numerical models, interesting works have been done in the microwave imaging community with 3D printed breast phantoms [80, 152] using Triton X-100 based mixtures to mimic biological tissues. In the 7T MRI community, 3D printed liquid phantoms [145] are also used as they are easy to handle and transport. A similar approach is followed here, to the best of our knowledge, for the first time in the framework of MWI of the brain, and a first attempt of using this simple, repeatable and over time stable procedure was published recently in [146]. For this, a spherically stratified head phantom has been built to experimentally estimate the power transmitted into the brain and to analyze the influence of the main layers of the head on the propagation of the EM wave.

4.2.1 Liquid Body Phantoms: Realization and Characterization

3D printed Multilayered Sphere Phantom

We developed a 3D printed model (see Fig. 4.7) as a multilayered sphere in order to confront measurements data to simulation data [153]. The prototype should be as close as possible to the representation of the brain depicted in Fig. 4.5. The model geometries, the waterproofing and gluing tests are shown in Appendix B.

The filling system consists of 5 entries, allowing to use a different liquid for each shell. The filling system and the holding system are designed in one piece to minimize its influence regarding the ideal multilayered concentric spherical model (see Fig. 4.5) that we want to subject to measurements. Each of the entries has a blockage cap, 3D printed in a flexible material. We used the Fused Deposition Modeling technology and white ABS (Acrylonitrile butadiene styrene) for the plastic. The materials and thicknesses were designed to ensure waterproofness. The dielectric properties of the ABS plastic structure of the 3D printed prototype were measured in the range of [0.5 – 4] GHz using the Agilent 85070E dielectric probe kit (see Fig. 4.8). The relative permittivity is 2.6 and constant while the conductivity is negligible in the frequency range of interest (see Fig. 4.9). The plastic shells are 2 mm thick.

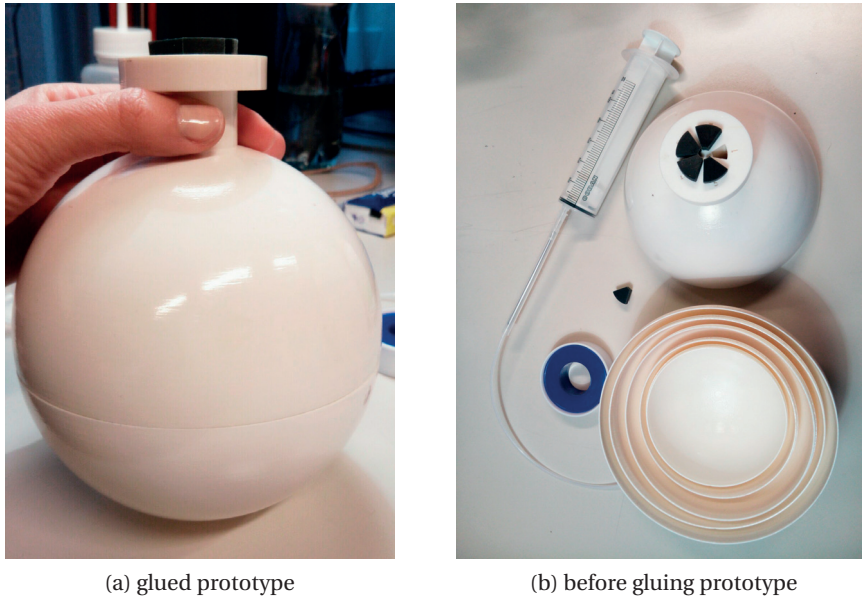


Figure 4.7 – Prototype Multilayered Sphere: (a) glued prototype; (b) before gluing prototype, with blocking caps and syringe.

Measurements of TritonX100 / Salted Water Mixtures to Mimic the Human Head

Several recipes are available to make liquids mimic the main human head tissues. Following the guidelines adopted in [77], Triton X-100-water mixtures with NaCl (salt) (see Table 4.1) are used to emulate the targeted tissues. The results for permittivity and conductivity measurements are depicted in Fig. 4.10, where the dispersive characteristics of their theoretical (targeted) values can be observed for the above frequency range.

Table 4.1 – Triton X-100 and NaCl concentrations for different biological tissues, and thickness of according layers for the multilayered spherical model.

Tissue	Volume concentration of Triton X-100 [%]	Concentration of NaCl [g/L]	Thickness of layer [mm]
Brain	35	4.3	43
CSF	7	14	3
Bone	85	0	7
Fat	100	0	4
Skin	30	4.3	4

For all the tissues the relative permittivity is very well matched over the total frequency band [0.5 – 4] GHz. For the conductivity all tissues match fairly well in the band [0.5 – 3] GHz, however, from 3 GHz to 4 GHz, the conductivity is overestimated especially for the mixtures mimicking the skin and the brain tissues.

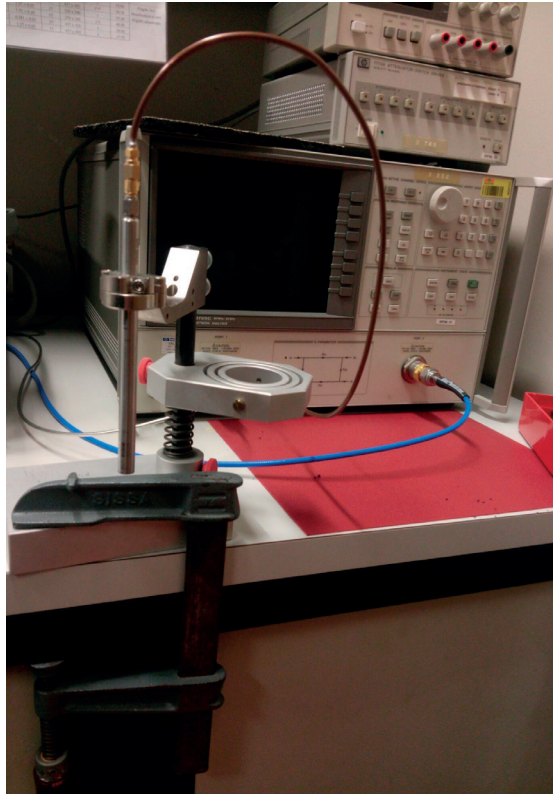


Figure 4.8 – Agilent measuring system: 85070E Dielectric Probe Kit

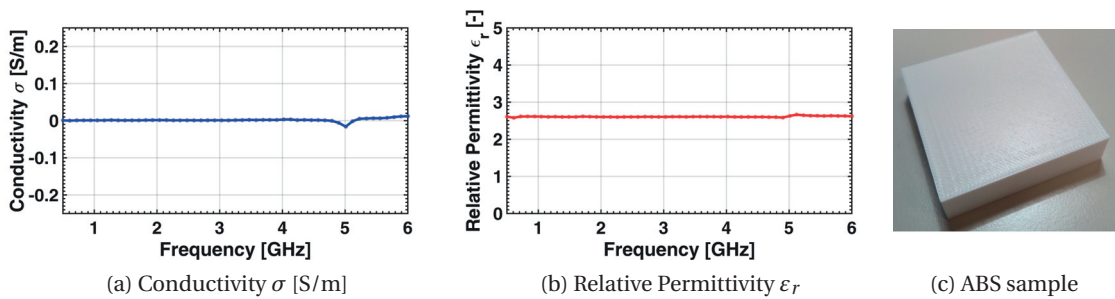
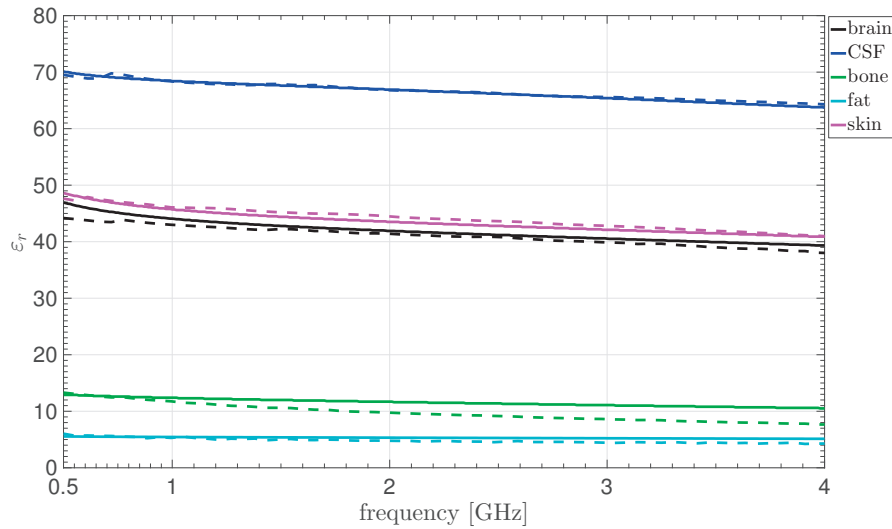


Figure 4.9 – Dielectric properties of ABS sample: (a) conductivity σ [S/m]; (b) Relative Permittivity ϵ_r ; (c) picture of ABS sample.

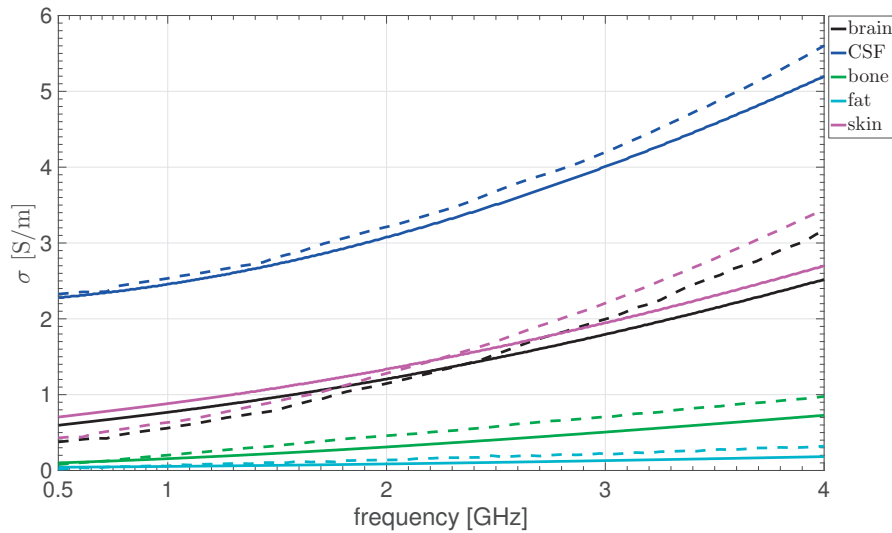
4.2.2 Measurement Results

Measurement Setup

The transmission parameter $|S_{12}|$ between a monopole antenna (port 2) vertically placed in the center of the head phantom and a vertically polarized horn antenna (port 1) placed at 1 m distance is measured between 0.5 and 4 GHz, as depicted in Fig. 4.11. The plastic shells are 2 mm thick. The radius of the brain is 43 mm. When the shells are empty, the attenuation A^2 and the power reflection coefficient Γ^2 are negligible. Additionally $S_{11}^f \approx S_{11}^e$ as the emitting



(a) relative permittivity ϵ_r



(b) conductivity σ [S/m]

Figure 4.10 – Theoretical (solid line) [143] and measured (dashed line) dielectric properties of the measurements of brain (black), CSF (blue), bone (green), fat (light blue) and skin (magenta). Solid lines are theoretical values and dashed lines are measurements: (a) relative permittivity ϵ_r and (b) conductivity σ [S/m].

horn antenna is for both configurations in air. As discussed in Section 4.1.3, the matching medium is essentially useful to increase the imaging resolution, therefore measuring with a horn antenna in air is acceptable since the purpose of this simple setup is to experimentally validate only the power transmission inside the head computed by the analytical modeling tool.

The measurements in the case of empty and filled spheres are denoted by S_{ij}^e and S_{ij}^f pa-

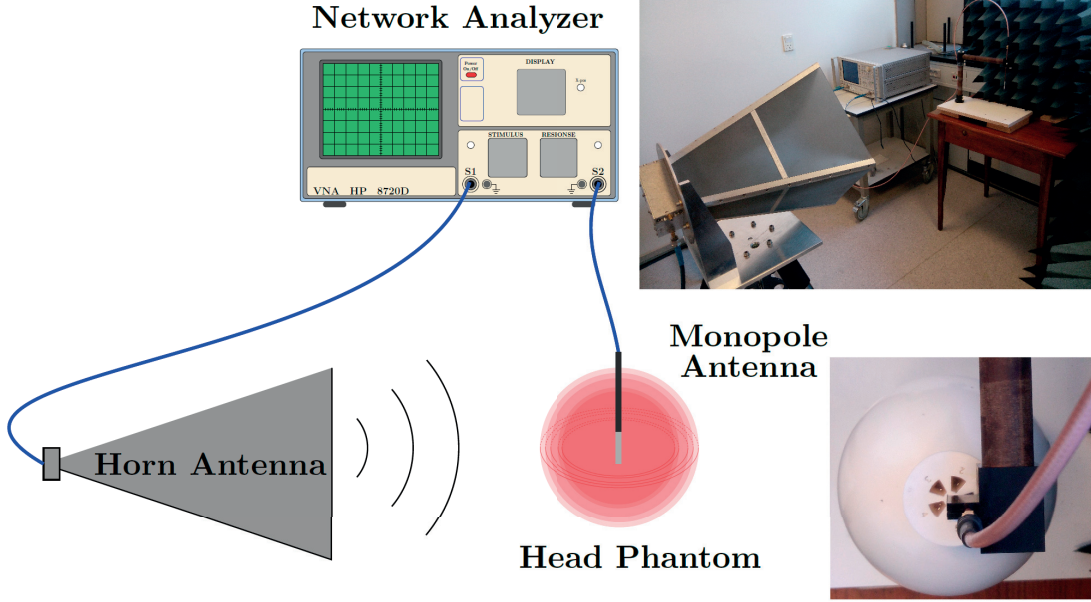


Figure 4.11 – Schematic and pictures of the measurement setup.

rameters, respectively. The ratio between these two measurements determines the amount of power injected into the brain from the horn antenna and is defined as the normalized transmitted power

$$P_{Nt} = F(\omega) \frac{|S_{12}^f|^2}{|S_{12}^e|^2}, \quad \text{with} \quad F(\omega) = \frac{(1 - |S_{22}^e|^2)}{(1 - |S_{22}^f|^2)} \quad (4.3)$$

The coefficient $F(\omega)$ accounts for the occurring mismatch of the receiving monopole inside the brain when immersed into the brain-mimicking mixture. The expression for the coefficient $F(\omega)$ comes from calculating the relative power transfer from a horn antenna to a monopole antenna placed inside of a head phantom. The reflected and transmitted powers are developed at each discontinuity with a local planar approximation. The Friis formula yields inside a lossy medium assuming a planar wavefront (the obvious frequency dependence is omitted for clarity reasons) with the time-harmonic convention $e^{+j\omega t}$:

$$|S_{12}|^2 = \frac{P_r}{P_t} = (1 - |S_{11}|^2)(1 - |S_{22}|^2)G_r G_t e^{-2\alpha R} \frac{\lambda_b^2}{R^2} \quad (4.4)$$

with λ_b the wavelength in the background medium, \mathbf{k}_b the (complex) wavenumber of the (lossy) medium, and α [Np/m] the linear attenuation defined as $\Re(j\mathbf{k}_b)$. The power attenuation is therefore 2α .

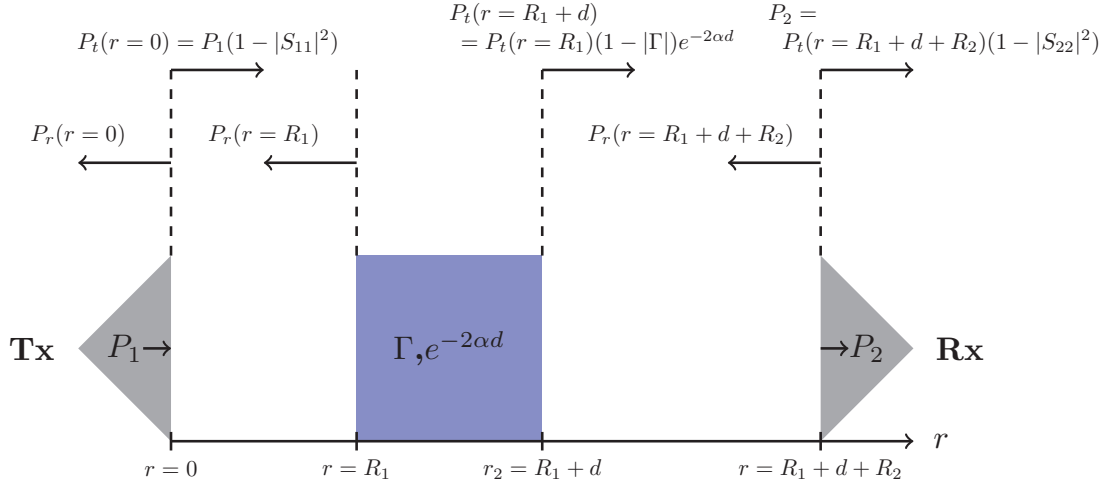


Figure 4.12 – Schematic of the transmission between the horn antenna (Tx) and the monopole antenna (Rx). The lossy material emulating the head phantom is represented as a planar layer with two interfaces in blue.

Equation (4.4) must be modified because the transmission media is composed of a lossless (air layer) and a lossy material (emulating the head). Therefore the mismatch between these two layers must be taken into account, and a similar procedure as in [154] is here followed. In the schematic depicted in Fig. 4.12 the distance $R_2 = 0$ was added only for schematic clarity.

$$\begin{aligned}
 P_2 &= P_t(r = R_1 + d + R_2)(1 - |S_{22}|^2) \\
 &= P_t(r = R_1)(1 - |\Gamma|)e^{-2\alpha d}(1 - |S_{22}|^2) \\
 &= P_t(r = 0)\frac{1}{R_1^2}(1 - |\Gamma|)e^{-2\alpha d}(1 - |S_{22}|^2) \\
 &= P_1(1 - |S_{11}|^2)\frac{1}{R_1^2}(1 - |\Gamma|)e^{-2\alpha d}(1 - |S_{22}|^2)
 \end{aligned} \tag{4.5}$$

Therefore,

$$\begin{aligned}
 |S_{12}|^2 &= \frac{P_2}{P_1} \\
 &= (1 - |S_{11}|^2)(1 - |S_{22}|^2)(1 - |\Gamma|)e^{-2\alpha d}\frac{1}{R_1^2}
 \end{aligned} \tag{4.6}$$

When the spheres are empty, $\Gamma = \Gamma^e \simeq 0$ and $\alpha = \alpha^e \simeq 0$ and:

$$|S_{12}^e|^2 = (1 - |S_{11}^e|^2)(1 - |S_{22}^e|^2) \frac{1}{R_1^2} \quad (4.7)$$

When the spheres are full:

$$|S_{12}^f|^2 = (1 - |S_{11}^f|^2)(1 - |S_{22}^f|^2)(1 - |\Gamma^f|) e^{-2\alpha^f d} \frac{1}{R_1^2} \quad (4.8)$$

Therefore, the relative transmitted power is:

$$\begin{aligned} \frac{|S_{12}^f|^2}{|S_{12}^e|^2} &= \frac{(1 - |S_{11}^f|^2)(1 - |S_{22}^f|^2)(1 - |\Gamma^f|) e^{-2\alpha^f d} \frac{1}{R_1^2}}{(1 - |S_{11}^e|^2)(1 - |S_{22}^e|^2) \frac{1}{R_1^2}} \\ &= \frac{(1 - |S_{11}^f|^2)(1 - |S_{22}^f|^2)(1 - |\Gamma^f|) e^{-2\alpha^f d}}{(1 - |S_{11}^e|^2)(1 - |S_{22}^e|^2)} \\ &= F(1 - |\Gamma^f|) e^{-2\alpha^f d} \end{aligned} \quad (4.9)$$

with $F = \frac{(1 - |S_{11}^f|^2)(1 - |S_{22}^f|^2)}{(1 - |S_{11}^e|^2)(1 - |S_{22}^e|^2)} \simeq \frac{(1 - |S_{22}^f|^2)}{(1 - |S_{22}^e|^2)}$. Because the emitting antenna, the horn, radiates in air in both configuration $S_{11}^f \simeq S_{11}^e$. Also $\frac{|S_{12}^f|^2}{|S_{12}^e|^2} = \frac{P_2^f / P_1^f}{P_2^e / P_1^e} \simeq \frac{P_2^f}{P_2^e}$ as the power delivered by the VNA is the same: $P_1^f = P_1^e$.

The monopole, similar to the one used in [155] for breast imaging purposes with the only difference of a longer pin (4 cm) to adapt to the brain mimicking environment is well-matched over the entire measured frequency band (see Fig. 4.13).

Transmitted Power Measurements

The 3D printed head phantom (see Fig. 4.7) and the simulated multilayered spherical model (see Fig. 4.5) are not exactly the same. Nonetheless, their differences are relatively small and therefore one can estimate the accuracy of the measurements with an analytical modeling tool instead of a full-wave solver. Indeed, the thinnest shells are 2 mm thick which would result in a very dense meshing which can be time consuming.

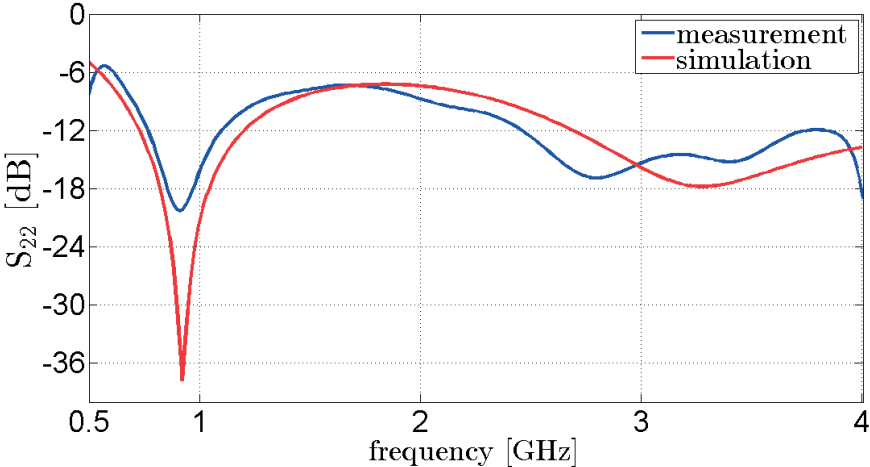


Figure 4.13 – Monopole antenna specifications: measurements (blue) and simulations (red).

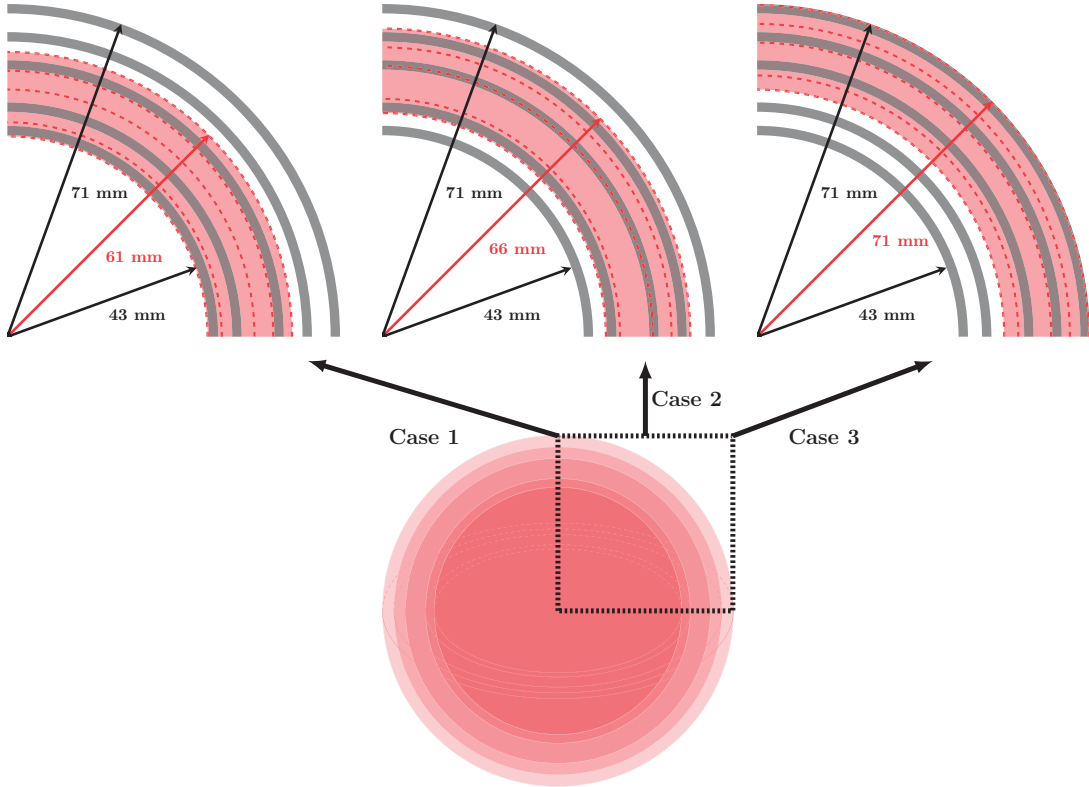


Figure 4.14 – Correspondance between the 3D printed head phantom and the multilayered spherical model. Plastic shells representation of the phantom in grey and spherical head model in red. Top: three possible configurations with 61 mm (left), 66 mm (middle), and 71 mm (right), outer diameters of the spherical head model.

The Fig. 4.14 shows three natural possibilities to make a correspondence between the 3D printed head phantom and the simulated multilayered spherical head model. For the simu-

lations results either the simulated head model is "small", with the brain sphere coinciding with the brain cavity in the 3D printed phantom which results in an outer radius of 61 mm for the simulated model, either the head model is "medium" with an outer radius of 66 mm, or finally, the head model is "large" with an outer radius of 71 mm coinciding with the outer shell of the 3D printed phantom. Of course any combinations of these choices are also valid. The normalized transmitted power is plotted for all three configurations in Fig. 4.15. The blue, red, and green lines correspond, respectively, to "small", "medium", and "large", simulated head model sizes. The results for the normalized transmission coefficient follow the same trend. There is a frequency shift in the power transmission, which grows with increasing frequency, at 1 GHz the difference is around 2 dB.

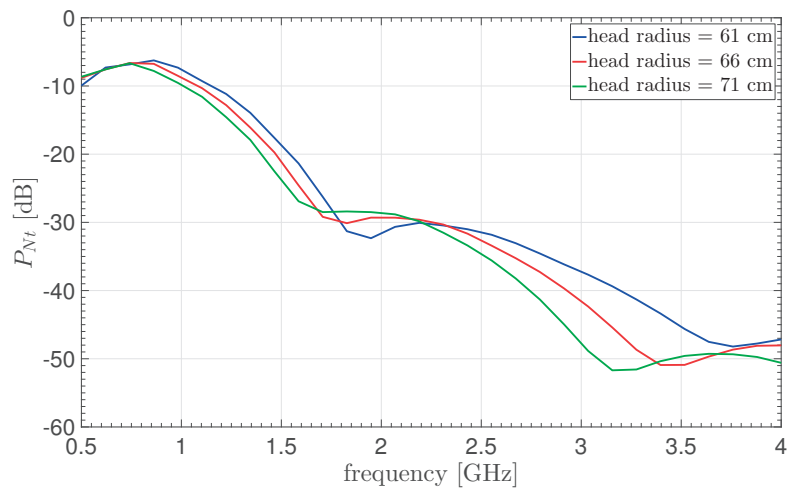


Figure 4.15 – Normalized transmitted power as a function of the frequency: with 61 mm (blue), 66 mm (red), and 71 mm (green), outer diameters of the spherical head model.

As a general remark, larger heads (and therefore larger distances from the outside of the head towards the center of the brain) suffer from overall bigger power attenuation which is worsened with higher frequencies.

In Fig. 4.16 the measured normalized transmitted power is plotted in green and compared to simulations obtained using a planar model (in blue, when $\epsilon_{mm} = 1$ in Fig. 4.6a) and with the spherical model (in red, when $\epsilon_{mm} = 1$ in Fig. 4.6b). The comparison of spherical models is made with a head of outer radius 61 mm, as the results matches the most. One can easily observe that in the range [1.5-3] GHz, the normalized transmitted power P_{Nt} drops very rapidly by -15 dB due to the strong attenuation in the tissues, which was predicted by both the planar and the spherical model.

The Fig. 4.16 shows reasonable agreements between the measured and the simulated data of the same configurations assuming a plane wave excitation. At 1.6 GHz the normalized transmitted power is -17 dB for both simulated and measured P_{Nt} . This figure experimentally confirms the analysis made with spherical and planar models. It reinforces the choice to perform measurements around 1 GHz as the power attenuation is less than 10 dB.

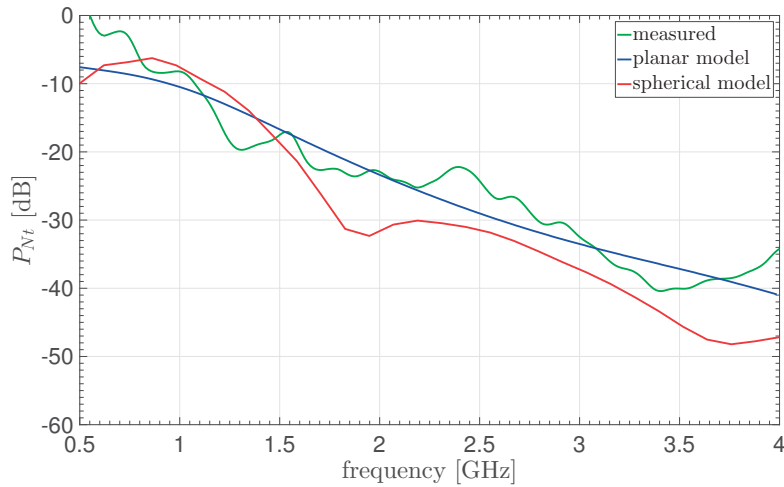


Figure 4.16 – Normalized transmitted power as a function of the frequency: measured (green) and simulated with planar (blue) and spherical (red) models.

The reasons for the differences between the measurements and the model are twofold. Firstly, the plastic layers take a certain physical space which were not included in our simulations. This choice is justified as the goal is to determine if the phantom can reproduce the model, which does not have plastic layers. Secondly, for the same reason which is to compare the measurements with the simulations obtained with the ideal model, the dielectric properties of the tissues are the theoretical ones (permittivity values depicted in solid lines in Fig. 4.10).

Measurement Setup Characterization

The phantom is also a useful tool to assess the microwave imaging system, in terms of sensibility, precision and calibration. For this purpose, the goal is to define the model as close as possible to the measured phantom. Basically, it implies using the measured permittivities of the Triton-based mixtures (dashed lines in Fig. 4.10) instead of the theoretical dielectric properties (solid lines in Fig. 4.10), and inserting the plastic layers in the simulations. This analysis is presented in Fig. 4.17. The measurements are compared with the physical model with plastic shells and measured dielectric properties of the Triton-based liquids. The green lines represent measurements with (solid line) and without (dotted line) correction for the mismatch of the monopole antenna immersed in the phantom. The red line represents the simulations with the spherical head model of outer radius 61 mm. The black lines represent simulations with the modified spherical head model which accounts for the plastic layers. The latter is simulated with theoretical values for the head tissue in solid line (permittivity values depicted in solid lines in Fig. 4.10) or with the measured values of the tissue mimicking Triton based mixtures in dotted lines (permittivity values depicted in dashed lines in Fig. 4.10).

For frequencies below 2 GHz, the realistic model with the plastic shells is very similar to the

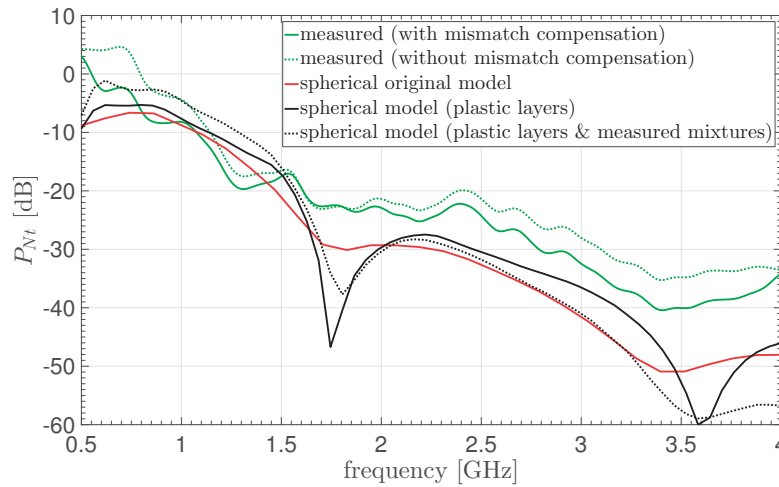


Figure 4.17 – Normalized transmitted power as a function of the frequency: measured with the mismatch correction (green solid line) and without the mismatch correction (green dotted line), with the simulated spherical models in the original case (red), in the case with plastic shells and theoretical values for the mixtures (black solid line) or measured values for the mixtures (black dotted line).

simulation results using the theoretical model. Firstly, the plastic shells are not influencing too much the wave propagation. Secondly, the Triton-based mixtures are close enough to the theoretical values and reflect the required transmission problem. On the other hand, for frequencies above 2 GHz, the plastic structure and the badly-matched measured permittivities of tissue mimicking liquids are starting to have an influence. Nevertheless, the simulations with the realistic model (with the plastic shells and the measured values of the permittivities) should be closer to the measured values, which is not the case in the latter measurements. Two hypotheses are plausible, either the dielectric measurements are not accurate above 2 GHz and the losses are overestimated, or more likely the calibration of the VNA was altered by cable movements. Indeed the 2-port calibration required some cable movements, which, even if kept as small as possible, introduce errors, which are amplified at higher frequencies. Cable movement could also explain the modulation in the measurements which are not visible in simulations. The latter hypothesis is also more plausible because the measurement seems to be shifted gradually with increasing frequency. Nevertheless, canonical phantoms, are a way to check whether the calibration is valid for the whole frequency range of interest.

Layers influences

As the filling process allowed to fill each layer on-site without moving the prototype (see 4.11), it is possible to estimate the influence of each layer on the power transmission. Each of these four layers have a very specific influence on the propagation of the wave from and into the brain, according to the frequency.

In Fig. 4.18 (upper part) are plotted ratios in dB of the n^{th} layer over the $(n-1)^{th}$ one, after the

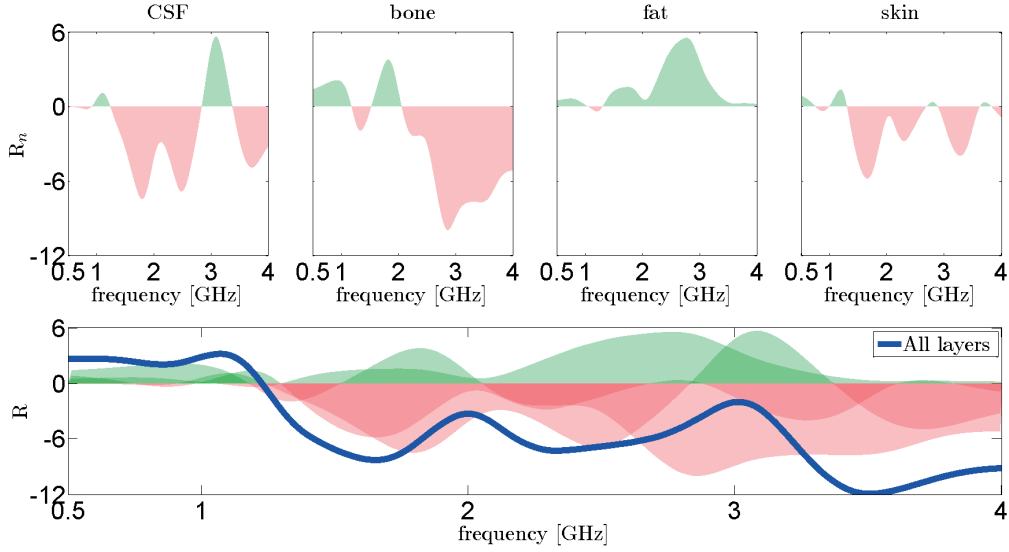


Figure 4.18 – CSF, bone, fat and skin influences on the propagation. Top: individual layer influences; bottom: superposition of the individual layer influence with the total influence depicted in blue solid line.

n^{th} layer is filled (from the brain to the skin layer). This power ratio $R_n(\omega)$ is expressed as:

$$R_n(\omega) = \frac{|S_{21}^{(n)}(\omega)|^2}{|S_{21}^{(n-1)}(\omega)|^2} \quad (4.10)$$

It represents the propagation of the wave between the monopole in the center of the brain region and the surrounding environment in the case when only the core layer, representing the brain, is filled. In this representation 0 dB means that there is no impact on the propagation of the wave when an additional layer is added. If this ratio is positive (green surface), it means that the added layer is beneficial to the propagation. A bad influence on the propagation is indicated by a red region. It appears clearly that the forbidden frequency band observed in [47] around 2 GHz is mainly dictated by the layers of CSF and skin. The bone strongly cuts the propagation around 3 GHz, however, as the attenuation is high at those frequencies, this additional forbidden band is somehow hidden by the low levels of transmitted powers. The fat layer is beneficial to the propagation in the investigated frequency band. In the lower part of Fig. 4.18, the product of all these influences gives the total influence $R(\omega)$, of all the layers on the wave propagation. Fig. 4.18 clearly shows that up to around 1.2 GHz the barrier formed by the CSF, bone, fat and skin, is beneficial to the power transmission and act as a matching medium. Beyond this limit the layers in between have a negative impact by decreasing the propagation of the wave.

4.3 Conclusion

In this chapter, the analysis of the normalized transmitted power of an impinging electromagnetic field onto the human head for MWI applications was presented using both planar and spherical multilayered TL models. To design an optimal MWI setup, the trade-off between penetration of the wave and imaging resolution should be taken into account. Indeed, a wave at low frequency is less attenuated through the tissue layers but would result in a bad imaging resolution. The strong attenuation of at least 15 dB between 1.5 GHz and 3 GHz in the measurements matches the predictions made with simple transmission line models. It experimentally confirms the trend to perform head MWI around 1 GHz as the power attenuation is less than 10 dB, for all considered matching media.

The experimental results have been compared to our modeling tool based on spherical wave expansion and showed reasonable agreement, and are in accordance to the predictions based on planar models. Additionally, a methodology to perform measurements outside and inside liquid phantoms using the 3D printing technology was presented. This convenient and accessible way of building prototypes can be used to develop complex and reliable phantoms for bio-medical applications. The phantom is transportable and robust, the glue did not seem to have changed after two sets of experiments separated by nine months. The possibility to exchange or build new quasi-identical phantoms allows comparing existing algorithms among researchers from different institutions. Today, anthropomorphic models based on 3D printed head phantoms for MRI lack of complexity for microwave applications, for which the wavelength is shorter.

This chapter presented a methodology to find optimal frequencies and matching mediums in accordance with acceptable power levels which are defined by the sensitivity of the data acquisition system of the imaging system, using simplified and fast analytical models. These parameters can be later fine-tuned using more complex EM solvers and anthropomorphic models of the head.

5 Microwave Inverse Scattering Problem

This chapter focuses on inverse scattering for brain imaging applications in the microwave range. Microwave Imaging suffers from two major challenges which are non-linearity and ill-posedness which are intrinsic to the physical reality governed by Maxwell equations. Depending on the application, different strategies can be adopted to tackle - partially or entirely - these issues. Every strategy comes with trade-offs, which must be carefully analyzed for each application. Microwave Imaging for bio-medical applications have the general requirement to be able to provide accurate tissue contrast information with the highest resolution possible, and most importantly have stable and trustworthy images with low false negative (non detection of existing tissue contrast), and low false positive (detection of non-existing tissue contrast) rates. This chapter addresses the following four tasks:

1. the presentation of the differential MWI (dMWI) for brain imaging applications;
2. the estimation and quantification of the Degree of Non-Linearity (DNL) for dMWI;
3. the analysis of different regularization schemes to solve the ill-posed inverse problems, by using simple and complex head models;
4. the experimental validation of brain dMWI using the multilayered head phantom presented in the previous chapter.

This part aims at presenting the strategies adopted to tackle first the **non-linearity** of the scattering problem for a dMWI scheme, in order to provide a continuous monitoring of the brain region. In a second step, the **ill-posedness** is discussed in simulations, which allows a complete analysis based on different models, stroke position and size. The last part presents the experimental validation of dMWI using a simple imaging setup and head phantom, which are representative to derive conclusions and confirm the possibility of using dMWI as a modality to detect, classify and monitor brain strokes.

5.1 Differential Microwave Imaging Setup

5.1.1 Setup

The multi-illumination, multi-view or tomographic configuration (see Fig. 5.1) consists of an investigation domain Γ surrounded by emitting and receiving probes. The target under investigation (domain Ω) is sequentially illuminated by P incident fields incoming from different directions. The scattered field is then measured by the M probes located in Γ and surrounding the target as depicted in Fig.5.1. The same probes can be switched from emitting to receiving mode depending on the multi-illumination strategy and setup.

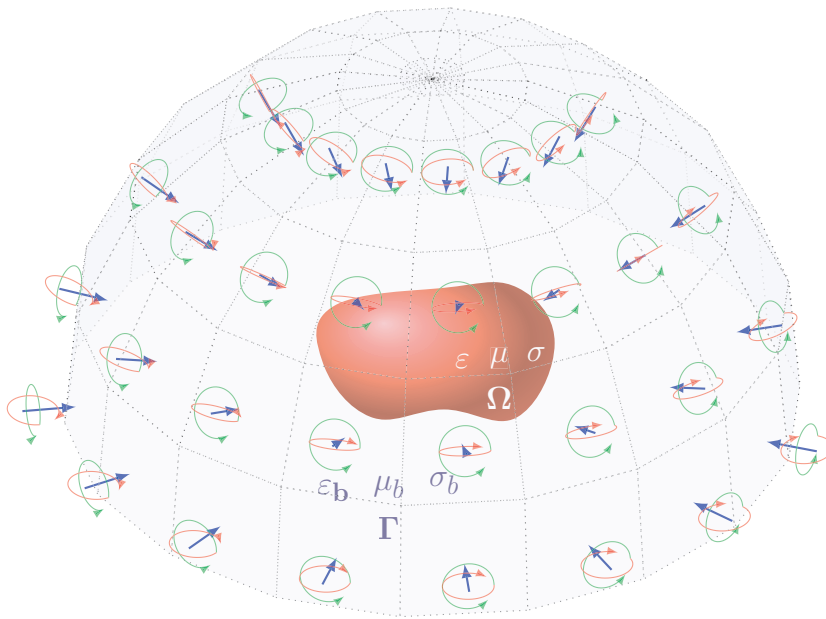


Figure 5.1 – Imaging configuration. Investigation domain Γ , with the dielectric properties of background medium ϵ_b , μ_b , and σ_b . The scatterer under investigation lays in Ω and has the constitutive parameters ϵ , μ , and σ .

In Fig. 5.1 the blue arrows represent what we define as the direction of propagation. The green and red circles represent, respectively, the Transverse Magnetic (TM) and Transverse Electric (TE) modes. These modes define whether the polarization is locally tangential to the surface of the object (TM-mode) or not (TE-mode).

Before starting the analysis on the non-linearity and ill-posedness of brain MWI, it is important to define some notions regarding the 2D and 3D related imaging configurations. Firstly, 2D-imaging refers to reconstructions obtained using 2D Green functions, which are set by making the assumption that the third direction (here always referred to as the z -direction) has translational symmetry. For example, a circle in 2D is solved as a infinitely thin slice in the xOy -plane of an infinite cylinder (in the z -direction). On the other hand, 3D-imaging refers to

any reconstruction obtained with the 3D Green function, which does not take into account any assumption on the space other than the space discretization (the grid) and the assigned basis functions. Since we use the VIE formulation, which is defined on 3D-grid elements (voxels), any reconstruction will be intrinsically a 3D reconstruction.

5.1.2 Microwave Imaging: Contrast-Source Formulation

As a recall (see Section 2.2.2), the target under investigation (see Fig. 2.4) is characterized by its constitutive parameters: the dielectric permittivity $\bar{\epsilon}$, the magnetic permeability $\bar{\mu}$, and the electric conductivity $\bar{\sigma}$. For linear, isotropic and conducting materials these tensorial quantities become scalars (ϵ , μ and σ). These quantities are dispersive as they depend on the operating angular frequency ω . The contrast is defined as:

$$\chi(\vec{r}, \omega) = \frac{\epsilon(\vec{r}, \omega)}{\epsilon_b(\omega)} - 1 \quad (5.1)$$

with $\omega = 2\pi f$ the angular frequency (rad Hz) and f the frequency (Hz). The scattering of monochromatic electromagnetic radiation is expressed by the VIE-formulation for purely dielectric targets (see Section 2.2.2):

$$\mathbf{E}(\vec{r}) = \mathbf{E}_b(\vec{r}) + \int_{\Omega} \bar{\bar{\mathbf{G}}}_e(\vec{r}, \vec{r}') \chi(\vec{r}') \mathbf{E}(\vec{r}') d\Omega' \quad (5.2)$$

with \mathbf{E} the total field, \mathbf{E}_b the background field, and $\bar{\bar{\mathbf{G}}}_e$ the dyadic Green function. To find the numerical solution of the total electric field in (5.2), the scatterer is discretized on a N -point homogeneous grid ($N = N_x \times N_y \times N_z$). Using matrix notations, after applying a Galerkin-type MoM, the scattering problem is converted into a system of linear equations, using piecewise constant testing and basis functions (see Section 3.2). The total field E is the superposition of the incident field E^i and the scattered field E^s , where the scattered field $E^s = GXE$. Therefore the total field E , is derived as:

$$E = (I - GX)^{-1} E^i \quad (5.3)$$

where I is the identity matrix of dimension $3N \times 3N$. The resulting dense matrix $A = I - GX$ is composed of complex numbers and is of dimension $3N \times 3N$.

5.1.3 Differential Microwave Imaging Scenario

dMWI consists of measuring the scattered fields at two different times, take their difference, and then reconstruct an image which reflects the contrast change. For brain stroke applications, with the assumption that only the region damaged by the stroke undergoes a permittivity

Chapter 5. Microwave Inverse Scattering Problem

change, this procedure has the potential to monitor the modifications of the stroke area and therefore provide useful information about the nature of the stroke. The three main purposes are:

- determining the nature, position, and changing size of the anomaly (short monitoring, first few minutes/hours);
- monitoring the evolution of the stroke after the administration of treatment to assess its efficiency; healing or not of the damaged area, rate of recovery, etc. (short and long term monitoring, few hours and up to a day);
- monitoring patients in coma: indeed if a bleeding inside the brain happens during the coma, very few tools are then available to detect the stroke as the patient does not have any visible changes (potentially long term monitoring).

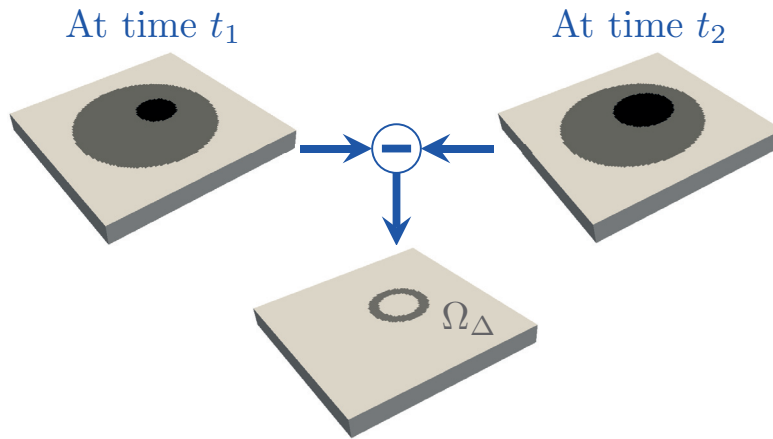


Figure 5.2 – dMWI scenario: contrast functions at times t_1 and t_2 , and their contrast difference, only non-zero on Ω_Δ .

In Fig. 5.2, $\Delta_\chi = X_2 - X_1$ where $X_i = X_{t_i}$. The contrast difference Δ_χ , (center) represents the change of the contrast function between time t_1 (left) and time t_2 (right). This contrast is only non-zero on a reduced region Ω_Δ . The total field at times t_1 and t_2 is expressed as:

$$E_1 = E^i + GX_1 E_1 \quad (5.4)$$

$$E_2 = E^i + GX_2 E_2 \quad (5.5)$$

with:

$$E_1 = (I - GX_1)^{-1} E^i \quad (5.6)$$

$$E_2 = (I - GX_2)^{-1} E^i \quad (5.7)$$

The differential scattered field, or equivalently the differential total field is obtained by subtracting (5.4) to (5.5):

$$\Delta_E = E_2 - E_1 \quad (5.8)$$

If the ℓ_2 -norm $\|GX\| < 1$, the inverse operators in (5.3) can be expanded in Neumann series around the point $X = 0$, i.e.,

$$(I - GX)^{-1} = I + \sum_{n=1}^{n=\infty} (GX)^n \quad (5.9)$$

For the differential scenario, if $\|GX_1\| < 1$ and $\|GX_2\| < 1$, expressions (5.6) and (5.7) can be expanded in Neumann series. They are inserted in equation (5.8) which becomes:

$$\begin{aligned} \Delta_E &= (GX_2 - GX_1) E^i + [(GX_2)^2 - (GX_1)^2] E^i + \dots + [(GX_2)^n - (GX_1)^n] E^i + \dots \\ &= \sum_{n=1}^{n=\infty} [(GX_2)^n - (GX_1)^n] E^i \end{aligned} \quad (5.10)$$

Note that the differences $[(GX_2)^n - (GX_1)^n]$ are only defined in domain Ω_Δ - where the contrast function changes between times t_1 and t_2 .

5.2 Non-Linearity of the Scattering Problem

5.2.1 Degree of Non-Linearity

As a recall of the recursive expansion introduced in Section 2.3, the total field in (2.10) can be rewritten as:

$$\begin{aligned}
 \mathbf{E}(\vec{r}) &= \mathbf{E}_b(\vec{r}) + \int_{\Omega} \bar{\bar{\mathbf{G}}}_e(\vec{r}, \vec{r}') \chi(\vec{r}') \left[\mathbf{E}_b(\vec{r}') + \int_{\Omega} \bar{\bar{\mathbf{G}}}_e(\vec{r}', \vec{r}'') \chi(\vec{r}'') \mathbf{E}(\vec{r}'') d\Omega'' \right] d\Omega' \\
 &= \mathbf{E}_b(\vec{r}) + \underbrace{\int_{\Omega} \bar{\bar{\mathbf{G}}}_e(\vec{r}, \vec{r}') \chi(\vec{r}') \mathbf{E}_b(\vec{r}') d\Omega'}_{\text{first order interaction}} + \underbrace{\int_{\Omega} \bar{\bar{\mathbf{G}}}_e(\vec{r}, \vec{r}') \chi(\vec{r}') \left[\int_{\Omega} \bar{\bar{\mathbf{G}}}_e(\vec{r}', \vec{r}'') \chi(\vec{r}'') \mathbf{E}_b(\vec{r}'') d\Omega'' \right] d\Omega'}_{\text{second order interaction}} \\
 &\quad + \underbrace{\int_{\Omega} \bar{\bar{\mathbf{G}}}_e(\vec{r}, \vec{r}') \chi(\vec{r}') \left[\int_{\Omega} \bar{\bar{\mathbf{G}}}_e(\vec{r}', \vec{r}'') \chi(\vec{r}'') \left[\int_{\Omega} \bar{\bar{\mathbf{G}}}_e(\vec{r}'', \vec{r}''') \chi(\vec{r}''') \mathbf{E}(\vec{r}''') d\Omega''' \right] d\Omega'' \right] d\Omega'}_{\text{higher order interactions}}
 \end{aligned} \tag{5.11}$$

This system is clearly non linear as the output (the electric field $\mathbf{E}(\vec{r})$) of the system is not directly proportional to the input (the contrast function $\chi(\vec{r})$). The non-linearity is modeled by the second and higher order interactions in (5.11).

A commonly used approximation consists in keeping only the first order interaction:

$$\mathbf{E}(\vec{r}) \simeq \mathbf{E}_b(\vec{r}) + \int_{\Omega} \bar{\bar{\mathbf{G}}}_e(\vec{r}, \vec{r}') \chi(\vec{r}') \mathbf{E}_b(\vec{r}') d\Omega' \tag{5.12}$$

This linear approximation is known as the first order Born approximation [156] and can be used for both direct and inverse scattering problems. It amounts to neglect the multiple scattering effects and is therefore valid for weak scatterers. To quantify the "weakness" of a scatterer and determine whether or not the first order Born approximation can be applied, it is necessary to introduce the Degree of Non-Linearity (DNL). The computation of the DNL has been derived for scalar two-dimensional inverse scattering problems in [44] and the main steps are now outlined. For the numerical solutions, the first order Born approximation is the linear approximation of the series (5.9), which consists of keeping only the first term of the summation and injecting it in (5.3):

$$E \simeq (I + GX)E^i \quad \text{whenever} \quad \|GX\| \ll 1 \tag{5.13}$$

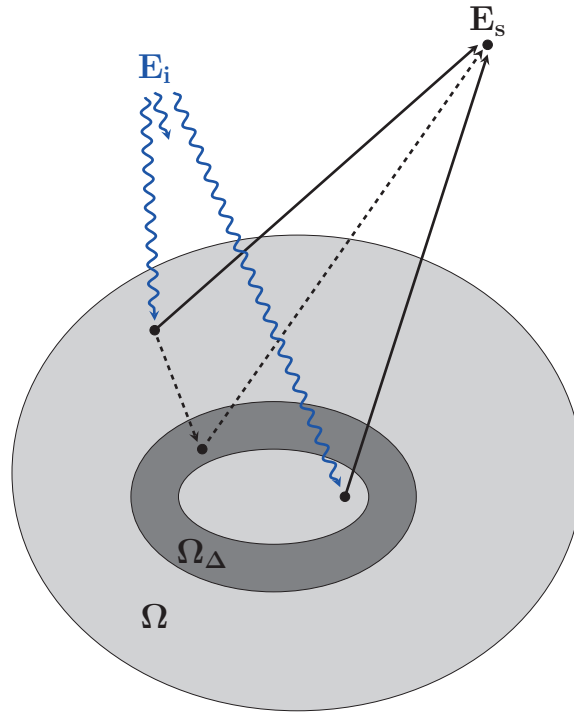


Figure 5.3 – Illustration of the non linear scattering problem in the domain Ω . In dMWI the contrast is only changing in the domain Ω_Δ . The incident field E_i , and the resulting scattered field E_s are depicted, respectively, with blue (zigzag) and black (straight) arrows. The first and second order interactions are depicted in, respectively, solid and dashed black lines.

The quantification of the DNL consists of giving values (stroke size, position, background medium permittivity, etc.) for which the ℓ_2 -norm $\|GX\|$ is considered small enough for either the EM modeling or the reconstruction, applying the first order Born approximation, to be reliable. In Fig. 5.3 the *multiple scattering phenomena* which lead to the non-linearity are illustrated. The solid line is an example of the component of the electric field which is caused by first order interactions, the dashed line is caused by the second order interactions. Higher interactions are not depicted. Linearizing the scattering problem by the first order Born approximation, consists of only considering the scattered fields produced by first order interactions and discarding all the others.

With the Cauchy-Schwarz inequality it is possible to separate the contribution to $\|GX\|$ between operator G (electric size of the domain) and constitutive parameters X (contrast):

$$\|GX\| \leq \|G\| \cdot \|X\| \tag{5.14}$$

A high DNL can be due either to a high value of the contrast function $\|X\|$ or a large value of $\|G\|$ (large electric size of the domain). This development is the same for a 2D or a 3D scenario.

5.2.2 Quantification of the Degree of Non Linearity for dMWI

The main difference between the MWI and the dMWI scenario is the integration domain which is smaller in the differential scenario $\Omega_\Delta \subset \Omega$. It means that the range of applicability of the first order Born approximation in the dMWI is in general broader. The first order Born approximation considers only the first term of (5.10),

$$\Delta_E \simeq G(X_2 - X_1) E^i \quad \text{whenever} \quad \|GX_1\|_{\Omega_\Delta} \ll 1 \quad \text{and} \quad \|GX_2\|_{\Omega_\Delta} \ll 1 \quad (5.15)$$

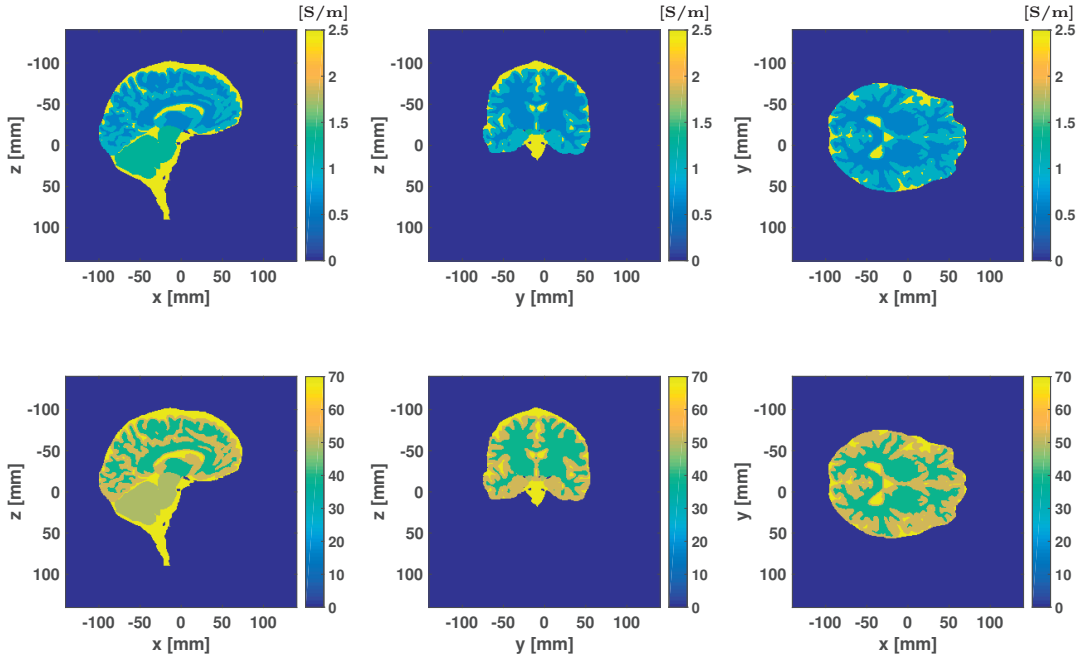


Figure 5.4 – Sagittal (left), coronal (center) and axial/transverse (right) views of the conductivity (top) and relative permittivity (bottom) of a realistic human model [83] of the brain region where the stroke can occur. Frequency was 1 GHz.

In (5.10) $\|GX\|$ is not evaluated on Ω but only on Ω_Δ to determine the validity of the linearization for dMWI. This approximation is valid when both $\|GX_1\|_{\Omega_\Delta} \ll 1$ and $\|GX_2\|_{\Omega_\Delta} \ll 1$. These two norms give a measure of the DNL of the dMWI. It provides a good image of the difficulty of resolution of the forward and inverse dMWI problems.

It is reasonable to say that the stroke can only happen in the white/grey matter, CSF, and

5.2. Non-Linearity of the Scattering Problem

Cerebellum regions as shown in Fig. 5.4. The median dielectric parameters of the domain, which could be subject to a stroke, are $\epsilon_r = 52$, $\sigma = 1$ [S/m] at 1 GHz. The worst case scenario would be if all the latter domain is subject to a stroke. The dielectric properties of blood at 1 GHz are $\epsilon_r = 61.1$, $\sigma = 1.58$ [S/m] (see Fig. 5.5).

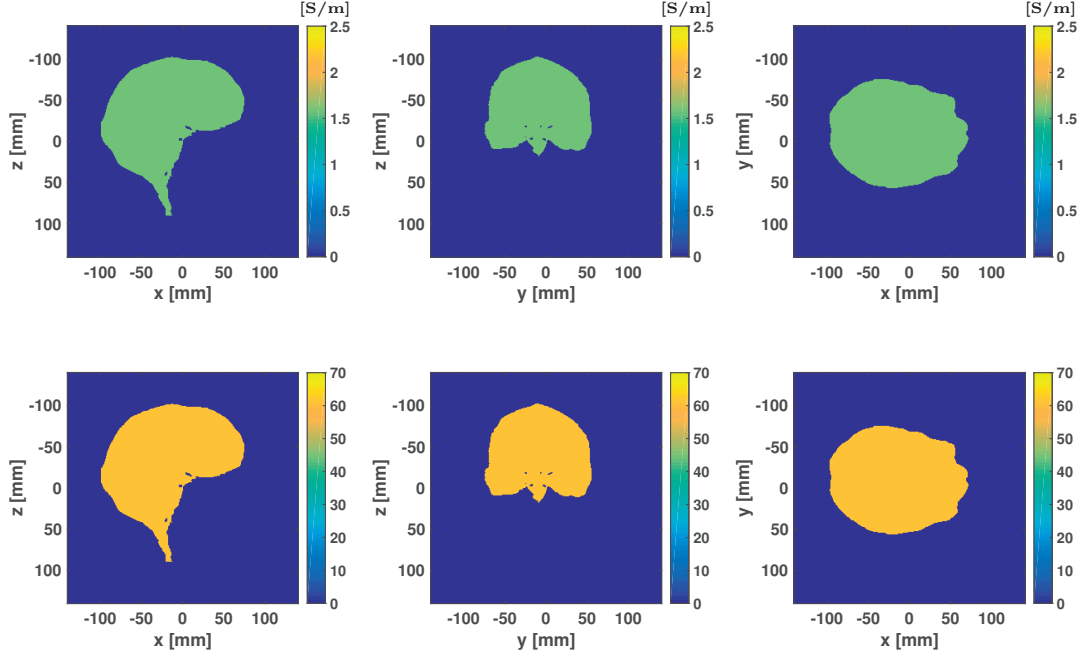


Figure 5.5 – Sagittal (left), coronal (center) and axial/transverse (right) views of the conductivity (top) and relative permittivity (bottom) of a realistic human model [83] of the brain region of Fig. 5.4 filled with blood. Frequency was 1 GHz.

The ℓ_2 -norm of $\|GX_1\|_{\Omega_\Delta}$ and $\|GX_2\|_{\Omega_\Delta}$ can be computed for the worst case scenario. In the latter case, $\|GX_1\|_{\Omega_\Delta}$ is the initial state depicted in Fig. 5.4, and $\|GX_2\|_{\Omega_\Delta}$ is the final state depicted in Fig. 5.5. For a fixed grid size, the latter two norms depend on the operating frequency and the dielectric complex permittivity of the background medium.

The influence of the background medium on the DNL are displayed in Fig. 5.6. Background media leading to a low DNL and therefore an easier to solve imaging problem are in the blue region. The operating frequency is 1 GHz, for a voxel size of $20 \times 20 \times 20$ mm³. The relative permittivity of the background medium ϵ_b , varies in the range [1 – 80] (approximately from air to water at 1 GHz), and the conductivity varies in the range [0 – 3] S/m. These ranges are covering all the dielectric properties of a human head model. In Fig. 5.6, it appears clearly that for low values of the relative permittivity ϵ_r for the background medium (< 10), both of the norms are above unity, and therefore the brain cannot be considered as a weak scatterer.

To better observe which values of the background medium minimize the DNL for both cases (no stroke present and the stroke at maximum size, which are depicted, respectively in Fig. 5.6a

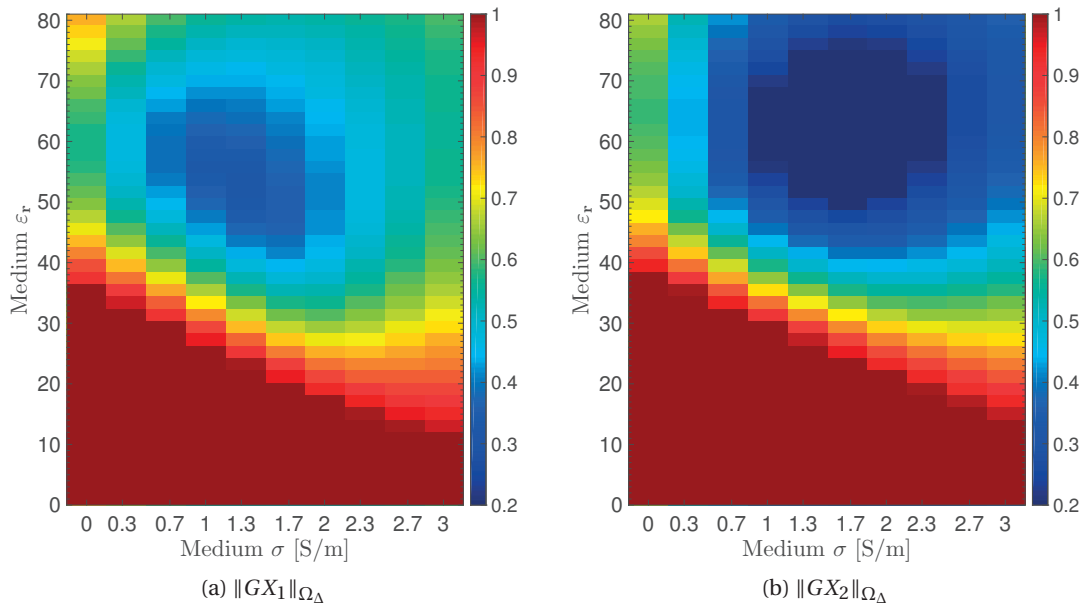


Figure 5.6 – DNL for dMWI as function of medium relative permittivity ($\varepsilon_b = [1 - 80]$) and conductivity ($\sigma_b = [0 - 3][\text{S/m}]$). The ℓ_2 -norm of $\|GX_1\|_{\Omega_{\Delta}}$ for the case depicted in Fig. 5.4 (left) and the ℓ_2 -norm of $\|GX_2\|_{\Omega_{\Delta}}$ for the case depicted in Fig. 5.5 (right).

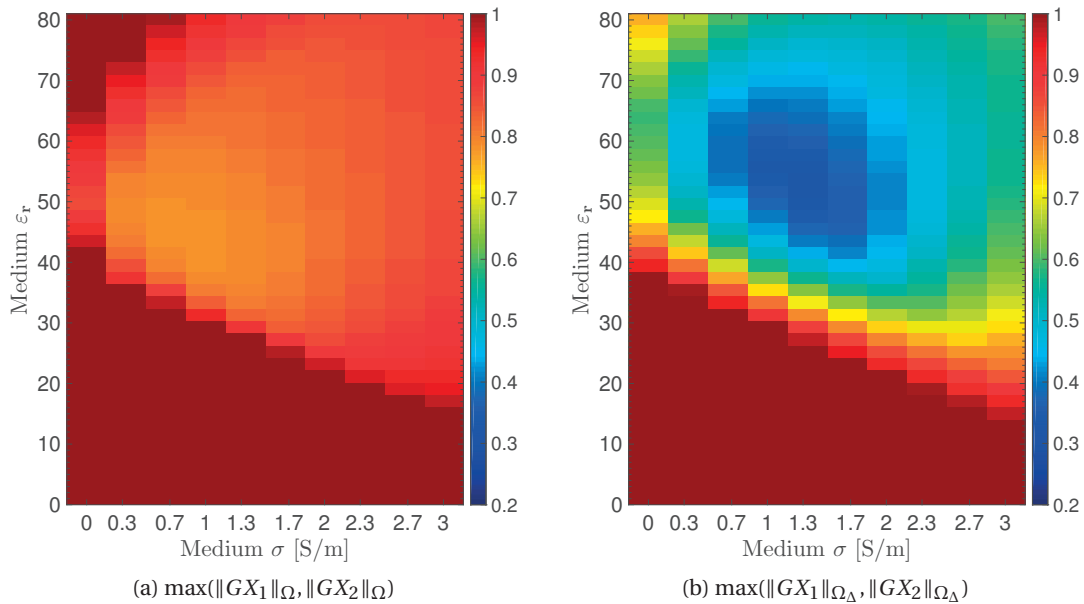


Figure 5.7 – DNL for MWI (left) and dMWI (right) as function of medium relative permittivity ($\varepsilon_b = [1 - 80]$) and conductivity ($\sigma_b = [0 - 3][\text{S/m}]$). The ℓ_2 -norm of $\max(\|GX_1\|_{\Omega_{\Delta}}, \|GX_2\|_{\Omega_{\Delta}})$ which are separately depicted in Fig. 5.6.

and Fig. 5.6b), one can compute the maximum between the two norms. The results are depicted in Fig. 5.7b. This value is compared to the analogue calculation for MWI and shown in Fig. 5.7a. As expected, we observe that the range of applicability of the first order Born approximation is wider for dMWI than for MWI for brain applications. The value which minimizes $\max(\|GX_1\|_{\Omega_\Delta}, \|GX_2\|_{\Omega_\Delta})$ is $(\epsilon_r = 52, \sigma = 1.3 \text{ [S/m]})$. In that case $\|GX_1\|_{\Omega_\Delta} = 0.32$ and $\|GX_2\|_{\Omega_\Delta} = 0.19$ and the first order Born approximation can be applied to linearize the problem.

5.3 Inverse Problem Resolution

A regularization technique is necessary to solve the ill-posed inverse scattering problem. The Truncated Singular Value Decomposition (TSVD) scheme [45] is a classical approach where only the main singular values of the scattering operator are kept. The differential MWI problem can be regularized by minimizing the ℓ_1 -norm which suggests that the difference of the contrast function through time is sparse [42]. The Total Variation norm regularizer [157], which promotes the sparsity of the gradient of the contrast function, has proven to also work well when the sparsity of the unknown is not pixel-wise.

Assuming the DNL is small (see Section 5.2.2), it is possible to approximate the physical microwave imaging problem as a linear problem:

$$\Delta_E = L\Delta_\chi \tag{5.16}$$

with $L = GE^i$ and $\Delta_\chi = (X_2 - X_1)$ for an isotropic medium. The linear operator L is of dimension $M \times N$. In our case, we have $M \ll N$ since the number M of measurement points ($M = 3 \times N_a \times N_a$, with N_a the number of sensors) is much smaller than the number N of unknowns (pixels/voxels). Typically, for brain stroke imaging with $N_a = 32$ ($M \leq 3072$) and for a voxel size of $4 \times 4 \times 4 \text{ mm}^3$, we have $N = 4056$ for only one slice of the Duke model in the xOy -plane. As a very recent example published in [39], for the prototype developed by EMTensor GmbH, Vienna, Austria [158], the imaging chamber is composed of 5 rings of 32 antennas, for a cylindrical imaging domain of radius 285 mm and 280 mm height. Depending on grid resolution, their algorithm is tested for an N which can raise to several dozen of millions with an M of a few thousands [39].

Our goal is to determine the contrast variation $\Delta_\chi \in \mathbb{C}^N$ from the measurements $\Delta_E \in \mathbb{C}^M$. This inversion problem is generally ill-posed because it admits many solutions due to limited insufficient information ($M \ll N$).

Several strategies are proposed to invert the problem (5.16). They involve a regularization scheme to restore the stability of the solution. The first approach, known as Truncated Singular

Chapter 5. Microwave Inverse Scattering Problem

Value Decomposition (TSVD), does not make any assumption about the problem at hand, whereas the following ones take advantage of some a priori information about the solution.

5.3.1 Truncated Singular Value Decomposition

Let us expand the linear operator $L \in \mathbb{C}^{M \times N}$ by its SVD [159]

$$L = USV^H \text{ with } U \in \mathbb{C}^{M \times M}, S \in \mathbb{R}^{M \times N} \text{ and } V \in \mathbb{C}^{N \times N} \quad (5.17)$$

$$= \sum_{k=1}^r \sigma_k \mathbf{u}_k \mathbf{v}_k^H \quad (5.18)$$

The matrix V^H is the Hermitian transpose (also known as conjugate transpose) of V . The number r is the rank of the matrix L . The diagonal entries S_{kk} of S are the singular values σ_k of L . These singular values are real and non negative. The columns of U and V are, respectively, the left and right singular vectors \mathbf{u}_k and \mathbf{v}_k of L .

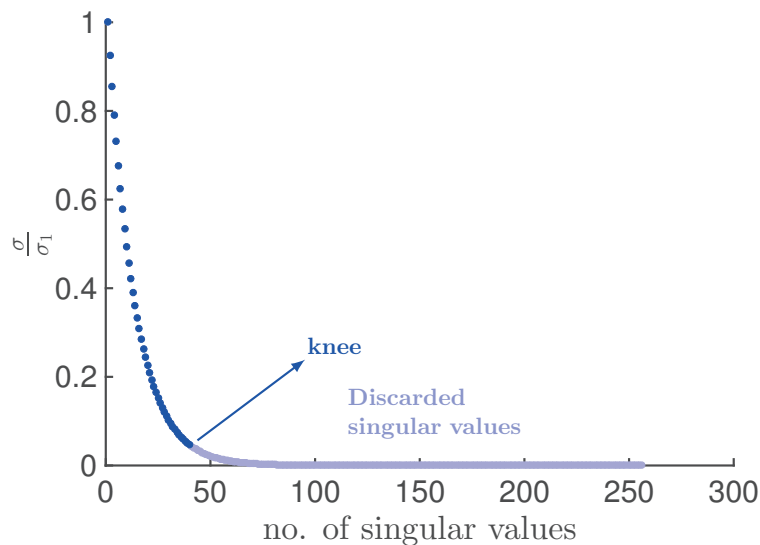


Figure 5.8 – Example of singular value distribution.

If we assume that the singular values are sorted in descending order, then σ_1/σ_r gives the condition number of the matrix. Thus, a well-conditioned matrix has a condition number close to one and is ‘easy’ to invert. The solution of (5.16) is given by:

$$\Delta_\chi = \frac{1}{\sigma_1} \left(\sum_{k=1}^r \frac{\sigma_1}{\sigma_k} \mathbf{v}_k \mathbf{u}_k^H \right) \Delta_E \quad (5.19)$$

In the presence of noise $\mathbf{n} \in \mathbb{C}^M$, i.e. when:

$$\Delta_E = L\Delta_\chi + \mathbf{n} \quad (5.20)$$

the solution becomes:

$$\Delta_\chi = \frac{1}{\sigma_1} \left(\sum_{k=1}^r \frac{\sigma_1}{\sigma_k} \mathbf{v}_k \mathbf{u}_k^H \right) \Delta_E + \frac{1}{\sigma_1} \left(\sum_{k=1}^r \frac{\sigma_1}{\sigma_k} \mathbf{v}_k \mathbf{u}_k^H \right) \mathbf{n} \quad (5.21)$$

The second term of (5.21) shows that the noise is exalted by the ratio σ_1/σ_k . This ratio can be very high in case of ill-conditioned matrices, the solution Δ_χ is then unreliable even in presence of a small noise.

One way to stabilize the solution is to truncate the summation in (5.19) and (5.21) to the first $r' < r$ elements. Thus, the ill-conditioning decreases from σ_1/σ_r to $\sigma_1/\sigma_{r'}$. The number of relevant singular values r' can be deduced by plotting the singular value distribution, identifying the knee of the curve and discarding all singular values after this knee, as depicted in Fig. 5.8.

5.3.2 Regularization via Norm Minimization

A standard approach for matrix inversion regularization is to introduce, when available, a priori information about the unknown to determine. An effective method to achieve this regularization is to minimize an appropriately chosen norm p of the solution vector Δ_χ . The optimization problem to solve is then of the form:

$$\min_{\Delta_\chi} \|\Delta_\chi\|_p \text{ subject to } \|\Delta_E - L\Delta_\chi\|_2 \leq \epsilon \quad (5.22)$$

where $\|\cdot\|_p$ stands for the ℓ_p norm, and the parameter ϵ depends on the noise and uncertainties affecting the data.

It is important to point out that there are many readily available routines to solve efficiently this type of convex optimization problems, e.g. [160–162].

ℓ_1 -norm

In a dMWI setup, it is reasonable to suppose that the solution Δ_χ is sparse since the contrast differences between t_1 and t_2 are localized. Consequently, the search space can be drastically reduced by introducing this a priori information. The real measure of sparsity is the quasi-norm ℓ_0 that counts the number of non-zero occurrences of a vector. Unfortunately, its resolution is intractable even for small scale problems. The ℓ_1 -norm ($\|\delta\chi\|_1 = \sum_k |\Delta_{\chi k}|$) is the best convex surrogate of the real measure of the sparsity. It has been successfully used to promote sparse solutions in a wide range of applications [163, 164]. The so-regularized inversion problem is:

$$\min_{\Delta_\chi} \|\Delta_\chi\|_1 \text{ subject to } \|\Delta_E - L\Delta_\chi\|_2 \leq \epsilon. \quad (5.23)$$

Let us point out that minimizing the ℓ_1 -norm enforces the sparsity of the solution point-wise, i.e. for each pixel/voxel of Δ_χ .

Total Variation Norm

We know a priori that our solution Δ_χ has a few discontinuities that are due to the localized tissue properties modifications between t_1 and t_2 . Apart from these spots, the contrast difference Δ_χ is expected to be flat (and very close to zero). Thus, the use of the Total Variation norm (TV-norm) is a good candidate to regularize Δ_χ . The TV-norm is indeed a smoothing function introduced in [165]. By minimizing the TV-norm of a matrix, we minimize its gradient, hence the smoothing effect. For a 2D dMWI setup, the complex data Δ_χ takes the form of a matrix of dimension $N_x \times N_y$ with $M = N_x \times N_y$. The TV-norm then reads:

$$\begin{aligned} \|\Delta_\chi\|_{\text{TV}} &= \sum_{m,n} |\Delta_{\chi_{m+1,n}} - \Delta_{\chi_{m,n}}| + |\Delta_{\chi_{m,n+1}} - \Delta_{\chi_{m,n}}| \\ &= \|\text{vec}(\nabla_x \Delta_\chi)\|_1 + \|\text{vec}(\Delta_\chi \nabla_y)\|_1 \end{aligned} \quad (5.24)$$

where $\text{vec}(\Delta_\chi)$ produces a vector of length $N_x \cdot N_y$ that contains the columns of Δ_χ , stacked below each other. The discrete gradient matrices ∇_x and ∇_y are of size $N_x \times N_x$ and $N_y \times N_y$ respectively, and equal to:

$$\nabla_x = \begin{pmatrix} -1 & 1 & & 0 \\ & \ddots & \ddots & \\ 0 & & -1 & 1 \end{pmatrix} \text{ and } \nabla_y = \begin{pmatrix} -1 & & 0 \\ 1 & \ddots & \\ & \ddots & -1 \\ 0 & & 1 \end{pmatrix} \quad (5.25)$$

The optimization problem (5.22) becomes:

$$\min_{\Delta_\chi} \|\Delta_\chi\|_{\text{TV}} \text{ subject to } \|\Delta_E - L\Delta_\chi\|_2 \leq \epsilon. \quad (5.26)$$

5.4 Differential Microwave Imaging Simulations

The quantification of the DNL and the comparison for different regularization schemes on the full Duke model [83] of 1 mm resolution is computationally heavy and interesting conclusions can already be found using smaller size problems. Direct solvers can then be used and therefore the convergence is ensured and the global accuracy known (equal to an order h^2 accuracy, where h is the grid resolution).

We will consider a reduced model which dramatically reduces the computational effort while keeping the key points which are to be tested in this section. The model is based on a single layer $N_z = 1$ in the z -direction and of dimensions $N_x N_y$ in the (xOy) plane (see Fig. 5.9).

In this case, the Green dyadic is simplified to:

$$G = \begin{pmatrix} G_{xx} & G_{xy} & O \\ G_{yx} & G_{yy} & O \\ O & O & G_{zz} \end{pmatrix} \quad (5.27)$$

as $G_{xz} = G_{yz} = G_{zx} = G_{zy} = O$, with O the zero matrix, because $\Theta_z = 0$ in (3.42) (the antenna and the scatterer are on the same z -coordinate). The operator L can be reduced depending on the orientation of the incident field. Indeed, G is a block diagonal matrix so its inverse is the

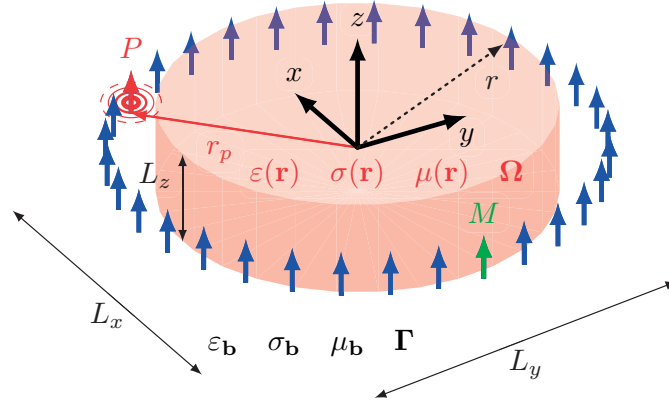


Figure 5.9 – Single layer imaging configuration. The scatterer (pink cylinder) described by its constitutive parameters $(\epsilon(\vec{r}), \mu(\vec{r}), \sigma(\vec{r}))$ in the domain Ω is surrounded by 32 antennas (red, green, and blue arrows) which lay in the background medium $(\epsilon_b(\vec{r}), \mu_b(\vec{r}), \sigma_b(\vec{r}))$ in the domain Γ . The emitting antenna is depicted in red and the receiving probe is illustrated in green.

inverse of its diagonal blocks:

$$\begin{pmatrix} G_{xx} & G_{xy} & O \\ G_{yx} & G_{yy} & O \\ O & O & G_{zz} \end{pmatrix}^{-1} = \begin{pmatrix} \begin{pmatrix} G_{xx} & G_{xy} \\ G_{yx} & G_{yy} \end{pmatrix}^{-1} & O \\ O & G_{zz}^{-1} \end{pmatrix} \quad (5.28)$$

Also, the inverse of an invertible matrix product, is the the product of the inverse matrices, therefore three cases can be distinguished:

1. the scalar case (one polarization excited).

The impinging field is a z -polarized plane wave ($E_x^i = E_y^i = O$):

$$L = \begin{pmatrix} G_{xx} & G_{xy} & O \\ G_{yx} & G_{yy} & O \\ O & O & G_{zz} \end{pmatrix} \begin{pmatrix} O \\ O \\ E_z^i \end{pmatrix} \quad (5.29)$$

In the differential scenario the equation to solve results in:

$$\Delta_{E_z} = L_z \Delta_{\chi} \quad \text{with} \quad L_z = G_{zz} E_z^i \quad (5.30)$$

The L operator shrinks from a size of $3 \times M \times N$ to a size of $M \times N$.

2. the small vectorial case (two polarizations excited).

The impinging field is a (xOy) -polarized plane wave ($E_z^i = 0$):

$$L = \begin{pmatrix} G_{xx} & G_{xy} & O \\ G_{yx} & G_{yy} & O \\ O & O & G_{zz} \end{pmatrix} \begin{pmatrix} E_x^i \\ E_y^i \\ O \end{pmatrix} \quad (5.31)$$

In the differential scenario the differential scattered field reduces to:

$$\Delta E_{xy} = L_{xy} \Delta \chi \quad \text{with} \quad L_{xy} = \begin{pmatrix} G_{xx} E_x^i + G_{xy} E_y^i \\ G_{yx} E_x^i + G_{yy} E_y^i \end{pmatrix} \quad (5.32)$$

The problem to solve shrinks from a size of $3M \times N$ to a size of $2M \times N$.

3. the full vectorial case (three polarizations excited).

The impinging field has a polarization oriented in any x, y , or z -directions, therefore L is of size $3M \times N$ and is dense.

The three configurations permit to quantify the DNL using the same model, and to test different regularization schemes.

5.4.1 Numerical Experiments for DNL of dMWI

The single layer investigation domain Γ (see Fig. 5.9) is illuminated by 32 successive incident plane waves from equally spanned incident angles over 360° . The frequency is set to 1 GHz. The measurements are performed at the same angles on a circle of radius r . The reconstructed images are analyzed on both quantitative and qualitative aspects. Quantitative imaging, implicates that the exact value of the imaged parameter, here the complex contrast function $\Delta \chi$, can be determined. Qualitative imaging, refers rather on the visual aspect of the reconstruction, in our case, whether a contrast change at the location of $\Delta \chi$ is visible or not.

Simplified Canonical Cases

A growing ischaemic stroke ($\epsilon_s = 36$, $\sigma_s = 0.7$ S/m) is inserted into a simplified homogeneous head ($\epsilon_r = 48$, $\sigma_r = 0.4$ S/m), called M model. The frequency of the incident plane wave is 1 GHz. The stroke is centered at $C_x = 1$ cm, $C_y = 2$ cm, $C_z = 0$ cm, and its radius grows from $R_1 = 2$ cm to $R_2 = 4$ cm on a domain of size $N = 40 \times 40 \times 1$ and resolution $h = 5$ mm. This growing stroke is represented in Fig. 5.10, where the light grey, the grey and the black domains represent, respectively, the background medium, the homogeneous head and the stroke.

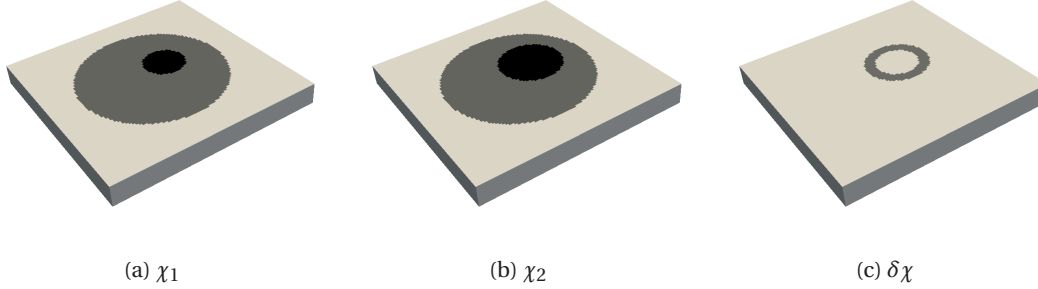


Figure 5.10 – Contrast of different scenarios. From left to right; contrast function at time t_1 , contrast function at time t_2 , and the resulting contrast difference.

The two ℓ_2 -norms $\max(\|GX_1\|_{\Omega}, \|GX_2\|_{\Omega})$ and $\max(\|GX_1\|_{\Omega_{\Delta}}, \|GX_2\|_{\Omega_{\Delta}})$, are computed for different dielectric parameters of the background medium and the maximum between the two is shown in Fig. 5.11, in the same fashion as Fig. 5.6.

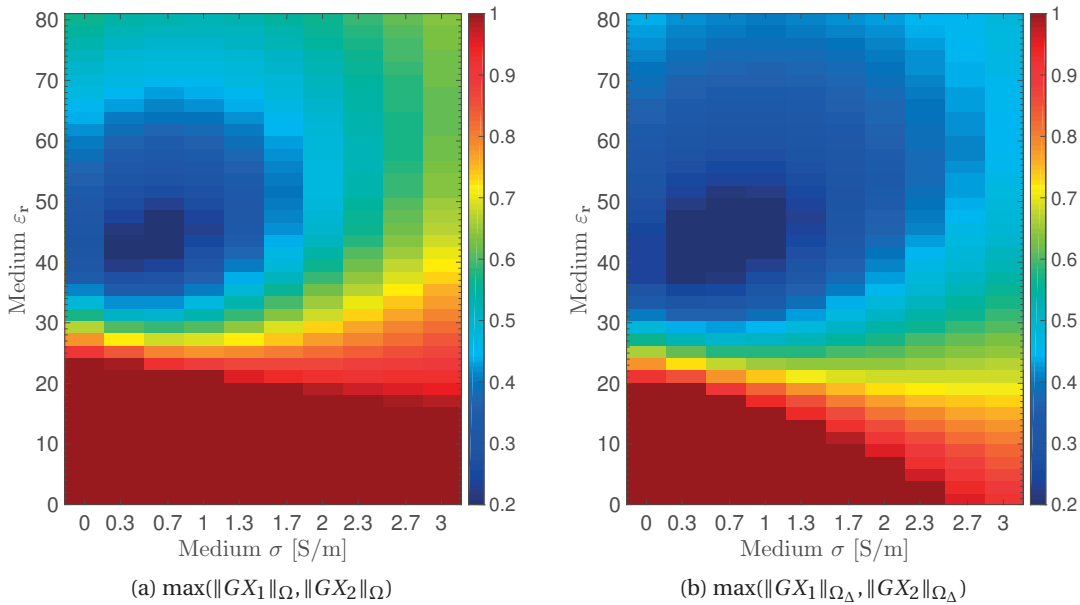


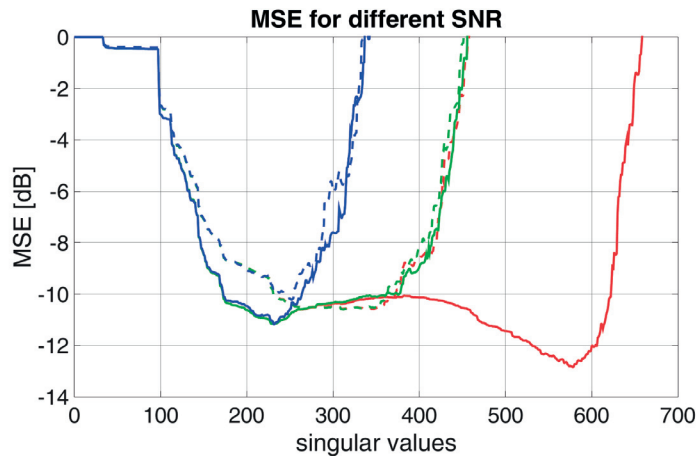
Figure 5.11 – DNL for MWI and dMWI of the example of Fig. 5.10 as function of medium relative permittivity ($\epsilon_b = [1 - 80]$) and conductivity ($\sigma_b = [0 - 3]$ S/m). The ℓ_2 -norm of $\max(\|GX_1\|_{\Omega}, \|GX_2\|_{\Omega})$ is depicted on the left, and the ℓ_2 -norm $\max(\|GX_1\|_{\Omega_{\Delta}}, \|GX_2\|_{\Omega_{\Delta}})$ on the right.

For further investigations, four interesting cases will be considered. Their description is summarized in Table 5.1.

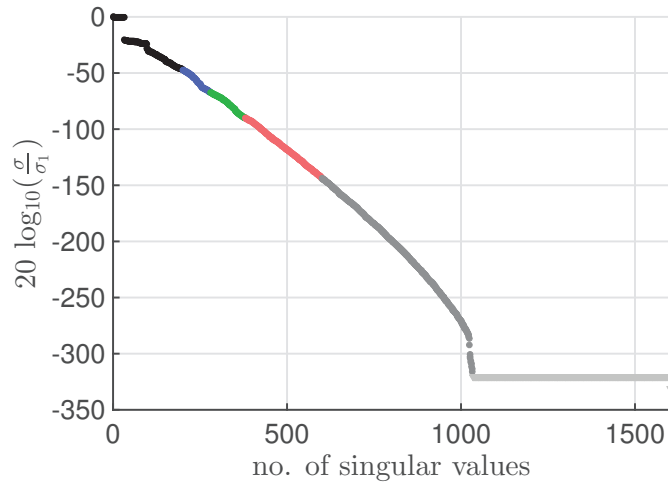
We first assess the influence of the first order Born approximation on the forward problem

Table 5.1 – Influence of the DNL on the forward MWI problem

Model	ε_b	σ_b [S/m]	$\ GX_2\ _{\Omega_\Delta}$	$\ GX_1\ _{\Omega_\Delta}$	$\ GX_2\ _{\Omega}$	$\ GX_1\ _{\Omega}$	MSE [dB]
M1	40	0.3	0.2	0.2	0.2	0.2	-46
M2	30	0.3	0.3	0.5	0.6	0.6	-37
M3	22	0.3	0.9	0.6	1.2	1.2	-33
M4	1	0.3	7.3	5.6	7.3	7.2	-30



(a) MSE for different SNR



(b) Threshold of the SVD for different SNR

Figure 5.12 – Inverse problem results at 1 GHz for non-approximated (dashed line) and linear-approximated simulated measurements (solid line) of the model $M1$ (see Table 5.1): (a) MSE as a function of the considered singular values for various SNR (100 (red), 50 (green), 20 (blue) [dB]); (b) considered singular value decomposition of the L operator (light grey triangles are below the numerical limit of the double precision floating numbers).

Chapter 5. Microwave Inverse Scattering Problem

results. For that purpose, we consider various background materials in order to emulate different norms (we here compute the ℓ_2 -norm) and therefore DNL. As reference, we use the fields computed with the first order Born approximation in the forward problem. We then compute the Mean Square Error (MSE) in dB between the scattered field of reference and the one computed at each probe using the full VIE solver [166]. The results are reported in Table 5.1. As expected, the smaller the norms, the lower the MSE. In other words, a small DNL leads to a more accurate field computation.

The "measurements" used in the inverse problem are actually the simulated forward responses. To ensure that the problem is not an "inverse crime" case [167], Gaussian white noise is injected in the simulated measurements, and is indicated as Signal-to-Noise Ratios (SNR). Moreover, the grids used for the forward problem and for the inverse problem do not match.

The MSE of the reconstructed Δ_χ , are plotted in Fig. 5.12a for the model *M1* (see Table 5.1). For the inverse scattering problem, the threshold used for the optimal number of singular values is set according to the noise Fig. 5.12b, in order to keep only the significant terms and therefore act on the noise reduction of our signal. The smaller the SNR, the less singular values are kept for the inverse scattering purpose.

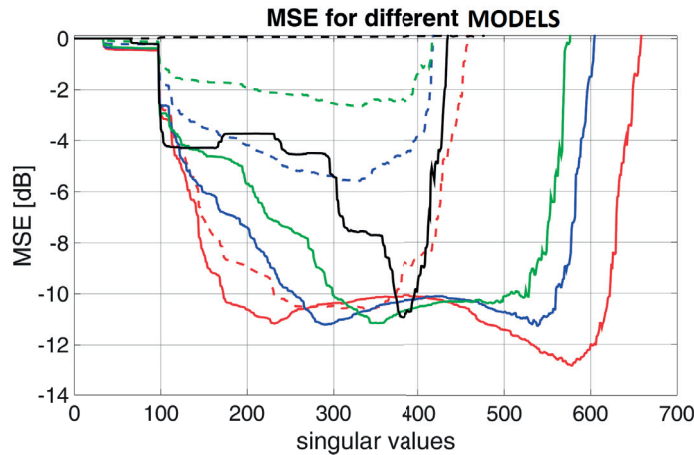


Figure 5.13 – Inverse problem results at 1 GHz for non-approximated (dashed line) and linear-approximated simulated measurements (solid line): Mean Square Error as a function of the considered singular values for various models (*M1* (red), *M2* (blue), *M3* (green) and *M4* (black), see Table 5.1) for a high SNR of 100 dB.

In the case of a high DNL (see Fig. 5.13), the inversion does not work for non-approximated simulated measurements (black dotted line) and is unstable with respect to noise when considering the first order Born approximation (black solid line). For a DNL smaller than unity the qualitative reconstruction is possible provided that a good threshold is used for the TSVD (green and blue lines). When the DNL is much smaller than unity (red line), for a reconstruction using between 250 and 380 singular values (when the dotted line and the solid line almost overlap), the reconstruction is even quantitative, as the complex value of

the contrast difference can be assessed. Moreover, the dMWI setting increases the range of validity of the first order Born approximation, as the DNL depends on the contrast and the considered volume.

Realistic Case

Next, a more realistic model has been considered (see Fig. 5.14) to highlight the potentialities of the proposed approach. It consists of a slice of the head ($\epsilon_r = [1; 69]$, $\sigma_r = [0; 2.5]$ S/m) obtained from [83], with a background medium of $\epsilon_b = 40$, $\sigma_b = 0.3$ S/m. The center of the stroke is positioned at (12, 24) mm and its radius is (18, 36) mm at times t_1 and t_2 . The grid resolution is $4 \times 4 \times 4$ mm³ for the reconstruction.

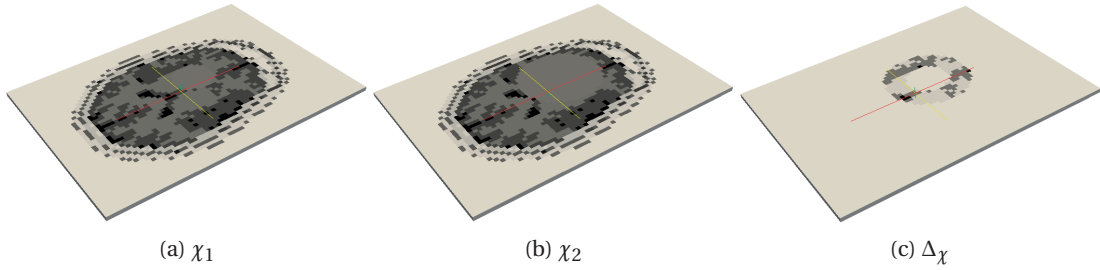


Figure 5.14 – Duke head model [83] at 1GHz. From left to right: domains of different values of the contrast function at times t_1 and t_2 , and the difference between the two times.

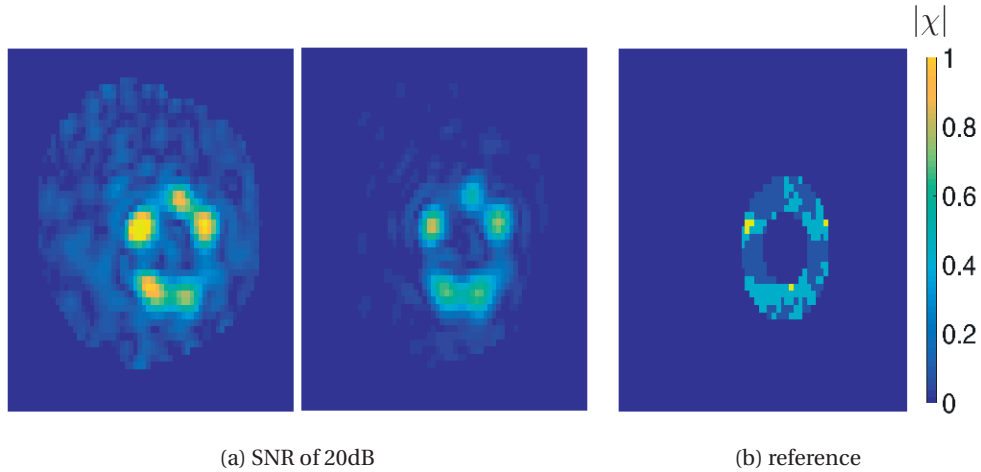


Figure 5.15 – Duke head model stroke detection. (a) Reconstruction using non-approximated simulated measurements (left) and approximated simulated measurements (right). (b) Normalized absolute value of the contrast difference reference.

The reconstruction shown in Fig. 5.15 has a high DNL for MWI ($\|GX_1\| = 1.1$ and $\|GX_2\| = 1.1$) but a DNL lower than unity in the case of dMWI ($\|GX_1\|_{\Omega_\Delta} = 0.6$ and $\|GX_2\|_{\Omega_\Delta} = 0.2$). For

a SNR of 20 dB we used for the reconstruction 400 singular values. In some parts of the brain the contrast according to the background medium can be significantly different. The reconstructions using Born-approximated data in the forward problem is less affected by the noise than when using the full VIE forward solver in the simulation. However, the absolute value of the contrast difference reconstruction is closer to the value of the actual difference, and this can be explained by the more realistic simulation of the measurements.

Summary

Test cases have been shown for simplified and realistic scenarios for dMWI for brain stroke monitoring. The expression for the DNL has been given for the differential scenario for several simplified and realistic models. The reconstruction of the stroke shown in Fig. 5.15 using the first order Born approximation is an example of a scenario where the classical MWI inverse scattering problem cannot be linearized whereas it can be in the dMWI case. The quality of the reconstructions of the differential contrast function has been quantified by computing the MSE. The DNL of the dMWI, and therefore the validity range of the first order Born approximation for brain stroke monitoring with dMWI, depends on three main factors for a given frequency: the contrast (χ) and the area (Ω_Δ) covered by the stroke between the two different times, and its position.

5.4.2 Numerical Experiments for Regularization of dMWI

First tests have been performed on a simplified 3D scenario on a grid of $100 \times 100 \times 1$ voxels of 2 mm side length (Fig. 5.10): a circular reference head of radius 7 cm, of $\epsilon_r = 48$, $\sigma = 0.4$ S/m, a small circular stroke of $\epsilon_r = 36$, $\sigma = 0.72$ S/m at t_1 of radius 2 cm, a bigger circular stroke at t_2 of radius 3 cm both with an offset of 1 cm and 2 cm in respectively the x and y directions, and with a matching medium surrounding the head of $\epsilon_r = 40$, $\sigma = 0.4$ S/m, in order to decrease the reflection of the incident field at the head interface. For this setup 32 antennas have been placed around the head, the incident field was set to 1 GHz and the SNR to 70 dB. The reconstruction has been performed on a grid of $50 \times 50 \times 1$ voxels of 4 mm side length using the TSVD regularization (5.21), the sparse optimization approach (5.23) and the TV regularization (5.26).

The value of the tolerance ϵ for both (5.23) and (5.26) is to be set with care above the noise level $\|\mathbf{n}\|_2$, as for the choice of the threshold in (5.21). To solve problems (5.23) and (5.26), we use CVX, a package for specifying and solving convex programs [161], [162].

The results of these three methods are compared in Fig. 5.16. In a first approximation, the scattered fields have been computed using the first order Born approximation in the forward problem (left column in Fig. 5.16). The right column presents the results when the exact forward problem has been solved using a full-wave VIE solver [166] in order to emulate more faithfully a realistic scenario.

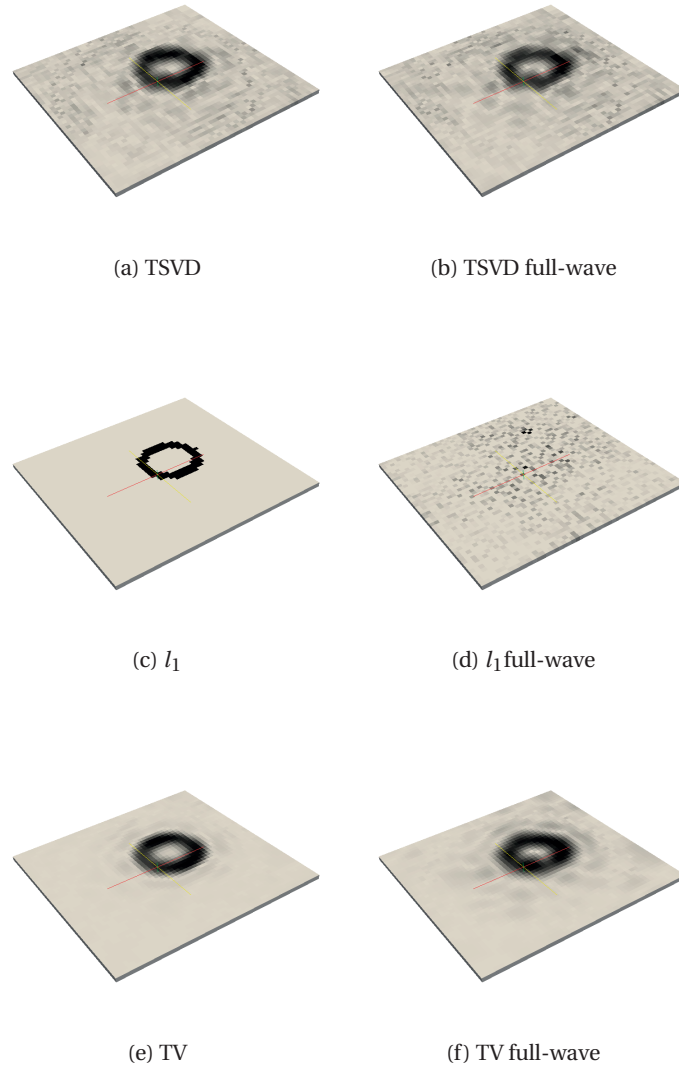


Figure 5.16 – Reconstructions using linearized forward problem (left) and using a full-wave VIE solver [166] (right).

The results of these first tests show that the TV regularization seems to work very well in both cases, better than the TSVD. The TV-norm provides a much better reconstruction than the l_1 -norm in the case of the full problem. It means that the TV-norm is more robust to a model difference. There is indeed a difference between the model to invert the problem (linear) and the model to generate the measured field (exact). The TV-norm is probably more robust because it works with a group of voxels (to compute the gradient) that are all affected by the same model error instead of considering the voxels individually.

Conclusion

Different regularization techniques have been compared in the framework of 3D differential microwave imaging. The study was very limited, however TV-norm regularization seems to give the best qualitative images in all cases. As for TSVD-regularization, it works reasonably well in both situations. On the contrary, l_1 regularization works very well if the forward problem is solved using the first order Born approximation while it seems to fail in the case of the full problem. Further investigation on this topic will be exposed in Section 5.5.3, in which reconstructions using experimental measurements will be compared to the ones using simulated measurements.

5.5 Differential Microwave Imaging Experiments

We have developed a 3D printed phantom [145] with liquid Triton X-100 based mixtures to mimic biological tissues [80, 146]. These phantoms are stable through time and transportable, and therefore can be reproduced and provided within several research groups using different imaging setups, in order to produce comparable results. This is not the case of more complex head phantoms [151] for which the realization involves more ingredients, which makes it more difficult to reproduce and more sensitive to time and temperature conditions.

We realized a 3D printed multilayered spherical structure to validate our numerical models. Such a multilayered spherical model can be solved analytically [147] and is representative. It can take into account all four layers potentially influencing the wave propagation into the head namely the Cerebrospinal Fluid (CSF), the cortical bone, fat and skin.

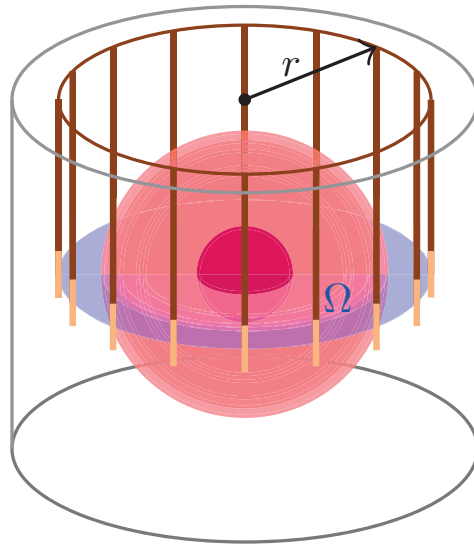
This part focuses on the influence of TSVD, l_1 and TV norm regularization techniques for dMWI based on both simulated and measured data.

5.5.1 Setup Configuration

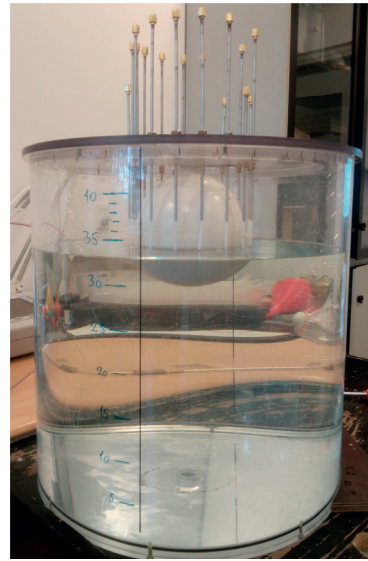
The multi-illumination configuration of the measurement setup consists of a cylindrical investigation domain Ω surrounded by emitting and measuring probes (see Fig. 5.17) placed on a circle c of radius 8 cm. The frequency of operation is 1 GHz. The target under investigation, here the head model or phantom (domain Ω), is sequentially illuminated by $P = 16$ incoming angles $\Theta_p = 22.5^\circ \times p$, with $p = 0, 1, \dots, 15$. The scattered field is then measured by $M = 16$ probes located on the same circle c , but with shifted angles $\Theta_p = 11.25^\circ + 22.5^\circ \times p$ (see Fig. 5.18).

5.5.2 Stroke Modeling and Tissue Characterization

The head model is the multilayered sphere described in Section 4.2.1. The core of the sphere is the brain with a radius of $r_1 = 43$ mm, the CSF, the cortical bone, the fat and the skin layers



(a) Setup schematic



(b) Picture of the measurement setup (side view)

Figure 5.17 – Measurement setup. Left; setup schematic, right; picture of the measurement setup.

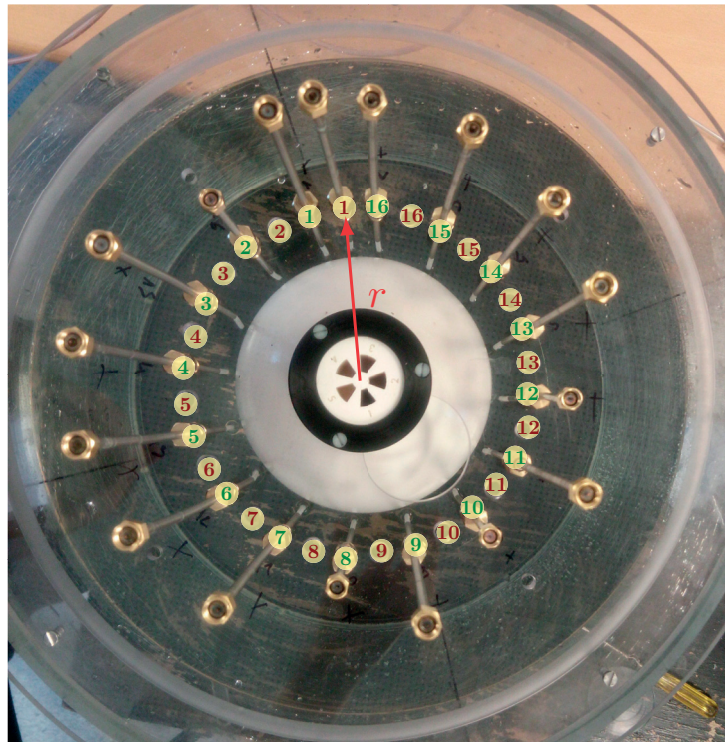


Figure 5.18 – Measurement setup probe positioning. The antenna positions for emission are numbered in red and the positions for the receiving probes are numbered in green.

Chapter 5. Microwave Inverse Scattering Problem

are, respectively, 3 mm, 7 mm, 4 mm and 4 mm thick (see Table 4.1). The radius of the total sphere is 7.1 cm, so the antennas are close to the sphere's surface. The matching medium is tap water. The stroke anomaly is inserted with a balloon catheter shown in Fig. 5.19. When the catheter is filled with 50 ml of liquid its cross section in the imaging plane has a diameter of 4 cm. The h-stroke (blood) mimicking Triton/water mixture is composed of 18 % Triton and 10 g/L of NaCl. The theoretical and measured dielectric properties of the tissue mimicking mixtures at 1 GHz are reported in Table 5.2.

Table 5.2 – Theoretical and measured dielectric properties at 1 GHz for the tissue mimicking mixtures.

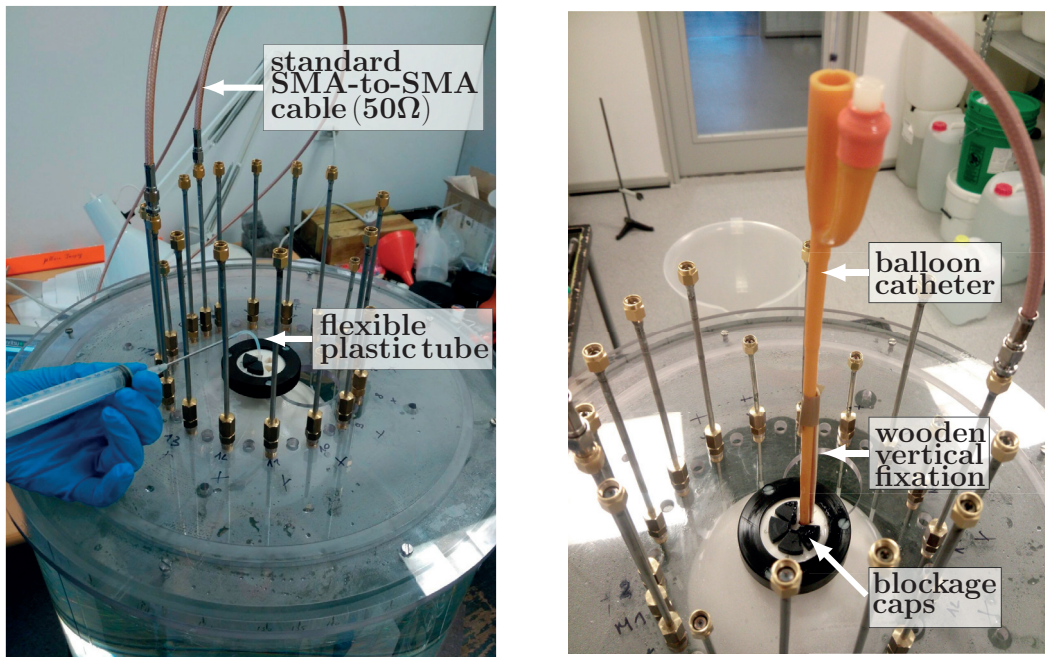
Tissue	ϵ_r (theory)	σ [S/m] (theory)	ϵ_r	σ [S/m]
Brain	48	0.88	47	0.70
CSF	68	2.46	67	2.37
Bone	12	0.15	13	0.27
Fat	5	0.05	6	0.07
Skin	46	0.88	45	0.68
Blood	61	1.58	62	1.56

The imaging consists of retrieving the differential contrast function Δ_{χ} . For that purpose, the simulation model is reduced to a slice that is located at the antenna's pin level. This imaging domain is discretized in a $41 \times 41 \times 1$ voxels grid resulting in a voxel side length of 4 mm in each direction (Fig. 5.20). The initial state (time t_1) is the head model, and the final state (time t_2) is when the balloon catheter simulating a haemorrhagic stroke is inserted for the measurements and placed as a 2 cm radius sphere in the middle of the model for the simulations. The background (water) permittivity was measured ($\epsilon_r = 69$, $\sigma = 0.28$ S/m) therefore the expected resolution lies between 9 mm ($\lambda/4$) and 18 mm ($\lambda/2$). Thus, the resolution of the voxel grid is sufficient to represent any details detectable by the measurement setup. Moreover, this background medium ensures that the DNL for the dMWI scenario is much smaller than 1 (here $\text{DNL} < 0.37$) for the used mixtures and therefore the first order Born approximation can be applied.

5.5.3 Regularization Techniques: Experimental Validation

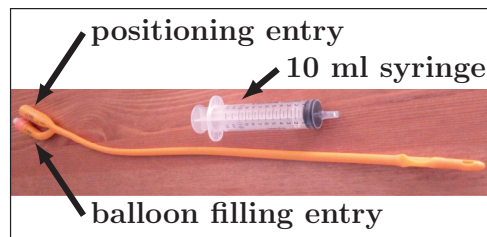
In this section the conclusions derived in Section 5.4.2 are further investigated for a specific scenario which is experimentally validated. The microwave inverse problem of (5.20) is composed of an operator L , differential scattered fields Δ_E , and a noise \mathbf{n} . For both simulation and measurement results, the operator L is formed using simulated measurements for the incident field, which are based on the simulated setup. The scattered fields Δ_E and noise \mathbf{n} are clearly different for the simulated and the measured results. Firstly, the simulation results are

5.5. Differential Microwave Imaging Experiments

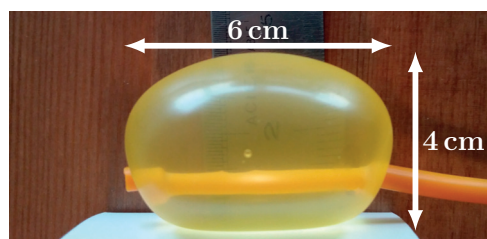


(a) Setup schematic

(b) Anomaly inclusion



(c) Empty balloon catheter



(d) Full balloon catheter

Figure 5.19 – Measurement setup; layer filling and stroke phantom.

discussed, then the measurements results are discussed and compared, which are compared to the predictions.

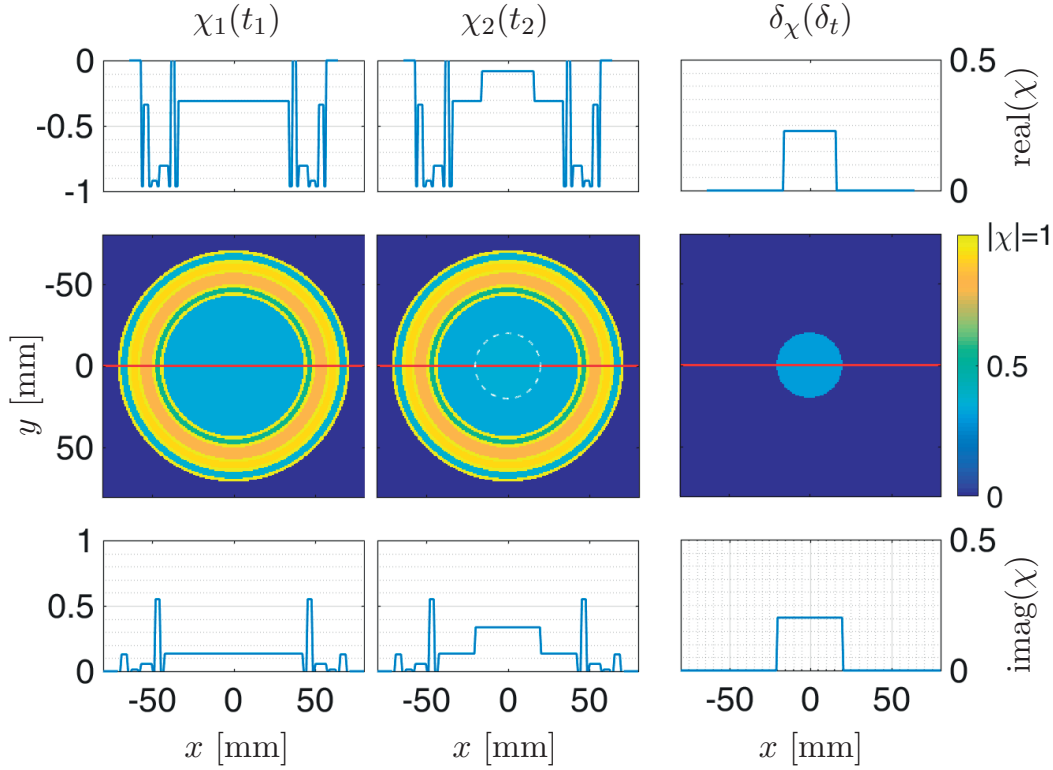


Figure 5.20 – Contrast function absolute value, with its real part (top) and imaginary part (bottom) at time t_1 (left), time t_2 (center), and their differential contrast Δ_χ (right).

Simulation Results

For the simulation results, both the scattered fields Δ_E and noise \mathbf{n} are simulated. The differential scattered fields are therefore the simulated measurements, and the noise is modeled as a Gaussian noise resulting in an SNR of 20 dB. The results using the investigated three different regularization schemes, are presented in Fig. 5.21.

The red circles represent the inner and outer shells of the head phantom, the white circle represents the circle c on which the antennas are placed and the black circle is the position of the inserted stroke at time t_2 . The images represent the absolute value of the reconstructed differential contrast function Δ_χ ; the theoretical results plotted in Fig. 5.20 are 0.3 inside the black circle and 0 elsewhere. For TSVD, following the L-curve method (the change of slope of the singular value spectrum) we kept the singular values σ_i greater than $\frac{\sigma_{max}}{210}$ (see Fig. 5.22 singular values up to opaque red limit). The value of the parameter ϵ in (5.23) resp. (5.26) should be chosen above the noise level $\|\mathbf{n}\|_2$ and the error induced by the linearization of the scattering operator. We use, as a starting point, for ϵ the error reached by the reconstruction done with TSVD, that is $\epsilon = \alpha \|L\Delta_\chi - \Delta_E\|_2$. For the performed simulations, the best results

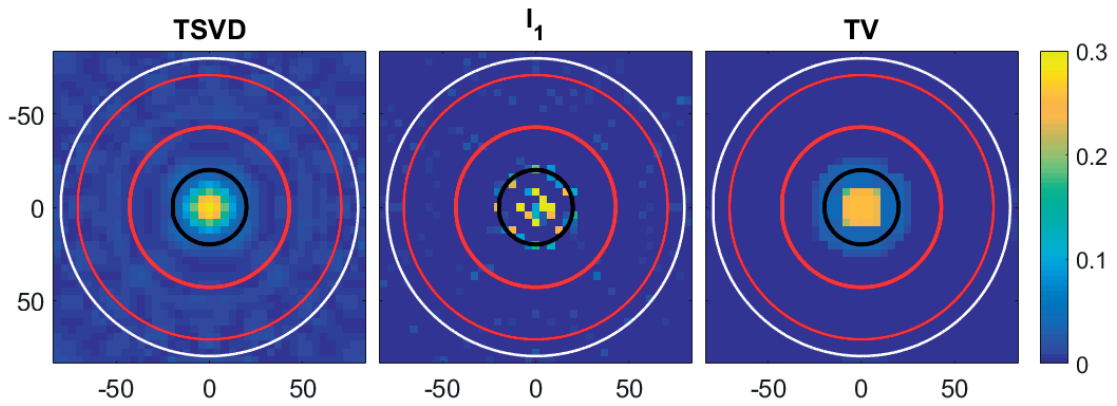


Figure 5.21 – Absolute value of the reconstructed $\Delta\chi$ based on TSVD (left), ℓ_1 -norm (center), and TV-norm (right) regularization schemes using simulated scattered fields as measurements.

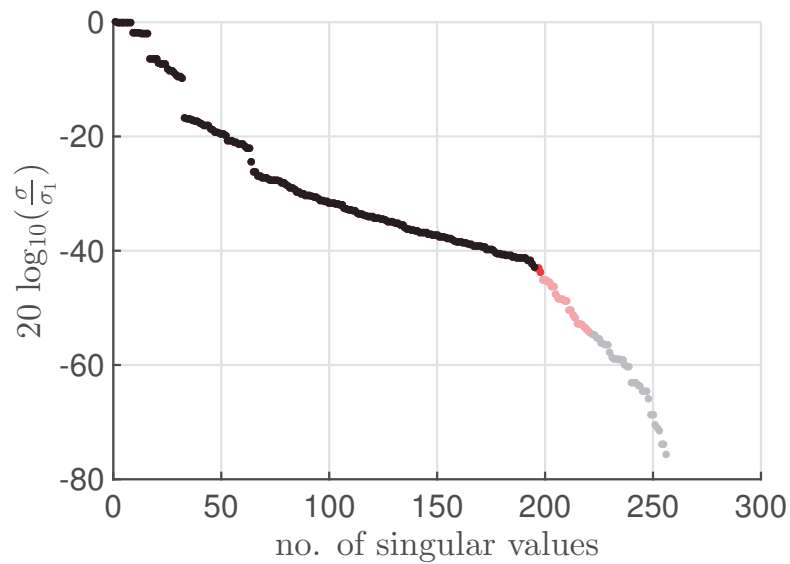


Figure 5.22 – Singular value distribution for the inverse scattering operator: considered singular values in opaque colors.

were obtained with $\alpha = 1.2$.

The results given by the TSVD are not too sensitive with respect to the singular value threshold, similar results are obtained for a threshold ranging from $\frac{\sigma_{max}}{180}$ to $\frac{\sigma_{max}}{645}$ (see Fig. 5.22 singular values range depicted in opaque and light red). The ℓ_1 -norm provides a sparse (pixel-wise) solution. The best recovery is obtained when applying the TV-norm as the region of permittivity change is well reconstructed.

Measurement Results

For the measurement results, the scattered fields are measured, and their difference is expressed by Δ_E . Clearly, these measurements are corrupted by noise. To estimate the nature of these unwanted perturbations, the measured scattered fields are compared to the simulated scattered fields. The results are depicted in Fig. 5.23, where the total scattered fields is depicted at 16 receiving antennas while the emitting antenna is placed between antennas #1 and #16. The total field at time t_1 (no stroke) is in solid lines, and at time t_2 (with stroke) in dashed lines. The simulations and measurements are depicted, respectively with red and blue lines.

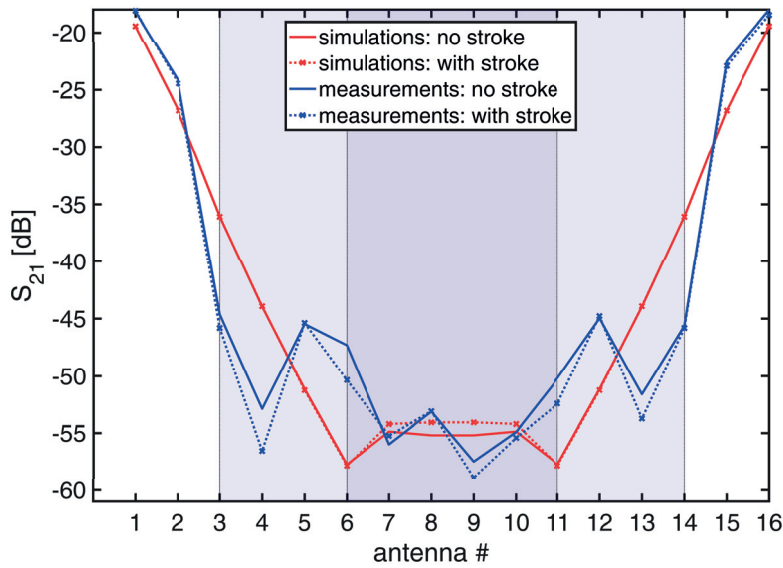


Figure 5.23 – Total scattered fields at 16 receiving antennas while the emitting antenna is placed between antennas #1 and #16. The total field at time t_1 (no stroke) is depicted in solid lines, and at time t_2 (with stroke) in dashed lines. The simulations and measurements are, respectively in red and blue.

From Fig. 5.23, we observe reasonable agreement between simulated and measured scattered fields, with the same symmetric shape. The overall shape is more stretched in the measurements. By stretched we mean here that the low values for simulations at the probes between #6 and #11 are observed in measurement for antennas between #4 and #13.

As we are here interested in the differential scattered field rather than the separate values of each measured fields, we also plot the comparison between the simulated and the measured differential scattered field (see Fig. 5.24), which is the difference between the solid line and dashed lines of Fig. 5.23.

In Fig. 5.24, the simulated differential scattered field (solid line) has a maximum absolute value at the antennas opposite to the emitting antenna, which means that the transmission is the key-point for the reconstruction. Indeed, the simulated S_{21} is more than 10 dB higher in transmission, compared to the ones in reflection. In both Fig. 5.23 and Fig. 5.24 the dark or light grey region represents, respectively, the antenna 6 to 12 opposite to the emitting probe. The simulations showed a significant change in the total field in the dark grey region. The

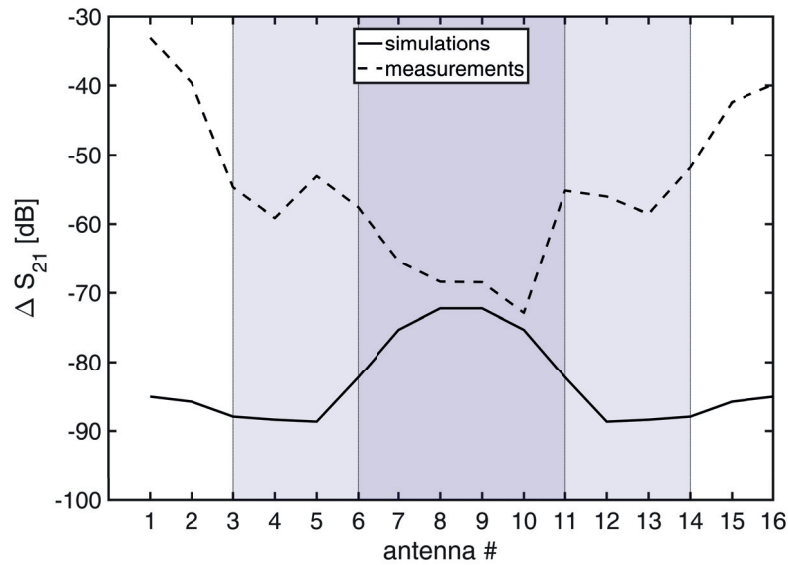


Figure 5.24 – Differential scattered fields at 16 receiving antennas while the emitting antenna is placed between antennas #1 and #16. The differential scattered field for simulations and measurements are depicted, respectively with solid and dashed lines.

measurements do not follow this trend and the differential scattered field is the highest at probes which are neighboring the emitting antenna. Our supposition is that the coupling between the emitting antenna and its direct neighbors is strong, and therefore any noise is amplified and results in a strong differential field, which does not reflect the contrast change we intend to image.

To minimize this unwanted noise, the strategy adopted here consists in considering only the opposite antennas. By doing so, we reduce the effects of the inevitable measurement uncertainties, like cable and antenna displacements. These artefacts are mainly visible in the reflected signal and captured by the antennas close to the emitting probe.

For both measurements and simulations, 10 out of 16 antennas are used for imaging. The results for simulations presented in Fig. 5.21 were already for 10 out of 16 antennas. Unlike for the reconstruction based on measured scattered fields, the reconstructions based on simulated scattered fields almost do not change, when considering up to only 6 opposite antennas. The reconstructions based on the measured differential fields and obtained using the investigated three different regularization schemes are presented in Fig. 5.25.

The reconstructions based on measurements show good agreement with the simulations (see Fig. 5.25). For TSVD we kept the singular values σ_i greater than $\frac{\sigma_{max}}{210}$ (see Fig. 5.22 singular values up to the opaque red limit). Unlike in the simulations, the choice of this threshold seems to be more sensitive. The tolerance used for both TV and ℓ_1 -norm regularizations is set around 10 percent above the error of the reconstruction done with a TSVD regularization. The best qualitative and quantitative reconstruction is obtained for the TV-norm regularization

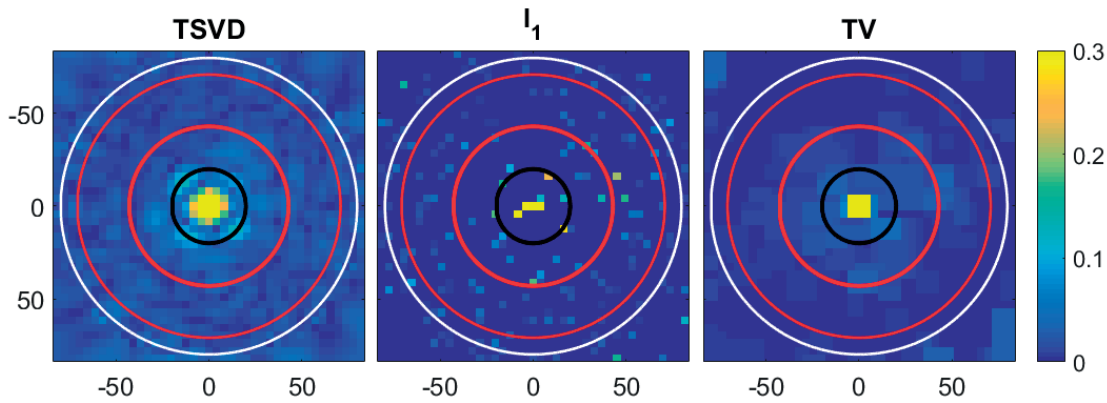


Figure 5.25 – Absolute value of the reconstructed $\Delta\chi$ based on TSVD (left), ℓ_1 -norm (center), and TV-norm (right) regularization schemes using measured scattered fields.

scheme, where again the signal in the background is close to zero and only the signal inside the targeted region has an amplitude change. The linear scattering operator is set with the a-priori information that the head geometry is known from simulations. This a-priori information does not dramatically change the shape of the reconstructions in both simulations and measurements qualitatively the same. However, the quantitative value is closer to the targeted one by using the simulated head model as a-priori information for the computed incident field. This could have an importance for differentiating haemorrhagic from ischaemic strokes. The reason why the detected stroke region is slightly smaller in measurements than in simulations could be explained by the fact that the maximal cross-section of the filled balloon catheter was 4 cm. However the effective diameter captured by the measuring monopoles is smaller than the center diameter of 4 cm.

5.6 Conclusion

The present work studied the performance of three different regularization schemes for dMWI of the head. The quantitative and qualitative results were compared for reconstruction using either simulated or measured scattered electric fields. The results showed similar behaviors for both simulations and measurements.

The multilayered 3D printed head phantom proved to be a good tool to assess by measurements the validity of dMWI for brain imaging applications and to compare inversion algorithms. Also, it experimentally confirms that electromagnetic waves around 1GHz can produce detectable signals created by an anomaly in the head.

6 Conclusions and Perspectives

For several decades, academic researchers have been interested in providing proofs towards the possibility of imaging biological tissues using the scattering of the electric field in the microwave range. The ever increasing computational power offers the possibility to solve larger EM problems. Possible applications have arisen in medical branches which suffer from a lack of practical solutions with existing imaging modalities. Detecting and imaging the evolution of the pathological state of a brain stroke with microwaves (MWI) could be a complementary approach to the existing imaging technologies (CT, MRI). The challenges and hopes for brain MWI were introduced in Chapter 2, and several industrial projects are getting more mature, leading towards clinical applications. However, several issues still need to be addressed to convince the medical community of the new capabilities and relevance of MWI. The actual gap between simulations and measurements needs to be bridged by improving both the direct and inverse solvers involved in MWI.

6.1 Thesis Summary

This thesis encompasses contributions for brain MWI on both the numerical and the experimental side.

Computational Contributions:

- *Direct Solver*: The higher the frequency, the wider the spectrum of the VIE operator is spread. For brain applications, the head tissue is highly heterogeneous and lossy. These two features justify the complexity of modeling the electromagnetic fields for brain MWI applications. In this thesis, a VIE formulation was investigated for brain MWI and large scale problems (published in [166]). The problem was approached from the point of view of different grid sizes (Multi-Grid Solver), by going back and forth between finer and coarser grids to solve the residual problem with the direct solver and then projecting its solution on finer grids. The latter strategy provided promising results which were presented in Section 3.3.2.

- *Transmitted Power and Layer Influence*: For imaging, a maximum of the incident power must be transmitted into the brain tissue so that the anomaly (a brain stroke) can scatter back an electromagnetic field that is detectable by the receiving probes. The first step is to choose accordingly the matching medium so that the coupling at the head interface is optimal, which means that the reflection towards the emitting antenna is minimized. In a second step it is important to quantify the influence of the layers in order to predict the attenuation in the head tissues. For that purpose, a multilayered spherical model was proposed in Section 4.1. This simple though representative model enables to include most significant phenomenon and provides meaningful interpretations (published in [153, 168]).
- *Microwave Inverse Scattering*: The non-linearity and the ill-posedness are the two main issues when performing MWI. Both issues are intrinsically linked to the volume of the body to be imaged. In this thesis, the DNL was derived and quantified for dMWI of brain stroke detection and monitoring in order to assess when the first order Born approximation can be applied. dMWI provides spatially sparse images as it reconstructs the contrast change in between two measurements, which is supposed to be small. It was demonstrated that the DNL is, under certain conditions, "small enough" to apply the first order Born approximation (presented in Section 5.2 and in Section 5.4.1). To tackle the ill-posedness of the inverse imaging problems, three regularization techniques (presented in Section 5.4.1 and Section 5.4.2) were compared. The advantages and drawbacks of each regularization technique were analyzed for specific problems in the framework of dMWI (published in [169–172]).

Experimental Contributions:

- *3D Printed Head Phantom*: A head phantom was designed and realized using the 3D printing technology and presented in Section 4.2.1. It is based on a multilayered spherical model, which allows the analytical solution of the scattering problem. The 3D printed structure is filled with tissue mimicking Triton-based liquids. This methodology permits the conception of reproducible and relatively low cost phantoms which can be shared among institutions to permit the comparison of both measurement setups and inverse scattering algorithms (published in [153, 168, 172]). The analytical treatment of the scattering phenomenon allows making exact comparisons without depending on the convergence of iterative solvers which are still not fully available and verified for all possible matching media and frequencies.
- *Stroke modeling and dMWI*: The experimental validation of inverse scattering algorithms was performed with a stroke phantom made with a balloon catheter and a Triton-based blood mimicking mixture (presented in Section 5.5). The experimental validation confirms the conclusions found for different regularization schemes and the possibility to detect brain strokes (published in [172]).

6.2 Perspectives

The computational and experimental tools proposed in this thesis are meant to facilitate further advancements towards the clinical applications of brain MWI. Nonetheless, these results call for further development and there are open issues which were not addressed in this thesis.

More Efficient Direct Solvers: This is a never ending perspective as there is always a need to solve larger problems with high accuracy. Especially for microwave biomedical applications, computing 3D volumes is mandatory as it gives an accurate field distribution. The IE formulations are attractive as they do not introduce physically non-existing boundaries. For MWI applications, the ultimate goal would be to use the VIE formulation for the human body and combine it with the SIE formulation for modeling the setup. Indeed, solving the Maxwell equations for the imaging setup can be based on SIE formulations which are a mature and very efficient technique, and solving the human body on voxels offers a flexible discretization for very inhomogeneous parts of the body, such as the head. With fast and accurate methods the development of personalized medicine by optimizing the devices to patients is achievable. Nonetheless, the efficiency and accuracy of such solvers are still to be assessed for very inhomogeneous and lossy media. Multigrid-based solvers seem to adapt well to this challenging task as seen in Chapter 2. However, this study is a first step that should be implemented in a more efficient and optimized manner, such that it could be useful to the community.

Accurate Dielectric Properties of Tissues in the Microwave Range: An important open issue in the MWI community is the access to accurate body tissue dielectric parameters. The values of the complex permittivity of human tissues are mainly taken from studies made by Gabriel et al. [143]. Even though these studies were made two decades ago, they are very useful and represent a convenient database. However, today, new dielectric measurements do exist [173]. Also, the community relies on a few ways to easily access the outcome of this analysis. The mostly used one is probably an open access website [142] which allows the download in convenient formats of a large number of biological tissues. A concrete example of this issue is the stroke modeling in this thesis. H-stroke (haemorrhagic) was modeled using the blood dielectric permittivities. It is clear that this is an approximation. Indeed, the part of the brain subject to an h-stroke does not disappear, but a rather more complex process takes place, resulting in an increased proportion of the blood quantity in this part of the brain. The same observations can be derived for the i-stroke (ischaemic) modeling. In [78] a trade-off was found by choosing the mean value between the blood and the baseline (tissue in the region of the stroke). Also, no available modeling for the subarachnoid h-stroke (when the region between the skull and the brain is affected) could be found in the literature. Thus, the accurate stroke modeling is still today an actual research issue. These approximations could induce minor differences in the modeling and the imaging outcome, however, an accurate standard would be useful for comparing results among researchers and industrial partners.

Chapter 6. Conclusions and Perspectives

Complex and Inhomogeneous Testing Structures Specialized for MWI Setups: For comparing simulation results to measurements, often, homogeneous shapes are used. Most of the time these comparisons give very similar results. However, as seen in Chapter 2, good convergence of the iterative solvers for homogeneous and low contrast cases does not guarantee that the solution provided by iterative solvers for complex and highly inhomogeneous structures will be accurate. The residual error of the solution of the iterative solver might give a solution that does not reflect the physical reality. To ensure that the measurements are well simulated by the EM solvers, one solution would be to construct a test phantom with multiple cavities of different sizes and shapes, filled with liquids whose dielectric permittivities are in the range of dielectric permittivities of the tissues present in the portion of the body which is imaged. This phantom does not have to be anatomically precise, as the goal is to test the correlation between the measurements and the simulated data on a known phantom, as it is usually done using homogeneous spheres and cylinders.

Stable and Low Cost Head Phantoms Specialized for MWI Applications: The 3D printed multilayered spherical phantom is a first step towards reproducible solutions (3D printed flexible cavities) which can be used to compare the performance of stroke detection and imaging algorithms, for different sizes and types of stroke. The first improvement would be to build the stroke cavity in a flexible material which can be fixed to the phantom in a precise location, which is not centered. As a later step, anthropomorphic phantoms can be developed using the same methodology, namely 3D printing and Triton-based mixtures. The MRI community [145, 174] provides the CAD for 3D printed anthropomorphic head phantoms. However, these models need to be adapted for MWI applications, for which the operating frequency is higher and therefore the wavelength is shorter. The integration of additional layers such as the ones used for the multilayered spherical head model of this thesis is necessary. These models could have flexible cavities for anatomically more faithful stroke insertions, and, of course could be used for both brain MWI and brain dMWI scenarios. Further work on this topic would be to test the same inversion schemes on several measurement setups and therefore being able to compare their influence on the image quality. Furthermore, more complex inversion schemes have to be tested with a higher number of non-centered anomalies.

A Spherical Wave Expansion: Scattering Framework and Mathematical Derivation

The four vectorial Maxwell equations for a source free, linear and isotropic medium, in harmonic regime (with a temporal evolution defined as $e^{+j\omega t}$, and ω the pulsation) are:

$$\nabla \times \begin{Bmatrix} \mathbf{E} \\ \mathbf{H} \end{Bmatrix} = \mp jk \begin{Bmatrix} \eta \\ \frac{1}{\eta} \end{Bmatrix} \begin{Bmatrix} \mathbf{H} \\ \mathbf{E} \end{Bmatrix} \quad \text{with:} \quad \eta = \sqrt{\frac{\mu}{\epsilon}} \quad (\text{A.1a})$$

$$\nabla \cdot \begin{Bmatrix} \mathbf{E} \\ \mathbf{H} \end{Bmatrix} = 0 \quad (\text{A.1b})$$

η is the intrinsic impedance of the medium. Taking the curl of the equation (A.1a) and substituting $\nabla \times \begin{Bmatrix} \mathbf{H} \\ \mathbf{E} \end{Bmatrix}$ by the right part of (A.1a), the system of equations become:

$$\nabla \times \left(\nabla \times \begin{Bmatrix} \mathbf{E} \\ \mathbf{H} \end{Bmatrix} \right) = k^2 \begin{Bmatrix} \mathbf{E} \\ \mathbf{H} \end{Bmatrix} \quad (\text{A.2})$$

With the vector identity $\nabla \times (\nabla \times \bullet) = \nabla(\nabla \cdot \bullet) - \Delta \bullet$ and as the divergence of the fields is null (see (A.1b)) the wave equation transforms into the vector Helmholtz equation ($\Delta = \nabla^2$ being the Laplacian):

$$\Delta \begin{Bmatrix} \mathbf{E} \\ \mathbf{H} \end{Bmatrix} + k^2 \begin{Bmatrix} \mathbf{E} \\ \mathbf{H} \end{Bmatrix} = \mathbf{0} \quad (\text{A.3})$$

Appendix A. Spherical Wave Expansion: Scattering Framework and Mathematical Derivation

Solution of the Wave Equation

The wave equation is a linear partial differential equation (PDE) called the vectorial Helmholtz equation. One classical approach of solving PDEs is to reduce them to a system of ordinary differential equations (ODEs) by means of the separation of variables. This technique, instead of searching for the global solution, assumes that the solution can be written as a product of terms each depending on a single parameter which solves the equation and satisfies the boundary conditions. Here we propose to solve the scalar Helmholtz equation first and use its solution for solving the vectorial Helmholtz equation.

The scalar Helmholtz equation is:

$$\Delta\psi + k^2\psi = 0 \quad (\text{A.4})$$

with ψ being a scalar wave function. The spherical coordinate system of Fig. A.1 is used, and therefore also the expression of the Laplacian in spherical coordinates. As a result, the scalar wave equation is expressed as:

$$\frac{1}{r^2} \frac{\partial}{\partial r} \left(r^2 \frac{\partial}{\partial r} \psi \right) + \frac{1}{r^2 \sin \theta} \frac{\partial}{\partial \theta} \left(\sin \theta \frac{\partial}{\partial \theta} \psi \right) + \frac{1}{r^2 \sin^2 \theta} \frac{\partial^2}{\partial \phi^2} \psi + k^2 \psi = 0 \quad (\text{A.5})$$

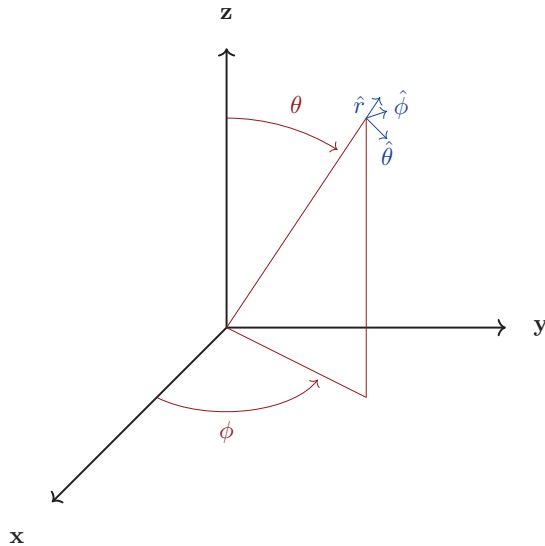


Figure A.1 – Definition of the spherical coordinate system

With the ansatz $\psi(r, \theta, \phi) = R(r)\Theta(\theta)\Psi(\psi)$, $r \geq 0$, $\theta \in [0, \pi]$, $\psi \in [0, 2\pi]$, and multiplying (A.5)

by $\frac{r^2}{R\Theta\Phi}$ we obtain:

$$\underbrace{\frac{1}{R} \frac{\partial}{\partial r} \left(r^2 \frac{\partial}{\partial r} R \right) k^2 r^2}_{\text{radial part}} + \underbrace{\frac{1}{\Theta \sin \theta} \frac{\partial}{\partial \theta} \left(\sin \theta \frac{\partial}{\partial \theta} \Theta \right) + \frac{1}{\Phi \sin^2 \theta} \frac{\partial^2}{\partial \phi^2} \Phi}_{\text{angular part}} = 0 \quad (\text{A.6})$$

The radial and the angular part being distinct they can be treated separately for simplicity as one appears as a constant in the solution of the other. First, we solve the equation for the angular part. We multiply (A.6) by $\Phi \sin^2 \theta$ introducing a constant m :

$$\frac{d^2 \Phi}{d\phi^2} + m^2 \Phi = 0 \quad (\text{A.7})$$

The solutions are circular functions of the form:

$$f_m^\sigma(\phi) = \begin{cases} \sin(m\phi), & \text{if } \sigma = e \\ \cos(m\phi), & \text{if } \sigma = o \end{cases} \quad (\text{A.8})$$

with m defined as a non-negative integer ($m = 0, 1, 2, \dots$) as the solutions must be the same for ϕ and $\phi + 2\pi$. Moving to the θ -dependent solution, we replace in the radial part of equation (A.6):

$$\frac{1}{\Theta \sin \theta} \frac{d}{d\theta} \left(\frac{1}{\sin \theta} \frac{d\Theta}{d\theta} \right) - \frac{m^2}{\sin^2 \theta} = -l(l+1) \quad (\text{A.9})$$

The constant l is defined like this for reasons that will become clear later. With the change of variable $z = \cos \theta$ and defining $\Theta_z(\cos \theta) = \Theta(\theta)$ the equation (A.9) multiplied by Θ becomes:

$$(1-z^2) \frac{d^2 \Theta_z}{dz^2} - 2z \frac{d\Theta_z}{dz} + \Theta_z \left(n(n+1) - \frac{m^2}{1-z^2} \right) = 0 \quad \text{with} \quad C_1 = n(n+1) \quad , \quad C_2 = m^2 \quad (\text{A.10})$$

The solution of equation (A.10) are the Legendre polynomial of the first kind P_n^m with n and m

Appendix A. Spherical Wave Expansion: Scattering Framework and Mathematical Derivation

natural integers:

$$P_n^m = (1 - z^2)^{\frac{m}{2}} \frac{d^m}{dz^m} P_n(z) \quad \text{and} \quad P_n(z) = \frac{1}{2^n n!} \frac{d^n}{dz^n} (z^2 - 1)^n \quad (\text{A.11})$$

Two important pieces of information are that these functions have regular singularities at $z = \pm 1, \pm \infty$ and that $P_n^{m>n} = 0$.

Moving to the solution of the radial part, substituting (A.9) into (A.6) and multiplying by R we obtain:

$$r^2 \frac{d^2 R}{dr^2} + 2r \frac{dR}{dr} + R(k^2 r^2 - l(l+1)) = 0 \quad (\text{A.12})$$

The solution are the spherical Bessel functions of order n positive (there are solutions for n being a negative integer, however we do not need them here). There exists several notations, here we will use these Bessel functions and combinations of it, as they can also be solutions of the aforementioned differential equation (A.12):

- $j_n(z)$: Spherical Bessel functions of the 1st kind and order n .
- $y_n(z)$: Spherical Bessel functions of the 2nd kind and order n .
- $h_n^{(1)}(z) = j_n(z) + jy_n(z)$: Spherical Hankel functions of the 1st kind and order n or alternatively Spherical Bessel functions of the 3th kind and order n .
- $h_n^{(2)}(z) = j_n(z) - jy_n(z)$: Spherical Hankel functions of the 2nd kind and order n or alternatively Spherical Bessel functions of the 4th kind and order n .

As the energy of the wave has to be finite at the origin and has a spherical propagation structure towards infinity, only the $j_n(z)$ fulfill the first requirement and $h_n^{(2)}(z)$ the second.

This is explained in [175] by introducing the concept of Wilcox spheres (see Fig. A.2).

For compactness we define $Z_n^1(z) = j_n(z)$ and $Z_n^4(z) = h_n^{(2)}(z)$ (based on the Bessel naming).

The solution Ψ of the scalar Helmholtz equation (A.4) in spherical coordinates is therefore a

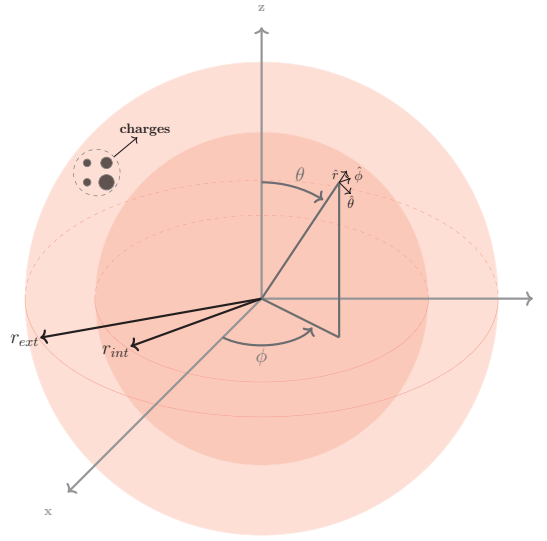


Figure A.2 – Wilcox spheres

superposition of those solutions of r -, θ - an ϕ - dependent differential equations:

$$\Psi(r, \theta, \phi) = \sum_{n=1}^{+\infty} \sum_{m=0}^n \sum_{s=\{1,4\}} \sum_{\sigma=\{e,o\}} \alpha_{mn}^{\sigma s} \Psi_{mn}^{\sigma s}(r, \theta, \phi) \quad (\text{A.13})$$

with $\Psi_{mn}^{\sigma s}(r, \theta, \phi) = Z_n^s(kr) P_n^m(\cos\theta) f_m^\sigma(\phi)$.

From (A.13), the vectorial solution to the Helmholtz equation can be found. First, vector spherical harmonics are defined as:

$$\mathbf{M}_{mn}^{\sigma s} = \nabla \times (\Psi_{mn}^{\sigma s}(r, \theta, \phi) \vec{r}) \quad (\text{A.14})$$

$$\mathbf{N}_{mn}^{\sigma s} = \frac{1}{k} \nabla \times \nabla \times (\Psi_{mn}^{\sigma s}(r, \theta, \phi) \vec{r}) \quad (\text{A.15})$$

$$\mathbf{L}_{mn}^{\sigma s} = \frac{1}{k} \nabla \Psi_{mn}^{\sigma s}(r, \theta, \phi) \quad (\text{A.16})$$

with $n = 1, 2, \dots, +\infty$, $m = 0, 1, 2, \dots, n$, $\sigma \in e, o$ and $s \in 1, 4$. If no source is present inside the spheres, only $\mathbf{M}_{mn}^{\sigma s}$ and $\mathbf{N}_{mn}^{\sigma s}$ are relevant and the fields are derived as:

$$\begin{Bmatrix} \mathbf{E} \\ \mathbf{H} \end{Bmatrix} = \begin{Bmatrix} 1 \\ j \\ \eta \end{Bmatrix} \left(\sum_{n=1}^{+\infty} \sum_{m=0}^n \sum_{s=\{1,4\}} \sum_{\sigma=\{e,o\}} \alpha_{mn}^{\sigma s} \begin{Bmatrix} \mathbf{M}_{mn}^{\sigma s} \\ \mathbf{N}_{mn}^{\sigma s} \end{Bmatrix} + \sum_{n=1}^{+\infty} \sum_{m=0}^n \sum_{s=\{1,4\}} \sum_{\sigma=\{e,o\}} \beta_{mn}^{\sigma s} \begin{Bmatrix} \mathbf{N}_{mn}^{\sigma s} \\ \mathbf{M}_{mn}^{\sigma s} \end{Bmatrix} \right) \quad (\text{A.17})$$

Appendix A. Spherical Wave Expansion: Scattering Framework and Mathematical Derivation

The coefficients $\alpha_{mn}^{\sigma s}$ and $\beta_{mn}^{\sigma s}$ contain all the information about the wave scattering. Finding the fields \mathbf{E} and \mathbf{H} means finding the coefficients $\alpha_{mn}^{\sigma s}$ and $\beta_{mn}^{\sigma s}$ which fulfill the boundary conditions for all the shells [147].

B 3D Printed Phantom: Geometries, Waterproofing and Gluing Tests

Before printing the final head phantom, we performed tests on a smaller prototype to test the critical aspects, namely waterproofing and gluing. The first prototype was manufactured with a 3D printer using Selective laser sintering (SLS) technique in PA2200. With the SLS technique it was impossible to print the whole spheres at once, but we had to split each sphere into two hemispheres, that will later be glued. Both the waterproofing and the filling mechanism (test if the liquid can transit smoothly) are tested on the small prototype depicted in Fig. B.1.

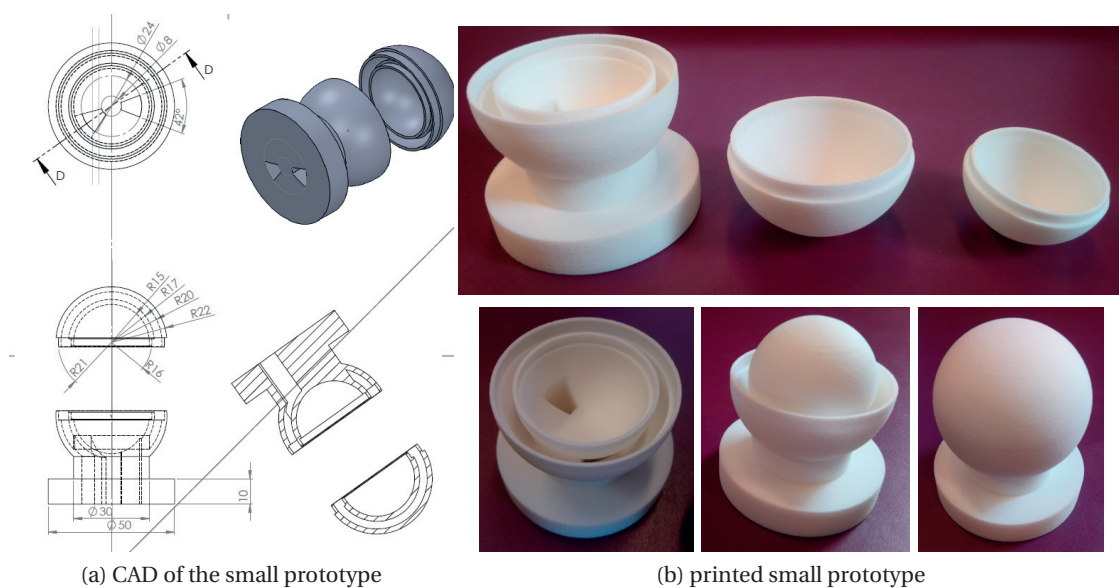


Figure B.1 – Small multilayered sphere prototype: (a) CAD details; (b) mounting pictures.

As TritonX100 is a detergent, an important test is to see if the glue (for example "Rapid Gel", GEISLICH which can easily be found in Switzerland) is compatible. This brand caught our attention as it explicitly sells compatibility to chemicals, cleaning products, humidity, salts and acids. It is also resistant to a wide set of temperatures, ranging from -60°C to $+80^{\circ}\text{C}$, which can be useful for building prototypes for applications such as hypothermia [176].

Appendix B. 3D Printed Phantom: Geometries, Waterproofing and Gluing Tests

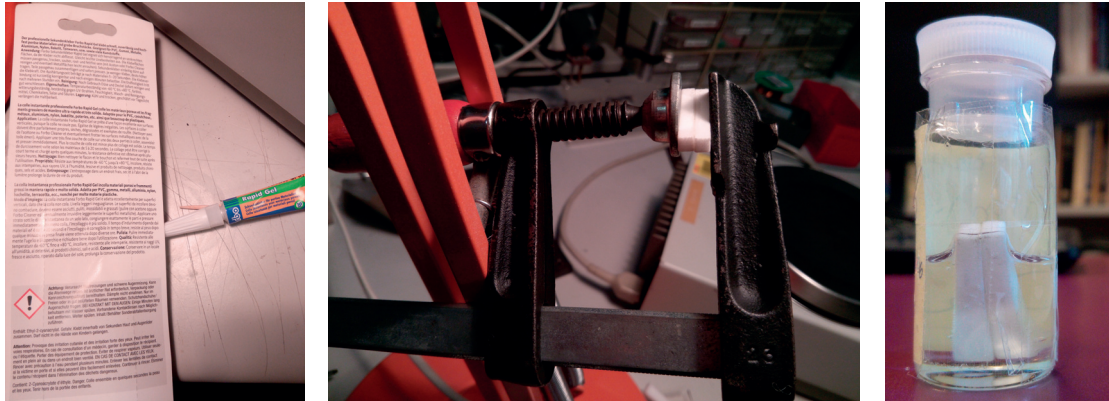


Figure B.2 – Glue tests steps

Test steps:

1. Weight PA2200 before gluing = 0.83g
2. Gluing the two part of PA2200 and waiting 2h
3. Weight PA2200 after gluing : 0.86g
4. immerse glued PA2200 in TritonX100 for 15 hours
5. Weight glued PA2200 after removing it from TritonX100 solution and cleaning: 0.86g

Conclusions: The glue is intact after the immersion (the two parts are still well glued together). However when we have put the TritonX100 inside of the spheres, the level has diminished. Probably absorbed by the porous material. To avoid the absorption of the material we decided to change to the Fused Deposition Modeling technology with white ABS (Acrylonitrile butadiene styrene) for the plastic, which can be made completely waterproof. The waterproofing process implies a "smoothing station" and the product used is SSF01P from MICROCARE. The product is heated inside the "smoothing station" where the 3D printed prototype is placed. The hot gas attacks the surface of the ABS, and after a few seconds (8-10 sec) the prototype is removed. The geometry of the final prototype is shown in B.3.

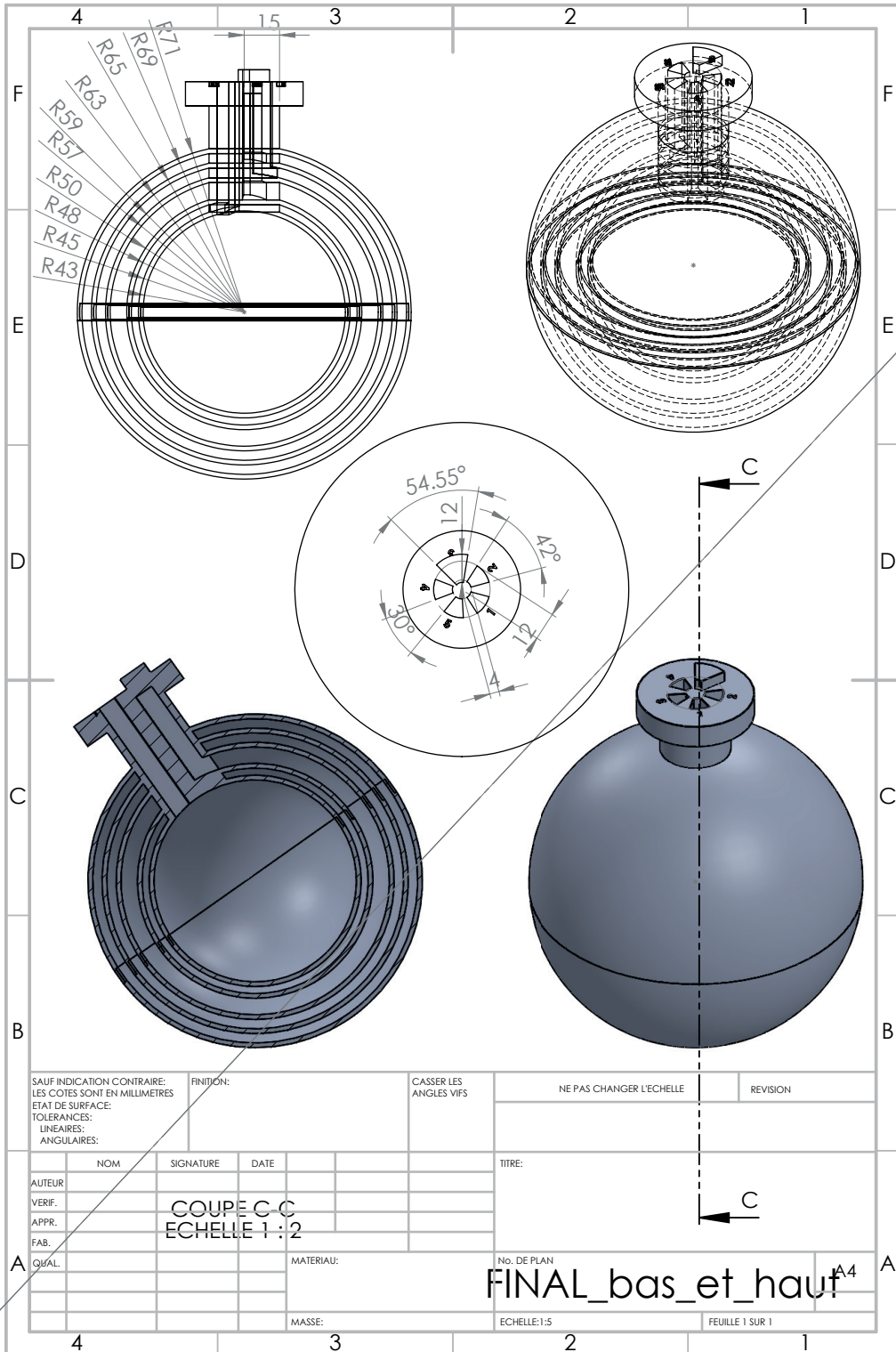


Figure B.3 – CAD of the multilayered sphere prototype

Bibliography

- [1] E. J. Benjamin, M. J. Blaha, S. E. Chiuve, M. Cushman, S. R. Das, R. Deo, S. D. de Ferranti, J. Floyd, M. Fornage, C. Gillespie, C. R. Isasi, M. C. Jiménez, L. C. Jordan, S. E. Judd, D. Lackland, J. H. Lichtman, L. Lisabeth, S. Liu, C. T. Longenecker, R. H. Mackey, K. Matsushita, D. Mozaffarian, M. E. Mussolino, K. Nasir, R. W. Neumar, L. Palaniappan, D. K. Pandey, R. R. Thiagarajan, M. J. Reeves, M. Ritchey, C. J. Rodriguez, G. A. Roth, W. D. Rosamond, C. Sasson, A. Towfighi, C. W. Tsao, M. B. Turner, S. S. Virani, J. H. Voeks, J. Z. Willey, J. T. Wilkins, J. H. Wu, H. M. Alger, S. S. Wong, and P. Muntner, “Heart disease and stroke statistics—2017 update: A report from the American heart association,” *Circulation*, 2017. [Online]. Available: <http://circ.ahajournals.org/content/early/2017/01/25/CIR.0000000000000485>
- [2] J. Redon, M. H. Olsen, R. S. Cooper, O. Zurriaga, M. A. Martinez-Beneito, S. Laurent, R. Cifkova, A. Coca, and G. Mancia, “Stroke mortality and trends from 1990 to 2006 in 39 countries from Europe and Central Asia: implications for control of high blood pressure,” *European Heart Journal*, vol. 32, no. 11, pp. 1424–1431, 2011. [Online]. Available: <http://dx.doi.org/10.1093/eurheartj/ehr045>
- [3] J. Olesen, M. G. Baker, T. Freund, M. di Luca, J. Mendlewicz, I. Ragan, and M. Westphal, “Consensus document on European brain research,” *Journal of Neurology, Neurosurgery & Psychiatry*, vol. 77, no. suppl 1, pp. i1–i49, 2006. [Online]. Available: http://jnnp.bmj.com/content/77/suppl_1/i1
- [4] M. Di Luca, M. Baker, R. Corradetti, H. Kettenmann, J. Mendlewicz, J. Olesen, I. Ragan, and M. Westphal, “Consensus document on European brain research,” *European Journal of Neuroscience*, vol. 33, no. 5, pp. 768–818, 2011. [Online]. Available: <http://dx.doi.org/10.1111/j.1460-9568.2010.07596.x>
- [5] T. Kjellström, B. Norrving, and A. Shatchkute, “Helsingborg declaration 2006 on European stroke strategies,” *Cerebrovasc Dis.*, pp. 231–241, 2007.
- [6] “Prevention of disabling and fatal strokes by successful carotid endarterectomy in patients without recent neurological symptoms: randomised controlled trial,” *The Lancet*, vol. 363, no. 9420, pp. 1491 – 1502, 2004. [Online]. Available: <http://www.sciencedirect.com/science/article/pii/S0140673604161461>

Bibliography

- [7] P. M. Meyers, H. C. Schumacher, E. S. Connolly, E. J. Heyer, W. A. Gray, and R. T. Higashida, "Current status of endovascular stroke treatment," *Circulation*, vol. 123, no. 22, pp. 2591–2601, 2011. [Online]. Available: <http://circ.ahajournals.org/content/123/22/2591>
- [8] W. Hacke, M. Kaste, E. Bluhmki, M. Brozman, A. Dávalos, D. Guidetti, V. Larrue, K. R. Lees, Z. Medeghri, T. Machnig, D. Schneider, R. von Kummer, N. Wahlgren, and D. Toni, "Thrombolysis with alteplase 3 to 4.5 hours after acute ischemic stroke," *New England Journal of Medicine*, vol. 359, no. 13, pp. 1317–1329, 2008, PMID: 18815396. [Online]. Available: <http://dx.doi.org/10.1056/NEJMoa0804656>
- [9] "onhealth," https://www.onhealth.com/content/1/stroke_signs_causes, accessed: 2018-01-21.
- [10] B. Norrving, "The 2006 Helsingborg consensus conference on European stroke strategies," *International Journal of Stroke*, vol. 2, no. 2, pp. 139–143, 2007. [Online]. Available: <http://dx.doi.org/10.1111/j.1747-4949.2007.00109.x>
- [11] L. E. Larsen and J. H. Jacobi, "Microwave scattering parameter imagery of an isolated canine kidney," *Medical Physics*, vol. 6, no. 5, pp. 394–403, 1979. [Online]. Available: <http://dx.doi.org/10.1118/1.594595>
- [12] J. H. Jacobi, L. E. Larsen, and C. T. Hast, "Water-immersed microwave antennas and their application to microwave interrogation of biological targets," *IEEE Transactions on Microwave Theory and Techniques*, vol. 27, no. 1, pp. 70–78, Jan 1979.
- [13] J. C. Bolomey and L. Jofre, "Three decades of active microwave imaging achievements, difficulties and future challenges," in *2010 IEEE International Conference on Wireless Information Technology and Systems*, Aug 2010, pp. 1–4.
- [14] M. Pastorino, *Microwave Imaging*. John Wiley & Sons, Inc, 2010.
- [15] M. Hawley, A. Broquetas, L. Jofre, J. Bolomey, and G. Gaboriaud, "Microwave imaging of tissue blood content changes," *Journal of Biomedical Engineering*, vol. 13, no. 3, pp. 197 – 202, 1991. [Online]. Available: <http://www.sciencedirect.com/science/article/pii/014154259190126R>
- [16] Z. Wu and H. Wang, "Microwave tomography for industrial process imaging: Example applications and experimental results." *IEEE Antennas and Propagation Magazine*, vol. 59, no. 5, pp. 61–71, Oct 2017.
- [17] Z. Wu, H. McCann, L. E. Davis, J. Hu, A. Fontes, and C. G. Xie, "Microwave-tomographic system for oil- and gas-multiphase-flow imaging," *Measurement Science and Technology*, vol. 20, no. 10, p. 104026, 2009. [Online]. Available: <http://stacks.iop.org/0957-0233/20/i=10/a=104026>
- [18] C. Pichot, J. Y. Dauvignac, C. Dourthe, I. Aliferis, and E. Guillaumont, "Inversion algorithms and measurement systems for microwave tomography of buried objects," in *IMTC/99*.

Proceedings of the 16th IEEE Instrumentation and Measurement Technology Conference (Cat. No.99CH36309), vol. 3, 1999, pp. 1570–1575 vol.3.

- [19] C. Dourthe, C. Pichot, J. Y. Dauvignac, and J. Cariou, “Inversion algorithm and measurement system for microwave tomography of buried object,” *Radio Science*, vol. 35, no. 5, pp. 1097–1108, 2000. [Online]. Available: <http://dx.doi.org/10.1029/1999RS002244>
- [20] E. R. Almeida, J. L. Porsani, I. Catapano, G. Gennarelli, and F. Soldovieri, “Microwave tomography-enhanced gpr in forensic surveys: The case study of a tropical environment,” *IEEE Journal of Selected Topics in Applied Earth Observations and Remote Sensing*, vol. 9, no. 1, pp. 115–124, Jan 2016.
- [21] C. Pichot, L. Jofre, G. Peronnet, and J. Bolomey, “Active microwave imaging of inhomogeneous bodies,” *IEEE Transactions on Antennas and Propagation*, vol. 33, no. 4, pp. 416–425, Apr 1985.
- [22] J. C. Bolomey, A. Izadnegahdar, L. Jofre, C. Pichot, G. Peronnet, and M. Solaimani, “Microwave Diffraction Tomography for Biomedical Applications,” *IEEE Transactions on Microwave Theory Techniques*, vol. 30, pp. 1998–2000, Nov. 1982.
- [23] N. K. Nikolova, “Microwave imaging for breast cancer,” *IEEE Microwave Magazine*, vol. 12, no. 7, pp. 78–94, Dec 2011.
- [24] R. C. Conceição, J. J. Mohr, and M. O’Halloran, *An Introduction to Microwave Imaging for Breast Cancer Detection*. Springer, 2016.
- [25] N. Celik, R. Gagarin, H. s. Youn, and M. F. Iskander, “A noninvasive microwave sensor and signal processing technique for continuous monitoring of vital signs,” *IEEE Antennas and Wireless Propagation Letters*, vol. 10, pp. 286–289, 2011.
- [26] M. Hopfer, R. Planas, A. Hamidipour, T. Henriksson, and S. Semenov, “Electromagnetic tomography for detection, differentiation, and monitoring of brain stroke: A virtual data and human head phantom study.” *IEEE Antennas and Propagation Magazine*, vol. 59, no. 5, pp. 86–97, Oct 2017.
- [27] A. T. Mobashsher, A. Mahmoud, and A. M. Abbosh, “Portable wideband microwave imaging system for intracranial hemorrhage detection using improved back-projection algorithm with model of effective head permittivity,” *Scientific Reports*, vol. Article number: 20459, no. 16, pp. 860–874, 2016.
- [28] S. M. Salvador, E. C. Fear, M. Okoniewski, and J. R. Matyas, “Exploring joint tissues with microwave imaging,” *IEEE Transactions on Microwave Theory and Techniques*, vol. 58, no. 8, pp. 2307–2313, Aug 2010.
- [29] G. Bellizzi, O. M. Bucci, and I. Catapano, “Microwave cancer imaging exploiting magnetic nanoparticles as contrast agent,” *IEEE Transactions on Biomedical Engineering*, vol. 58, no. 9, pp. 2528–2536, Sept 2011.

Bibliography

- [30] M. T. Bevacqua and R. Scapaticci, "A compressive sensing approach for 3d breast cancer microwave imaging with magnetic nanoparticles as contrast agent," *IEEE Transactions on Medical Imaging*, vol. 35, no. 2, pp. 665–673, Feb 2016.
- [31] E. Burdette, F. Cain, and J. Seals, "In situ permittivity at microwave frequencies: perspectives, techniques, results," in *Medical Applications of Microwave Imaging*. L.E. Larsen and J.H. Jacobi Eds, New-York, IEEE, 1986, pp. 13–40.
- [32] R. Chandra, H. Zhou, I. Balasingham, and R. M. Narayanan, "On the opportunities and challenges in microwave medical sensing and imaging," *IEEE Transactions on Biomedical Engineering*, vol. 62, no. 7, pp. 1667–1682, July 2015.
- [33] "Medfield diagnostics AB (Strokefinder™)," <http://www.medfielddiagnostics.com/en/products/>, accessed: 2018-01-21.
- [34] J. Ljungqvist, S. Candefjord, M. Persson, L. E. Jönsson, T. S. Skoglund, and M. Elam, "Clinical evaluation of a microwave-based device for detection of traumatic intracranial hemorrhage," vol. 34, p. 2176–2182.
- [35] "Emtensor GmbH," <http://emtensor.com/technology/>, accessed: 2018-01-21.
- [36] M. Persson, A. Fhager, H. D. Trefná, Y. Yu, T. McKelvey, G. Pegenius, J. E. Karlsson, and M. Elam, "Microwave-based stroke diagnosis making global prehospital thrombolytic treatment possible," *IEEE Transactions on Biomedical Engineering*, vol. 61, no. 11, pp. 2806–2817, Nov 2014.
- [37] J. C. Lin and M. J. Clarke, "Microwave imaging of cerebral edema," *Proceedings of the IEEE*, vol. 70, no. 5, pp. 523–524, May 1982.
- [38] E Hecht, "New development in FreeFem++." *Journal of Numerical Mathematics*, vol. 20, no. 3-4, pp. 251–266, 2013.
- [39] P. H. Tournier, M. Bonazzoli, V. Dolean, F. Rapetti, F. Hecht, F. Nataf, I. Aliferis, I. E. Kanfoud, C. Migliaccio, M. de Buhan, M. Darbas, S. Semenov, and C. Pichot, "Numerical modeling and high-speed parallel computing: New perspectives on tomographic microwave imaging for brain stroke detection and monitoring." *IEEE Antennas and Propagation Magazine*, vol. 59, no. 5, pp. 98–110, Oct 2017.
- [40] M. Slaney, A. C. Kak, and L. E. Larsen, "Limitations of imaging with first-order diffraction tomography," *IEEE Transactions on Microwave Theory and Techniques*, vol. 32, no. 8, pp. 860–874, Aug 1984.
- [41] G. Oliveri, M. Salucci, N. Anselmi, and A. Massa, "Compressive sensing as applied to inverse problems for imaging: Theory, applications, current trends, and open challenges." *IEEE Antennas and Propagation Magazine*, vol. 59, no. 5, pp. 34–46, Oct 2017.

- [42] M. T. Bevacqua, L. Crocco, L. D. Donato, and T. Isernia, "Microwave imaging of nonweak targets via compressive sensing and virtual experiments," *IEEE Antennas and Wireless Propagation Letters*, vol. 14, pp. 1035–1038, 2015.
- [43] D. Ireland, K. Bialkowski, and A. Abbosh, "Microwave imaging for brain stroke detection using Born iterative method," *IET Microwaves, Antennas & Propagation*, vol. 7, no. 11, pp. 909–915, August 2013.
- [44] O. M. Bucci, N. Cardace, L. Crocco, and T. Isernia, "Degree of nonlinearity and a new solution procedure in scalar two-dimensional inverse scattering problems," *J. Opt. Soc. Am. A*, vol. 18, no. 8, pp. 1832–1843, Aug 2001. [Online]. Available: <http://josaa.osa.org/abstract.cfm?URI=josaa-18-8-1832>
- [45] R. Scapatucci, O. M. Bucci, I. Catapano, and L. Crocco, "Differential microwave imaging for brain stroke followup," *International Journal of Antennas and Propagation*, vol. 2014, p. 11 pages, 2014.
- [46] I. Bisio, A. Fedeli, F. Lavagetto, M. Pastorino, A. Randazzo, A. Sciarrone, and E. Tavanti, "A numerical study concerning brain stroke detection by microwave imaging systems," *Multimedia Tools and Applications*, Jun 2017. [Online]. Available: <https://doi.org/10.1007/s11042-017-4867-7>
- [47] R. Scapatucci, L. D. Donato, I. Catapano, and L. Crocco, "A feasibility study on microwave imaging for brain stroke monitoring," *Progress In Electromagnetics Research B*, vol. 40, pp. 305–324, 2012.
- [48] M. M. Botha, "Solving the volume integral equations of electromagnetic scattering," *Journal of Computational Physics*, vol. 218, no. 1, pp. 141 – 158, 2006. [Online]. Available: <http://www.sciencedirect.com/science/article/pii/S0021999106000763>
- [49] J. Markkanen, C. C. Lu, X. Cao, and P. Yla-Oijala, "Analysis of volume integral equation formulations for scattering by high-contrast penetrable objects," *IEEE Transactions on Antennas and Propagation*, vol. 60, no. 5, pp. 2367–2374, May 2012.
- [50] C. S. Geyik, F. Wei, J. W. Massey, and A. E. Yilmaz, "FDTD vs. AIM for bioelectromagnetic analysis," in *Proceedings of the 2012 IEEE International Symposium on Antennas and Propagation*, July 2012, pp. 1–2.
- [51] J. M. Song and W. C. Chew, "Multilevel fast-multipole algorithm for solving combined field integral equations of electromagnetic scattering," *Microwave and Optical Technology Letters*, vol. 10, no. 1, pp. 14–19, 1995. [Online]. Available: <http://dx.doi.org/10.1002/mop.4650100107>
- [52] J. M. Song, C. C. Lu, W. C. Chew, and S. W. Lee, "Fast Illinois solver code (FISC)," *IEEE Antennas and Propagation Magazine*, vol. 40, no. 3, pp. 27–34, Jun 1998.

Bibliography

- [53] J. R. Phillips and J. K. White, "A precorrected-FFT method for electrostatic analysis of complicated 3-D structures," *IEEE Transactions on Computer-Aided Design of Integrated Circuits and Systems*, vol. 16, no. 10, pp. 1059–1072, Oct 1997.
- [54] S. Tissari and J. Rahola, "A precorrected-FFT method to accelerate the solution of the forward problem in magnetoencephalography," *Physics in Medicine & Biology*, vol. 48, no. 4, p. 523, 2003. [Online]. Available: <http://stacks.iop.org/0031-9155/48/i=4/a=308>
- [55] E. Bleszynski, M. Bleszynski, and T. Jaroszewicz, "AIM: Adaptive integral method for solving large-scale electromagnetic scattering and radiation problems," *Radio Science*, vol. 31, no. 5, pp. 1225–1251, 1996. [Online]. Available: <http://dx.doi.org/10.1029/96RS02504>
- [56] J. M. Taboada, L. Landesa, F. Obelleiro, J. L. Rodriguez, J. M. Bertolo, M. G. Araujo, J. C. Mouriño, and A. Gomez, "High scalability FMM-FFT electromagnetic solver for supercomputer systems," *IEEE Antennas and Propagation Magazine*, vol. 51, no. 6, pp. 20–28, Dec 2009.
- [57] J. M. Taboada, M. G. Araujo, J. M. Bertolo, L. Landesa, F. Obelleiro, and J. L. Rodriguez, "MLFMA-FFT parallel algorithm for the solution of large-scale problems in electromagnetics," *Progress In Electromagnetics Research*, pp. 15–30, 2010.
- [58] M. Schick, R. Fiedler, E. Lezar, and U. Jakobus, "Car-to-car communication using efficient far-field RCS simulations to account for reflecting objects in the communication path," in *2012 6th European Conference on Antennas and Propagation (EUCAP)*, March 2012, pp. 2039–2042.
- [59] O. Ergül and L. Gürel, "Accurate solutions of extremely large integral-equation problems in computational electromagnetics," *Proceedings of the IEEE*, vol. 101, no. 2, pp. 342–349, Feb 2013.
- [60] D. T. Borup and O. P. Gandhi, "Fast-Fourier-transform method for calculation of SAR distributions in finely discretized inhomogeneous models of biological bodies," *IEEE Transactions on Microwave Theory and Techniques*, vol. 32, no. 4, pp. 355–360, Apr 1984.
- [61] C. Y. Shen, K. J. Glover, M. I. Sancer, and A. D. Varvatsis, "The discrete Fourier transform method of solving differential-integral equations in scattering theory," *IEEE Transactions on Antennas and Propagation*, vol. 37, no. 8, pp. 1032–1041, Aug 1989.
- [62] P. Zwamborn and P. M. van den Berg, "The three dimensional weak form of the conjugate gradient FFT method for solving scattering problems," *IEEE Transactions on Microwave Theory and Techniques*, vol. 40, no. 9, pp. 1757–1766, Sep 1992.
- [63] M. F. Catedra, E. Gago, and L. Nuno, "A numerical scheme to obtain the RCS of three-dimensional bodies of resonant size using the conjugate gradient method and the fast Fourier transform," *IEEE Transactions on Antennas and Propagation*, vol. 37, no. 5, pp. 528–537, May 1989.

- [64] W. C. Chew, J. H. Lin, and X. G. Yang, "An FFT T-matrix method for 3D microwave scattering solutions from random discrete scatterers," *Microwave and Optical Technology Letters*, vol. 9, no. 4, pp. 194–196, 1995. [Online]. Available: <http://dx.doi.org/10.1002/mop.4650090408>
- [65] J. H. Lin and W. C. Chew, "BiCG-FFT T-matrix method for solving for the scattering solution from inhomogeneous bodies," *IEEE Transactions on Microwave Theory and Techniques*, vol. 44, no. 7, pp. 1150–1155, Jul 1996.
- [66] J. J. Mallorqui and M. Rodriguez, "GRATMA method for biomedical applications: comparison with the CGM-FFT," in *IEEE Antennas and Propagation Society International Symposium. 1995 Digest*, vol. 3, June 1995, pp. 1581–1584 vol.3.
- [67] K. Lumme and J. Rahola, "Light scattering by porous dust particles in the discrete-dipole approximation," *Astrophysics Journal*, vol. 425, p. 653–667, 1994.
- [68] C. H. Chan and L. Tsang, "A sparse-matrix canonical-grid method for scattering by many scatterers," *Microwave and Optical Technology Letters*, vol. 8, no. 2, pp. 114–118, 1995. [Online]. Available: <http://dx.doi.org/10.1002/mop.4650080217>
- [69] E. Bleszynski, M. Bleszynski, and T. Jaroszewicz, "A fast integral-equation solver for electromagnetic scattering problems," in *Proceedings of IEEE Antennas and Propagation Society International Symposium and URSI National Radio Science Meeting*, vol. 1, June 1994, pp. 416–419 vol.1.
- [70] J. R. Phillips and J. K. White, "Efficient capacitance extraction of 3D structures using generalized pre-corrected FFT methods," in *Proceedings of 1994 IEEE Electrical Performance of Electronic Packaging*, Nov 1994, pp. 253–256.
- [71] V. Okhmatovski, M. Yuan, I. Jeffrey, and R. Phelps, "A three-dimensional precorrected FFT algorithm for fast method of moments solutions of the mixed-potential integral equation in layered media," *IEEE Transactions on Microwave Theory and Techniques*, vol. 57, no. 12, pp. 3505–3517, Dec 2009.
- [72] X. C. Nie, N. Yuan, L. W. Li, and Y. B. Gan, "Fast analysis of RCS over a frequency band using pre-corrected FFT/AIM and asymptotic waveform evaluation technique," *IEEE Transactions on Antennas and Propagation*, vol. 56, no. 11, pp. 3526–3533, Nov 2008.
- [73] S. S. Bindiganavale, J. L. Volakis, and H. Anastassiou, "Scattering from planar structures containing small features using the adaptive integral method (AIM)," *IEEE Transactions on Antennas and Propagation*, vol. 46, no. 12, pp. 1867–1878, Dec 1998.
- [74] T. F. Eibert and J. L. Volakis, "Adaptive integral method for hybrid FE/BI modeling of 3D doubly periodic structures," in *IEEE Antennas and Propagation Society International Symposium. 1998 Digest. Antennas: Gateways to the Global Network. Held in conjunction with: USNC/URSI National Radio Science Meeting (Cat. No.98CH36*, vol. 3, June 1998, pp. 1754–1757 vol.3.

Bibliography

- [75] F. Ling, C.-F. Wang, and J.-M. Jin, "Application of adaptive integral method to scattering and radiation analysis of arbitrarily shaped planar structures," in *IEEE Antennas and Propagation Society International Symposium. 1998 Digest. Antennas: Gateways to the Global Network. Held in conjunction with: USNC/URSI National Radio Science Meeting (Cat. No.98CH36, vol. 3, June 1998, pp. 1778–1781 vol.3.*
- [76] K. Yang, F. Wei, and A. E. Yilmaz, "Truncated multigrid versus pre-corrected FFT/AIM for bioelectromagnetics: When is $O(n)$ better than $O(n \log n)$?" in *Computational Electromagnetics International Workshop (CEM), 2011, Aug 2011, pp. 153–158.*
- [77] "MiMed," TD1301, COST Action MiMed. <http://cost-action-td1301.org>.
- [78] M. Hopfer, R. Planas, A. Hamidipour, T. Henriksson, and S. Semenov, "Electromagnetic tomography for detection, differentiation, and monitoring of brain stroke: A virtual data and human head phantom study." *IEEE Antennas and Propagation Magazine*, vol. 59, no. 5, pp. 86–97, Oct 2017.
- [79] R. Sahathevan, T. Linden, V. Villemagne, L. Churilov, J. Ly, C. Rowe, G. Donnan, and A. Brodtmann, "Positron emission tomographic imaging in stroke: Cross-sectional and follow-up assessment of amyloid in ischemic stroke," *Stroke*, vol. 47, no. 1, pp. 113–119, 1 2016.
- [80] N. Joachimowicz, C. Conessa, T. Henriksson, and B. Duchêne, "Breast phantoms for microwave imaging," *IEEE Antennas and Wireless Propagation Letters*, vol. 13, pp. 1333–1336, 2014.
- [81] C. Hahn and S. Noghianian, "Heterogeneous breast phantom development for microwave imaging using regression models," *Journal of Biomedical Imaging*, vol. 2012, pp. 6:6–6:6, Jan. 2012. [Online]. Available: <http://dx.doi.org/10.1155/2012/803607>
- [82] M. Lazebnik, L. McCartney, D. Popovic, C. B. Watkins, M. J. Lindstrom, J. Harter, S. Sewall, A. Magliocco, J. H. Booske, M. Okoniewski, and S. C. Hagness, "A large-scale study of the ultrawideband microwave dielectric properties of normal breast tissue obtained from reduction surgeries," *Physics in Medicine & Biology*, vol. 52, no. 10, p. 2637, 2007. [Online]. Available: <http://stacks.iop.org/0031-9155/52/i=10/a=001>
- [83] A. Christ, W. Kainz, E. Hahn, K. Honegger, M. Zefferer, E. Neufeld, W. Rascher, R. Janka, W. Bautz, J. Chen, B. Kiefer, P. Schmitt, H. Hollenbach, J. Shen, M. Oberle, D. Szczerba, A. Kam, J. Guag, and N. Kuster, "The virtual family - development of surface-based anatomical models of two adults and two children for dosimetric simulations," *Physics in Medicine and Biology*, vol. 55, no. 2, 2010.
- [84] P. M. Meaney, C. J. Fox, S. D. Geimer, and K. D. Paulsen, "Electrical characterization of glycerin: Water mixtures: Implications for use as a coupling medium in microwave tomography," *IEEE Transactions on Microwave Theory and Techniques*, vol. 65, no. 5, pp. 1471–1478, May 2017.

- [85] A. J. Devaney, "Inverse problems in scattering and imaging," *Current research topics in diffraction tomography*, p. 47–58, 1992.
- [86] F.-C. Chen and W. C. Chew, "Experimental verification of super resolution in nonlinear inverse scattering," *Applied Physics Letters*, vol. 72, no. 23, pp. 3080–3082, 1998. [Online]. Available: <https://doi.org/10.1063/1.121547>
- [87] P. M. Meaney, K. D. Paulsen, A. Hartov, and R. K. Crane, "Microwave imaging for tissue assessment: initial evaluation in multitarget tissue-equivalent phantoms," *IEEE Transactions on Biomedical Engineering*, vol. 43, no. 9, pp. 878–890, Sept 1996.
- [88] S. Y. Semenov, R. H. Svenson, A. E. Bulyshev, A. E. Souvorov, A. G. Nazarov, Y. E. Sizov, V. G. Posukh, A. V. Pavlovsky, P. N. Repin, and G. P. Tatis, "Spatial resolution of microwave tomography for detection of myocardial ischemia and infarction-experimental study on two-dimensional models," *IEEE Transactions on Microwave Theory and Techniques*, vol. 48, no. 4, pp. 538–544, Apr 2000.
- [89] M. J. Pallone, P. M. Meaney, and K. D. Paulsen, "Surface scanning through a cylindrical tank of coupling fluid for clinical microwave breast imaging," *Medical Physics*, 2012.
- [90] D. Ireland and M. Bialkowski, "Feasibility study on microwave stroke detection using a realistic phantom and the FDTD method," in *2010 Asia-Pacific Microwave Conference*, Dec 2010, pp. 1360–1363.
- [91] J. V. Bladel, *Singular Electromagnetic Fields and Sources*. Oxford: Oxford University Press, 1991.
- [92] T. Sarkar, D. Weiner, and V. Jain, "Some mathematical considerations in dealing with the inverse problem," *IEEE Transactions on Antennas and Propagation*, vol. 29, no. 2, pp. 373–379, March 1981.
- [93] J. Hadamard, "Sur les problèmes aux dérivés partielles et leur signification physique," *Princeton University Bulletin*, vol. 13, pp. 49–52, 1902.
- [94] T. M. Grzegorzcyk, P. M. Meaney, P. A. Kaufman, R. M. diFlorio Alexander, and K. D. Paulsen, "Fast 3-d tomographic microwave imaging for breast cancer detection," *IEEE Transactions on Medical Imaging*, vol. 31, no. 8, pp. 1584–1592, Aug 2012.
- [95] H. Gan and W. Chew, "A discrete BCG-FFT algorithm for solving 3D inhomogeneous scatterer problems," *Journal of Electromagnetic Waves and Applications*, vol. 9, no. 10, pp. 1339–1357, 1995. [Online]. Available: <http://www.tandfonline.com/doi/abs/10.1163/156939395X00082>
- [96] J. Markkanen, P. Yla-Oijala, and A. Sihvola, "Discretization of volume integral equation formulations for extremely anisotropic materials," *IEEE Transactions on Antennas and Propagation*, vol. 60, no. 11, pp. 5195–5202, Nov 2012.

Bibliography

- [97] A. Polimeridis, J. Villena, L. Daniel, and J. White, "Stable FFT-JVIE solvers for fast analysis of highly inhomogeneous dielectric objects," *Journal of Computational Physics*, vol. 269, pp. 280 – 296, 2014. [Online]. Available: <http://www.sciencedirect.com/science/article/pii/S0021999114002071>
- [98] D. Schaubert, D. Wilton, and A. Glisson, "A tetrahedral modeling method for electromagnetic scattering by arbitrarily shaped inhomogeneous dielectric bodies," *IEEE Transactions on Antennas and Propagation*, vol. 32, no. 1, pp. 77–85, Jan 1984.
- [99] J. J.-H. Wang, *Generalized Moment Methods in Electromagnetics*. New York: John Wiley, 1991.
- [100] E. K. Miller, L. N. Medgyesi-Mitschang, and E. H. Newman, *Computational Electromagnetics: Frequency Domain Method of Moments*. New York: IEEE Press, 1992.
- [101] K. Lumme and J. Rahola, "Comparison of light scattering by stochastically rough spheres, best-fit spheroids and spheres," *Journal of Quantitative Spectroscopy and Radiative Transfer*, vol. 60, no. 3, pp. 439 – 450, 1998. [Online]. Available: <http://www.sciencedirect.com/science/article/pii/S0022407398000181>
- [102] L. Tsang, K. H. Ding, S. E. Shih, and J. A. Kong, "Scattering of electromagnetic waves from dense distributions of spheroidal particles based on monte carlo simulations," *J. Opt. Soc. Am. A*, vol. 15, no. 10, pp. 2660–2669, Oct 1998. [Online]. Available: <http://josaa.osa.org/abstract.cfm?URI=josaa-15-10-2660>
- [103] K. Tanaka and M. Tanaka, "Analysis and numerical computation of diffraction of an optical field by a subwavelength-size aperture in a thick metallic screen by use of a volume integral equation," *Appl. Opt.*, vol. 43, no. 8, pp. 1734–1746, Mar 2004. [Online]. Available: <http://ao.osa.org/abstract.cfm?URI=ao-43-8-1734>
- [104] —, "Optimized computer-aided design of i-shaped subwavelength aperture for high intensity and small spot size," *Optics Communications*, vol. 233, no. 4, pp. 231 – 244, 2004. [Online]. Available: <http://www.sciencedirect.com/science/article/pii/S0030401804000525>
- [105] J. Avelin, R. Sharma, I. Hanninen, and A. H. Sihvola, "Polarizability analysis of cubical and square-shaped dielectric scatterers," *IEEE Transactions on Antennas and Propagation*, vol. 49, no. 3, pp. 451–457, Mar 2001.
- [106] C. C. Lu, "Indoor radio-wave propagation modeling by multilevel fast multipole algorithm," *Microwave and Optical Technology Letters*, vol. 29, no. 3, pp. 168–175, 2001. [Online]. Available: <http://dx.doi.org/10.1002/mop.1119>
- [107] W. Chew, E. Michielssen, J. M. Song, and J. M. Jin, *Fast and Efficient Algorithms in Computational Electromagnetics*. Norwood, MA, USA: Artech House, Inc., 2001.

-
- [108] C. C. Lu and W. C. Chew, "A coupled surface-volume integral equation approach for the calculation of electromagnetic scattering from composite metallic and material targets," *IEEE Transactions on Antennas and Propagation*, vol. 48, no. 12, pp. 1866–1868, Dec 2000.
- [109] L. S. Mendes and S. A. Carvalho, "Scattering of em waves by homogeneous dielectrics with the use of the method of moments and 3d solenoidal basis functions," *Microwave and Optical Technology Letters*, vol. 12, no. 6, pp. 327–331, 1996. [Online]. Available: [http://dx.doi.org/10.1002/\(SICI\)1098-2760\(19960820\)12:6<327::AID-MOP7>3.0.CO;2-H](http://dx.doi.org/10.1002/(SICI)1098-2760(19960820)12:6<327::AID-MOP7>3.0.CO;2-H)
- [110] S. Kulkarni, R. Lemdiasov, R. Ludwig, and S. Makarov, "Comparison of two sets of low-order basis functions for tetrahedral vie modeling," *IEEE Transactions on Antennas and Propagation*, vol. 52, no. 10, pp. 2789–2795, Oct 2004.
- [111] I.-T. Chiang and W.-C. Chew, "New formulation and iterative solution for low-frequency volume integral equation," *Journal of Electromagnetic Waves and Applications*, vol. 19, no. 3, pp. 289–306, 2005. [Online]. Available: <https://doi.org/10.1163/1569393054139633>
- [112] A. F. Peterson, "A magnetic field integral equation formulation for electromagnetic scattering from inhomogeneous 3d dielectric bodies," in *Proceedings of the 5th Annual Review of Progress in Applied Computational Electromagnetics*, 1989, p. 387–403.
- [113] J. L. Volakis, "Alternative field representations and integral equations for modeling inhomogeneous dielectrics," *IEEE Transactions on Microwave Theory and Techniques*, vol. 40, no. 3, pp. 604–608, Mar 1992.
- [114] B. C. Usner, K. Sertel, M. A. Carr, and J. L. Volakis, "Generalized volume-surface integral equation for modeling inhomogeneities within high contrast composite structures," *IEEE Transactions on Antennas and Propagation*, vol. 54, no. 1, pp. 68–75, Jan 2006.
- [115] M. C. van Beurden and S. J. L. van Eijndhoven, "Gaps in present discretization schemes for domain integral equations," in *2007 International Conference on Electromagnetics in Advanced Applications*, Sept 2007, pp. 673–675.
- [116] L. E. Sun and W. C. Chew, "A novel formulation of the volume integral equation for electromagnetic scattering," *Waves in Random and Complex Media*, vol. 19, no. 1, pp. 162–180, 2009. [Online]. Available: <https://doi.org/10.1080/17455030802545658>
- [117] J. P. Webb, "Hierarchical vector basis functions of arbitrary order for triangular and tetrahedral finite elements," *IEEE Transactions on Antennas and Propagation*, vol. 47, no. 8, pp. 1244–1253, Aug 1999.
- [118] N. A. Ozdemir and J. F. Lee, "A nonconformal volume integral equation for electromagnetic scattering from penetrable objects," *IEEE Transactions on Magnetics*, vol. 43, no. 4, pp. 1369–1372, April 2007.

Bibliography

- [119] K. Sertel and J. L. Volakis, "Multilevel fast multipole method solution of volume integral equations using parametric geometry modeling," *IEEE Transactions on Antennas and Propagation*, vol. 52, no. 7, pp. 1686–1692, July 2004.
- [120] T. K. Sarkar, E. Arvas, and S. Ponnappalli, "Electromagnetic scattering from dielectric bodies," *IEEE Transactions on Antennas and Propagation*, vol. 37, no. 5, pp. 673–676, May 1989.
- [121] M. S. Tong, Z. G. Qian, and W. C. Chew, "Nyström method solution of volume integral equations for electromagnetic scattering by 3d penetrable objects," *IEEE Transactions on Antennas and Propagation*, vol. 58, no. 5, pp. 1645–1652, May 2010.
- [122] C. Balanis, *Advanced Engineering Electromagnetics*. New York: John Wiley, 1989.
- [123] D. Wilton, S. Rao, A. Glisson, D. Schaubert, O. Al-Bundak, and C. Butler, "Potential integrals for uniform and linear source distributions on polygonal and polyhedral domains," *IEEE Transactions on Antennas and Propagation*, vol. 32, no. 3, pp. 276–281, Mar 1984.
- [124] R. D. Graglia, "On the numerical integration of the linear shape functions times the 3-d Green's function or its gradient on a plane triangle," *IEEE Transactions on Antennas and Propagation*, vol. 41, no. 10, pp. 1448–1455, Oct 1993.
- [125] S. Jarvenpaa, M. Taskinen, and P. Yla-Oijala, "Singularity subtraction technique for high-order polynomial vector basis functions on planar triangles," *IEEE Transactions on Antennas and Propagation*, vol. 54, no. 1, pp. 42–49, Jan 2006.
- [126] M. G. Duffy, "Quadrature over a pyramid or cube of integrands with a singularity at a vertex," *SIAM Journal on Numerical Analysis*, vol. 19, no. 6, pp. 1260–1262, 1982. [Online]. Available: <https://doi.org/10.1137/0719090>
- [127] C. Schwab and W. L. Wendland, "On numerical cubatures of singular surface integrals in boundary element methods," *Numerische Mathematik*, vol. 62, no. 1, pp. 343–369, Dec 1992. [Online]. Available: <https://doi.org/10.1007/BF01396234>
- [128] Ismatullah and T. F. Eibert, "Adaptive singularity cancellation for efficient treatment of near-singular and near-hypersingular integrals in surface integral equation formulations," *IEEE Transactions on Antennas and Propagation*, vol. 56, no. 1, pp. 274–278, Jan 2008.
- [129] A. G. Polimeridis and T. V. Yioultsis, "On the direct evaluation of weakly singular integrals in galerkin mixed potential integral equation formulations," *IEEE Transactions on Antennas and Propagation*, vol. 56, no. 9, pp. 3011–3019, Sept 2008.
- [130] A. G. Polimeridis, F. Vipiana, J. R. Mosig, and D. R. Wilton, "DIRECTFN: Fully numerical algorithms for high precision computation of singular integrals in Galerkin SIE methods," *IEEE Transactions on Antennas and Propagation*, vol. 61, no. 6, pp. 3112–3122, June 2013.

-
- [131] A. D. Yaghjian, "Electric dyadic Green's functions in the source region," *Proceedings of the IEEE*, vol. 68, no. 2, pp. 248–263, Feb 1980.
- [132] D. E. Livesay and K. Chen, "Electromagnetic fields induced inside arbitrarily shaped biological bodies," *IEEE Transactions on Microwave Theory and Techniques*, vol. 22, no. 12, pp. 1273–1280, Dec 1974.
- [133] N. V. Budko and A. B. Samokhin, "Spectrum of the volume integral operator of electromagnetic scattering," *SIAM Journal on Scientific Computing*, vol. 28, no. 2, pp. 682–700, 2006. [Online]. Available: <https://doi.org/10.1137/050630660>
- [134] S. T. Choi, "Minimal residual methods for complex symmetric, skew symmetric, and skew hermitian systems," *CoRR*, vol. abs/1304.6782, 2013. [Online]. Available: <http://arxiv.org/abs/1304.6782>
- [135] S.-C. T. Choi, C. C. Paige, and M. A. Saunders, "MINRES-QLP: A Krylov subspace method for indefinite or singular symmetric systems," *SIAM Journal on Scientific Computing*, vol. 33, no. 4, pp. 1810–1836, 2011. [Online]. Available: <https://doi.org/10.1137/100787921>
- [136] J. Liesen and P. Tichý, "Convergence analysis of Krylov subspace methods," *GAMM-Mitteilungen*, vol. 27, no. 2, pp. 153–173, 2004. [Online]. Available: <http://dx.doi.org/10.1002/gamm.201490008>
- [137] A. Brandt, "Multi-level adaptive solutions to boundary-value problems," *Mathematics of Computation*, vol. 31, no. 138, pp. 333–390, 1977. [Online]. Available: <http://www.jstor.org/stable/2006422>
- [138] M. Hopfer, R. Planas, A. Hamidipour, T. Henriksson, and S. Semenov, "Electromagnetic tomography for detection, differentiation, and monitoring of brain stroke: A virtual data and human head phantom study." *IEEE Antennas and Propagation Magazine*, vol. 59, no. 5, pp. 86–97, Oct 2017.
- [139] L. Johan, C. Stefan, P. Mikael, J. Lars, S. Thomas, and E. Mikael, "Clinical evaluation of a microwave-based device for detection of traumatic intracranial hemorrhage," *Journal of Neurotrauma*, vol. 34, no. 13, pp. 2176–2182, July 2017.
- [140] A. P. Moneda, M. P. Ioannidou, and D. P. Chrissoulidis, "Radio-wave exposure of the human head: analytical study based on a versatile eccentric spheres model including a brain core and a pair of eyeballs," *IEEE Transactions on Biomedical Engineering*, vol. 50, no. 6, pp. 667–676, June 2003.
- [141] Y. Taki, B. Thyreau, S. Kinomura, K. Sato, R. Goto, R. Kawashima, and H. Fukuda, "Correlations among brain gray matter volumes, age, gender, and hemisphere in healthy individuals," *PLOS ONE*, vol. 6, no. 7, pp. 1–13, 07 2011. [Online]. Available: <https://doi.org/10.1371/journal.pone.0022734>

Bibliography

- [142] D. Andreuccetti, R. Fossi, and C. Petrucci, "An internet resource for the calculation of the dielectric properties of body tissues in the frequency range 10 Hz - 100 GHz."
- [143] S. Gabriel, R. W. Lau, and C. Gabriel, "The dielectric properties of biological tissues: III. parametric models for the dielectric spectrum of tissues," *Physics in Medicine & Biology*, vol. 41, no. 11, p. 2271, 1996. [Online]. Available: <http://stacks.iop.org/0031-9155/41/i=11/a=003>
- [144] W. C. Chew, *Waves and fields in inhomogeneous media*. New York: IEEE Press, 1995.
- [145] B. Guerin, J. P. Stockmann, M. Baboli, A. Torrado-Carvajal, A. V. Stenger, and L. L. Wald, "Robust time-shifted spoke pulse design in the presence of large b_0 variations with simultaneous reduction of through-plane dephasing, b_{11} effects, and the specific absorption rate using parallel transmission," *Magnetic Resonance in Medicine*, vol. 76, p. 540–554, 2016.
- [146] N. Joachimowicz, B. Duchêne, C. Conessa, and O. Meyer, "Reference phantoms for microwave imaging," in *2017 11th European Conference on Antennas and Propagation (EUCAP)*, March 2017, pp. 2719–2722.
- [147] R. A. Shore, "Scattering of an electromagnetic linearly polarized plane wave by a multi-layered sphere: Obtaining a computational form of Mie coefficients for the scattered field." *IEEE Antennas and Propagation Magazine*, vol. 57, no. 6, pp. 69–116, Dec 2015.
- [148] A. T. Mobashsher and A. M. Abbosh, "On-site rapid diagnosis of intracranial hematoma using portable multi-slice microwave imaging system," *Scientific Reports*, vol. 6, p. 37620, 2016.
- [149] A. T. Mobashsher, K. S. Bialkowski, A. M. Abbosh, and S. Crozier, "Design and experimental evaluation of a non-invasive microwave head imaging system for intracranial haemorrhage detection," *PLOS ONE*, vol. 11, no. 4, pp. 1–29, 04 2016. [Online]. Available: <https://doi.org/10.1371/journal.pone.0152351>
- [150] M. Persson, A. Fhager, H. D. Trefná, Y. Yu, T. McKelvey, G. Pegenius, J. E. Karlsson, and M. Elam, "Microwave-based stroke diagnosis making global prehospital thrombolytic treatment possible," *IEEE Transactions on Biomedical Engineering*, vol. 61, no. 11, pp. 2806–2817, Nov 2014.
- [151] A. T. Mobashsher and A. M. Abbosh, "Three-dimensional human head phantom with realistic electrical properties and anatomy," *IEEE Antennas and Wireless Propagation Letters*, vol. 13, pp. 1401–1404, 2014.
- [152] M. J. Burfeindt, T. J. Colgan, R. O. Mays, J. D. Shea, N. Behdad, B. D. V. Veen, and S. C. Hagness, "MRI-derived 3-D-printed breast phantom for microwave breast imaging validation," *IEEE Antennas and Wireless Propagation Letters*, vol. 11, pp. 1610–1613, 2012.

- [153] M. Bjelogrić, B. Fuchs, J. P. Thiran, J. R. Mosig, and M. Mattes, “Experimental verification of optimal frequency range for microwave head imaging,” in *International Conference on Electromagnetics in Advanced Applications (ICEAA)*, Sept 2017, pp. 1008–1011.
- [154] R. Lee and M. Baddour, “Absolute gain measurement by the image method under mismatched condition,” in *Antennas and Propagation Society International Symposium*, vol. 25, June 1987, pp. 398–401.
- [155] T. Rubæk, O. S. Kim, and P. Meincke, “Computational validation of a 3-d microwave imaging system for breast-cancer screening,” *IEEE Transactions on Antennas and Propagation*, vol. 57, no. 7, pp. 2105–2115, July 2009.
- [156] M. Born, “Zur Quantenmechanik der Stoßvorgänge,” *Zeitschrift für Physik*, vol. 37, no. 12, pp. 863–867, Dec 1926. [Online]. Available: <https://doi.org/10.1007/BF01397477>
- [157] S. L. Keeling, “Total variation based convex filters for medical imaging,” *Applied Mathematics and Computation*, vol. 139, no. 1, pp. 101 – 119, 2003. [Online]. Available: <http://www.sciencedirect.com/science/article/pii/S0096300302001716>
- [158] S. Semenov, B. Seiser, E. Stoegmann, and E. Auff, “Electromagnetic tomography for brain imaging: From virtual to human brain,” in *2014 IEEE Conference on Antenna Measurements Applications (CAMA)*, Nov 2014, pp. 1–4.
- [159] G. Golub and C. V. Loan, *Matrix Computation*, 2nd ed. The Johns Hopkins University Press, 1989.
- [160] YALL1 basic solver code: Y. Zhang, J. Yang, and W. Yin. YALL1: Your ALgorithms for L1, online at yall1.blogs.rice.edu, 2011.
- [161] M. Grant and S. Boyd, “CVX: Matlab software for disciplined convex programming, version 2.1,” <http://cvxr.com/cvx>, Mar. 2014.
- [162] M. C. Grant and S. P. Boyd, *Graph Implementations for Nonsmooth Convex Programs*. London: Springer London, 2008, pp. 95–110. [Online]. Available: https://doi.org/10.1007/978-1-84800-155-8_7
- [163] D. L. Donoho, “Compressed sensing,” *IEEE Transactions on Information Theory*, vol. 52, no. 4, pp. 1289–1306, April 2006.
- [164] E. J. Candès, M. B. Wakin, and S. P. Boyd, “Enhancing sparsity by reweighted ℓ_1 minimization,” *Journal of Fourier Analysis and Applications*, vol. 14, no. 5, pp. 877–905, Dec 2008. [Online]. Available: <https://doi.org/10.1007/s00041-008-9045-x>
- [165] L. I. Rudin, S. Osher, and E. Fatemi, “Nonlinear total variation based noise removal algorithms,” *Physica D: Nonlinear Phenomena*, vol. 60, no. 1, pp. 259 – 268, 1992. [Online]. Available: <http://www.sciencedirect.com/science/article/pii/016727899290242F>

Bibliography

- [166] M. Bjelogrić, M. Mattes, I. Koufogiannis, S. Capdevila, and J. R. Mosig, "Volume integral equation formulation for medical applications," in *9th European Conference on Antennas and Propagation (EuCAP)*, May 2015, pp. 1–2.
- [167] A. Wirgin, "The inverse crime," Jan. 2004, working paper or preprint. [Online]. Available: <https://hal.archives-ouvertes.fr/hal-00001084>
- [168] M. Bjelogrić, M. Volery, B. Fuchs, J. P. Thiran, J. R. Mosig, and M. Mattes, "Stratified spherical model for microwave imaging of the brain: Analysis and experimental validation of transmitted power," *Microwave and Optical Technology Letters*, 2018.
- [169] M. Bjelogrić, B. Fuchs, J. R. Mosig, and M. Mattes, "On the Born approximation for differential microwave imaging using volume integral equation formulation," in *International Conference on Electromagnetics in Advanced Applications (ICEAA)*, Sept 2016, pp. 487–490.
- [170] M. Bjelogrić, B. Fuchs, and M. Mattes, "Contributions to 3D differential microwave imaging," in *10th European Conference on Antennas and Propagation (EuCAP)*, April 2016, pp. 1–3.
- [171] M. Bjelogrić, R. Scapatucci, J. R. Mosig, L. Crocco, and M. Mattes, "Numerical assessment of brain stroke follow-up via differential microwave imaging," in *International Conference on Electromagnetics in Advanced Applications (ICEAA)*, Sept 2015, pp. 484–485.
- [172] M. Bjelogrić, B. Fuchs, J. P. Thiran, and M. Mattes, "Comparison of regularization techniques for microwave imaging of brain stroke," in *accepted in 12th European Conference on Antennas and Propagation (EuCAP)*, 2018.
- [173] M. Hofmann, G. Fischer, R. Weigel, and D. Kissinger, "Microwave-based noninvasive concentration measurements for biomedical applications," *IEEE Transactions on Microwave Theory and Techniques*, vol. 61, no. 5, pp. 2195–2204, May 2013.
- [174] "A.a. martinis center / wald group anthropomorphic phantom builder's wiki." [Online]. Available: https://phantoms.martinos.org/Main_Page
- [175] C. H. Wilcox, "An expansion theorem for electromagnetic fields," *Communications on Pure and Applied Mathematics*, vol. 9, no. 2, pp. 115–134, 1956. [Online]. Available: <http://dx.doi.org/10.1002/cpa.3160090202>
- [176] D. A. M. Iero, L. Crocco, and T. Isernia, "Thermal and microwave constrained focusing for patient-specific breast cancer hyperthermia: A robustness assessment," *IEEE Transactions on Antennas and Propagation*, vol. 62, no. 2, pp. 814–821, Feb 2014.

List of Figures

1.1	Stroke representations [9]. CT scan of an ischaemic stroke (left) and NMR image of a haemorrhagic stroke (right) ©2016, WebMD LLC All rights reserved.	2
2.1	Current technologies and main characteristics for imaging brain stroke pathologies. MRI: Magnetic Resonance Imaging; CT: Computed Tomography; PET: Positron Emission Tomography; US: Ultra-Sound Imaging; MWI: Microwave Imaging.	13
2.2	Sagittal (left), coronal (center) and axial/transverse (right) views of the conductivity (top) and relative permittivity (bottom) of a human realistic model [83] at 1 GHz.	14
2.3	Statistics about dispersion of the overall head tissues; median (blue circled dot), 25 th and 75 th percentiles (blue boxes), extreme data points (whiskers) and outliers (red crosses).	15
2.4	Representation of a scatterer (red) with its domain denoted by Ω with constitutive parameters $\epsilon(\vec{r})$, $\mu(\vec{r})$ and $\sigma(\vec{r})$, immersed in an infinite background medium of dielectric properties ϵ_b , μ_b and σ_b . The dark blue lines represent the incident field and the black (full and dashed lines) represent the scattered field (produced by currents $\mathbf{J}_p(\vec{r})$).	19
2.5	Framework of Forward and Inverse scattering problems.	20
2.6	Representation of the field incident on and scattered by the head model. The solid line represents a direct or first order interaction (5.11), while the dashed line is an example of a second order interaction.	21
2.7	Well-conditioned and ill-conditioned 1D representations.	22
3.1	Schematic summary of the singularity management in VIE for the contrast-source formulation.	36
3.2	Integral Equation solver layout. From core to surface: Integral Equation (IE) formulation, mesh, basis functions, MoM/curvature, matrix assembly, linear system solver, post-processing.	37

List of Figures

- 3.3 Effect of frequency on the spectrum. Left: quasi-static, right: dynamic (cf. Table 3.1). From top to bottom background permittivity $\epsilon_b = 10, 50, 70$, and $\sigma = 0.3, 0.3, 1$ [S/m]. Sphere permittivity is $\epsilon_r = 46$, $\sigma = 0.9$ [S/m]. Grey circles represent the geometrical bounds of the location of each discrete eigenvalue in the complex plane; blue crosses are the discrete eigenvalues; and red dots are the ratios $\chi + 1 = \left(\frac{\epsilon(\vec{r})}{\epsilon_b}\right)$ 44
- 3.4 Effect of frequency on the spectrum. Left: quasi-static, right: dynamic (cf. Table 3.1). From top to bottom background permittivity $\epsilon_b = 10, 50, 70$, and $\sigma = 0.3, 0.3, 1$ [S/m]. Sphere permittivity is a random distribution around $\epsilon_r = 46$, $\sigma = 0.9$ [S/m], with variance equal to a third of the median values for both ϵ_r and σ . Grey circles represent the geometrical bounds of the location of each discrete eigenvalue in the complex plane; blue crosses are the discrete eigenvalues; and red dots are the ratios $\chi + 1 = \left(\frac{\epsilon(\vec{r})}{\epsilon_b}\right)$ 45
- 3.5 Real part (a) and imaginary part (b) of the contrast function χ for a slice of the Duke model (3 mm side voxel length) with a haemorrhagic stroke at 1 GHz.(c) Discrete eigenvalues of the VIE operator. The background medium corresponds to the cases of Table 3.1: case 1 (blue), case 2 (violet), and case 3 (green). 47
- 3.6 Static case. Convergence of the relative error of J_p in % for different grid size h (red), and the total simulation time for different number of unknowns (total number of unknowns) in black. 49
- 3.7 Dynamic case. Residual error in dB vs. number of iterations of the iterative solver at 1, 100, 1000 MHz (blue, green, black). Convergence without preconditioner is plotted using dotted lines and with diagonal preconditioning using solid lines. 50
- 3.8 Schematic of Full-MG (FMG) procedure, with the V-cycle procedure highlighted in yellow. Green, red and black arrows represent, respectively, Restriction, Smoothing and Prediction operations. 52
- 3.9 Error in dB vs. number of iterations of the MG solver at 1, 100, 1000 MHz (blue, green, red) for the homogeneous half sphere of cases 1, 2, 3 (see Table 3.1) with voxels of 8 mm side length. The residue is plotted in solid lines and the absolute error with respect to the solution with the direct solver is plotted with cross markers. 52
- 3.10 Error in dB vs. number of iterations of the MG solver at 1 MHz, 1 GHz, and 2 GHz (blue, green, red) for the inhomogeneous half sphere of case 2 (see Table 3.1) with voxels of 8 mm side length. The residue is plotted in solid lines and the absolute error with respect to the solution with the direct solver is plotted with cross markers. 53
- 3.11 Absolute value of the contrast function of the Duke Model [83] at 1 GHz on a $128 \times 128 \times 16$ grid with voxels of 2 mm side length. The background medium properties are $\epsilon = 50$, $\sigma = 0.3$ [S/m]. 54

3.12	Absolute value of the electric field produced by an impinging z -polarized plane wave on the Duke Model [83] (see Fig. 3.11) at 1 GHz on a $128 \times 128 \times 16$ grid with voxels of 2 mm side length. The background medium properties are $\epsilon = 50$, $\sigma = 0.3$ [S/m].	54
3.13	Residual error in dB vs. number of iterations of the MG solver for the solution for the electric field produced by an impinging z -polarized plane wave on the Duke Model [83] (see Fig. 3.11) at 1 GHz on a $128 \times 128 \times 16$ grid with voxels of 2 mm side length. The background medium properties are $\epsilon = 50$, $\sigma = 0.3$ [S/m].	55
4.1	Planar multilayered model to analyze the power transmitted into the human head. . .	58
4.2	Theoretical dielectric properties [143] of brain (black), CSF (blue), bone (green), fat (light blue) and skin (magenta): (a) relative permittivity ϵ_r ; (b) conductivity σ [S/m].	59
4.3	Amplitude of the transmission coefficient as a function of frequency and medium permittivity [47]. (a) variable relative permittivity $\epsilon_r = [1 - 80]$, lossless medium $\sigma = 0$ [S/m]; (b) variable conductivity $\sigma = [0 - 1]$ [S/m], relative permittivity $\epsilon_r = 40$	60
4.4	Approximation of power attenuation through the head tissues in the exterior limit of the brain: close to the CSF (blue) and middle of the brain (at 43 mm from the CSF) in red. .	61
4.5	Spherical multilayered model to analyze the power transmitted into the human head.	62
4.6	Normalised transmitted power according to the frequency [0.5-4]GHz applying (a) the planar model, (b) the spherical model, for a matching medium of $\epsilon_{mm} = [1-80]$. Cuts for $\epsilon_{mm} = 14, 56$ and 80 of the P_{Nt} computed with the planar (full lines) and spherical (dotted lines) models are shown in (c).	64
4.7	Prototype Multilayered Sphere: (a) glued prototype; (b) before gluing prototype, with blocking caps and syringe.	66
4.8	Agilent measuring system: 85070E Dielectric Probe Kit	67
4.9	Dielectric properties of ABS sample: (a) conductivity σ [S/m]; (b) Relative Permittivity ϵ_r ; (c) picture of ABS sample.	67
4.10	Theoretical (solid line) [143] and measured (dashed line) dielectric properties of the measurements of brain (black), CSF (blue), bone (green), fat (light blue) and skin (magenta). Solid lines are theoretical values and dashed lines are measurements: (a) relative permittivity ϵ_r and (b) conductivity σ [S/m].	68
4.11	Schematic and pictures of the measurement setup.	69
4.12	Schematic of the transmission between the horn antenna (Tx) and the monopole antenna (Rx). The lossy material emulating the head phantom is represented as a planar layer with two interfaces in blue.	70

List of Figures

4.13 Monopole antenna specifications: measurements (blue) and simulations (red).	72
4.14 Correspondance between the 3D printed head phantom and the multilayered spherical model. Plastic shells representation of the phantom in grey and spherical head model in red. Top: three possible configurations with 61 mm (left), 66 mm (middle), and 71 mm (right), outer diameters of the spherical head model.	72
4.15 Normalized transmitted power as a function of the frequency: with 61 mm (blue), 66 mm (red), and 71 mm (green), outer diameters of the spherical head model.	73
4.16 Normalized transmitted power as a function of the frequency: measured (green) and simulated with planar (blue) and spherical (red) models.	74
4.17 Normalized transmitted power as a function of the frequency: measured with the mismatch correction (green solid line) and without the mismatch correction (green dotted line), with the simulated spherical models in the original case (red), in the case with plastic shells and theoretical values for the mixtures (black solid line) or measured values for the mixtures (black dotted line).	75
4.18 CSF, bone, fat and skin influences on the propagation. Top: individual layer influences; bottom: superposition of the individual layer influence with the total influence depicted in blue solid line.	76
5.1 Imaging configuration. Investigation domain Γ , with the dielectric properties of background medium ϵ_b , μ_b , and σ_b . The scatterer under investigation lays in Ω and has the constitutive parameters ϵ , μ , and σ	80
5.2 dMWI scenario: contrast functions at times t_1 and t_2 , and their contrast difference, only non-zero on Ω_Δ	82
5.3 Illustration of the non linear scattering problem in the domain Ω . In dMWI the contrast is only changing in the domain Ω_Δ . The incident field E_i , and the resulting scattered field E_s are depicted, respectively, with blue (zigzag) and black (straight) arrows. The first and second order interactions are depicted in, respectively, solid and dashed black lines.	85
5.4 Sagital (left), coronal (center) and axial/transverse (right) views of the conductivity (top) and relative permittivity (bottom) of a realistic human model [83] of the brain region where the stroke can occur. Frequency was 1 GHz.	86
5.5 Sagital (left), coronal (center) and axial/transverse (right) views of the conductivity (top) and relative permittivity (bottom) of a realistic human model [83] of the brain region of Fig. 5.4 filled with blood. Frequency was 1 GHz.	87

5.6	DNL for dMWI as function of medium relative permittivity ($\epsilon_b = [1 - 80]$) and conductivity ($\sigma_b = [0 - 3]$ [S/m]). The ℓ_2 -norm of $\ GX_1\ _{\Omega_\Delta}$ for the case depicted in Fig. 5.4 (left) and the ℓ_2 -norm of $\ GX_2\ _{\Omega_\Delta}$ for the case depicted in Fig. 5.5 (right).	88
5.7	DNL for MWI (left) and dMWI (right) as function of medium relative permittivity ($\epsilon_b = [1 - 80]$) and conductivity ($\sigma_b = [0 - 3]$ [S/m]). The ℓ_2 -norm of $\max(\ GX_1\ _{\Omega_\Delta}, \ GX_2\ _{\Omega_\Delta})$ which are separately depicted in Fig. 5.6.	88
5.8	Example of singular value distribution.	90
5.9	Single layer imaging configuration. The scatterer (pink cylinder) described by its constitutive parameters ($\epsilon(\vec{r}), \mu(\vec{r}), \sigma(\vec{r})$) in the domain Ω is surrounded by 32 antennas (red, green, and blue arrows) which lay in the background medium ($\epsilon_b(\vec{r}), \mu_b(\vec{r}), \sigma_b(\vec{r})$) in the domain Γ). The emitting antenna is depicted in red and the receiving probe is illustrated in green.	94
5.10	Contrast of different scenarios. From left to right; contrast function at time t_1 , contrast function at time t_2 , and the resulting contrast difference.	96
5.11	DNL for MWI and dMWI of the example of Fig. 5.10 as function of medium relative permittivity ($\epsilon_b = [1 - 80]$) and conductivity ($\sigma_b = [0 - 3]$ S/m). The ℓ_2 -norm of $\max(\ GX_1\ _{\Omega}, \ GX_2\ _{\Omega})$ is depicted on the left, and the ℓ_2 -norm $\max(\ GX_1\ _{\Omega_\Delta}, \ GX_2\ _{\Omega_\Delta})$ on the right.	96
5.12	Inverse problem results at 1 GHz for non-approximated (dashed line) and linear-approximated simulated measurements (solid line) of the model $M1$ (see Table 5.1): (a) MSE as a function of the considered singular values for various SNR (100 (red), 50 (green), 20 (blue) [dB]); (b) considered singular value decomposition of the L operator (light grey triangles are below the numerical limit of the double precision floating numbers).	97
5.13	Inverse problem results at 1 GHz for non-approximated (dashed line) and linear-approximated simulated measurements (solid line): Mean Square Error as a function of the considered singular values for various models ($M1$ (red), $M2$ (blue), $M3$ (green) and $M4$ (black), see Table 5.1) for a high SNR of 100 dB.	98
5.14	Duke head model [83] at 1GHz. From left to right: domains of different values of the contrast function at times t_1 and t_2 , and the difference between the two times.	99
5.15	Duke head model stroke detection. (a) Reconstruction using non-approximated simulated measurements (left) and approximated simulated measurements (right). (b) Normalized absolute value of the contrast difference reference.	99
5.16	Reconstructions using linearized forward problem (left) and using a full-wave VIE solver [166] (right).	101
5.17	Measurement setup. Left; setup schematic, right; picture of the measurement setup.	103

List of Figures

5.18	Measurement setup probe positioning. The antenna positions for emission are numbered in red and the positions for the receiving probes are numbered in green.	103
5.19	Measurement setup; layer filling and stroke phantom.	105
5.20	Contrast function absolute value, with its real part (top) and imaginary part (bottom) at time t_1 (left), time t_2 (center), and their differential contrast $\Delta\chi$ (right).	106
5.21	Absolute value of the reconstructed $\Delta\chi$ based on TSVD (left), ℓ_1 -norm (center), and TV-norm (right) regularization schemes using simulated scattered fields as measurements. 107	107
5.22	Singular value distribution for the inverse scattering operator: considered singular values in opaque colors.	107
5.23	Total scattered fields at 16 receiving antennas while the emitting antenna is placed between antennas #1 and #16. The total field at time t_1 (no stroke) is depicted in solid lines, and at time t_2 (with stroke) in dashed lines. The simulations and measurements are, respectively in red and blue.	108
5.24	Differential scattered fields at 16 receiving antennas while the emitting antenna is placed between antennas #1 and #16. The differential scattered field for simulations and measurements are depicted, respectively with solid and dashed lines.	109
5.25	Absolute value of the reconstructed $\Delta\chi$ based on TSVD (left), ℓ_1 -norm (center), and TV-norm (right) regularization schemes using measured scattered fields.	110
A.1	Definition of the spherical coordinate system	116
A.2	Wilcox spheres	119
B.1	Small multilayered sphere prototype: (a) CAD details; (b) mounting pictures.	121
B.2	Glue tests steps	122
B.3	CAD of the multilayered sphere prototype	123

List of Tables

3.1	Case Study Parameters for the Sphere. Values of the wavenumber k_b [1/m], the contrast χ , and the grid size [m] for three different scattering scenarios with variable contrast, for quasi-static (left) and dynamic (right) illuminations. . . .	43
3.2	Condition Number and Convergence Estimate for increasing wavenumber / frequency without (left) and with (right) diagonal preconditioning.	51
4.1	Triton X-100 and NaCl concentrations for different biological tissues, and thickness of according layers for the multilayered spherical model.	66
5.1	Influence of the DNL on the forward MWI problem	97
5.2	Theoretical and measured dielectric properties at 1 GHz for the tissue mimicking mixtures.	104

List of Acronyms and Abbreviations

1D	one dimensional
2D	two dimensional
3D	three dimensional
ABC	Absorbing Boundary Condition
ABS	Acrylonitrile Butadiene Styrene
AIM	Adaptive Integral Method
COST	European Cooperation in Science & Technology
CS	Compressed Sensing
CT	Computed Tomography
CVD	CerebroVascular Disease
dMWI	differential MicroWave Imaging
EM	ElectroMagnetic
EPFL	Ecole Polytechnique Fédérale de Lausanne
FFT	Fast Fourier Transform
FEM	Finite Element Method
FDTD	Finite Difference Time Domain
GMRES	Generalized Minimal Residual Method
HP	Hewlett-Packard
HPC	High Performance Computing
IE	Integral Equation
IEEE	Institute of Electrical and Electronics Engineers

Appendix B. List of Acronyms and Abbreviations

ISM	Industrial, Scientific, and Medical
LEMA	Laboratoire d'ElectroMagnetisme et d'Acoustique
LTS5	Laboratoire de Traitement des Signaux 5
MINRES	Minimal Residual Method
MLFMA	Multi-Level Fast Multipole Algorithm
MoM	Method of Moments
MRI	Magnetic Resonance Imaging
MWI	MicroWave Imaging
MWT	MicroWave Technology
NASA	National Aeronautics and Space Administration
NMR	Nuclear Magnetic Resonance
pFFT	pre-corrected Fast Fourier Transform
RF	Radio Frequency
RFID	Radio Frequency IDentification
SIE	Surface Integral Equation
SRR	Short Range Radars
STI	Science et Technique de l'Ingénieur (EPFL)
SWE	Spherical Wave Expansion
TD1301 MiMed	Development of a European-based Collaborative Network to Accelerate Technological, Clinical and Commercialisation Progress in the Area of MEDical MICrowave Imaging
VIE	Volume Integral Equation

Curriculum Vitae

Mina Bjelogric
Chemin des Pépinières 1, CH-1180 Rolle
+ 41 78 900 89 29, minabjelo@gmail.com
French, Serbian, Swiss

Currently PhD student at EPFL in the Laboratoire de Traitement des Signaux 5

Research topics: Computational bio-electromagnetics, inverse problems, regularization, microwave imaging.

EDUCATION

- **Master of Science, Electrical Engineering**
Ecole Polytechnique Fédérale de Lausanne (EPFL) Switzerland 2011 – 2013
Specialization: Information Technology
- **Bachelor of Science, Electrical Engineering**
Ecole Polytechnique Fédérale de Lausanne (EPFL) Switzerland 2008 – 2011
Specialization: Signal Processing and Nanoelectronics

ACADEMIC EXPERIENCE

- **National COST project** 2015-2017
High accuracy volume integral equation methods for computational bio-electromagnetics.
Position: Scientist in charge
- **Hasler Foundation** 2014-2015
High accuracy volume integral equation solver for MRI grids
Position: Scientist in charge
- **ABB research center** 2012 – 2013
Applied Physics group for HVDC Insulation
Position: Internship

LIST OF PUBLICATIONS

Journal

[1] **M. Bjelogrljic**, M. Volery, B. Fuchs, J.-P. Thiran and J. R. Mosig and Michael Mattes, "Stratified Spherical Model for Microwave Imaging of the Brain: Analysis and Experimental Validation of Transmitted Power", *Microwave and Optical Technology Letters*, vol.60, no. 4, pp.1042-1048, April 2018.

Book Chapter

[1] R. Scapatucci, **M. Bjelogrljic**, J. A. Tobon Vasquez, F. Vipiana, M. Mattes, and L. Crocco. *Microwave Technology for Brain Imaging and Monitoring: Physical Foundations, Potentials and Limitations*, Springer, 2018.

Conferences

[1] R. Gremaud, **M. Bjelogrljic**, M. Schneider, E. Logakis, C. Schlegel, S. Fürsich, A. Krivda, T. Christen and U. Riechert "Surface charge decay on HVDC insulators: Temperature and Field effects," *IEEE International Conference on Solid Dielectrics (ICSD)*, pp.1056-1059, 2013. doi=10.1109/ICSD.2013.6619685, ISSN=1553-5282.

[2] **M. Bjelogrljic**, M. Mattes, I. Koufogiannis, S. Capdevila and J. R. Mosig, "Volume integral equation formulation for medical applications," *9th European Conference on Antennas and Propagation (EuCAP)*, Lisbon, Portugal, 2015, pp. 1-2.

[3] **M. Bjelogrljic**, R. Scapatucci, J. R. Mosig, L. Crocco and M. Mattes, "Numerical assessment of brain stroke follow-up via Differential Microwave Imaging," *International Conference on Electromagnetics in Advanced Applications (ICEAA)*, Turin, Italy, 2015, pp. 484-485.

[4] **M. Bjelogrljic**, B. Fuchs, and M. Mattes, "Contributions to 3D differential microwave imaging," *10th European Conference on Antennas and Propagation (EuCAP)*, Davos, Switzerland, 2016, pp. 1-3.

[5] **M. Bjelogrljic**, B. Fuchs, M. Mattes and J.R.Mosig, "On the Born approximation for differential microwave imaging using volume integral equation formulation ," *International Conference on Electromagnetics in Advanced Applications (ICEAA)*, Cairns, Australia, 2016.

[6] **M. Bjelogrljic**, B. Fuchs, J.-P. Thiran, J. R. Mosig and M. Mattes, "Experimental verification of optimal frequency range for microwave head imaging," *International Conference on Electromagnetics in Advanced Applications (ICEAA)*, Verona, Italy, 2017.

[7] **M. Bjelogrljic**, B. Fuchs, J.-P. Thiran and M. Mattes, "Comparison of Regularization Techniques for Microwave Imaging of Brain Stroke," *12th European Conference on Antennas and Propagation (EuCAP)*, London, UK, April, 9-13, 2018.

